PhD Thesis

MSc. Eng. Armando Zagaroli

Behavior of external clay brick façade walls made of lime-based mortars - experiments and simulation approach of irregular settlements and seismic type cyclic shear loads

Doctoral dissertation submitted in the course of proceedings for the granting of the PhD degree in the discipline of civil engineering, geodesy, and transport

Supervisors:
Prof. Jan Kubica, PhD, DSc. Eng.

Department of Structural Engineering
Faculty of Civil Engineering

Presentation arising from this study

1. 14th North American Masonry Conference, Omaha Campus on June 9-14, 2023 in Omaha, Nebraska, USA.
2. Towards the next generation of sustainable masonry systems: Mortars, renders, plasters and other challenges on November 11-12 in Madeira, Portugal.
3. COMPDYN 2025, 15-18 June 2025, Rhodes Island, Greece, 10th International Conference on Computational Methods in Structural Dynamics and Earthquake Engineering

Publications arising from this study

1. Zagaroli A., Kubica J., Galman I., Falkjar K.: Study on the mechanical properties of two general-purpose cement - lime mortars prepared based on air lime. Materials 2024, 17, 1001. https://doi.org/10.3390/ma16062171.
2. De Vico F.S., Zagaroli A., Rodríguez-Navarro C., Kubica J., Gorski M., Ruiz Agudo E. 2023. A Physico-chemical Study of Lime-based Mortars from Different Historical Periods. NanoWorld J 9(S2): pp.256-S261. DOI:10.17756/nwj.2023-s2-044..
3. Zagaroli, A., De Vico, F.S., Ruiz Agudo E., Kubica, J., Rodríguez-Navarro, C. and Gorski, M., 2023. A comparative study of the composition and physico-mechanical properties of bricks from different periods. Proceedings of 14th North America Masonry Conference, USB device.
4. Zagaroli A., Galman I., Kubica J. " COMPARATIVE EXPERIMENTAL AND NUMERICAL ANALYSIS OF THE IN-PLANE LATERAL CYCLIC BEHAVIOR OF CLAY BRICK AIR LIME-BASED MASONRY WALLS". Proceedings of COMPDYN 2025 10th ECCOMAS Thematic Conference on Computational Methods in Structural Dynamics and Earthquake Engineering. (https://2025.compdyn.org/proceedings).

Acknowledgement

I would like to express my gratitude to all those who have supported and guided me throughout the course of my PhD research. First and foremost, I extend my sincere thanks to my supervisor, Prof. Jan Kubica whose encouragement and constant positive attitude have been invaluable in the most crucial moments of my research path.
I am also deeply grateful to Prof. Marcin Górski for his continuous assistance within and beyond the SUBLime network.
A special thanks goes to all my external colleagues from the SUBLime team, as well as my Polish colleagues and the laboratory staff at the Silesian University of Technology. Your essential assistance and engaging multi-disciplinary discussions during the experimental and analytical phases of this work have been invaluable. Your collaboration and friendship have made this journey both productive and enjoyable, and they have played a significant role in my personal growth.
I would also like to acknowledge the funding support from the Marie Skłodowska-Curie Action for this Innovative Training Network (ETN ITN) and the participation in the Sustainable Building Lime Applications via Circular Economy and Biomimetic Approaches -SUBLime project, which made it possible to carry out this research. This financial support was crucial to facilitate various aspects of this study. Additionally, I extend my gratitude to all the industrial partners who participated in discussions and provided theoretical and realistic material support, making the research process run more smoothly.
Finally, I want to thank my family and old friends from my hometown in Italy for their support from afar and their occasional close visits. I also extend my gratitude to all the new friends I have made in Poland and around Europe for their support and understanding throughout this entire process.
Thank you all.

CONTENT

Presentation arising from this study ..... *i*

Publications arising from this study ..... *i*

CHAPTER 1 - INTRODUCTION **1**

1.1 Background and motivation *1*

1.2 Aim of the Thesis *2*

1.3 Organization of the thesis *3*

CHAPTER 2 - LITERATURE-CRITICAL REVIEW **5**

2.1 General remarks *5*

2.2 Material Characterization *6*

2.2.1 Masonry units 6

2.2.2 Masonry mortars 8

2.2.3 Comparative Analysis of Historical and Modern Masonry Materials 11

2.3 Unreinforced masonry in-plane loaded *16*

2.3.1 Masonry assemblage behavior 18

2.3.2 URM under vertical static shearing – irregular settlements 25

2.3.3 URM under horizontal cyclic loading – seismic type loads 30

2.4 Numerical modelling and simulations *34*

2.4.1 Micro models 34

2.4.2 Continuous models: macro, multi-scale and homogenization models 39

2.4.3 Macro elements (panel-scale) models 41

2.5 Summary and Critical Remarks *43*

CHAPTER 3 - EXPERIMENTAL CAMPAIGN **45**

3.1 Supplementary materials tests – clay bricks *45*

3.2 Supplementary materials tests – mortars *49*

3.3 Masonry behavior tests *57*

3.2.1 Shear triplet tests 58

3.2.2 Compressive tests 60

3.2.3 Diagonal compression tests 62

3.3 Large scale tests *66*

3.3.1 URM walls under static vertical shearing 66

3.3.2 URM walls under horizontal cyclic loading 80

3.4 Elaboration and analysis of the results *93*

3.4.1 Mortar behavior 93

3.4.2 Masonry specimen's behavior 95

3.4.2 URM walls under static vertical shearing 100

3.4.3 URM walls under horizontal cyclic loading 103

CHAPTER 4 - NUMERICAL SIMULATIONS **108**

4.1 Adopted numerical strategy *108*

4.2 Prediction of behavior of masonry larger scale masonry wallettes *111*

4.2.1 Masonry walls subjected to statically vertical shearing 111

4.2.2 Masonry walls under horizontal cyclic loads 112

4.3 Validation of prediction methods by experimental data 113

4.3.1 Masonry walls subjected to static vertical shearing 113

4.3.2 Masonry walls under horizontal cyclic loads 116

CHAPTER 5 - ANALYTICAL OR SEMI-ANALYTICAL METHODS AND PROCEDURES 123

5.1 Existing calculating methods and procedures 123

5.2 Verification of existing methods by experimental results 126

CHAPTER 6 - SUMMARY AND CONCLUSIONS 134

CHAPTER 7 - DIRECTION FOR FURTHER RESEARCH 137

CHAPTER 8 – APPENDIX 139

8.1 Physical and mechanical properties of clay bricks 139

8.2 Mechanical properties of mortar samples 143

8.3 Mechanical properties of masonry samples 146

CHAPTER 1 - INTRODUCTION

1.1 Background and motivation

The building construction industry is currently facing significant challenges related to the environmental impact of buildings and its consequences on human health, resource depletion, and life expectancy. Construction activities account for a significant share of global greenhouse gas emissions, resource consumption, and waste generation. These issues have led to increasing pressure from society, regulatory bodies, and governments to develop sustainable building practices and to introduce environmentally friendly materials that can replace or complement those traditionally used.

Concrete, the most widely used construction material worldwide, exemplifies this issue, being responsible for approximately 4-8% of global CO_2 emissions. The production of clinker, the main component of cement, is particularly energy-intensive and carbon-intensive [1]. Consequently, reducing reliance on Portland cement and finding alternative, lower-carbon binders is considered a key strategy to meet international climate goals, including those set by the Paris Agreement and various national sustainability targets.

Within this broader context, the specific sector of masonry construction offers a promising opportunity for decarbonization efforts. Traditional masonry practices, which historically relied on natural binders such as air lime, offer advantages not only in terms of environmental impact but also in terms of material compatibility, durability, and cultural heritage preservation. The partial substitution of cement with air lime-based mortars and plasters in new masonry constructions, as well as in the renovation of heritage structures, could represent an effective strategy for reducing the carbon footprint of the construction sector.

Until the early 20th century, air lime mortars were the primary binding materials for masonry constructions across many regions of the world. They were valued for their workability, adaptability, and long-term performance. However, they were gradually replaced by Portland cement mortars, mainly due to the latter's faster hardening rate and higher initial strength. Moreover, the incorporation of lime into cementitious binders was found to reduce the overall mechanical strength of the mix, as discussed in several studies [2-4].

Despite these shifts, air lime mortars have continued to be recognized for several advantageous properties, particularly with regard to the durability of masonry structures. Their enhanced ability to withstand freeze-thaw cycles, improved workability, breathability, and resistance to water penetration make them an attractive option for sustainable construction [5-7]. Furthermore, unlike cement, lime-based materials participate in the carbonation process, wherein they reabsorb a portion of the CO_2 emitted during their production. According to the analyses presented in [8-9], approximately 33% of the CO_2 emissions generated during the calcination process are reabsorbed over time across several application sectors, which together constitute 82% of the European lime market.

In addition to their environmental and mechanical properties, lime-based mortars offer benefits in terms of the conservation of historic structures. Their physical and chemical

compatibility with historic masonry materials reduces the risk of damage and ensures better performance in restoration projects, contributing to the preservation of architectural heritage.

Given these considerations, there is a growing interest in revisiting and modernizing the use of lime-based mortars. Developing sustainable and functional air lime mortars that meet contemporary performance standards is crucial to achieving a balance between environmental sustainability, material durability, and structural safety.

This thesis is framed within this broader objective. Specifically, it investigates the mechanical behavior of large-scale masonry walls constructed with clay bricks and air lime-based mortars with varying lime content, aiming to evaluate their structural viability and sustainability benefits. The research was carried out within the framework of the Horizon 2020 project *Sustainable Building Lime Applications via Circular Economy and Biomimetic Approaches - SUBLime*, a Marie Skłodowska-Curie Action European Training Network (ETN-ITN), which promotes cross-disciplinary research on innovative lime-based materials for construction applications.

In this context, the motivation of this thesis is also tied to the structural application of cement-lime mortars for the construction of façade walls, particularly the external leaves of masonry cavity walls (Fig. 1a) and masonry façade systems (Fig. 1b) in buildings exposed to irregular vertical displacements (e.g., due to ground subsidence or mining-induced deformations) and/or horizontal shear forces generated by seismic or para-seismic actions. The specific research question addressed is how an increased air lime content in the mortar affects, on the one hand, the overall deformability of clay brick masonry, and on the other hand, its shear resistance under both vertical and horizontal loading conditions.

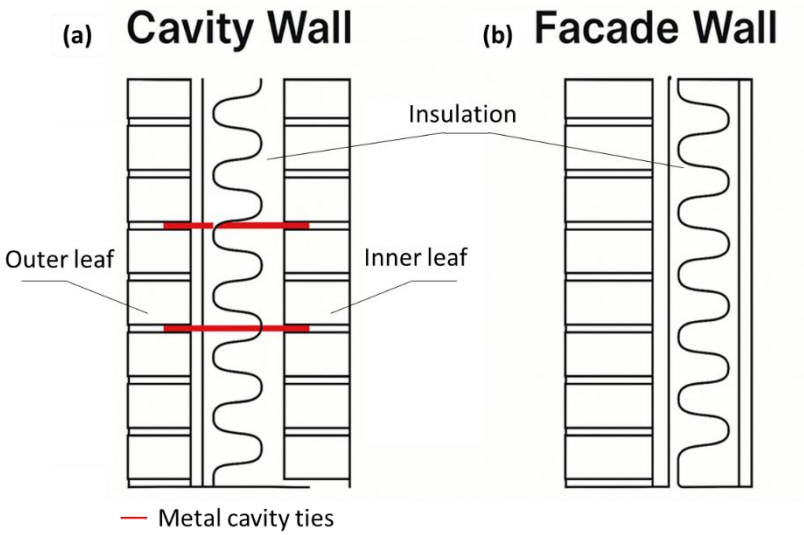

Figure 1: Schematic example of masonry cavity wall **(a)** and masonry façade **(b)**.

1.2 Aim of the Thesis

Understanding the global response of masonry walls under in-plane loading conditions requires a thorough knowledge of the mechanical properties of the constituent materials.

Therefore, the research also includes a comprehensive experimental characterization at different scales: material level (bricks and mortars), interface level (brick-mortar interaction), and assemblage level (triplets and wallettes). This multiscale approach ensures that the numerical models developed are firmly based on experimental evidence and that the conclusions drawn are robust. The three following research theses have been formulated and are addressed throughout the study:

- Mortar mixtures containing higher contents of air lime as a partial substitute for cement binders, despite lower mechanical strength, can still provide adequate structural performance of masonry walls, especially in the façade layers of cavity or diaphragm walls, while offering environmental benefits.

- Changes in the air lime content in the mortar composition significantly, yet positively due to their crack resistance, affect the global behavior of masonry walls, in particular in terms of stiffness, strength, deformability and failure mechanisms.

- Simplified numerical models and existing standard's and analytical recommendations can describe the mechanical response of masonry elements constructed with air lime mortars, although they may require calibration or adjustment to ensure an adequate level of safety and reliability.

By investigating these theses, this research aims to contribute to the development of more sustainable and structurally efficient masonry systems suitable for modern construction and renovation scenarios.

1.3 Organization of the thesis

The thesis is organized as follows:

- **Chapter 1** introduces the research topic, outlines its scientific and practical relevance, and defines the main hypothesis guiding the study.

- **Chapter 2** presents a critical review of the literature related to the main topics of the research. It covers the physical, chemical, and morphological properties of masonry materials, including comparisons between modern and historic clay bricks and mortars. It also discusses the mechanical behavior of masonry under complex loading conditions and reviews the numerical modeling strategies, particularly finite element methods, used for simulating masonry structures.

- **Chapter 3** describes the materials selected for the research and the experimental program designed to investigate their mechanical behavior. The chapter details the test setups, methodologies, and results obtained from both small-scale and large-scale testing, with a particular focus on the elaboration of global mechanical parameters for masonry walls.

- **Chapter 4** focuses on the numerical modeling of the tested walls using finite element macro-modeling approaches. The models are calibrated based on the experimental results from small-scale tests and are employed to simulate the behavior of walls under both vertical and lateral loading conditions.

- **Chapter 5** presents a comparative evaluation of the experimental results against existing analytical and semi-analytical models, including those provided by Eurocodes. The reliability and predictive accuracy of these models are critically assessed.

- **Chapter 6** summarizes the key findings of the research, discusses the main conclusions, and reflects on the implications for sustainable masonry construction.

- **Chapter 7** outlines possible future research directions aimed at addressing the limitations identified in this study and further advancing the understanding and application of air lime-based masonry.

Additionally, the Appendix presents data reports, including statistical analyses related to the experimental tests described in the previous subsections. Its purpose is to provide a broader and more comprehensive view of all the results obtained throughout the experimental campaign.

CHAPTER 2 - LITERATURE-CRITICAL REVIEW

2.1 General remarks

Masonry structures are the oldest and most prevalent architectural forms. Their enduring strength, cost-effectiveness in material usage, fire resistance, and aesthetic appeal are just a few of the benefits that continue to push their use to this day. These buildings often serve as not only the heritage of each nation but also as common residential structures, each with their unique characteristics. As highlighted by Roca et al. [10], masonry building complexities arise from variations in geometry, composition, and arrangement of units, as well as the presence or absence of mortar, which contribute to the definition of masonry material more properly as a composite material (Fig. 2a-d). In fact, it is its heterogeneous nature that makes impossible to comprehensively characterize masonry without a deep analysis of the constituent elements. Consequently, the transition from individual element properties to the assemblage behavior is generally obtained by means of various no-trivial numerical techniques [11], involving different material scales. In this context, Kubica [12] emphasizes how the evolution of masonry construction systems continues to influence current design strategies and future directions within a framework 15 years, particularly in the pursuit of sustainable and low-emission building practices. His review of masonry techniques from antiquity to modern times highlights the importance of understanding traditional systems to guide future innovations in masonry research and design.

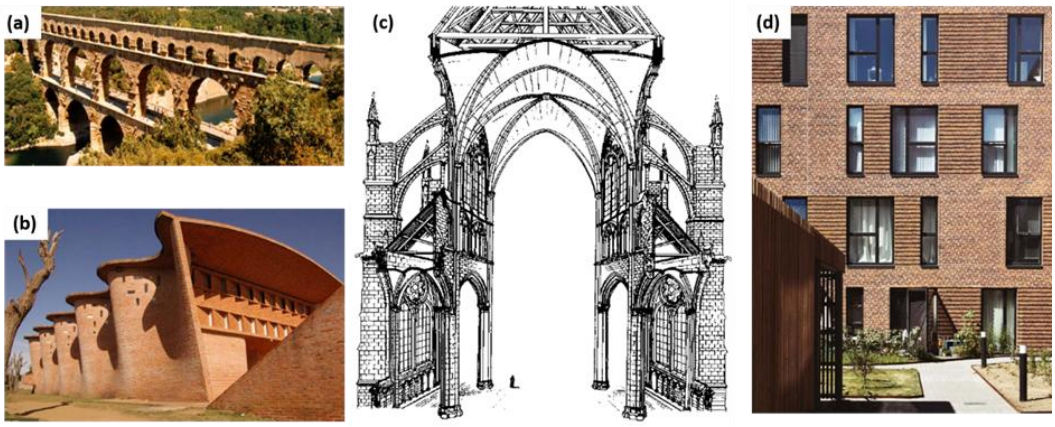

Figure 2: Examples of masonry from different historical periods: Pont du Gard (50) **(a)**, Church of Christ the Worker and Our Lady of Lourdes (1958) **(b)**, Amiens Cathedral (c. 1300) **(c)** and a modern masonry façade **(d)**.

Subsequently, in the context of the assessment of existing structures, the requirement to assess materials on a case-by-case basis in order to determine appropriate mechanical properties has prompted the formulation of different national annexes to Eurocode 6 [13], and more recently, the establishment of databases [14], for helping designers and reducing the testing costs. These recommendations assume even more importance in relation to masonry historical structures where sampling material is limited and complementary mineralogical, petrographic, and physical investigations are preferable for understating

production processes, imperfections, and actual state of the masonry, in view of finding the most compatible unit and mortar with the original material [15-16].

In this part, the mechanical behavior of masonry elements from micro (masonry units and mortar layers) to macro scale (masonry panels) are reviewed. Concerning the former aspect, beyond mechanical characterization, an analysis of physical, chemical, and mineralogical properties is also conducted. The latter examinations consider different methodologies reviewed by means of two case studies, involving different clay brick samples and mortars from distinct historical periods. A useful comparison between materials is carried out for showing the differences in time evolution of masonry constituents, particularly for designers working in central Europe. Related to the latter aspect, existing numerical models and standard relationships for the structural analysis and assessment of masonry structures are also reviewed and classified based on their principal scale modelling function.

2.2 Material Characterization

2.2.1 Masonry units

Clay bricks are one of the first form of building materials together with stone, adobe and wood with first traces even dating back to 8000 B.C. in Mesopotamia. Their growing use during the centuries, across several civilizations, is mainly connected with the intuitive masonry building practice, that was already started to be critically studied and improved by Romans with Marco Pollio Vitruvius [17]. For building clay masonry units, raw materials are principally constituted by clay minerals, including fine grains with dimensions inferior to 0.1 mm. From a chemical point of view, clay minerals belong to the phyllosilicate group with complex tetrahedral and octahedral crystalline units connected between them in order to obtain plane layers (Fig. 3a-b). Generally, within the tetrahedral unit, silicon occupies the central position and forms connections with four oxygen ions located at its vertices. On the other hand, the octahedral unit, containing either an aluminum or magnesium ion along with six oxygen or hydroxyl ions, gives rise to lattice structures comprising two planes of oxygen ions, one of which accommodates aluminum ions [18]. By arranging several of these units in various three-dimensional configurations, different types of clay minerals are formed, with the most prevalent ones being kaolinite, montmorillonite, illite, talc and pyrophyllite.

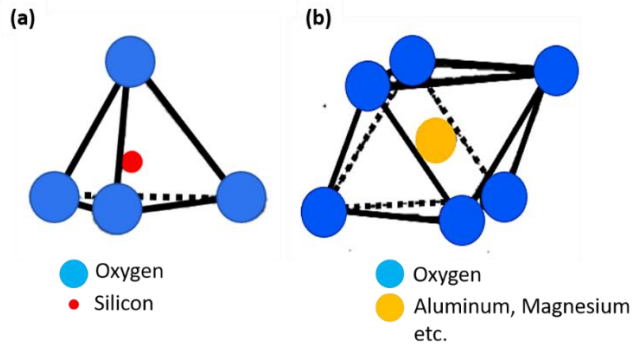

Figure 3: Representation of silicate structures: silicon tetrahedral unit **(a)** and octahedral unit **(b)**. Adapted from [18].

Naturally, given the heterogeneity of the soils, it is possible that other components beyond clay minerals are present in the raw materials, having a positive or negative impact on the final physical and mechanical performance of the brick. Within this context, the presence of limestone during the firing process brings the drawback of converting into calcium oxide. When exposed to water, this conversion leads to an expansion in volume, creating an accumulation of stresses and cracks, deteriorating the durability of the units [19].

Concerning the production procedure of clay units, despite its complete automation process, it remains possible to identify four main phases: selection and preparation of the clay materials, water mixing and molding, air drying and finally hardening of the bricks by means of firing processes [20]. During the initial stage of the procedure, multiple layers of diverse clay types are collected and stored in deposits for several weeks. Throughout this duration, the material undergoes a homogenization procedure with the aim of diminishing the size of larger particles. At this point, the clays are mixed with water and molded. This stage was subjected to the evolution with time from the more ancient hand-molding and wire cut molding to the more recent machine molding for large scale production. Following the molding process, bricks retain a certain level of moisture. Consequently, it is necessary to facilitate drying to prevent potential cracking during the subsequent firing phase. Typically, the drying period for clay bricks spans a week or longer, depending on the prevailing climatic conditions of the site. Ultimately, the concluding phase involves the hardening of the bricks. These bricks are generally placed inside clamps or kilns at temperatures reaching around 1000°C. The firing process significantly modify the properties of final brick and early kilns generally have the disadvantage of irregularity firing of the units, generating differences in their performances.

The performance of clay bricks, which plays a vital role in enhancing building resilience against gravitational and seismic actions, is substantially affected by the raw materials and the firing procedures employed. Among the most relevant properties influenced, it is possible to consider: chemical and mineralogical properties, physical properties (i.e. porosity, water absorption, initial suction rates) and compressive strength [21]. Based on the analysis reviewed in Ghiassi et al. [19], the most common chemical elements that is possible to find in clay bricks are Silicon Oxide (SiO_2) in 30-70 % of content and Aluminum Oxide (Al_2O_3) in 10-25% of content. Also, the presence of Iron Oxides (Fe_2O_3) or Ferrous Oxide (Fe_3O_4) can be present in different quantities, mainly being responsible for the reddish color of the material. Almesfer et al. [22], in their characterization of existing masonry building from New Zealand, analyzing different brick colors, showed no clear trend between the compressive strength and the color of existing clay bricks. The mineralogical composition also is modified by the differences in the firing temperature together with impurities of raw materials, generating subsequent modification of the porosity and compressive strength. Cultrone et al. [23] showed how generally low firing temperature increase the level of porosity. Furthermore, carbonate rich clays subjected to firing temperature inferior to 1000°C present higher pore connectivity and an elevated quantity of small pores (<1 μm), affecting negatively the performance. On the contrary, clays without carbonates subjected to firing temperature ranging from 1000-1100°C, present the best physical properties. The same factors influence the compressive strength of the bricks. Typically, raising the firing temperature is linked with

a more pronounced level of vitrification, especially evident in clays low in carbonate content. This results in an overall improvement in compressive strength, as showed in Elert et al. [24]. Furthermore, high firing temperatures (≥ 900°C) can be detected from the presence of mullite in the mineralogical composition, according to Cultrone et al. [25], being therefore connected with the degree of vitrification and densification. These considerations led Dizhur et al. [26] classifying different vintage clay bricks based on the presence of mullite and cristobalite, indicating a high average compressive strength for the ones containing these elements.

The knowledge of the compressive strength of the bricks appears significant for the structural safety, allowing to estimate the value of the compressive strength of masonry [27]. In the case of old masonry, direct tests, as the ones performed on full modern units, are typically conducted on non-standardized specimens [28]. The feasibility of this approach remains an open issue due to multiple variables influencing test results. These factors encompass the confinement effects exerted by the platens, the slenderness of the specimens and the anisotropic nature of the response arising from the manufacturing process. Moreover, the compressive strength of clay bricks currently in use displays a broad spectrum of values with coefficients of variation ranging from 10% to 55% [29]. Particularly, when reducing the dimensions of samples under compression testing, the ability of compressive strength to effectively reflect a uniaxial value is compromised. Consequently, the standard EN 772-1 [30], which establishes guidelines for determining the compressive strength of masonry units, addresses this concern by incorporating the value of normalized compressive strength, through the application of shape factors, functions of the sample dimensions. In order to overcome the non-standard dimensions of the unit samples, in usual practice, different treatments for the top-bottom sample surfaces are used, including cement mortars, metallic elements, gypsum and plywood sheets. In this context, the representatives of the non-standard cubic sample 40 x 40 x 40 mm have been recently faced from an experimental statistical point of view by Cabané et al. [31]. In their study, based on testing more than 400 samples, recommended a conservative ratio of 1.45 for the compressive strength of standard samples 100 x 100 x 40 mm to the compressive strength of the non-standard specimens aforementioned. The same Authors in their subsequent work [32] studied the compressive strength relations between different brick shapes recommended by different international standards [33-35] and surfaces treatments. In particular, they recommend the use of polytetrafluoroethylene leaves, being able to reduce the level of frictions between the platens, showing similar compressive strength results regardless the shape. Additionally, the American and Canadian standards offer procedures resulting in the most elevated compressive strength values, whereas the Australian code present the least elevated values.

2.2.2 Masonry mortars

In a general sense, the term "mortar" refers to a range of composite materials primarily employed as binding agents. These materials are typically formed by mixing cementitious or adhesive components (such as lime or cement) with finely graded aggregate, along with water. Based on Eurocode 6 [13], referring to EN 998-2 [36] concerning mortars for masonry, it is possible to identify two types of mortars:

1. designed masonry mortar - mortar whose composition and manufacturing method is chosen in order to achieve specified properties (performance concept);
2. prescribed masonry mortar - mortar made in predetermined proportions, the properties of which are assumed from the stated proportions of the constituents (recipe concept).

Additional requirements are also defined based on this first distinction, defining:

1. General purpose mortar - without any specific requirements;
2. Thin layer masonry mortar - designed masonry mortar with a maximum aggregate size less than or equal than 2 mm;
3. Lightweight masonry mortar - designed masonry mortar with a dry hardened density equal or less than 1300 kg/m^3.

In addition to the compressive strength of bricks, the compressive strength of mortars holds significant importance. Notably, achieving the same compressive strength can be accomplished by blending diverse mortar constituents. In this regard, National Annexes to Eurocode 6 [13] propose different correlations between the minimum strength (Strength Class) at 28 days, given by the number following the letter M, and the volume proportions of constituents, based on the territorial traditions of each European Member State (Fig. 4a-b). In this case, the distinction based on the constituents is also fundamental.

(a)

Type of mortar	Strength Class	Prescribed constituents (by volume)		
		cement	lime	sand
Cement	M20	1	–	2
	M15	1	–	3
	M10	1	–	4
Cement-lime	M15	1	0,25	3
	M10	1	0,5	4
	M5	1	1	6
	M2.5	1	2	9
Lime	M1	–	1	1,5
	M0.5	–	1	2
	M0.25	–	1	4

(b)

Type of mortar	Strength Class	Prescribed constituents (by volume)				
		cement	air lime	hydraulic lime	sand	pozzolan
Cement	M12	1	–	–	3	–
Cement-lime	M8	2	–	1	8	–
	M5	1	–	1	5	–
	M2.5	1	–	2	9	–
Pozzolanic	M2.5	–	1	–	–	3
Hydraulic	M2.5	–	–	1	3	–

Figure 4: Examples of correlation between constituent proportions and minimum of compressive strength from different: polish PN-EN 1996-1 [37] **(a)** and Italian NTC-2018 [38] **(b)**.

Generally, cement is produced by subjecting a blend of limestone, clay and sand, to high temperatures, typically reaching around 1450°C. During the process, the clinker, obtained with the calcination, shows the fusion, leading to the formation of nodules and particles with dimensions ranging from 1 mm to 25 mm. These clinker nodules are then combined with a small percentage of calcium sulfate and finely crushed to create cement. The presence of calcium sulfate regulates the setting rate and also impacts the rate of hardening. This calcium sulfate is often referred to as gypsum, although it can be partially or completely substituted with alternate forms of calcium sulfate [39]. From a chemical point of view, the most common Portland Cement shows different constituents. Alite (Ca_3SiO_5) stands as the predominant component in typical Portland cement clinkers, comprising 50-70% of their composition. This compound is the main responsible for the gain in strength in 28 days. Belite (Ca_2SiO_4) is another constituent with 15-30%. It reacts slowly with the water and on the contrary of the first compound is the responsible for strength development after long time. Ferrite (Ca_2AlFeO)

and Alluminate ($Ca_3Al_2O_6$) are the remaining elements present in the minimum of 5%. Cement is normalized at European level according to the code EN 197-1 [40], defining five classes of cements, consisting in twenty-seven different products with different constituent materials. Together with chemical requirements, a distinction based on the strength gain is also given in the codes, defining six strength classes, two (ordinary and high early strength) for each minimum values of compressive strength at 28 days: 32.5 MPa, 42.5 MPa and 52.5 MPa.

Lime can be classified into hydraulic lime and air lime and also lime putty, which is mainly used for making fine plasters, e.g. during renovation in historic buildings. The principal difference is relative to the presence of silicate and aluminates in hydraulic lime that when combined with water, give birth to a hydraulic reaction, allowing for faster solidification than in the case of air lime. The use of air lime mortars is mainly associated with historical building conservation, being one of the most compatible products, even though its use faced challenges encompassing a scarcity of both scientific and technical understanding [41]. Air lime is derived by the processing of limestone rocks, mainly composed of calcium carbonate ($CaCO_3$). The calcination of the limestone with temperatures superior to 900°C, with consumption of CO_2, creates calcium oxide (CaO), known as Quicklime [42-43]. Calcium oxide is promptly allowed to react with water, undergoing a transformation into calcium hydroxide ($Ca(OH)_2$), known also as hydrated or slaked lime [44]. Precisely, the slaking process can be done with precise stochiometric quantity of water obtaining dry powder or with abundant water, resulting in a lime putty. The term air lime, used in industrial practices, refers to hydrated lime and its property to react with carbon dioxide of the air, in order to form calcium carbonate, in a closed loop (Fig. 5). This process, known as carbonation, is the responsible for the hardening of the lime mortars in a more elevated time of the process involving the hardening of cement.

Specifically, Van Balen [45] noted how the speed of this processes in ambient conditions does not depend on the CO_2 concentration but it is more related to the physical properties of the limes, especially the specific surface and pore distribution. Recent research on blended cement-air lime mortars incorporating an air-entraining agent [46] indicated enhanced mortar strength without compromising porosity. It is hypothesized that the air-entraining agent facilitates the integration of CO_2 into the structure of the material, improving its performance. From a code perspective, EN 459-1 [47] establishes different types of limes based on their composition, proposing the differentiation in calcium and dolomitic limes. In the context of the utilization of mortars for masonry historical conservation purposes without a specific structural function, the majority of application focuses on: pure air lime [48], mixed hydraulic-air lime mortars [49] and mixed cement-hydraulic lime mortars [50]. In this scenario, when aiming for a minimum strength requirement, selecting an appropriate binder-to-aggregate ratio and the type of aggregate becomes crucial as it is responsible for influencing the alteration of mechanical strength even among the same material constituents [51-52].

Regarding the mechanical properties, the values of compressive strength of hardened mortars results of complementary importance to the strength of bricks, for masonry structural safety. The European standard 1015-11 [53] is applied for the characterization of the materials in this case. First a three-point bending test is carried out on a minimum of three samples with standard dimensions of 40 x 40 x 160 mm, then the resulting six half prisms are tested in compression. Differences in the curing conditions have to be taken into account based on the

quantity of lime and cement in the mortar, involving the use of climatic chamber with 20 ± 2 °C and relative humidity value 65±5%, for the last 21 days.

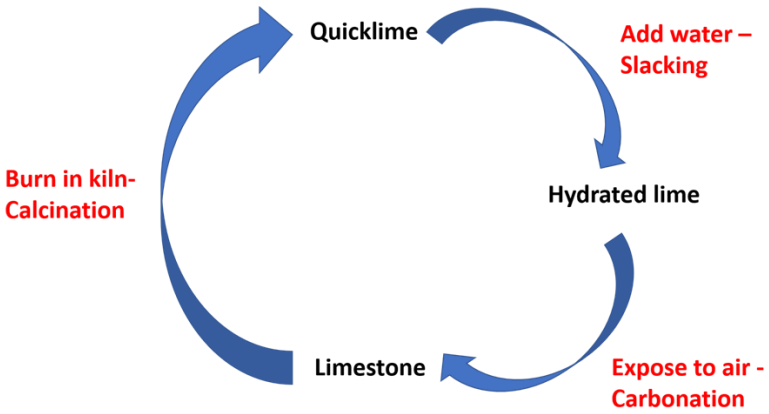

Figure 5: Closed loop of air lime.

While the characterization of new mortars is straight-forward, evaluating the mechanical properties of existing mortar joints can be challenging. This complexity stems from factors such as size, shape, and limitations associated with collecting lime-based samples from historical structures. Executing standard engineering tests in such contexts is demanding, which often leads to a greater reliance on chemical, mineralogical and physical analyses within this field [54]. From a mechanical point of view, Almesfer et al. [22] tested non-standard cubic samples according to ASTM C 109 [55]. Working under the assumption of failure within cubic samples, restricted by the platens due to the achievement of a maximum principal compressive strength, the researchers conducted numerous experimental tests reproduced by finite element modeling. This process ultimately led to the development of two shape factors tailored for non-standard dimensions. Magalhães and Veiga [56] conformed the shape of mortar samples to match that of standard specimens, aligning with the guidelines in EN 1015-11 [53], using a cement mortar for confinement. Double punch compressive strength is also usually performed on mortar joints extracted and cut from into plates, where the application of the vertical load is carried out by means of a cylindrical steel punch with diameters ranging from 20 to 30 mm. In this case, it is possible to direct assess the mortar joints, offering insights into compressive strength and serving as a valuable tool for enhancing in-situ investigations [57-58].

2.2.3 Comparative Analysis of Historical and Modern Masonry Materials

For the examination of the fundamental properties of mortars and clay bricks as previously discussed, a specific case study has been chosen. This selection aims to introduce the methodologies employed to analyze these materials on a small scale. Moreover, it adds to the historical assessment of materials and report a comparison between the properties of historical materials and those utilized in contemporary practices, in the same area. Complete investigations on the materials subsequently analyzed is given in the contribution De Vico Santoro et al. [59] and Zagaroli et al. [60].

In order to investigate the fundamental differences between historical and modern masonry materials, a comparative analysis was carried out using bricks and mortars originating from different centuries. The samples were retrieved from the remains of the Schloss Neudeck complex, a historical structure originally built in the 14th century and later expanded in the 18th-19th centuries. However, the focus of this section is not on the specific architectural context of the building, but rather on the comparative study of the materials themselves.

The selected dataset includes clay bricks (CB) and air lime-based (MR) mortars from two historical periods (14^{th} series 1 and 18^{th}-19^{th} centuries series 2), as well as contemporary counterparts commercially available on the Polish market (series 3) (Fig. 6). All samples were subjected to detailed laboratory analysis, including microstructural characterization (via SEM-EDS and MIP), evaluation of physical properties, and compressive strength testing.

The comparison highlights key differences in porosity, binder composition, aggregate morphology, and mechanical behavior, offering insights into the performance evolution of masonry materials over time. This type of analysis is essential for assessing material compatibility in conservation projects and for developing more sustainable lime-based alternatives in modern construction. The results are presented in the following figures and tables.

X-ray powder diffraction (XRD) is an extensively non-destructive method for assessing the mineralogical composition of substances. It relies on detecting the constructive interference (diffraction) patterns of X-rays when they interact with various solid materials. Consequently, the intensities of recorded diffraction peaks offer insight into the compound type, atomic number, and atomic arrangement within the crystal's smallest repeating component (unit cell). Additionally, the position of these diffraction peaks furnishes details about the dimensions and configuration of the unit cell [61]. Several examples are available in literature concerning the chemical study of different masonry building materials from different ages [62-63]. Anyway, other techniques (i.e. Fourier Transform Infrared Spectroscopy) are usually employed as supportive to the mineralogical characterization, for double-checking the results obtained by the previous one [64].

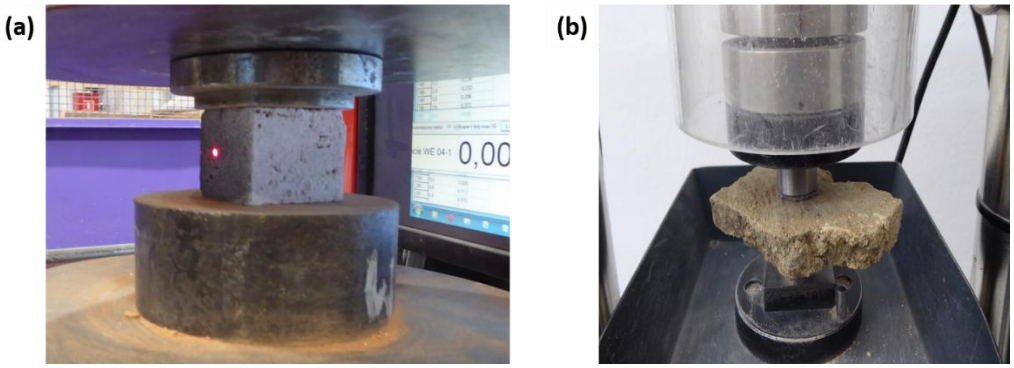

Figure 6: Historical brick ready to be tested **(a)** and mortar fragment ready to be tested according double punch compressive procedure **(b)**.

Results of the investigations on bricks and mortars carried out on polish materials are given in Fig. 7a-b and Fig. 8a-b, respectively. For the bricks, in the CB1 case, it is possible to

notice the presence of mullite in 13%, with the highest content among all the brick specimens, but no feldspars. CB2 and CB3 see the reduction of mullite but an always increasing content of feldspars. In terms of the mortars, MR1 displays the highest amount of calcium silicate, reaching up to 2 wt%, which is the most abundant among all the examined mortar samples. In contrast, the composition of the MR2 sample is the most straightforward, with quartz constituting 86% and calcite 14%. The MR3 sample comprises feldspars (anorthite and microcline) with concentrations of 9 wt% and 11 wt%, respectively.

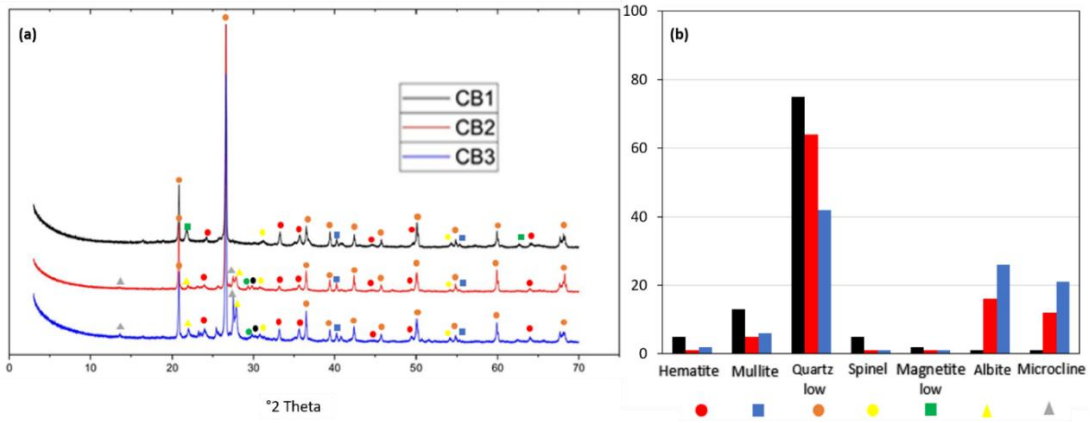

Figure 7: XRD patterns of three bricks **(a)** and phase content of the bricks determined from semi-quantitative phase analysis using the RIR method **(b)** [60].

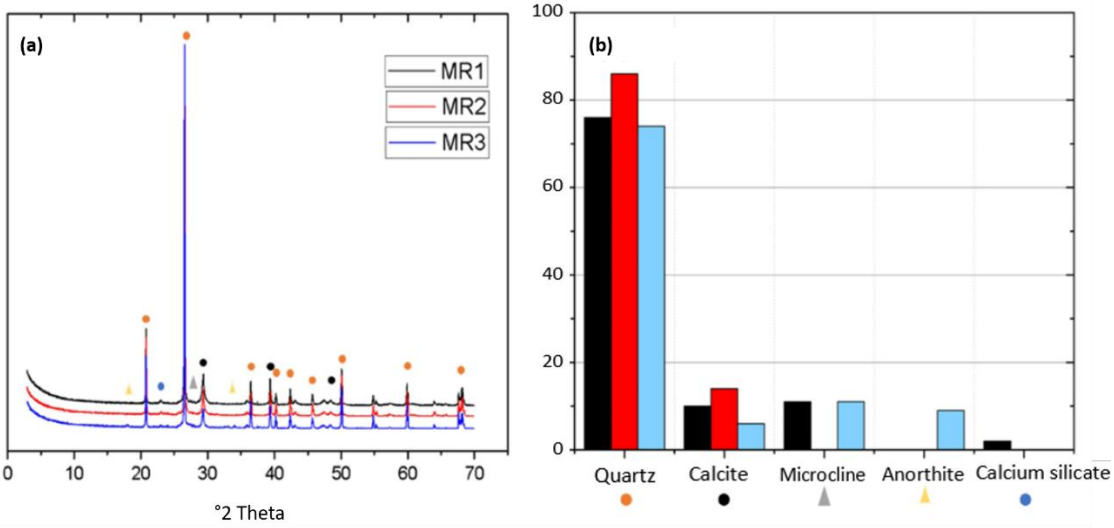

Figure 8: XRD patterns of three mortars **(a)** and phase content of the mortars determined from semi-quantitative phase analysis using the RIR method **(b)** [59].

The Scanning Electron Microscope (SEM) is utilized as an imaging technique to explore fundamental material attributes, encompassing elements like surface features, grain proportions, and chemical composition. In the SEM configuration, an electron beam is precisely concentrated into a designated point that traverses the surface of the sample. At each location, the specimen emits signals, which are captured by detectors. When an electron beam strikes a sample, the primary signals emitted are named scattered primary electrons.

Among these, backscattered electrons refer to those scattered at 90° and 180° angles, emerging from the specimen's surface. Another outcome is the formation of secondary electrons due to interactions that cause a reduction in the energy of the incoming primary electrons. These detector signals are harmonized with the known beam position on the specimen, influencing the corresponding image pixel according to signal intensity.

As these signals are progressively accumulated, they are integrated to generate an image with pixel distribution dependent on the selected scanning pattern [65]. SEM can reveal the differences in the texture of brick materials in order to understand their degree of vitrification [66]. The enhancement of the examination of material microstructures through SEM can also be obtained by analyzing three-dimensional samples using X-ray Micro computed tomography. This non-destructive approach is founded on the distinct X-ray attenuation properties of materials. As the X-ray beam traverses the material, certain X-ray photons are absorbed, depending on the linear attenuation coefficient of different materials. On the opposing side of the sample, a detector captures the photons that manage to pass through, resulting in the creation of a single two-dimensional attenuation map. Through the rotation of the sample, multiple shadow projection images are acquired from various angles.

From this collection of images, algorithms for image reconstruction work to establish the detailed three-dimensional structure of the samples. Given their non-destructive nature, micro-CT analyses are particularly fitting for temporal investigations, offering the ability to subject samples to external loads and subsequently reconstruct the evolving 3D image at each load step (in-situ and ex situ micro-Ct) [67-69]. In their work, Shetty et al. [70] applied this method to evaluate the predictive potential of X-ray micro-CT in anticipating the onset and progression of cracks in masonry subjected to compressive loads. This technique is also widely used for measuring also the porosity of the samples. Effectively, Micro-CT scanning provides a three-dimensional visualization of the internal structure of the bricks that it is influenced by different artifacts such as: misalignment compensation, ring artifacts reduction and beam hardening correction. As a result, the voxel edges are limited, making it unable to detect pores with inferior dimensions to the maximum resolution, that could be obtained from Mercury intrusion porosimetry analysis, more suitable for quantitative assessment of pore distribution [71]. Based on these considerations, results from brick and mortar investigation on their microstructure are given in Fig. 9a-e and Fig. 10a-f. As it is easy to note the medieval brick shows great heterogeneity with zones more intact than others and a more irregular shape of voids when compared to the samples from XVIII and modern brick (Fig. 9a and Fig. 9c-d). These outcomes naturally result from both the homemaking procedure and the degradation phenomena that the materials have undergone over centuries. For the mortar analyzed, all the samples show a round porosity with a regular shape but the numbers of voids of the modern mortar MR3 is evidently inferior to both the mortars from XVIII and XIV century (Fig. 10 a-b-c).

Regarding compressive strength analyzed, the load is generally applied by means of steel plates in load control or displacement control test set ups. In the latter case, it is possible to investigate the post peak softening behavior of the materials. Analysis of the bricks were carried out in load control with cubic specimens of mean dimension of 40 mm. For the mortars, double punch test, according to German standard [72] was performed on historical

mortar joints and plates of M7 mortars cut from standard beam specimens, according to EN 1015-11 [53].

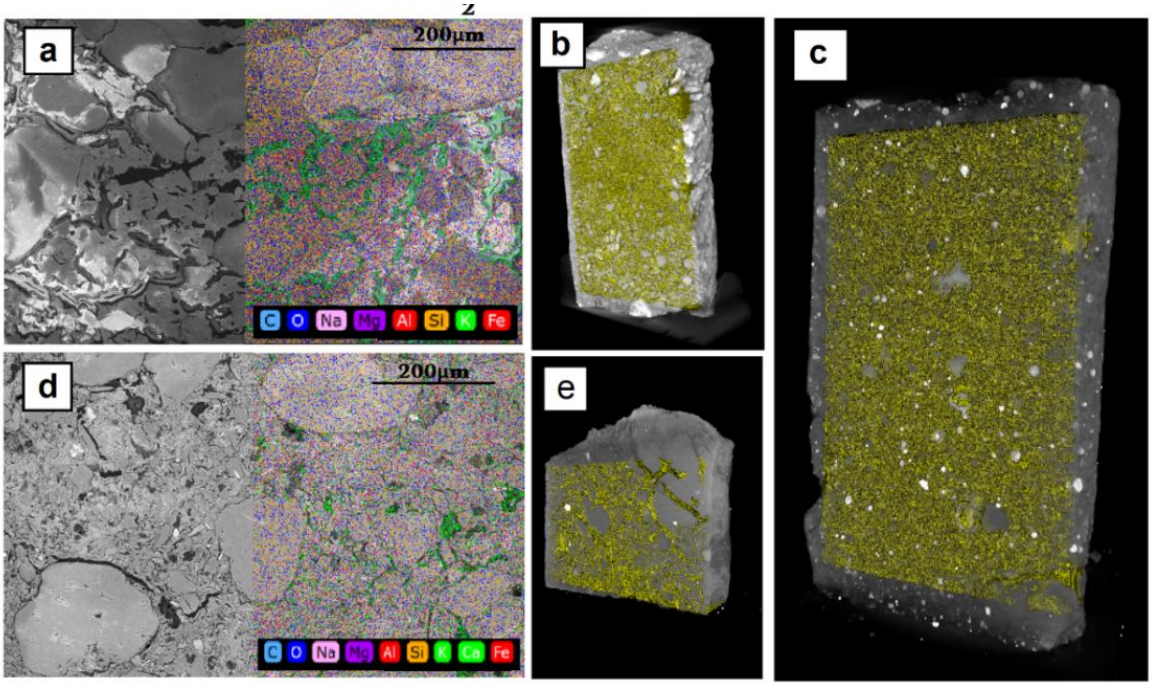

Figure 9: SEM with elemental maps of brick CB1 **(a)** brick CB2 **(d)**. Micro-CT of bricks CB1**(b)**, CB2 **(e)** and CB3 **(c)** [60].

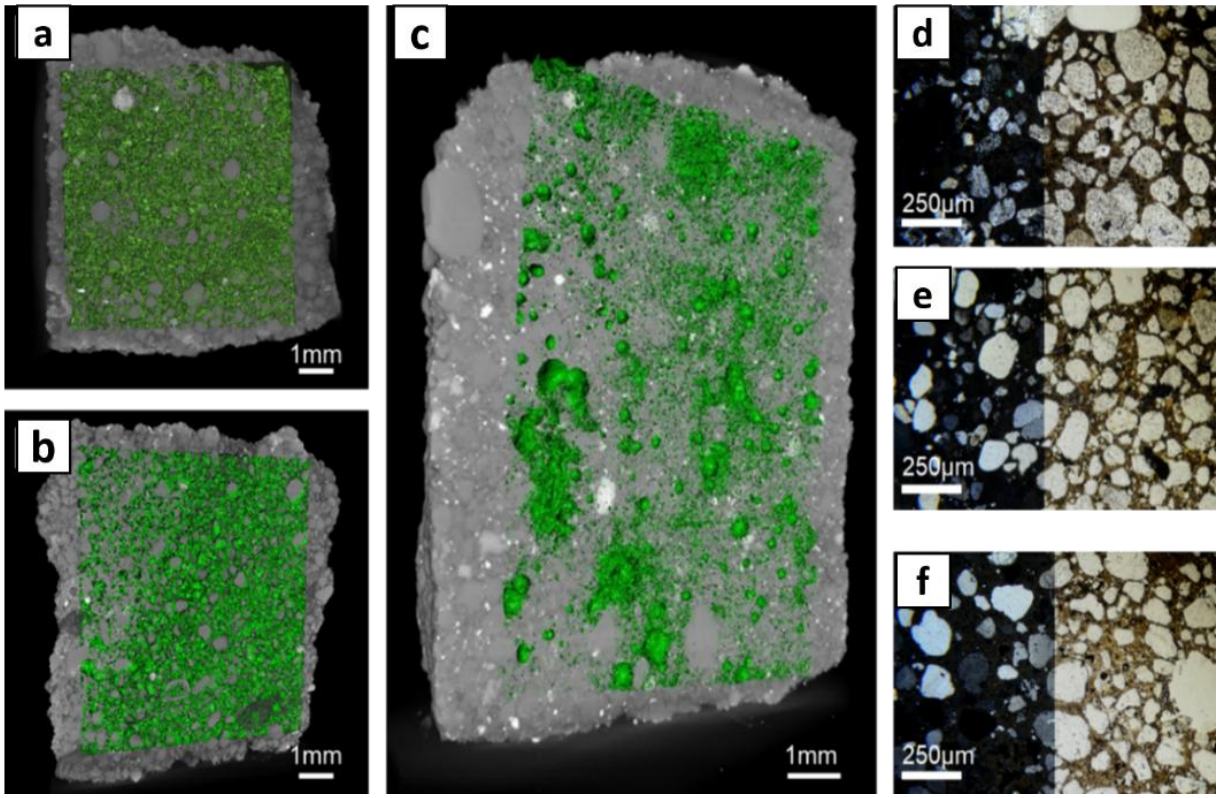

Figure 10 Micro-CT and petrographic thin section of mortars MR1 **(a-d)**, MR2 **(b-e)** and MR3 **(c-f)** with details of the porosity evidenced in green areas [59].

In this case, no specific correlation is evidenced with the porosity. Effectively, this comparison is affected by the different curing conditions of in-situ historical mortars and standard conditions for MR3. Sassoni et al. [73] have previously observed that the double punch compressive strength of mortars extracted from masonry walls can exceed both the double punch compressive strength of plates cut from standard specimens, as well as the standard compressive strength on full prismatic sample (40 x 40 x160 mm) of the identical mortar. In their study [73], besides differences due to confinement, shape, and sample dimensions between the standard and double punch tests, changes in the microstructure of the specimens played a significant factor, with standard prisms displaying approximately 50% higher open porosity compared to samples derived from masonry joints. In this context, shape and scale effects ratio for the determination of standard compressive strength from double punch tests on mortar joints of existing masonry should take into account this aspect and should not be determined on mortars cured in the same standard conditions [74]. Values of the total porosity obtained by the investigations and the compressive strength of the materials is given in Table 1.

Table 1: Results of compressive strength of cubic sample from bricks and plates cut from standard samples of the mortar. Elaboration from [59-60].

Materials	Period (century)	Total Porosity [%]	Compressive strength [MPa]
CB1	XIV	29.7	10.64
CB2	XVIII/XIX	13.3	42.34
CB3	XXI	35.9	27.15
MR1	XIV	30.3	3.01
MR2	XVIII/XIX	37.1	26.84
MR3	XXI	5.6	7.08

Information on these properties can be further improved with the determination of the compressive strength of the materials with different shapes and porosity with different techniques such as: mercury intrusion porosimetry and/or measurements of the water accessible to pores [75]. Beyond the elastic mechanical properties that are generally determined on masonry components, post-peak mechanical properties of mortars and bricks have a relevant importance for predicting masonry performance at ultimate limit states. In this context, relationships based on concrete experimentations are commonly used. MODEL CODE 90 [76] proposes recommendations for the ductility indexes depending on the compressive strength ranges of the materials analyzed.

2.3 Unreinforced masonry in-plane loaded

Nowadays, earthquakes represent the world deadliest natural hazard. On a European scale, the significant concern lies in the seismic vulnerability exhibited by the architectural heritage of Member States facing moderate to high seismic hazards, such as Italy and Greece. However, the impact of earthquakes can extend to other European nations as well, including Spain, Portugal, France, and the Netherlands. In the case of the Netherlands, the seismic risk is recently increased resulting from gas extraction activities and vulnerability of constructions,

built before 2005 without seismic design provision [77]. It should be noted that in Poland, seismic and para-seismic impacts are primarily associated with anthropogenic activities, particularly deep mining operations. These include hard coal mining in the Upper Silesia region and copper extraction in the areas of Lubin and Polkowice in Lower Silesia. According to Kubica [78], these induced vibrations are a relevant factor in the design and performance assessment of masonry wall enclosures in these regions.

In recent years, our understanding of earthquake engineering principles applied to masonry structures has been swiftly advancing. While seismic events offer a distinctive chance to obtain insights from the shortcomings of current structures on a broad spectrum, there is a continual need for comprehensive investigations on full-scale masonry structures. These investigations are essential for gaining deeper insights into the mechanisms of failure, thus facilitating the development of accurate predictive models.

At masonry structural level, a hierarchical order exists within failure modes since the occurrence of in-plane failure is contingent upon the prevention of more critical failure modes [79]. Among these, the first is masonry disgregation, which occurs when a portion of masonry is unable to withstand nearly any horizontal forces, resulting in fragmentation of the texture. Subsequently, there are out-of-plane modes that are characteristic of inadequately designed structures, unwise alterations to original constructions, or historical architectural heritage built prior to the establishment of systematic engineering codes. An example of the latter scenario is evident in cases where the horizontal connections of masonry walls are weak, leading to a lack of box structural behavior [80]. Only after, the development of in-plane failure modes is obtained with different crack patterns and failure mechanisms. The sequence of failure modes resulting from masonry damage during the Lesvos earthquake [81] is illustrated in the Fig. 11a-b-c. From the observed failures modes, tests for masonry have been elaborated from different Authors for evaluating their basic mechanical features. Following the 2010-2011 Canterbury earthquake, some unreinforced cavity masonry walls exhibited diagonal cracking along the mortar-brick joints (Fig. 12a-b), which is indicative of in-plane shear deformation. This failure mode was particularly observed where out-of-plane collapse was prevented, allowing the two leaves to act partially together [82]. This failure mode aligns with broader concerns highlighted in the literature regarding the seismic vulnerability of façade systems, which, although non-structural, require specific design attention to mitigate shear-induced damage and ensure continuity in performance-based seismic design frameworks [83].

In the next paragraph the attention is given to the experimental mechanical behavior of masonry at meso-scale, from small assemblage to large scale elements, with main concentration to in-plane loadings.

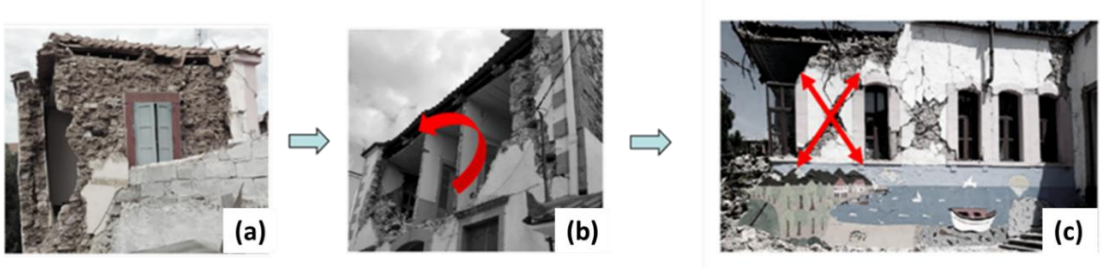

Figure 11: Hierarchy of failure modes for masonry buildings from Lesvos case study [81]: masonry disgregation **(a)**, out of plane mode **(b)** and in-plane mode **(c)**.

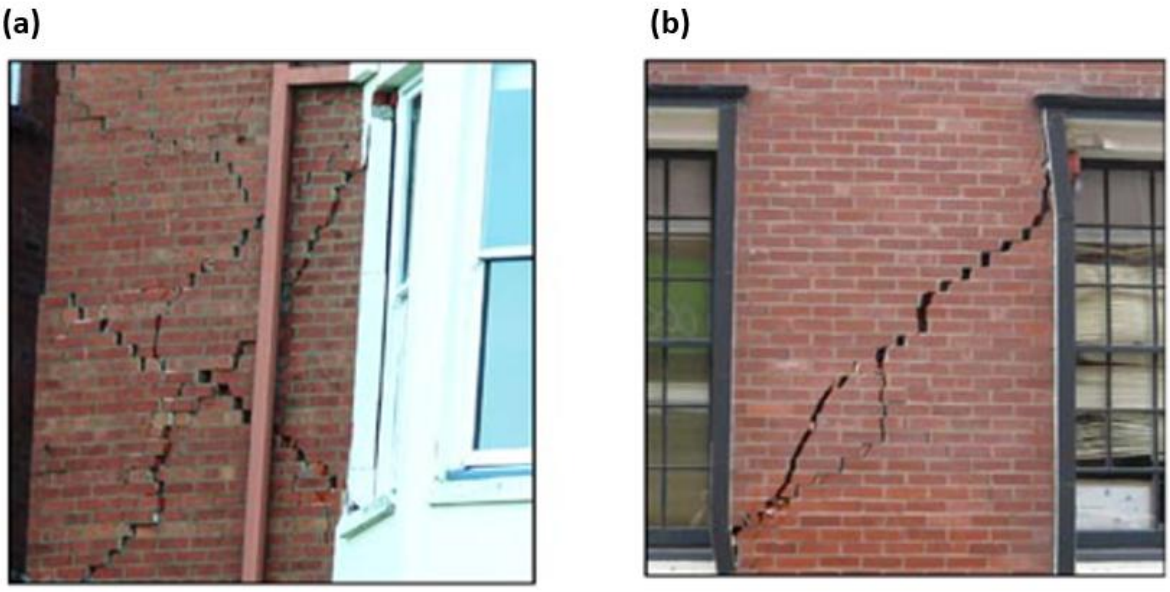

Figure 12: Examples of diagonal shear cracking through **(a)** mortar joints and **(b)** through bricks for masonry cavity walls. Adapted by [82].

2.3.1 Masonry assemblage behavior

The smallest masonry configuration consists of two units connected by a mortar joint, offering the opportunity to investigate the unit-mortar interface, typically the most vulnerable element in masonry. Two distinct testing methods are employed to assess these interfaces: direct tensile tests and shear bond tests, primarily aiming to explore the respective failure modes, known as first and second modes, respectively.

Typical response of direct tensile test on couplet with displacement control is represented in Fig. 13a with a linear behavior till the peak followed by a softening exponential branch. Van der Pluijm [84] tested several clay and calcium silicate (Ca-Si) units in combinations with different mortar types, evaluating the fracture energy of the first mode G_{ft} and tensile strength f_t. Results showed no clear correlation between these two variables but a trend with increasing value of fracture energy corresponding to high value of tensile strength. Furthermore, the surface of fracture in the tensile tests is inferior to the total cross section of the couplets on average of 35%, probably due to setting of the mortar in its plastic phase and shrinkage (Fig. 13b). From these tests, values of the fracture energy of the first mode ranging from 0.002 to 0.02 N/mm are reported. Values obtained from the experimentation carried out in Barros et al. [85] are slightly higher probably due to the process of manufacturing the masonry specimens that enforced a loaded area similar to the cross-section.

The bond wrench test setup is also employed [86-87] for assessing the tensile bond characteristics of couplets or stack-bonded prism interfaces (Fig. 14a). This value holds significance as it is linked to the ability of masonry to withstand out-of-plane loads and maintain stability against wind loads, real issue due to the use of lightweight roofs in modern practice. Several tests set-up have been elaborated but the principle is applying a load F by means of a clamp and a lever with a certain distance L to the top unit of the specimens, while

maintaining restrained the lower part of the sample. Kubica and Galman [88] recently tested according EN1052-5 [89] the influence of mixing content water and curing time on the bond behavior of clinker units intended for façade walls. Effectively, the reliability of the wrench test results is questionable when comparing different experimental campaigns due to the differences in shapes of samples and in the test set-up features allowed. In this context, Gaggero and Esposito [90] proposed a comparative study on the influence of different wrench test set-ups on cement and lime-based masonry samples. Both manual and computer-controlled test setups exhibited comparable coefficients of variation, indicating no elevated differences in the accuracy. However, stack-bonded couplets appeared to underestimate bond strength compared to the test results obtained on running bond wallettes. In terms of flexural strength of masonry in out of plane movements, the EN1052-2 [91] is the widest used allowing tests in direction perpendicular and parallel to the bed joints [92] (Fig. 14b-c). Effectively, Van der Pluijm [84] evidenced the relations between the flexural strength on wallettes tested parallel to bed joints in four point bending and the bond strength from prisms tested with the wrench test. Theoretical and experimental ratios of 0.7 and 0.87 were found for wrench bond strength and flexural strength of clay masonry.

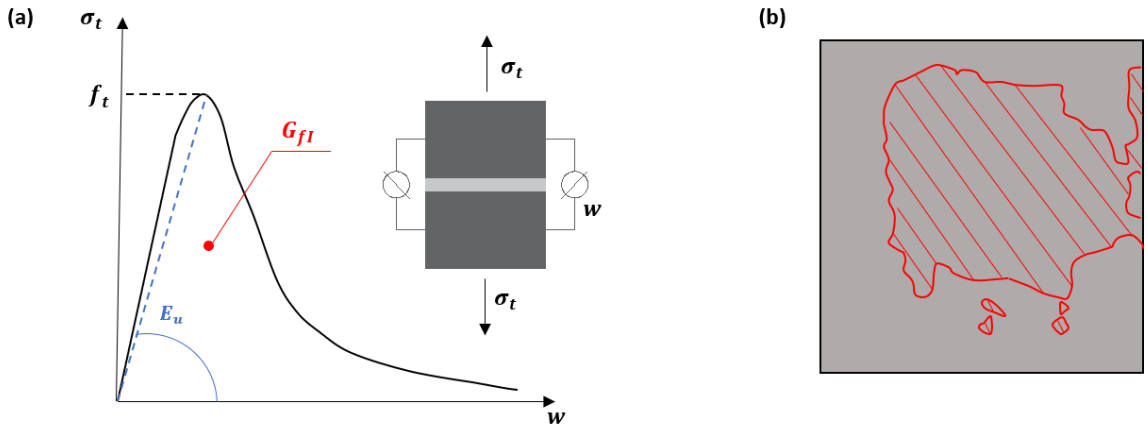

Figure 13: Typical response of masonry couplet tested in tension **(a)** and result for the actual bonding cross-section (evidenced in red) from tensile prism made of clay units and mortar with volumetric proportions 1:2:9 of cement:lime:sand from Van der Pluijm [84] **(b)**.

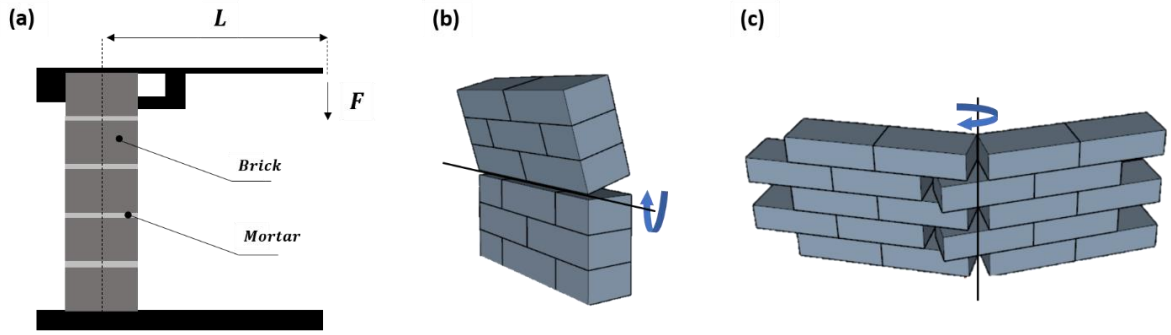

Figure 14: Typical wrench bond test set-up as for EN1052-5 [89] **(a)**. Failure modes involved in flexural tests as for EN1052-2 [91]: parallel to bed joints **(b)** and perpendicular to bed joints **(c)**. Adapted from Singhal et al. [92].

Shear behavior of couplets were also investigated by Van Der Pluijm [84] with two different tests set-ups. Effectively several Authors studied different test set-ups with the main objective of enforcing a uniform state of stress in the joints. In the first tests on couplet specimens subjected by a fixed compression orthogonal to the bed joint and shearing force parallel to the bed joint are performed. The experimental outcomes of these tests showed a typical diagram with a softening tail that does not fall to zero but becomes stable at a certain level. This level corresponds with the dry friction of two non-bonded surfaces. Furthermore, it is possible to associate to the specimens a value for the fracture energy for the II mode G_{fII} (Fig. 15a). Successively, a new test set-up was elaborated with the purpose to experience masonry specimens under programmable combination of tension and compression, thus, to establish a complete failure envelope for joints (Fig. 15b). At European level, the shear strength is evaluated according to the standard EN1052-3 [93], where the specimens are triplets, subjected to at least three level of increasing pre-compressions. In this scenario, setting up the test and establishing the envelope are relatively straightforward tasks. However, obtaining the softening behavior can be challenging because joints typically do not fail simultaneously, and the initial failure of one joint leads to the rotation of the specimens. From the experimental outcomes emerged also the phenomenon of the of dilatancy ψ namely: the occurrence of a vertical displacement un perpendicular to the imposed shear force. Physically, it is due to a non-perfectly smooth cracked surface, so the shearing goes united with an uplift of the bricks.

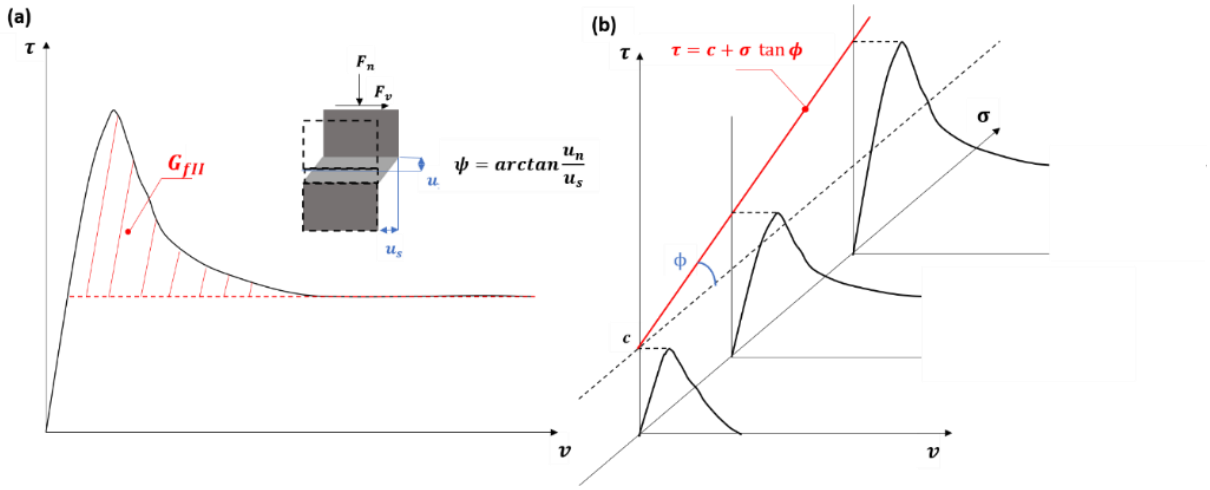

Figure 15: Results from shear test on couplet subjected to constant vertical load F_n **(a)** Envelope model of the interface brick-mortar for increasing level of pre-compression **(b)**. Adapted from Van Der Pluijm [84].

Hilsdorf [94] made the initial effort to describe the axial compression behavior of masonry, relying on stiffness relationships between mortars and bricks within stack-bonded prisms. Typically, there are two distinct scenarios to consider. In the first scenario, which is common in historical structures, the mortar exhibits greater deformability compared to the units. In this case, the lateral deformations of the mortar joints are constrained by the stiffer units, causing them to be in a triaxial state of compression, while the units experience a biaxial state of tension. In this scenario, prism failure occurs through the tensile splitting of units if the confined mortar strength surpasses the tensile strength of the units; otherwise, it results

from the crushing of the mortars. In the second scenario, where the mortar is stiffer than the units, the joints are subjected to a biaxial tensile state of stress, while the bricks themselves are under triaxial compression. In this situation, a brittle failure occurs due to the crushing of the units [95].

The American standard ASTM C1314 [96] employs prism tests to assess compressive behavior, while the European Standards EN 1052-1 [97] rely on wallettes tests for the same purpose. Naturally, it is crucial to accurately characterize the compression stress-strain behavior of masonry in order to investigate material-dependent aspects of masonry structural performance and apply realistic numerical models. In this sense, the first stress-strain relations used for masonry structure analysis at macro-scale were taken by the concrete experimentations. The Kent and Park model [98], calibrated using experimental tests on masonry, remains a prominent example utilized in panel-scale modeling [99]. This is due to its straightforwardness, characterized by a representation of a parabolic branch up to the peak load followed by a linear softening branch.

More properly related to masonry, Eurocode 6 [13] proposes stress-strain relationship of masonry in compression for designing purposes with parabolic and rectangular shapes, defining the peak and ultimate strains based on the types of units. The compressive strength is given by (1):

$$f_k = K f_b^{\alpha} f_m^{\beta} \tag{1}$$

where:

- f_k is the characteristic compressive strength of the masonry;
- K is a constant to be defined depending on the brick and the brick-mortar joint types (ranging from 0.35 to 0.55 for clay bricks) and usually specified in National Annex to use in given country;
- α is a constant (now taken as 0.7 for masonry other than dimensioned natural stone masonry, made with general purpose mortar and lightweight mortar);
- β is a constant (now taken as 0.3 for masonry other than dimensioned natural stone masonry, made with general purpose mortar and lightweight mortar);

According to EN 1052-1 [97], if the secant modulus of elasticity is not determined experimentally, a simplified estimation may be adopted by using a coefficient k multiplied by the compressive strength of the masonry. The recommended default value for k is 1000, which provides a conservative estimate on the safe side. However, this coefficient can vary significantly depending on national recommendations and the type of masonry units used. For example, the German National Annex to EN 1996-1-1 (DIN EN 1996-1-1/NA:2012-05 [100]) suggests differentiated k values depending on the masonry unit category (e.g., vertically perforated clay units, lightweight concrete blocks), typically ranging from 700 to 1200. Other National Annexes also provide specific values tailored to their regional materials and construction practices. This variability highlights the empirical nature of the k factor and its sensitivity to local material properties and manufacturing standards.

Kaushik et al. [101] re-adapted Kent-Park model [98], performing compressive tests on mortars, bricks and masonry assemblages in order to predict their uniaxial stress-strain. A part

the stress-strain definition, an insightful conclusion is depicted by numerous tests on masonry prisms made of strong and weak mortars. In fact, experimental results have revealed that the conventional assumption that masonry exhibits compressive behavior intermediate to that of bricks and mortar no longer applies when the strength and stiffness of bricks and mortar are similar. In this case, it is better in terms of masonry performance using soft instead of strong mortars. The peak strength f'_m (2) and deformation ε'_m (3) of the stress-strain proposed is given based on the results of four types of bricks and three types of mortars:

$$f'_m = 0.63 f_b^{0.49} f_j^{0.32} \tag{2}$$

$$\varepsilon'_m = \frac{0.27}{f_j^{0.25}} \frac{f'_m}{E_m^{0.7}} \tag{3}$$

Where f_b the compressive strength of the bricks, f_j the compressive strength of the mortar, E_m the elastic modulus of masonry.

With a stress-strain shape parabolic till the decreasing of 0.9 of the peak strength of the masonry and then a conventional linear softening branch with last deformation ranging from 2 to 2.75 times the peak deformation. The last value introduced because masonry incorporating lime mortar possess a higher ductility (Fig. 16).

Lumantarna et al. [102] calibrated the same stress-strain relationship proposed by Kaushik et al. [101], using experimental data from both laboratory-produced and existing masonry materials. In their study [102], the peak compressive strength f'_m (4) and the corresponding strain ε'_m (5) were defined using the same notation as in Kaushik et al. [101]:

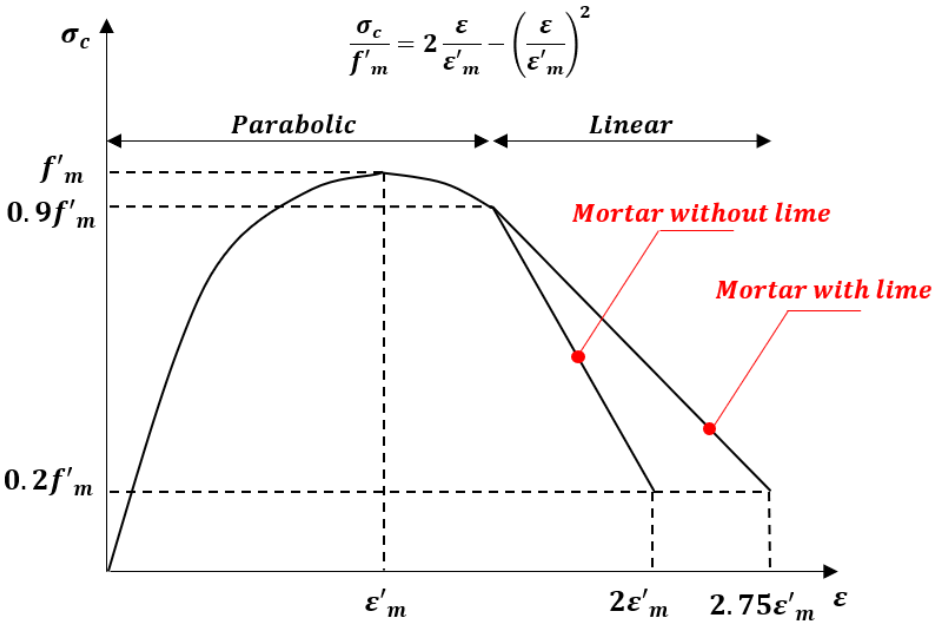

Figure 16: Compressive stress-strain relationship proposed by Kaushik et al. [99].

$$f'_m = 0.75 f_b^{0.75} f_j^{0.31} \tag{4}$$

$$\varepsilon'_m = \frac{0.21}{f_j^{0.25}} \frac{f'_m}{E_m^{0.7}} \quad (5)$$

Specifically, the Authors [102] observed that prisms constructed using mortars with an average strength exceeding 5MPa and those constructed with mortars having an average strength below 5MPa could be characterized using the Kaushik equation [101], with this 5MPa value serving as the demarcation between masonry made of strong and weak mortars.

Most of the research in the literature concentrates on establishing the compressive strength of masonry wallets and prisms through regression analysis of experimental tests. Generally, the shape of these formulations finds in the form of power model or linear expression of the strength of constituents. The US commentary on Specification for Masonry Structures [103] proposes for example a linear equation (6):

$$f_m = \frac{A(400 + B\, f_b)}{145} \quad (6)$$

Where the factor 145 is due to the passage from Psi in MPa unit, A depends on the type of masonry (1 for inspected masonry) and B depends on the ASTM strength classification for mortars. In only a limited number of instances, these relationships explicitly consider factors that influence strength, such as sample slenderness, joint thickness, or local effects [104]. In this context, Thaickavil and Thomas [105], based on prism testing, elaborated a formulation (7) accounting for height-to-thickness ratio of the masonry prism (*h/t*), volume fraction of brick (V_{Fb}) and volume ratio of bed joint to mortar (VR_{mH}):

$$f_m = \frac{0.54\, f_b^{1.06}\, f_m^{0.004}\, VF_b^{3.3}\, VR_{mH}^{0.6}}{\left(\frac{h}{t}\right)^{0.28}} \quad (7)$$

In addition to the examination of the compressive properties, the shear and tensile properties of walls play a crucial role in predicting the structural performance of masonry. To investigate these properties in both in-situ and laboratory settings, diagonal shear tests are conducted [106-107] (Fig. 17).

Typically, these tests involve applying force along the main diagonal of the specimen using hydraulic jacks and two steel shoes positioned at opposing edges until failure occurs. Dimensions of the steel shoes should be limited in order to avoid modifications of the failure modes from ones associated with shear stress to ones connected to the compression of masonry. However, this effect is only appreciable for long shoes in the range of 1/3 of the specimen length [108]. It is also not unusual to find literature cases where the first rows of bricks are removed at the opposite edges of the wallettes, to avoid sliding between the first rows of bricks and the rest of the panel. This last instance may occur in the case of old masonry materials (e.g. adobe masonry [109]) but, also, in the case of new masonry solutions with poor mechanical properties [110]. Two main standards are commonly followed: the American ASTM E 519-10 [111] and RILEM TC-76 (LUMB6) [112]. These standards are founded on two

distinct hypotheses for interpreting the stresses at the center of the panel (Fig. 18). ASTM E 519 [111] operates under the assumption of pure shear stress at the center of the panel, considering an isotropic linearly elastic material. In this scenario, the principal tensile strength aligns with the pure shear strength. On the other hand, RILEM TC-76 [112] relies on the solution to the elastic problem for a plane stress element, as proposed by Frocht [113], under the assumption of a homogeneous and isotropic material. In this case, the principal tensile strength at the center of the panel is obtained as $\sigma_I = -0.5P/A$. However, several Authors [108,114] have observed through finite element analysis that the RILEM [112] approach is based on a more accurate assumption regarding the stress states.

Figure 17: Typical test set up scheme for diagonal compressive test on masonry wallettes. From Silva et al. [106].

In instances of diagonal cracking, the principal tensile strength of the diagonal test can be associated with the one determined through the shear-compression test, as per the Turnšek and Čačovič model [115]. According to this model, the panel experiences diagonal failure when, while maintaining a constant compressive stress, the shear strength is increased to the point where it equals the tensile resistance of the material's principal tensile strength. By reversing the relationship presented of Turnšek and Čačovič [115], one can derive the principal tensile strength of the masonry (Fig. 19). In Fig. 19, the coefficient p considers the slenderness of the cross-section of the panel and can assume values of 1.5 and 1.0 for slender and squat walls, respectively. In most international codes, this parameter is an assumed variable with the aspect ratio [116-117]. Effectively, Celano et al. [118] showed, based on parametric numerical analysis, the possibility of using values superior than 1.0 even for squat walls.

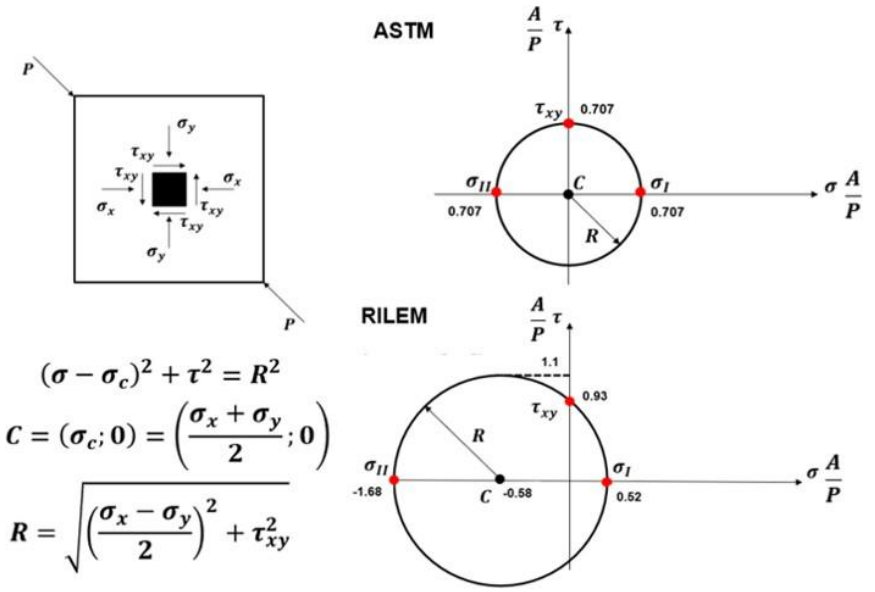

Figure 18: Representation of the tensional state at the center of the panel according to ASTM [111] and RILEM (Frotch) [113] interpretations, by the Mohr's circles. (σ_x, σ_y represent axial stresses at the center of the panel while τ_{xy} denotes the shear stresses acting in both the horizontal and vertical directions, σ_I and σ_{II} principal stresses, *C* center of the Mohr circle, *R* radius of the Mohr circle, *P* diagonal load applied).

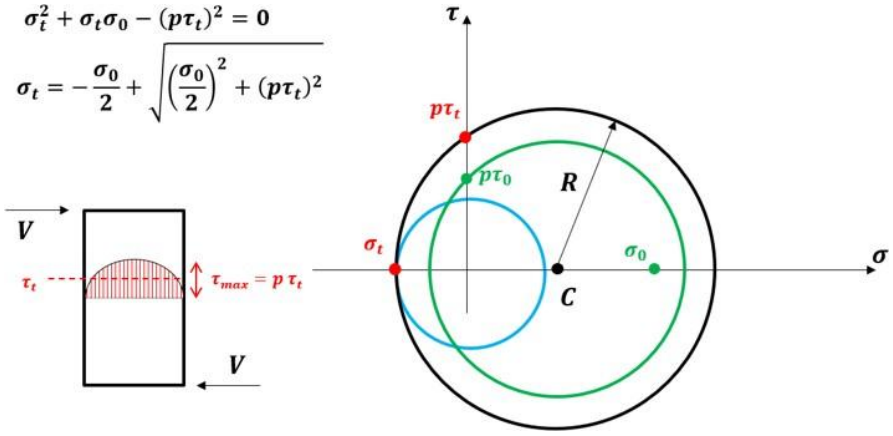

Figure 19: Mohr's circles relative to the initial state of the panel (green) defined with coordinates (σ_0; $p\ \tau_0$) of compressive and shear stress, failure associated to Turnšek and Čačovič (black) with maximum shear stress $p\ \tau_t$ corresponding to the σ_t principal tensile stress [115] and failure for pure shear stress (ASTM) (blue) [111]. Adapted from Augenti et al. [14]. (*C* center of the Mohr circle, *R* radius of the Mohr circle, *V* horizontal load applied, *p* factor for the redistribution of the shear stresses at center of the panel).

2.3.2 URM under vertical static shearing – irregular settlements

In-plane lateral response of masonry walls has been intensively studied in the last two decades but still limited attention has been given to the vertical shear response due to para-seismic impacts resulting from mining activities (e.g. hard coal mining, copper mining) as well as due to various subsidence of foundations, tunneling and intensive urban and/or rail traffic. The problem connected with this action pertains not just to loading and non-loading bearing walls of new constructions experiencing cracks from minor differential settlements, but also to the assessment of life safety factors for more brittle historical masonry structures [119].

Currently, there are limited predictive formulations available for designing at serviceability limit states under these stress conditions.

The majority of experimental tests carried out in this area concerns reduced scale specimens. In the European panorama, within the context of the assessment of risk damage due to tunnel excavations, an experimental test and numerical modelling on a 1/10th scaled façade model is reported in [120-121]. Based on these studies, Authors [120-121] concluded that the soil-structure interaction so the way of modelling the interface plays an important role in the structural response of walls. Furthermore, the final damage observed strongly depends on the presence of openings with a concentration of stresses at their corners. Other examples cover the performance of masonry walls with dry-joints. In this case, the modeling strategies preferable are discrete element models where the units are considered as rigid bodies interacting at their contact interfaces [122-124]. Different large-scale test set-ups for the determination of the performance of masonry walls subjected to vertical shear loads were developed at the Silesian University of Technology [125-126]. The first test stand developed by Kubica [127] was designed to investigate the behavior of unreinforced masonry walls subjected to shear deformations caused by differential vertical displacements. The experimental setup consisted of a rigid steel frame supporting generally full-scale walls made of running bond solid clay bricks and AAC blocks bonded with lime-cement mortar of different proportions. The walls were seated on two independent supports: one fixed, and the other vertically displaced upward using a hydraulic actuator, thereby inducing a controlled angular distortion across the panel. This configuration allowed the simulation of realistic shear deformation without applying lateral loads. Measurements included vertical and horizontal displacements via LVDTs, strain development through gauges, and visual monitoring of crack formation and propagation (Fig. 20a-b).

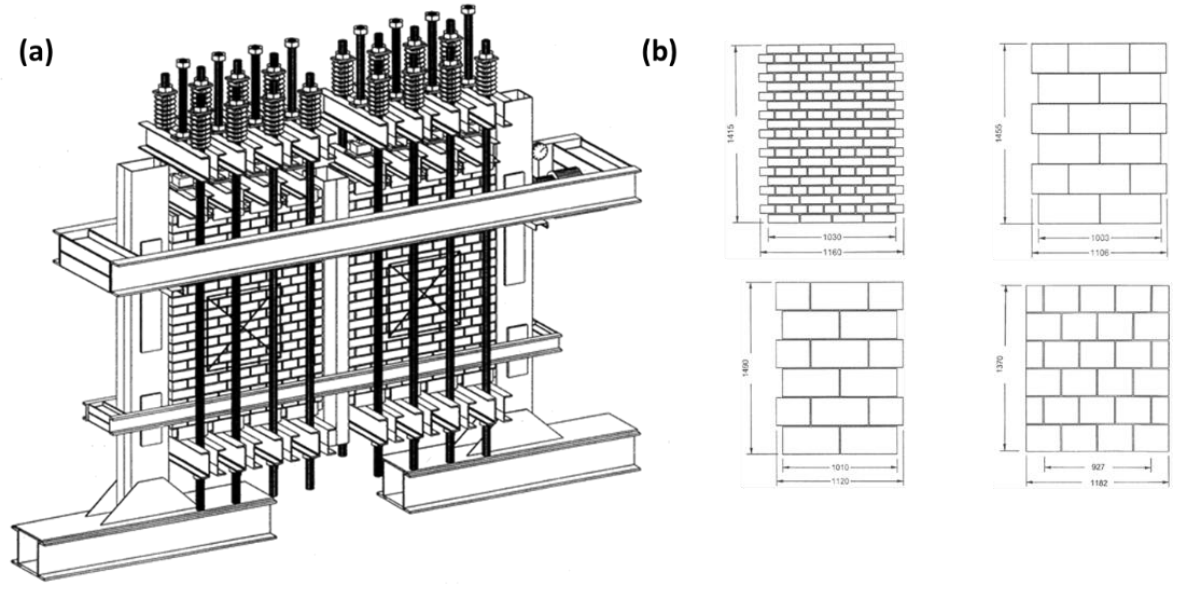

Figure 20: Test set up **(a)** and specimens **(b)** adopted in the experimental investigation by Kubica [127].

The results showed that cracking initiated near the loaded corner and progressed diagonally across the wall, indicating classic shear failure. The walls exhibited nonlinear load-deformation

behavior, with progressive stiffness degradation and reduced shear capacity as displacement increased (Fig. 21a-b). The observed shear angles at failure and crack patterns were used to propose new criteria for assessing deformation limits in masonry, with direct implications for evaluating serviceability in structures subjected to foundation movement.

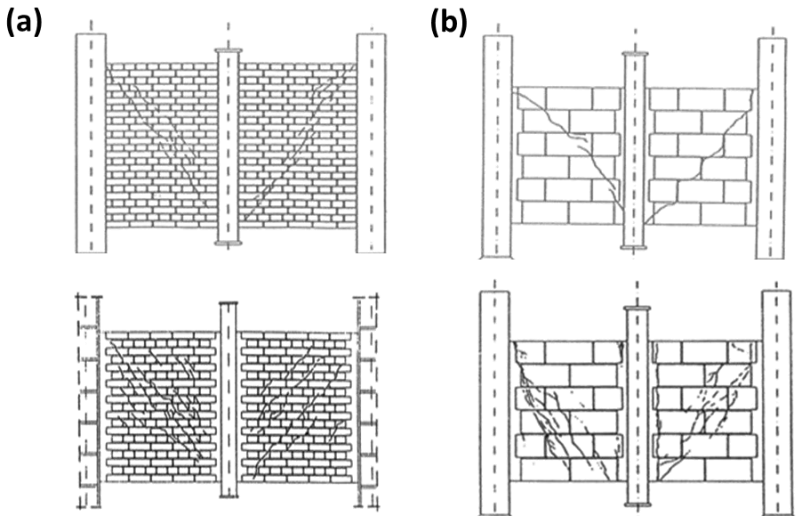

Figure 21: Example of failure of wallettes made of clay solid bricks (a) and AAC blocks with common joints (b) tested without pre-compression (top figures) and with pre-compression (bottom figures) - from Kubica [127]).

A modification of the previous test stand was thought to study the shear behavior of single elements subjected simultaneously to compressive loads and increasing vertical shearing. In particular, it was built by bonding the two vertical sides of the walls with two steel columns by means of concrete made of fast-setting cement. The wall bottom and top bases are first subjected to vertical compressive loads realized using series of tension members. In a second step, while one column is fixed to the strong floor during all the test, the other transmits to one or eventually two masonry wallettes an increasing vertical shearing load, till the failure (Fig. 22).

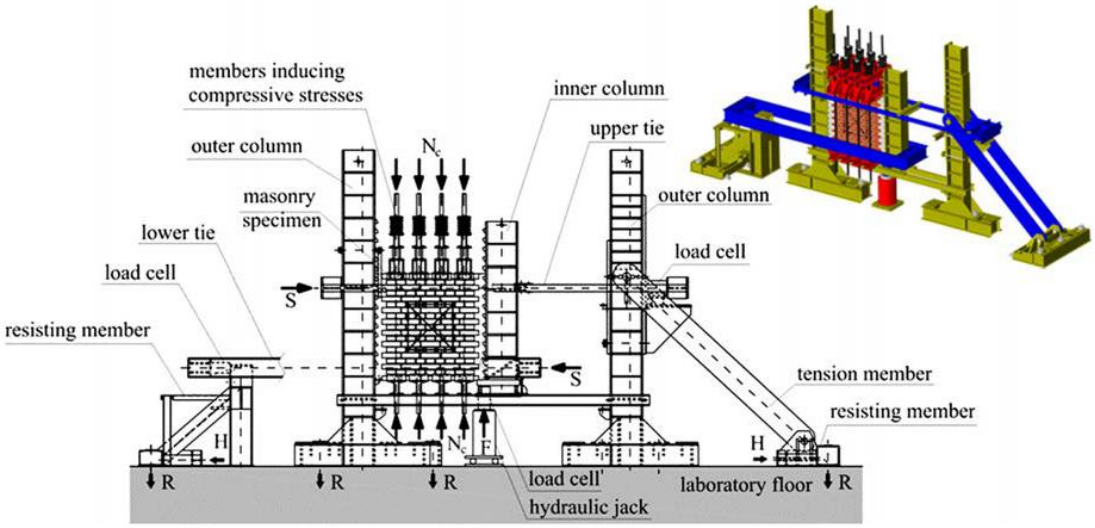

Figure 22: Vertical shear test set up developed at SUT [125].

Piekarczyk [125] examined the behavior of ten masonry wallettes built with solid clay units and blended cement-lime mortars. The wallettes were subjected to shearing forces and progressively elevated vertical compression levels. The objective was to investigate the correlation between shear stress and the angle of distortion, assessed by monitoring modifications in the length of a square frame equipped with strain gauges. The findings demonstrated an elastic-plastic response in terms of distortion and shear stress. The hardening phase was observed to begin when a critical shear value, indicating the onset of diagonal cracking, was reached. Additionally, pre-compressive stresses were found to have a beneficial effect on enhancing the resistance to cracking in walls (Fig. 23a-b). In the work [128], the same Author extended the experimental analysis to the assessment of walls made of aerated autoclaved concrete blocks (AAC) with thin joint thickness. The AAC block samples exhibited an altered crack pattern, wherein the distinctive diagonal crack was replaced by multiple vertical cracks. These cracks varied in intensity, transitioning from no compression to higher levels of compression, respectively, in contrast with main diagonal cracking for all levels of compression for clay bricks. On the basis of the same experimentation in Piekarczyk [129], the Author proposed a further theoretical description of the results with the Mann and Muller criterion [130]. Kubica [126] summarized the main evidence on the in-plane response of masonry wallettes subjected to shearing action in vertical direction on bed joints, with or without pre-compression. Assuming a failure criterion with visible cracks of width exceeding 0.3 mm (Serviceability Limit State), Kubica [126] noted the possibility to use safely for design purposes the Coulomb-Mohr criterion given in Eurocode 6 [13] also for vertical shearing.

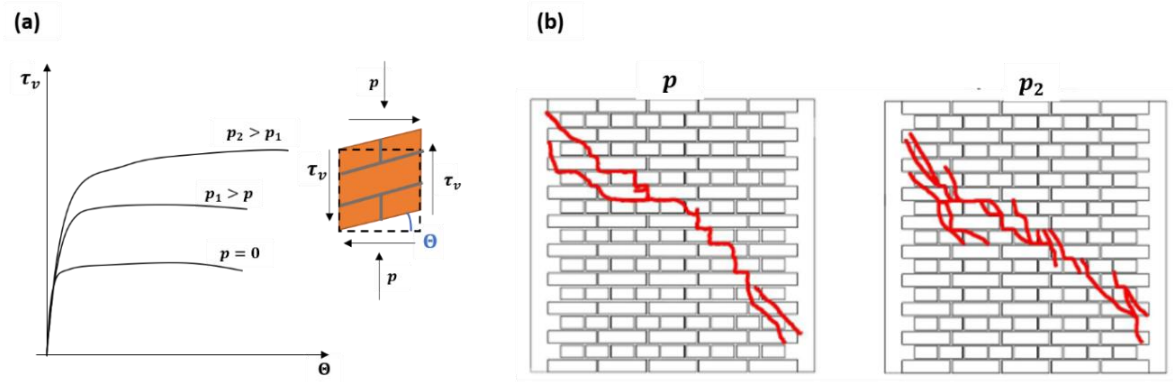

Figure 23: Typical vertical shear stress-angular deformation response [125] **(a)**. Crack pattern for clay masonry wallettes subjected to vertical shear loads with zero pre-compression p and 1.5 MPa of pre-compression p2. Adapted from Piekarczyk [128] **(b)**.

The need to examine the vertical displacements of masonry walls with realistic base dimensions and to speed up the specimen preparation process without using cement connections, prompted the creation of another test set up [131].

Specifically, this testing apparatus incorporates a flexible steel beam positioned on the top of vertical load cells, enabling the construction of the wall directly without the need for lateral connections to adjacent steel columns. Under this setup, only a single wall can be tested at a time. Specimens are first subjected to vertical loads F and then the load cells through connections with the steel beam, allow for the application of various displacement patterns δ_{vi} (Fig. 24).

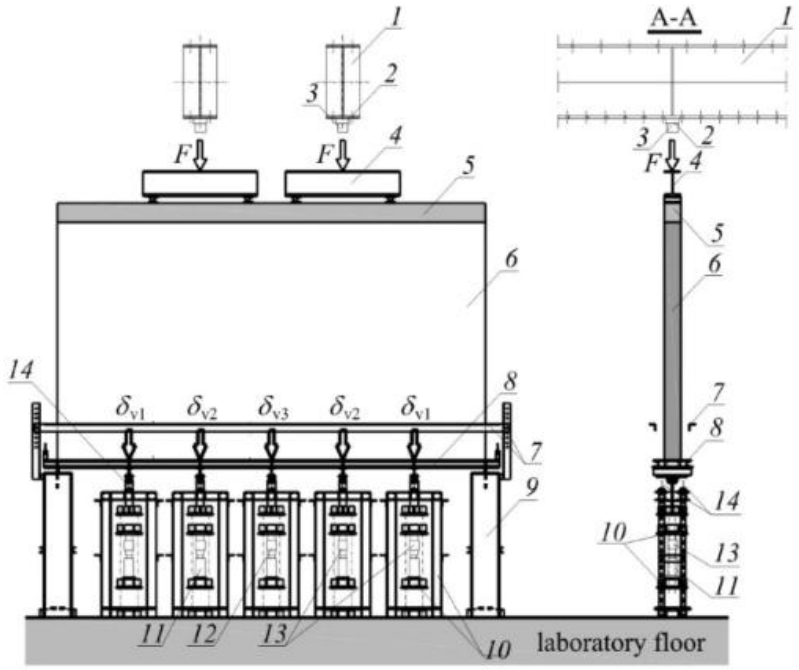

Figure 24: Test stand: 1 – steel frame, 2 – force gauge with range with the range to 500 kN, 3 – hydraulic jack with the range to 500 kN, 4 – steel beam, 5 – reinforced concrete top beam, 6 – tested wall, 7 – members of the system for measuring the vertical displacements, 8 – flexible support (steel beam), 9 – external support of the beam, 10 – elements of the system enforcing vertical displacements, 11,12,13 – hydraulic jack with range to 150 kN, 14 – screws for fixing the deflections. From Piekarczyk [131].

Similar test set-up has been used before on masonry walls on with and without openings in Holanda et al. [132-133], where only a load cell acting as support, positioned in the middle of wall, was pulled to enforce a vertical displacement till the elimination of its vertical reactions. In this case, the vertical shear reaction was applied to a reinforced concrete beam. Furthermore, in their tests a simplified macro-model approach showed the necessity to consider the contact interface between the deflecting concrete beam and the wall for more reliable results. Loots et al. [134] conducted an experiment involving a masonry wall with dimensions of 3 meters in length and 1 meter in height. They subjected this wall to a deflection by means of a supporting I steel beam and observed the development of a non-symmetric crack in the wall at approximately a 1/1200 deflection ratio. Also, Meyerhof [135] suggested that the ratio of support beam deflection to its span should not surpass 1/2000, and additionally the tensile strength of the wall should be at least 0.21 N/mm². A new tilting table has been elaborated by Savalle et al. [136]. In this case, the settlement system comprises a mobile component (with one degree of freedom represented by vertical translation) and a stationary component represented by the tilting table at rest. Test specimens are placed on both tables, and the downward motion of the settlement table replicates differential soil settling. In a construction site case study conducted by Kania et al. [137], partition masonry walls featuring a central door opening were subjected to increased deflections by means vertical actuator, acting on a refaced concrete floor. The investigation encompassed two walls, with one wall utilizing lateral connections composed of flexible steel anchors, while the other wall had a rigid connection to cross walls. The first wall showed a first crack with deflection of 1/958, while the deflection of the rigid wall was able to sustain a double deflection without

showing damage. The works [138-139] described the results of full-scale tests on calcium silicate masonry walls with and without symmetrical and asymmetrical openings, subjected to vertical deflection, based on the test set up of Fig. 24. The analysis of crack patterns revealed varying behavior, primarily influenced by several factors: the presence of openings, the inclusion of redistribution elements for vertical loads, and the simultaneous occurrence of increasing vertical loads alongside increasing floor deflections.

Specifically, walls without openings exhibited critical cracks for detachment of their base from the support, showing deflection values below 1.5 mm when not subjected to any top compressive loads. In contrast, walls with identical dimension (4.55 x 2.45 m), when subjected to increasing vertical loads and vertical displacements, exhibited higher deflections up to 26 mm, accompanied by a crack pattern characterized by diagonal cracking, starting from the edges, or cracking along the mid height of the walls (Fig. 25).

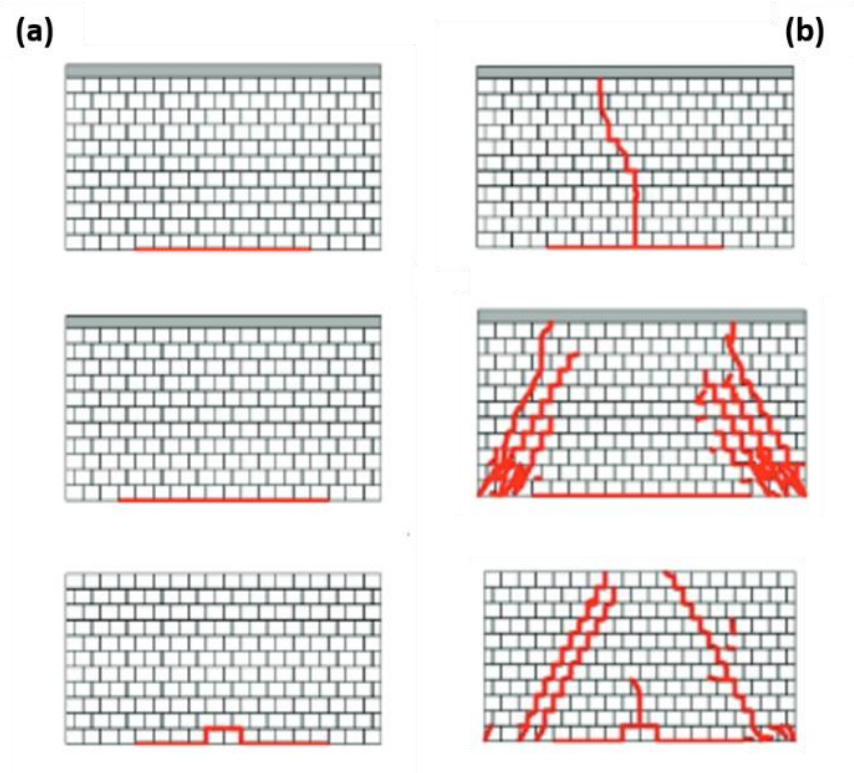

Figure 25 Crack patter of calcium silicate masonry walls 4.55 x 2.45 m tested without vertical loads and increasing vertical displacements **(a)** and with increasing vertical load and deflection **(b)**. Adapted from Piekarczyk [139].

2.3.3 URM under horizontal cyclic loading – seismic type loads

The experimental investigation of masonry wall cyclic lateral behavior has started receiving significant attention in the past twenty years. Due to this scientific interest, comprehensive datasets and test results have been systematically gathered [140-142], providing valuable information at the design level of masonry building. Various factors impact on the lateral wall responses, including slenderness of the wall, vertical stress, masonry textures, and boundary conditions [143]. In any case, the lateral response of masonry walls can be distinguished based on the different crack patterns and failure mechanisms observed

experimentally. Specifically, a flexural failure mode can happen when the compressive and tensile strength thresholds are reached on opposite sides of the base of the wall known as rocking (Fig. 26a). Alternatively, elevated compressive loads may only lead to failure when the maximum compressive strength is reached at one edge of the wall base (toe crushing) in Fig. 26b.

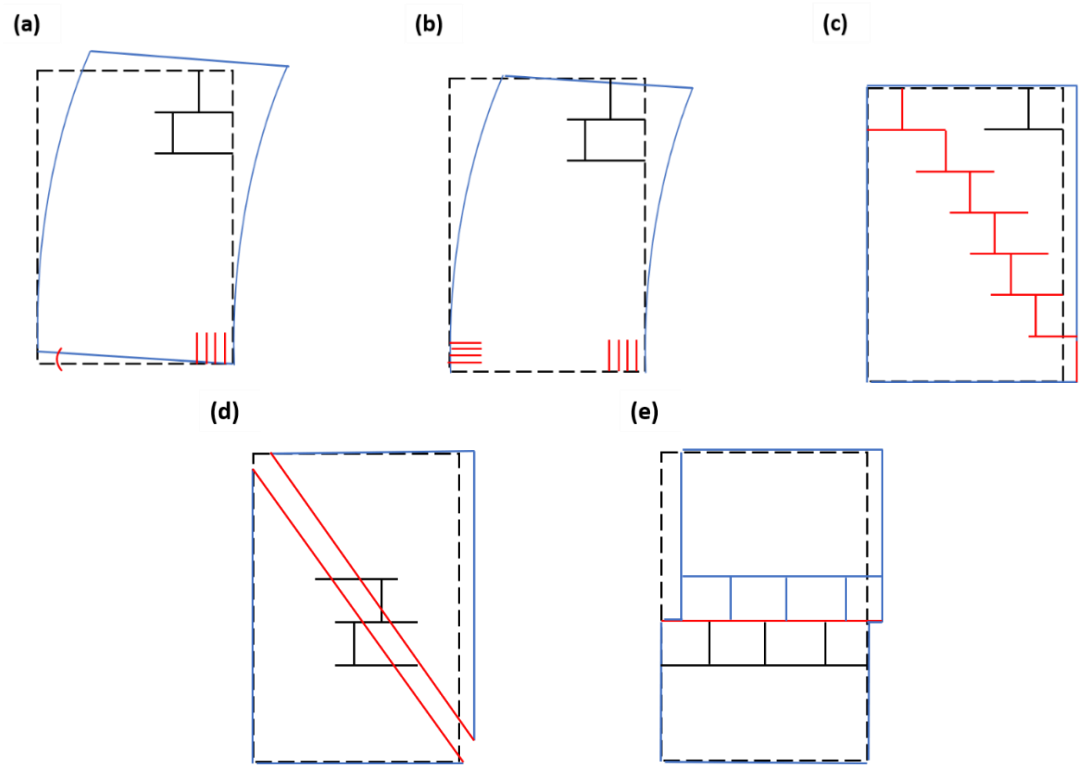

Figure 26: In-plane masonry walls failure modes when subjected to vertical and lateral load: rocking flexural behavior **(a)**, toe crushing **(b)**, diagonal shear sliding **(c)**, diagonal cracking **(d)** and horizontal sliding **(e)**.

In contrast to previous flexural responses, a shear failure mode can manifest, characterized by different resistance mechanisms: diagonal cracks along the mortar head and bed joints (diagonal sliding) in Fig. 26c, diagonal cracks through bricks and mortar (diagonal shear cracking) in Fig. 26d and horizontal sliding along bed joints (sliding) in Fig. 26e [144-145]. In real-world scenarios, multiple failure modes may concurrently manifest in the same masonry element, complicating the establishment of precise relationships for defining these failure modes.

Anthoine et al. [146] examined the influence of wall geometry, testing in quasi-static cyclic loads two walls, with the same vertical force of 150 kN and double-fixed boundary conditions, with different heights height to width ratio. Tests highlighted a shear response of the squat wall with high energetic dissipation and softening behavior after the peak shear load. Based on the previous study and others [147], Magenes and Calvi [148] introduced modification of the simplified formulation for the determination of lateral response according to the existing codes. Raijmakers and Vermeltfoort [149] tested the influence of increasing the vertical pre-compression loads on clay masonry walls. Increasing the level of pre-compressive loads lead to an increase of lateral shear strength but a more brittle failure, characterized by

diagonal cracking. Triller et al. [150] performed cyclic static tests considering different boundary conditions. Precisely, four types of restraints were considered: type I (cantilever), type II (fixed-fixed rotations with constant axial force), type III (fixed-fixed rotations and fixed vertical displacements with variable axial force) and type IV (fixed position of the moment inflection point at mid-height of the wall). Only the cantilever boundary conditions (type I) produced flexural failure while all other boundary conditions produced shear type response.

Effectively, the most common boundary conditions reproduced by experimental tests are the cantilever and the double-fixed conditions, which may not be the most realistic of the structural walls of masonry building, as shown in Petry and Bayer by means of pushover analysis of a masonry façade using macro-modelling approach [151]. Furthermore, these experimental tests are inherently limited by the specific experimental conditions and sample dimensions reproduced in each test. This limitation is linked to the size/scale effect, wherein increasing the size of a specimen results in a reduction of its structural strength, as highlighted numerically by Lourenco [152]. This aspect is critical because, as observed by Petry and Bayer [151] the majority of cyclic tests conducted to establish standards for the drift capacities of masonry walls, used for assessing existing structures, and more recently, for displacement-based design, have employed masonry walls with heights lower than the typical storey height for masonry buildings, thus yielding non-conservative results. Other studies focus on investigations related to different materials. Aoki et al. [153] conducted parametric studies on the cyclic lateral behavior, with key variables including the aspect ratio and various mortar types representative of both historical constructions and contemporary structures. In particular, walls made of cement and mixed cement lime mortars with higher strength characteristics showed flexural rocking failure mode. Walls with lime-based mortars with low strength mortar showed diagonal shear cracking failure mode. Interestingly, the failure modes observed for the walls were irrespective of the different aspect ratios and were completely governed by the mortar types. Also, while the peak in-plane lateral load carrying capacity of lime-based walls were lower than the cement-based walls, their energy absorption and equivalent damping were higher. Upon the episodes of induced seismicity in the north of the Netherlands, an extensive testing program has been conducted by Messali et al. [154], in order to understand the response of masonry walls made of Ca-Si bricks. On the basis of this work, the researchers concluded that the failure modes strongly depend on the shear ratio with flexure governing for high shear ratios, and shear failure occurring for low shear ratios. Moreover, while the initial stiffness of the tested walls can be fairly approximated by the elastic stiffness computed according to the Timoshenko beam theory and the peak shear force can be preliminary estimated with an empirical equation, the displacement capacity of the walls at near collapse cannot be predicted accurately. In order to assess the seismic response in dry and wet conditions for walls, Elghazouli et al. [155] carried out an experimental campaign on walls made of solid clay units and hydraulic lime mortar, based on their previous experiences with triplets and couplets in dry and wet conditions. Preliminarily to the displacement-controlled cyclic tests, also diagonal compressive tests were performed on wallets. Results on diagonal panels showed that moisture reduced both the elastic stiffness and strength. Furthermore, moisture reduced for large scale walls both the stiffness and lateral strength in range between 10% and 20% approximately, compared to the dry counterparts.

From a code perspective, several relationships are available for the shear strength of masonry walls subjected to both vertical and lateral loads. Tariq et al. [156] proposes a review of the main existing international formulations, hereafter summarized in Tables 2-3 with the main analytical expressions. ASCE 41-13 [157] and NZSEE-17 [158] from New Zealand exhibit analogous relationships for flexural toe crushing, rocking failures, and diagonal cracking, although differences arise in the context of sliding failure. Eurocodes EC6 [13], EC8 [159], and the Italian code NTC-18 [38] with its explanatory circular [160] do not provide analytical expressions for rocking failure modes while the toe crashing varies just on the coefficient describing the stress-block distribution for the compressive stress along the sections.

Table 2: Analytical code expressions for the shear strength of masonry walls subjected to lateral loads for American ASCE 41-13 [157] and New Zealand NZSEE-17 [158]. In table: α: 1 or 0.5 for fixed-fixed or cantilever boundary conditions, P_D: dead load, P_W: weight load, L: wall length, h_{eff}: height to resultant of seismic force, f_a: axial compressive stress, f_m: masonry compressive strength, f_{dt}: masonry diagonal tensile strength, β: 0.67 for h_{eff}/L>1.5 or1 for h_{eff}/L<1.5, μ_f: friction coef., c: cohesion, t: wall thickness, υ_{te}: mean bed-joint strength.

Failure modes	ASCE 41-13 [157]	NZSEE-17 [158]
Rocking	See NZSEE-17 [158]	$V_r = 0.9(\alpha P_D + 0.5P_w)\frac{L}{h_{eff}}$
Toe crushing	See NZSEE-17 [158]	$V_{tc} = 0.9(\alpha P_D + 0.5P_w)\frac{L}{h_{eff}}\left(1 - \frac{f_a}{0.7f_m}\right)$
Diagonal shear cracking	See NZSEE-17 [158]	$V_{dc} = f_{dt}A_n\beta\sqrt{1 + \frac{f_a}{f_{dt}}}$
Sliding	$V_s = \frac{0.75\left(0.75\nu_{te} + \frac{P_D}{A_n}\right)A_n}{1.5}$	$V_s = 0.7\left(tLc + \mu_f(P_D + P_w)\right)$

Table 3: Analytical code expressions for the shear strength of masonry walls subjected to lateral loads for European EC6 [13] - EC8 [159] and Italian NTC-18 [160]. In the table, identical parameters as those in Tab.2 are included, along with additional parameters: b: $1/\beta$, A_w: area of horizontal wall cross-section, γ_M: partial safety factor, f_{tk}: characteristic masonry diagonal tensile strength, l_c: compressed part of the wall, σ_d: axial stress, f_{vk}: characteristic shear strength equal to $f_{vk0}+0.4\ \sigma_d$ for filled head and bed joints or $0.5f_{vk0}+0.4\ \sigma_d$ for only filled bed joints, f_{vk0}: the characteristic value of f_{vm0} which is how the NTC indicate the cohesion c.

Failure modes	EC-6 [13], EC-8 [159]	NTC-18/19 [38,160]
Rocking	-	-
Toe crushing	$V_{tc} = \frac{\alpha\ P_D L}{2h_{eff}}\left(1 - \frac{f_a}{0.87f_m}\right)$	$V_{tc} = \frac{\alpha\ P_D L}{2h_{eff}}\left(1 - \frac{f_a}{0.85f_m}\right)$
Diagonal shear cracking	$V_{dc} = \frac{f_{tk}\ A_w}{b\ \gamma_M}\sqrt{1 + \frac{\gamma_M\sigma_d}{f_{tk}}}$	$V_{dc} = \frac{Lt\ f_{dt}}{b}\sqrt{1 + \frac{f_a}{f_{dt}}}$
Sliding	$V_s = \frac{f_{vk}}{\gamma_M}tl_c$	$V_s = \frac{1.5\ f_{vm0}Lt + 0.4\ P_D}{1 + \frac{3h_0 t f_{vm0}}{P_D}}$

Besides the code formulations, the SLAMA-URM methodology [161] offers a simplified approach for describing the seismic capacity of masonry buildings at a macro-scale, from individual elements to complex assemblies of masonry piers and spandrels. Regarding the displacement capacity of masonry piers, codes also provide information based on the failure

modes (shear and flexural) and limit states: significant damage (life safety) limit State (SDLS) and near collapse limit state (NCLS). These assume the form of limits to the maximum drift capacity based on empirical test results. An overview of the Eurocode 8 [159], Italian [38, 160] and New Zealand [158] is given in Table 4. Considering the development of the new generation of Eurocode 8, [159] Beyer et al. [162] suggested adjusting the drifts of hollow clay masonry walls to better align with the experimental results for their cyclic response found in European databases.

Table 4: Drift capacity models for in plane behavior masonry walls according to different codes. In table: *h*: height to zero bending moment, *l*: length of the wall.

Limit states	**EC-8 [159]**	**NTC-18/19 [38-160]**	**NZSEE-17 [158]**
	Flexural - Shear	Flexural - Shear	Flexural - Shear
SDLS	0.8 h/l % - 0.4 %	0.75 % - 0.375 %	-
NCLS	1.07 h/l % - 0.53 %	1.0 % - 0.5 %	Min (0.3 h/l; 1.1) % - 0.3 %

2.4 Numerical modelling and simulations

Assessing the structural response of masonry structures remains a significant challenge due to the mentioned heterogeneity, necessitating the development of precise and efficient modeling methods. One of the primary challenges in ensuring the structural safety of masonry elements is the nonlinear mechanical behavior that initiates even with minor levels of deformation [163]. Furthermore, masonry structures present a difference to reinforced concrete and steel structures, as the latter can be straightforwardly represented using one-dimensional beam elements with flexural responses. In masonry elements, however, it is necessary to consider the shear contribution to their load-bearing capacity, which cannot be disregarded and not always captured by one-dimensional frame elements. Nonetheless, in recent years, various modeling approaches have emerged, spanning from simplistic to highly accurate ones. While a sophisticated model has the potential to offer a more accurate representation of masonry crack pattern, it typically necessitates a greater number of parameters. Obtaining these parameters through experimental tests may be challenging and expensive beyond the introduction of additional sources of uncertainty. As highlighted in NZSEE part C-2 [164], achieving a delicate balance between accuracy, reliability, cost, and complexity is essential in structural analysis. Following the literature review in the work [165], modeling strategies for masonry structures may be mainly dived in: block-based models, continuum models and macro-element models.

2.4.1 Micro models

Micromodels, which are also known as block-based models, entail the detailed representation of masonry at the individual block level, with interconnecting elements to simulate the mortar. These models excel in accurately capturing the failure modes, crack patterns and the bonding characteristics of masonry. A well-known micromodel was

elaborated by Lourenço and Rots [166]. Specifically, the Authors [166] proposed a multi-surface interface model capable to include the fundamental failure types of masonry specimens at small scales, such as: masonry crashing due to tension parallel and orthogonal to mortar joints, diagonal failure of masonry due to shear-compression loads, joint tension cracking and joint sliding (Fig. 27 a-e). This modeling approach is specifically categorized under the "simplified micro-modeling approach." In this case, the mortar joint is treated as having no thickness, and the bricks are expanded into the mortar thickness. As a result, the bricks are interconnected through their own interface surfaces. For these interfaces, the Authors [166] suggested a composite yield surface. This composite yield surface is used to replicate the tensile failure of mortar joints (8), the shear response of joints (9), and the crushing of units under monotonic loading with a compression cap (10) (Fig. 28). The three surfaces are subsequently defined by:

$$f_{tens\_cut-off}(\sigma_n, k_1) = \sigma_n - f_t \exp\left(-\frac{f_t k_1}{G_f}\right) \tag{8}$$

$$f_{shear}(\tau, \sigma_n, k_2) = |\tau| + \sigma_n \tan\phi_0 \exp\left(-\frac{\tan\phi_0\, k_2}{G_\phi}\right) - c\ \exp\left(-\frac{c\, k_2}{G_c}\right) \tag{9}$$

$$f_{cap}(\tau, \sigma_n, k_3) = \left(\frac{\sigma_n}{f_c \exp\left(-\frac{f_c k_3}{G'_c}\right)}\right)^2 + \left(\frac{\tau}{\tau_{max}}\right)^2 - 1 \tag{10}$$

where:

- σ_n denotes the normal stress, which is considered positive in tension and negative in compression.
- τ represents the shear stress acting tangentially to the interface.
- k_1, k_2, and k_3 are internal history variables used to model the progressive evolution of damage in tension, shear, and compression, respectively.

Material strength parameters are defined as follows:

- f_t is the initial tensile strength of the masonry interface.
- f_c is the initial compressive strength.
- c denotes the initial cohesion, while ϕ_0 is the initial friction angle of the material.

In addition, τ_{max} represents the maximum allowable shear stress in the compression cap region. Fracture energy terms define the rate of softening:

- G_f is the fracture energy in tension.
- G_c is the fracture energy in shear.
- G'_c is the fracture energy in compression
- G_ϕ is the fracture energy associated with friction angle degradation.

Haach et al. [167] employed an identical micro-modeling approach to conduct a parametric analysis on the lateral cyclic behavior of masonry walls. This involved introducing potential cracks within the units to prevent an overestimation of both the collapse load and stiffness. As a result, potential cracks located at the midpoint of the units were added using

discrete cracking model interface elements. Further developments of the micro-modelling approach are given in Abdulla et al. [168] and Guo et al. [169] with differences on constitutive behavior assigned to bricks and mortar joint interfaces as well as introducing 3D models of masonry elements based on the Abaqus software. Alternatively, the "continuous micro-modeling" approach follows inside the category of micro models but with interfaces entirely disregarded, and stress-strain relationships are exclusively assigned to mortar joints and bricks [170], that are in this case full defined in their dimensions.

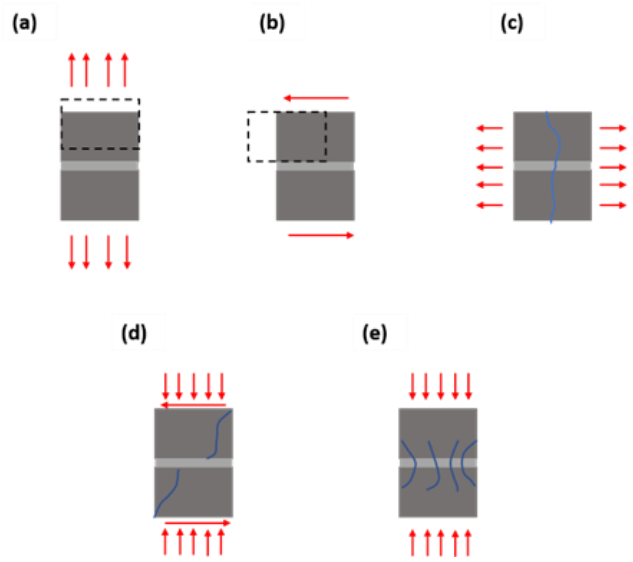

Figure 27: Failure mechanisms considered in micro-modelling: joint tension cracking **(a)**, joint slip **(b)**, unit tension cracking **(c)**, unit diagonal cracking **(d)** and masonry crushing **(e)**. Adapted from Lourenço and Rots [166].

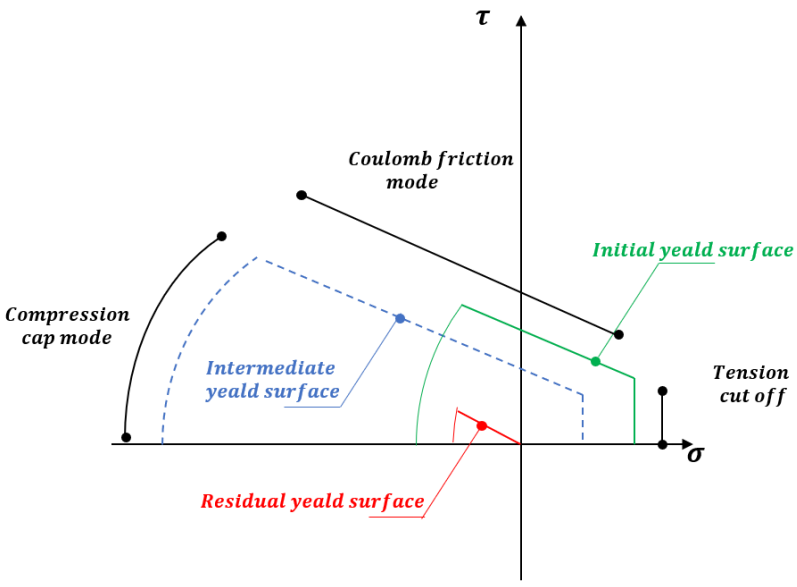

Figure 28: Composite yield surface proposed by Lourenço and Rots [166].

In the context of modeling complex structural materials such as concrete and masonry, the Willam-Warnke failure [171] criterion has served as a foundational basis for the elasto-

plastic material models developed by Majewski [172-173]. The Author [172-173] extended this approach within his custom-developed MAFEM software, adapting it into a “double-cap” plasticity model for concrete, masonry and subsoil settlements. In this case, this model uses a boundary surface constructed from rectilinear and parabolic segments, which connect key stress states such as uniaxial tension, uniaxial compression, and biaxial compression (Fig. 29). The cap on the compressive side allows the model to reflect volumetric hardening and softening under high confining pressures. Based on Kubica [174], once defined parameters α, β and $Y(k)$ as per equations (11-13):

$$\alpha = \frac{f_{c,i} - f_{t,i}}{f_{c,i} + f_{t,i}} \frac{1}{\sqrt{3}} \tag{11}$$

$$\beta = \frac{f_{c,i}\, f_{t,i}}{f_{c,i} + f_{t,i}} \frac{2}{\sqrt{3}} \tag{12}$$

$$Y(k) = C_4 + (1 - C_4)(C_2 k + C_3) \exp(1 - C_3 - C_2 k) \tag{13}$$

where:

- $f_{c,i}$ denotes the compressive strength in uni-axial load conditions.
- $f_{t,i}$ represents the tensile strength in uni-axial load conditions.
- $Y(k)$ is a hardening/softening function.
- κ is a hardening/softening internal variable.
- C_1, C_2, C_3 and C_4 are material constants governing the shape and evolution of $Y(\kappa)$.

The equation F1 (14), F2 (15) and F3 (16) describe the relative domain for the yield surface of this model.

$$F_1(\sigma_i, \sigma_m, k) = \bar{\sigma} + (3\alpha\sigma_m - \beta)Y(k) \tag{14}$$

$$F_2(\sigma_i, k) = \bar{\sigma}^2 + {\sigma_m}^2 + \left(\frac{\beta\, Y(k)}{[1 + 9\,\alpha^2 (Y(k))^2]^{1/2}}\right)^2 \tag{15}$$

$$F_3(\sigma_i, k) = \frac{(\sigma_m - c)^2}{a^2} + \frac{\bar{\sigma}^2}{b^2} - 1 \tag{16}$$

where:

- F_1, F_2 and F_3 are respectively a conical surface, a spherical cap and an ellipsoidal cap.
- σ_i is representing the principal stresses in the direction i= 1, 2, 3
- σ_m is the mean stress (first invariant I_1): $\sigma_m = 1/3(\sigma_1 + \sigma_2 + \sigma_3)$
- $\bar{\sigma}$ is the square root of the second invariant I_2:
  $\bar{\sigma} = [(\sigma_x - \sigma_m)^2 + (\sigma_y - \sigma_m)^2 + (\sigma_z - \sigma_m)^2 + \tau_{xy}^2 + \tau_{yz}^2 + \tau_{zx}^2]^{1/2}$
- a is the major semi-axis of the elliptical compressive cap.
- b is the minor semi-axis of the elliptical compressive cap
- c defines the center coordinates of the cap in compression.

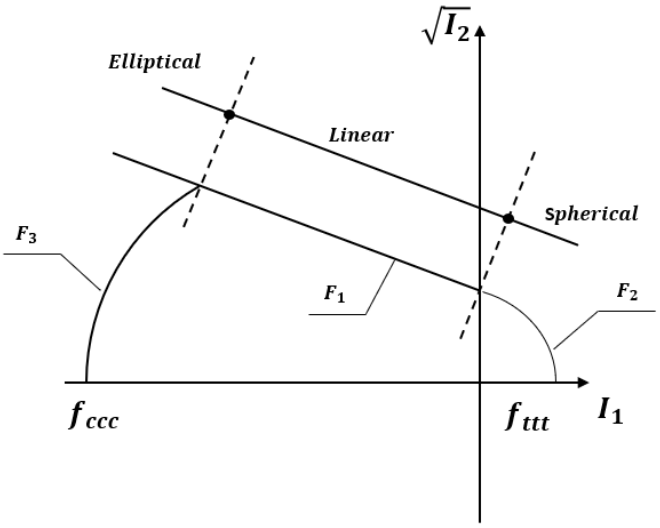

Figure 29: Yield surface adopted by Majewski in the invariant stress plane (I_1–I_2) with f_{ccc} triaxial compression and f_{ttt} triaxial tension, along with info of its three-dimensional segment envelope, as adapted by Kubica [174].

Numerical simulations, corroborated by Kubica [174] with comprehensive laboratory experiments, demonstrated that this criterion allows for highly accurate prediction of crack initiation, deformation patterns, and failure zones in masonry elements. Its predictive capability makes it a valuable benchmark for calibrating finite element models aimed at capturing the vertical shear behavior of masonry panels under complex loading conditions (Fig. 30a-b).

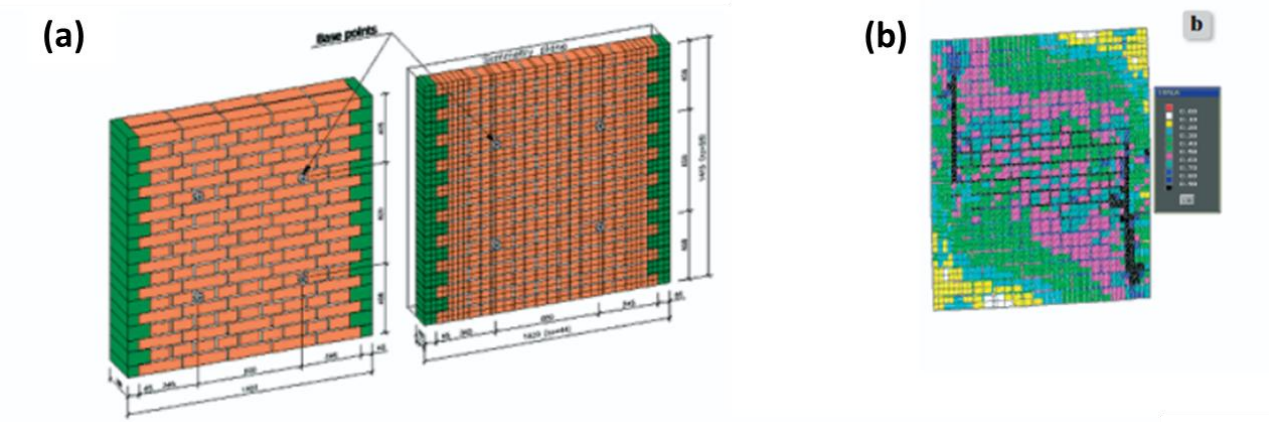

Figure 30: Numerical model for vertical shearing load tests **(a)** and principal stresses in the heterogeneous numerical model **(b)**. Adapted from Kubica et al. [174].

Definitely, micro models prove effective in modeling individual structural components when the aim is to analyze their inter-relationships across varying scales. This is also the case of masonry retrofitting strategies composed by reinforcements embedded in mortar matrixes. Ungureanu et al. [175] developed a detailed micro-model of the wallettes retrofitted by textile reinforced mortars (TRM). The bricks and mortars were simulated using tetrahedron finite elements, while the matrix layers of the TRM were shell elements with the reinforcement modelled as truss elements.

2.4.2 Continuous models: macro, multi-scale and homogenization models

Continuum models represent masonry as a unified element with a single stress-strain relationship. One of their primary benefits is the ability to employ a coarser mesh that does not need to conform to the details of the masonry texture, unlike micro-models. Specifically, in macro-mechanical (or macro) models, this stress-strain relationship, aiming to emulate the material behavior of masonry, is directly determined by testing masonry samples at meso-scale.

In this context, a frequently employed group of constitutive models is referred to as smeared crack models. These models describe the deterioration caused by external loads with the formation of localized cracks, though they do not delve into fracture mechanics and still operate on a continuity assumption. Particularly, the crack formation in quasi-brittle materials modelled according to this approach occurs when the material reaches its peak tensile strength. In this case, the material loses its isotropic properties and become an anisotropic material. Generally, the deformation due to strain is partitioned into two components: an elastic one, representing the deformation of the uncracked material, and a nonlinear one, accounting for the additional deformation resulting from cracking [176]. The DIANA finite element software offers various models within this framework, including the Total Strain Crack Model (TSC) as one illustrative example (Fig. 31a-b). This model can be categorized as either "fixed" or "rotating." In the "fixed" model, once a crack is formed, its direction remains constant. In contrast, in the "rotating" model, the orientation of the crack, and consequently the directions of the principal stresses, vary during the analysis for each load increment. Within this model, the stress-strain response under uniaxial loading is characterized by a linear segment leading to the maximum compressive strength, followed by a parabolic segment that illustrates the degradation in strength under compression. Conversely, for tensile stress, there is an initial linear segment leading up to the peak stress, followed by a softening branch described by an exponential decay based on fracture energy. “Engineering Masonry model” is also part of the same software where several improvements are added for modelling the lateral cyclic response of masonry walls [177]. First, the anisotropy of the masonry resulting from different stiffness in the direction of the bed- and head-joints is considered. Subsequently, a more realistic description of the unloading phases in compression is achieved by introducing a λ factor that enhances dissipation through a combination of secant and elastic stiffness unloading branches, while the unloading in tension is kept secant to zero. Sousamli et al. [178] recently proposed an improvement of the latter model particularly for the post-peak and the unloading/reloading responses in tension. These values are calculated based on the crack orientation when cracking initiates. Basili et al. [179-180] investigated the suitability of TSC model in reproducing the response of unreinforced and reinforced masonry wallettes subjected to diagonal compressive loads. Masonry and reinforcement with lime-based mortar and basalt mesh were modelled as an isotropic continuum, with the same mesh and plane-stress elements but considering two different layers for plaster and grid. No interface properties were defined between the reinforcement and the masonry substrates, assuming the hypothesis of a perfect bond between them. However, to reproduce the effect of a limited bond, a reduced value for the textile tensile strength was assumed with respect to the

effective fiber tensile strength. The results showed the capability of the model to predict the panel response up to failure, also in a non-symmetrical configuration of reinforcement. Recently, Fages et al. [181] proposed a calibration method for masonry adobe of the TSC models based on compressive and diagonal compressive tests.

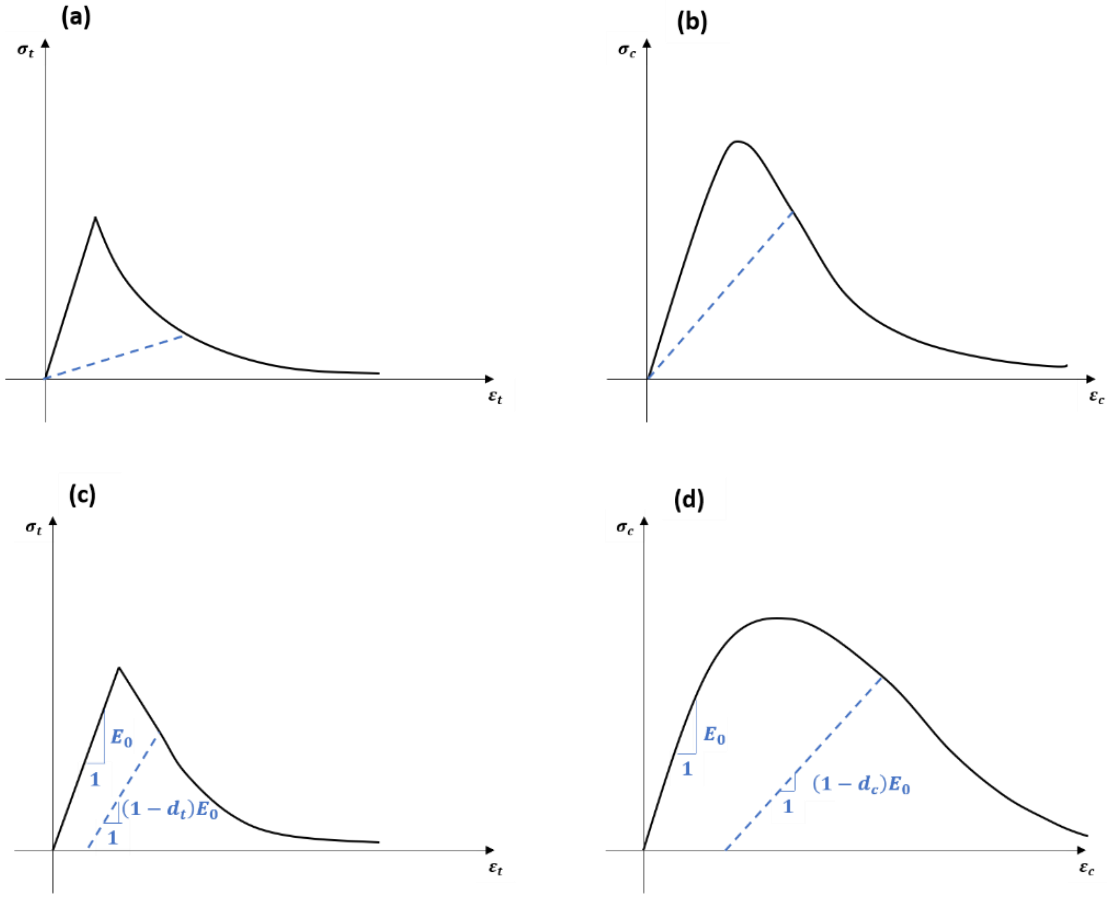

Figure 31: Uniaxial stress-stain relationships of Total Strain Crack Model of DIANA Fea: **(a)** tension and **(b)** compression with secant loading/reloading. Uniaxial stress stain relationships of Concrete Damage Plasticity model of Abaqus: **(c)** tension and **(d)** compression with loading/reloading defined by damage parameters d_t and d_c.

Another set of models frequently employed in the macro-mechanical modeling of masonry consists of the damage models [176]. These models rely on defining damage parameters to consider distinctions between cracked and undamaged cross-section elements, describing the degradation processes as loading-reloading cycles increase. An instance in this category is the Concrete Damage Plasticity model (CDP), which was first formulated by Lubliner et al. [182] with a focus on a single scalar damage. Subsequently, Lee and Fenves [183] further improved and modified it by incorporating two distinct scalar damage parameters for tension and compression. Gatta et al. [184] also introduced a plastic damage model that considers two distinct damage parameters. Additionally, they incorporated a non-local constitutive formulation to address analytical issues associated with mesh dependency. Rainone et al. [185] conducted a parametric analysis on the lateral response of masonry walls

utilizing the CDP implemented in the Abaqus software. The latter with axial-stress strain illustrated in the Fig. 31c-d.

On the contrary, stress-strain for a continuum model can be obtained by means of a theoretical homogenization approach. The basic idea of the homogenization is deducing the property for an equivalent homogeneous, isotropic, or anisotropic medium representing the masonry by considering a representative volume element (REV) that contains in itself all the heterogeneities of the material. One of the first application of this mathematical concept to masonry was developed by Anthoine [186]. The Author [186] deduced the in-plane characteristic of masonry in the linear elastic range, under the assumption of Kirchhoff-Love plate theory. Pande et al. [187], in the same linear elastic case, formulated the so-called "two-step homogenization" in which the procedure is divided into two steps in order to take into account firstly the presence of the discontinuities of bed joints and then that of the bed joints. More recently, homogenization approaches for the determination of masonry failure surfaces by means of limit analysis have been proposed in Milani et al. [188-189]. In all the cases, the process of multi-scale modeling entails a minimum of two sequential steps, beginning with the creation of a homogenized model and leading to its practical implementation for static or dynamic analyses in real structural cases.

Addessi et al. [190] introduced a multi-scale methodology that starts from a 3D micro-scale representation, simplified as an arrangement of elastic bricks and nonlinear zero-thickness interfaces. This micro-scale is then transitioned to a macro-scale model, assumed as per Mindlin-Reissner theory for flat shells, through a homogenization process founded on Transformation Field Analysis (TFA). Bertolesi et al. [191], proposed a homogenization procedure, based on a FE discretization of the reference element, that can be used to calibrate, i.e. to introduce to the structural-scale model, non-linear flexural/shear/axial springs, representing the interfaces, placed between quadrilateral shell elements (Fig. 32). Anyway, this model is affected by localization after the post-peak. Mesh sensitivity issues appear principally in brittle materials when trying to describe their softening behavior. Several solutions of these problems have been obtained among which the use of fracture energy and the characteristic length of the mesh are the most common [192].

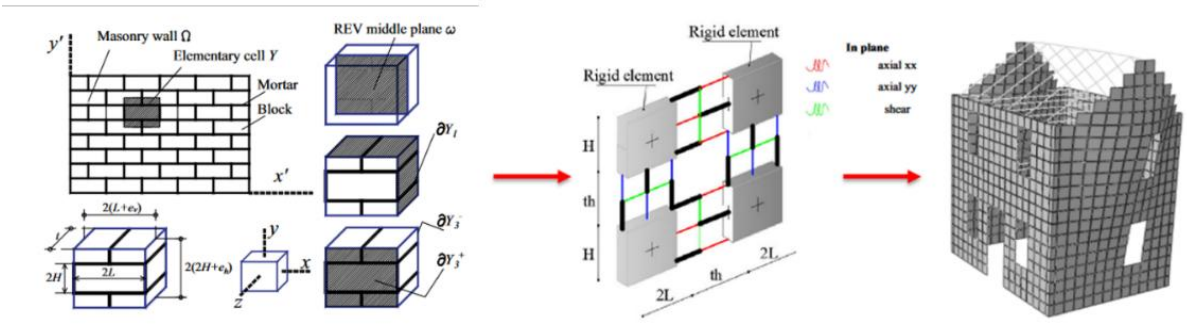

Figure 32: Multi-scale Fem model based on homogenization approach adapted from Bertolesi et al. [191].

2.4.3 Macro elements (panel-scale) models

Macro-element models, known also as panel-scale or structural component models, idealize the structure into panel structural components with a phenomenological or

mechanical based nonlinear response. This approach finds its primary application in evaluating the impact of seismic forces on masonry buildings and large-scale structural elements. An illustrative implementation can be found in the software TREMURI [193], which relies on the subdivision of the structure into fundamental elements (piers, spandrel, intersection areas) to derive an equivalent frame model. They have manageable computational effort but cannot take in account for the crack pattern details and some of them assume that the out-of-plane behavior of masonry is prevented. It has to be noted that effectively also macro-elements are continuum elements, but the differences are in the determination of the stress-strain behavior of masonry, that in this case, aim at the reproduction of the global response of the masonry. First Raka et al. [194] and then Peruch et al. [195] proposed for the in-plane behavior of masonry structures an extension of an existing distributed plasticity frame model, originally developed for the analysis of reinforced concrete elements. The model consists of essentially a Timoshenko beam based on the assumption that plane sections remain plane. In particular, the axial-bending behaviors are obtained from a fiber-section model of the wall cross-section, while the shear response is obtained through a phenomenological shear force-shear deformation law. In this way, bending and shear forces are in equilibrium during all the analysis and the wall lateral response is the sum of the flexural and shear flexibilities, while strength is governed by the weaker of the two existing mechanisms. In this context, the modelling of the masonry structure is carried out idealizing the facades into beam elements (Fig. 33). Effectively, lateral panel stiffness calibration should be performed focusing the attention to the shear stiffness not only for panel-scale elements but also for macro-mechanical modelling approaches, as shown by D'Altri et al. [196]. In a recent study, Camata et al. [197] conducted a comparison between the equivalent frame approach [195] and established micro-modelling technique on reproducing large scale tests on masonry buildings. The results highlighted the effectiveness of the frame model with variations in terms of base shear between 1% and 12%. However, it exhibited limitations in accurately predicting mixed failure modes. Also, Cattari et al. [198] observed that in modelling regular masonry facades, equivalent frame models yield nearly similar results, irrespective of the criteria used for determining the height of the piers, of finite element models. However, in addition to addressing frame regularity, deficiencies have been identified in the capacity of these models to accurately capture the behavior of spandrels. This inadequacy becomes relevant in the need for distinct strength criteria from the ones of the piers and in representing structural configurations with complex artistic geometry that can couple out-of-plane to in-plane movements [199]. Indeed, these topics represent, research gaps to be still addressed [200].

Recently, Vanin et al. [201] introduced a three-dimensional macro-element formulation within the OpenSees software for the assessment of unreinforced masonry (URM) buildings, taking into consideration the out-of-plane behavior of masonry panels. In this context, the macro-element was demonstrated to accurately replicate rigid block limit analyses of one-way bending out-of-plane mechanisms. Caliò et al. [202] developed a noteworthy macro-element that comprises an articulated quadrilateral connected by diagonal springs to describe masonry shear behavior. Subsequently, the element was improved by adding discrete arrangements of vertical, horizontal and sliding springs to connect with other components and simulate compressive and in-plane/out of plane sliding

behavior of masonry panels (Fig. 34a) [203]. The same approach can be used for studying the influence of the non-structural load-bearing partitioning walls in reinforced concrete structures (Fig. 34b) [204-205]. As evident, various software programs employ diverse modeling approaches for analyzing masonry structures, occasionally revealing significant discrepancies among results for the same structure due to differing theoretical assumptions at the base of each modelling [206]. Consequently, there recently arises a need to study benchmark structures to elucidate disparities stemming from various modeling and parameter assumptions [207].

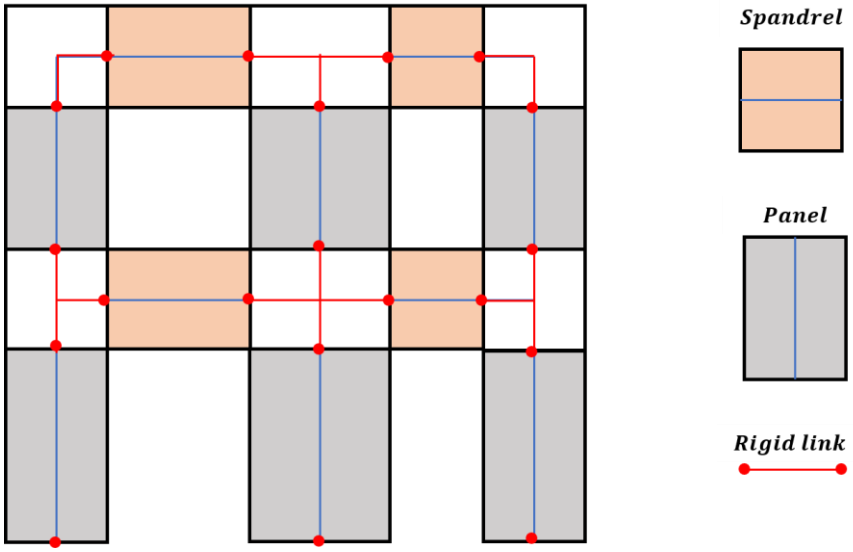

Figure 33: Equivalent frame method discretization for a masonry façade. Adapted from Raka et al. [194].

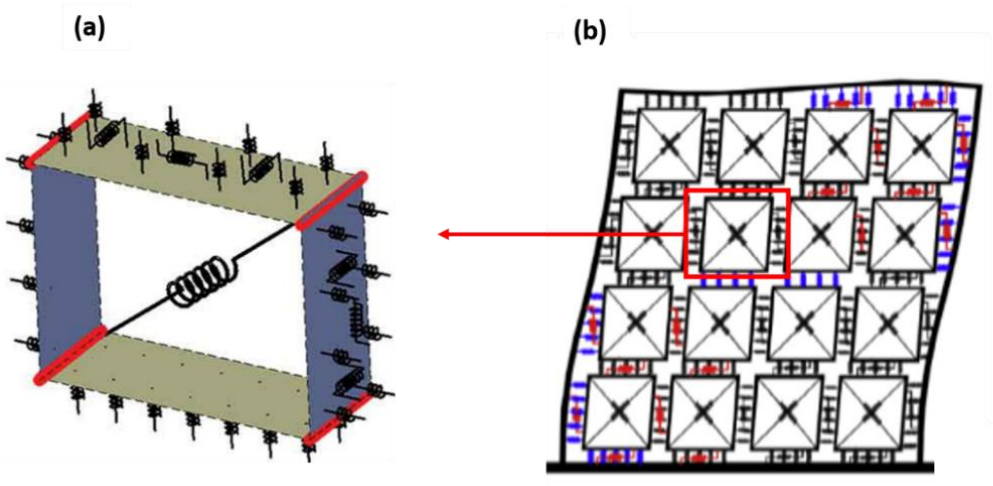

Figure 34: Three-dimensional macro-element with axial and shear springs elaborated by Pantò et al. [203] for in/out of plane loads **(a)**. Mesh discretization for infill masonry wall subjected to both in and out of plane loads **(b)** [204-205].

2.5 Summary and Critical Remarks

The literature review conducted in this chapter indicates several well-established research directions and also defines still open issues that are the subject of research. The

mechanical and physical characteristics of masonry components (bricks and mortars), including the influence of microstructure and porosity, have been widely studied and discussed in recent decades. However, especially in the case of masonry structures constructed in past historical periods, due to the large variability in the composition and manufacturing techniques of these materials, the information is still incomplete.

However, it can be assumed that the overall response of in-plane masonry walls and the related failure modes under lateral loading are already well understood experimentally and described, with several proven numerical strategies proposed in the literature. However, the response of masonry subjected to in-plane loads, especially in terms of vertical shear (due to non-uniform settlements or displacements induced by various factors) and/or mainly horizontal shear due to seismic or para-seismic effects (mining tremors, vibrations induced by urban transportation systems, etc.) remains still less documented. The lack of extensive data (experimental and analytical solutions) regarding the modification of mortar composition in the case of sustainable alternatives to mortars with an increased air lime content is particularly noticeable.

Regarding the application of numerical modeling, although there are several approaches to numerical modeling at a macro scale, the calibration of such models for new, environmentally friendly materials still requires further validation.

An attempt to fill some of the above gaps and deficiencies through targeted experimental tests and numerical studies has been undertaken within the framework of this thesis and is presented in its subsequent chapters.

CHAPTER 3 - EXPERIMENTAL CAMPAIGN

The purpose of this chapter is to provide an overview of the materials selected for the experimental analysis and the results of experimental tests carried on them. To begin with, the chapter presents an analysis of the compressive properties of bricks. Subsequently, it delves into the investigation of masonry bedding mortars. In the latter case, the chapter also explores more detailed mechanical properties for the two selected bedding mortars, including flexural strength, compressive strength, splitting tensile strength and fracture energy.

At the level of small masonry assemblages, the chapter includes investigations into mechanical properties such as shear, compressive strength and diagonal compressive strength for masonry wallettes. The same approach is adopted for full-scale masonry walls subjected to complex stress states resulting from lateral cyclic displacements and vertical settlements. In all the cases, the analysis of the results centers on the observed crack patterns during the experiments with their subsequent interpretation and comparative analysis in the last section 3.4 of the chapter.

3.1 Supplementary materials tests – clay bricks

The clay bricks selected for this research were provided by Wienerberger AG, a building products company, along with a datasheet that included information on geometry and specific limits for physical and mechanical properties. The units produced through a particular process of hand-made mimic bricks in appearance as produced in past centuries. This type of clay solid bricks is recommended for the construction of façade walls of new buildings located in historic city centers. They are also used for renovation and repair of walls of existing historic buildings. All bricks had frog on the upper surface, as it has been shown in Fig. 35.

Figure 35: View of the frogged clay solid bricks used in presented investigations.

However, certain properties, such as flexural strength and elastic modulus, were not included or were only indicated ranges values in the datasheet. In order to have more accurate

information relative to the latter properties, in this part of the thesis, tests on compressive and flexural strength, water absorption and initial rate of absorption (IRA) are conducted.
In Table 5, an overview of tests carried out on bricks is given with the individual test series identified by a code. The first part of the code indicates the type of test:

- WA - for water absorption test,
- IR - for initial rate of water absorption,
- BT - for full size bricks subjected to a three-point bending test,
- CT - for solid bricks subjected to compression test. The second code number recalls the type of material analyzed i.e. CB for clay bricks.

Table 5: Overview of the test types carried out on brick samples.

Material	Testing Series	Sample shape (mm)	Number of samples	Sample size (mm)	Standard
Clay units	WA_CB	Solid brick	6	215 × 102 × 65 mm	EN 772-21 [208]
	IR_CB	Solid brick	6	215 × 102 × 65 mm	EN 772-11 [209]
	BT_CB	Solid brick	12	215 × 102 × 65 mm	-
	CT_CB	Solid brick	6	215 × 102 × 65 mm	EN 772-1 [30]

Water absorption was determined using six full size specimens, following the guidelines outlined in EN 772-21 [208]. After drying of the bricks, they were subsequently immersed in water for a period of 24±0.5 hours (Fig. 36). The initial and post-immersion masses of each specimen were recorded, and the difference was calculated in order to quantify the amount of water absorbed during the immersion period. The final value expressed in percentage corresponds to the average of all six measurements and is 10.27% (13.8%) with coefficient of variation indicated in brackets.

Figure 36: Full size units in submersion for water absorption measurements.

Also, the initial rate of absorption (IRA) was determined by testing six solid bricks, following the procedures described in EN 772-11 [209]. This involved immersing one face of the bricks in water to a standard depth of 5±1 mm for one minute and recording the changes in mass before and after the immersion period. Finally, IRA is calculated as the mass difference, divided by the product of the exposed area of immersion and the time of the test. Average value of the IRA for selected material is 3.09 kg/(m^2 min) (11.7%).

Flexural strength was determined through three-point bending tests conducted on full units, considering similar testing procedures performed on mortars. A load-control test setup was utilized with a loading speed of 0.05 kN/s. Two loading directions were evaluated for applying the load perpendicular to the bed joints: one on the plain side and the other on the frogged side (Fig. 37a-b-c). In total, 12 bricks were tested, with 6 tested on each side. The distance between the support points was considered for the test equal to 180 mm. Naturally, calculating the flexural strength necessitated determining the inertial properties of the central cross-section and locating the neutral axis, which corresponds to the cross-section with a C shape. Average value of the flexural strength with load direction on the plain side ($\sigma_{f\text{-}Plain}$) showed value of 4.44 MPa (29.3%). The analogous value for the frogged side ($\sigma_{f\text{-}Frog}$) is 3.93 MPa (39.2 %) (Table 6). The failure modes in both loading directions exhibited comparable patterns. Typically, cracks emerged within the central cross-section of the brick (Fig. 38a). In certain instances, crack initiation was irregular, commencing in the middle cross-section and progressing asymmetrically from various sides of the bricks (Fig. 38b). Such irregularities might account for the heightened variability observed in the results.

Table 6: Values of the flexural strength with load direction on the plain side ($\sigma_{f\text{-}Plain}$) and frogged side ($\sigma_{f\text{-}Frog}$).

Bricks	**$\sigma_{f\text{-}Plain}$ [MPa] (CoV)**	**$\sigma_{f\text{-}Frog}$ [MPa] (CoV)**
Clay units	4.44 (29.3)	3.93 (39.2)

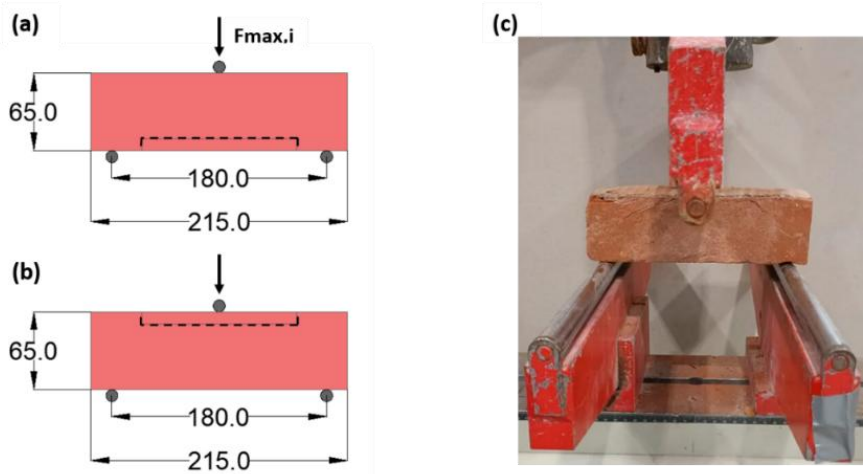

Figure 37: Flexural tests on full unit samples with static scheme and dimension in mm on the plain side **(a)**, on the frogged side **(b)** and example of the brick ready to be tested (on plain side) **(c)**.

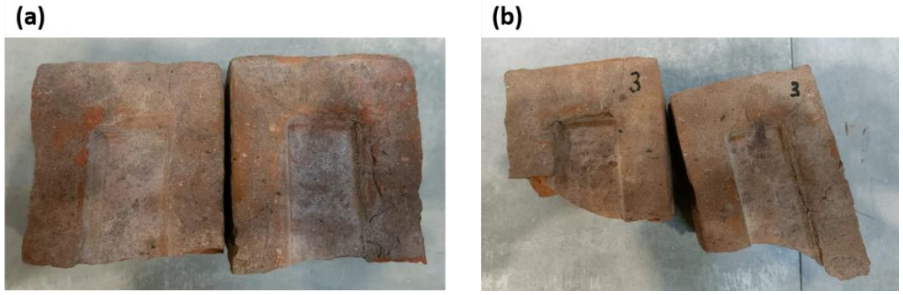

Figure 38: Failed unit with regular surface **(a)** and failed sample with irregular development of cracks from the middle cross-section **(b)**.

The compressive strength of the bricks was assessed by conducting tests on six full units. Specifically, the clay units provided by the company were divided into frogged units and full units. Frogged units were exclusively used for constructing masonry, reserving the use of full units solely for evaluating the compressive strength of the batch at this stage. The same process would apply anyway to frogged units since their net loaded area is superior to 35%, therefore without predicting any cement capping of the frogs, as recommended by the standard EN 772-1 [30]. Tests on compressive strength were carried out in accordance with the relative standard [30] after a process of surface top and bottom rectification. The force of the specimen, perpendicular to bed-joint, was incrementally raised by means of a hydraulic actuator in displacement control at a rate of 5 μm/s. Subsequently, the normalized compressive strength of the bricks was determined using shape factors specified in the appendix of the EN 772-1 [30], taking into account the height-to-width ratio of each specimen. The axial deformation measurements are carried out with the use of a digital image correlation (DIC) system which involved the previous creation of a white and black dotted background. The camera was positioned at distance of 50 cm from the specimens (Fig. 39a-b). Knowing the deformations, a value of the elastic modulus is obtained considering the slope of the stress-strain curves, between 5% and 30% of the maximum peak compressive stress. The average normalized compressive strength was calculated using a mean shape factor of 0.75, as specified in Table A.1 of the relevant standard EN 772-1 [30], given the dimensions of tested bricks. This value corresponds to the product of the measured compressive strength and the shape factor. Additionally, Table 7 provides the corresponding values of the elastic modulus.

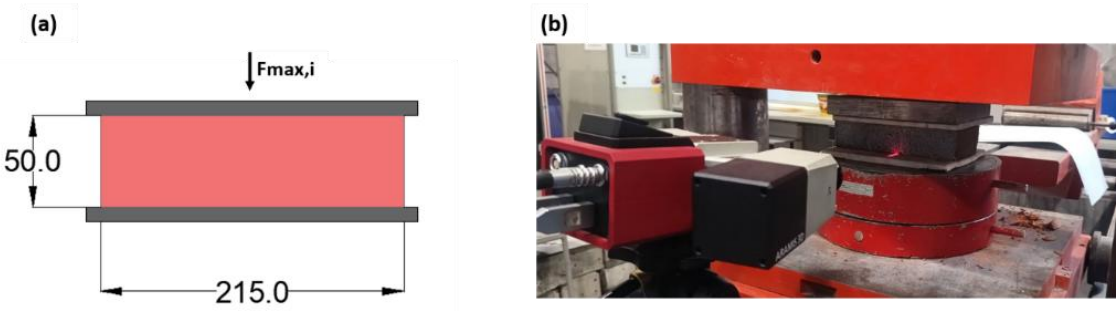

Figure 39: Compressive tests on full units with static scheme and dimension in mm **(a)** and position of the sample in the testing machine DIC system **(b)**.

Table 7: Compressive elastic mechanical properties of masonry units.

Bricks	Compressive strength [MPa] (CoV)	Normalized compressive strength [MPa] (CoV)	Elastic modulus [MPa] (CoV)
Clay units	24.62 (4.3)	18.44 (4.8)	7085.7 (20.2)

Regarding the failure modes, the cracks started to develop in direction parallel to the load application. At peak load, failure showed typical lateral expulsion of the material (Fig. 40a), resulting with the further progressive loads to the complete disgregation of the sample (Fig. 40b).

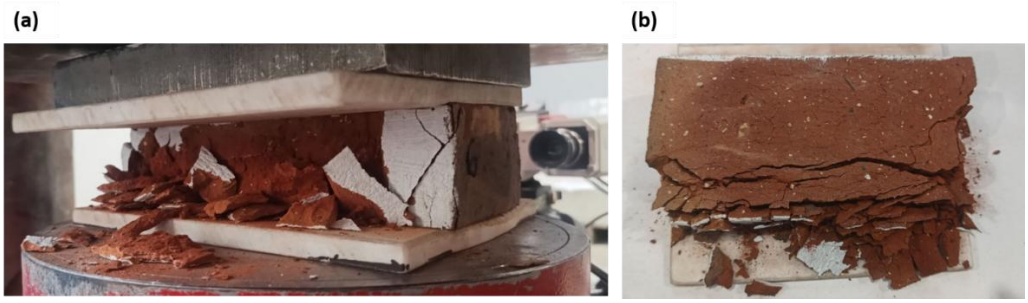

Figure 40: Expulsion of material in correspondence of the peak load **(a)** and top view of failed brick not able to sustain more vertical loads **(b)**.

A comprehensive review of all experimental results related to the calculation methods for flexural and compressive strength as well as for the physical properties of bricks is provided in the Appendix, with reference to Section 8.1.

3.2 Supplementary materials tests – mortars

Two mixed cement-air lime mortars are selected to prepare the bedding masonry samples, incorporating air lime CL90-S [210] and Portland cement CEM II/B-L 32.5 R [211]. Siliceous sand with a grading of 0/2 mm was selected as the aggregate for these mixtures (Fig. 41). The experimental campaign, encompassing specifics of testing setups, procedures, and sample curing, is comprehensively outlined in the original contribution by Zagaroli et al. [212], and is briefly recalled here.

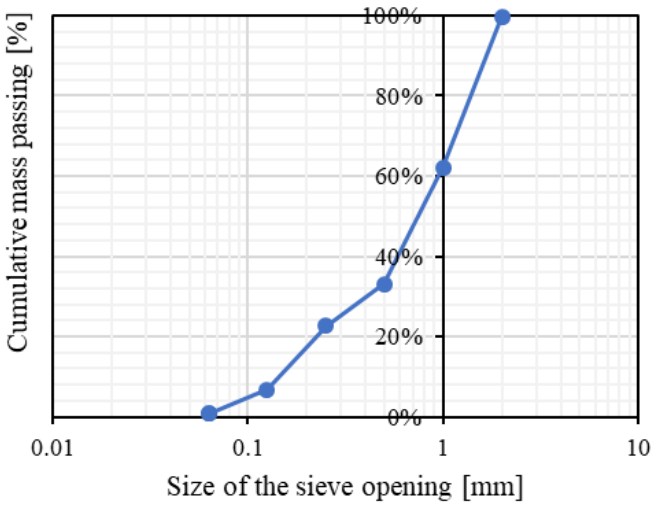

Figure 41: Adopted sand granulometry from Zagaroli et al. [212].

The mortar mixes, denoted as MIX-1 and MIX-2, have volumetric ratios of cement, lime, and sand at 1:1:6 and 1:2:9, considering the popularity of these mix proportions for bedding mortars. Table 8 provides the masses of the constituents based on the volumetric proportions and bulk densities of the constituents. The water-to-binder ratio was adjusted through the flow table test EN1015-3 [213] to ensure the workability of these mortars,

maintaining a slump within the range of 175±10 mm for both mixes. The analysis was conducted in the same sequence as that employed for bricks, starting with the assessment of physical characteristics and then proceeding to investigate mechanical properties.

Table 8: Mortar mix compositions of mixed cement-lime mortars [212].

Mixes Composition (Cement:Air-lime:Sand) by volume	Cement [g]	Air lime [g]	Sand [g]	Water/Binder (by mass)
MIX-1 (1:1:6)	153	78	1350	0.92
MIX-2 (1:2:9)	102	104	1350	1.04

Similarly, to the brick protocol, Table 9 provides an overview of the tests conducted on mortars, with each test series distinguished by a unique code. The first part of the code indicates the type of test:

- BT - for prism specimens subjected to three-point bending tests,
- CT - for half prisms subjected to a compression test,
- CCT - for cylindrical specimens subjected to compression tests,
- SCT - for cylindrical specimens subjected to a Brazilian splitting tests, and
- FT - for beams used to determine fracture energy.

The second code number recalls the volume proportions of the mortars i.e. “116” for MIX-1 and “129” for MIX-2.

Table 9: Testing protocol with dimension specifications. Adapted from Zagaroli et al. [212].

Mixes	Testing Series	Sample shape (mm)	Number of samples	Sample size (mm)
MIX-1 (1:1:6)	BT_116	Prisms	6	40 × 40 × 160 mm
	CT_116	Half prisms	6	40 × 40 × ~80 mm
	CCT_116	Cylinders	7	60 × 120 mm
	SCT_116	Cylinders	5	60 × 120 mm
	FT_116	Beams	5	100 × 100 × 500 mm
MIX-2 (1:2:9)	BT_129	Small beams	6	40 × 40 × 160 mm
	CT_129	Half prisms	6	40 × 40 × ~80 mm
	CCT_129	Cylinders	6	60 × 120 mm
	SCT_129	Cylinders	5	60 × 120 mm
	FT_129	Beams	6	100 × 100 × 500 mm

Mortar curing conditions are the ones specified in European standard EN 1015-11 [53]. All specimens were kept at stable temperature of 20±2˚C and humidity conditions of 65%±5% for 21 days after previous 7 days of curing in polyethylene bags. Only the beams (100 × 100 × 500 mm) for fracture energy evaluation were kept in the climatic chamber for 75 days before testing.

First, three points bending tests on BT_116 and BT_129 were carried out on standard prisms (40 × 40 × 160 mm), in accordance with EN 1015-11 [53]. The static scheme is the same used for brick samples with a distance between the supports, standardized at 100 mm (Fig. 42a-b). A load control test set-up was used with load speed of 0.05 kN/s. The half prisms obtained from the previous tests, CT_116 and CT_129, are subjected to axial compression using the same load rate. Fig. 43a presents the static diagram featuring dimensions of the

compressed halve, while Fig. 43b showcases a representative sample positioned in the machine. Average values of the flexural and compressive strength with relative coefficients of variation are given in Table 10. Regarding the failure modes, no differences between the two mortars were evidenced. During the three-point bending test, cracks formed primarily in the middle cross-section of the prisms (Fig 44a-c), whereas half-prisms failing under compression demonstrated a conical failure pattern, with material expulsion from the lateral surfaces (Fig. 44b-d).

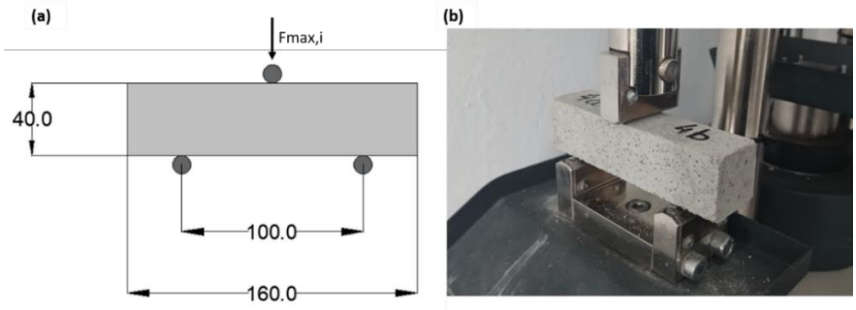

Figure 42: Static scheme of three-point bending test EN 1015-11 [53] with dimensions in mm **(a)** and example of the prims ready to be tested **(b)**. From Zagaroli et al. [212].

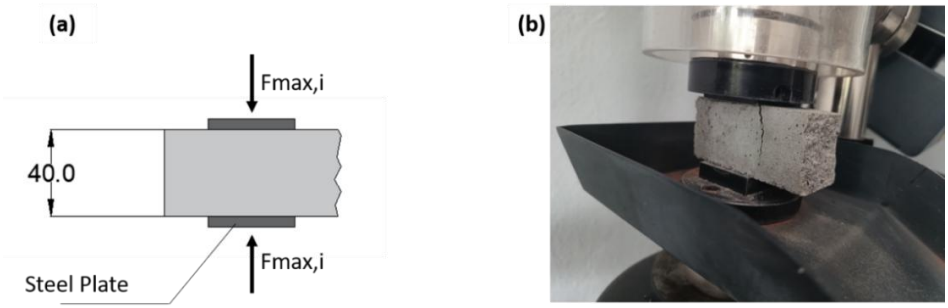

Figure 43: Compression tests conducted on samples of half prism, displaying the static scheme **(a)**, and view of the relative sample positioned within the testing apparatus **(b)**. From Zagaroli et al. [212].

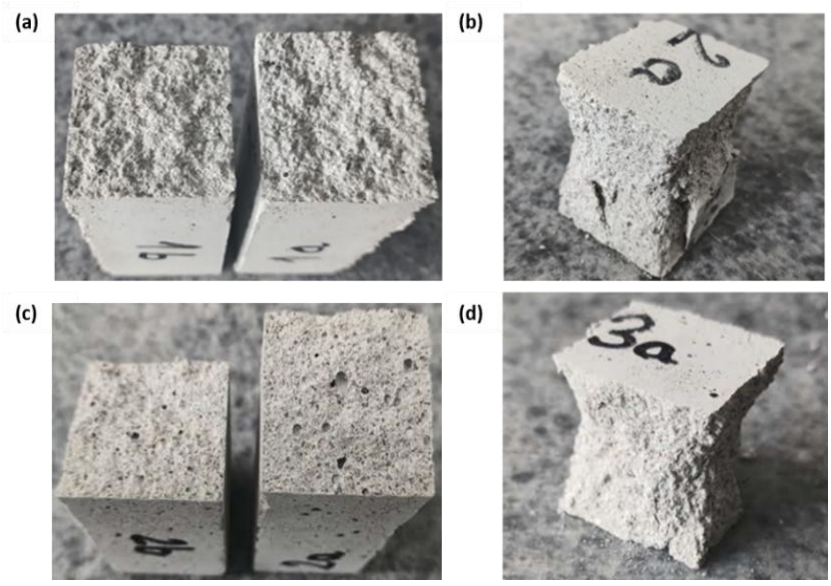

Figure 44: Failed sample from 3-point bending test for MIX-1 **(a)** and for MIX-2 **(c)**. Failed samples from compressive test for MIX-1 **(b)** and MIX-2 **(d)**. From Zagaroli et al. [212].

Table 10: Flexural and compressive strength results for EN 1015-11 [53] test. From Zagaroli et al. [212].

Mixes	Flexural strength [MPa] (CoV%)	Compressive strength [MPa] (CoV%)
MIX-1 (1:1:6)	2.21 (16.2)	7.91 (13.1)
MIX-2 (1:2:9)	1.23 (11.2%)	4.16 (7.6)

Additionally, compressive tests were conducted on cylindrical specimens measuring 60 mm in diameter and 120 mm in height. The test adhered to the guidelines outlined in EN 12390-13 [214] for pre-peak behavior but extended until the sample experienced complete failure. In this case, a test arrangement working in displacement control was employed with a loading rate of 0.05 mm/s. Measurements of vertical and lateral deformation on the samples were carried out using 4 strain gauges directly attached to the lateral surfaces of the samples. This enabled the assessment of Poisson's ratio v as the ratio of horizontal and axial strain within the elastic range.

This range was defined at the same way for the calculation of the Elastic modulus E_c, utilizing a secant value of stress and strain between 30% and 50% of the peak values. Being the test carried out till complete failure of the sample, it was possible to calculate a conventional value of the ductility μ. There is no available standard information regarding the definition of material ductility for mortars. Therefore, a criterion based on equal areas under the stress-strain curves is considered, similar to the approach used for determining the displacement ductility at structural level. This ductility is specifically obtained through an elastic-plastic bilinearization of the stress-strain relationship for each mix. The adopted bilinearization entails fixing a secant stiffness at 0.75 of the peak compressive strength f_{cc}, the peak compressive strength and determining the ultimate deformation by ensuring equal area under the bilinear curve and relative experimental stress-strain, for each stress-strain.

Table 11 showcases the results for all the mixes. Axial and transversal stress-strain relationships for both mixes are given in Fig. 45a-b for MIX-1 and Fig. 46a-b for MIX-2, while relationships of Poisson's ratio with increasing compressive load is shown in Fig. 47a-b for both mixes. In terms of failure modes observed in compressed cylinders, both mixes typically displayed three types: conical failure, shear-tensile cracks extending throughout the entire height of the sample, and a combination of these, rendering the sample unable to support vertical loads any further (Fig. 48a-b).

Table 11: Cylindrical compressive test results for both mixes. From Zagaroli et al. [210].

Mixes	fcc [MPa] (CoV%)	Ec [MPa] (CoV%)	v [-] (CoV%)	μ [-] (CoV%)
MIX-1 (1:1:6)	3.89 (9.6)	7188.49 (5.1)	0.15 (19.2)	3.02 (11.6)
MIX-2 (1:2:9)	1.87 (7.7)	5078.12 (2.3)	0.19 (35.2)	4.05 (2.1)

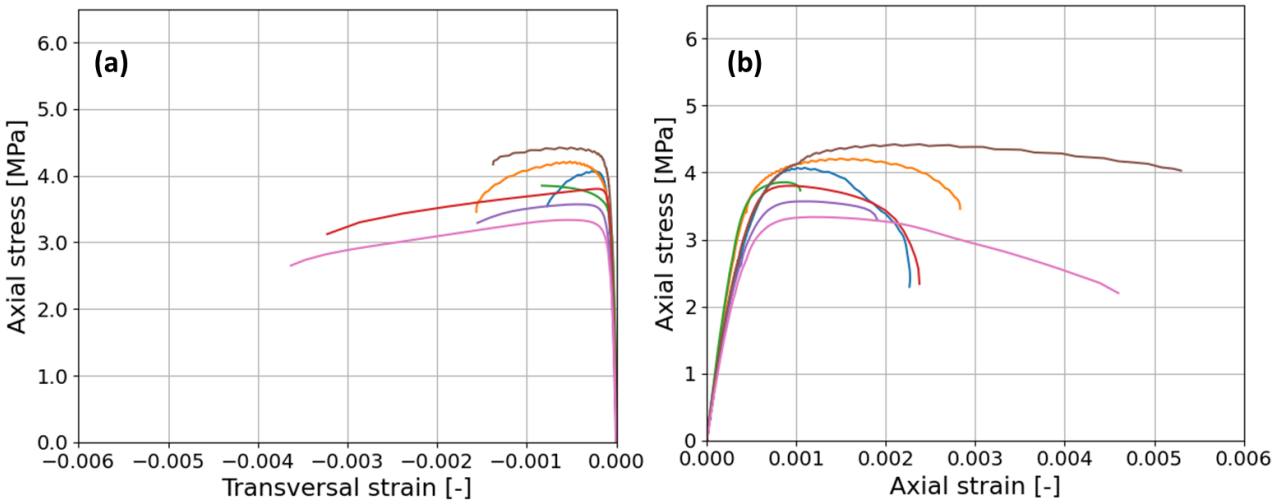

Figure 45: Axial stress – transversal strain **(a)** and axial strain **(b)** for MIX-1. From Zagaroli et al. [212].

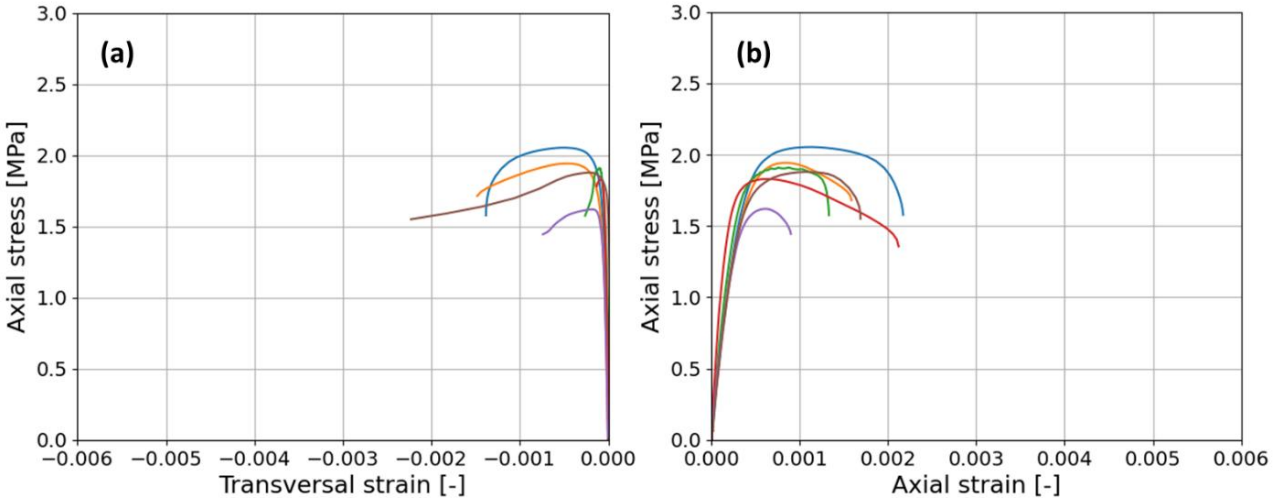

Figure 46: Axial stress – transversal strain **(a)** and axial strain **(b)** for MIX-2. From Zagaroli et al. [212].

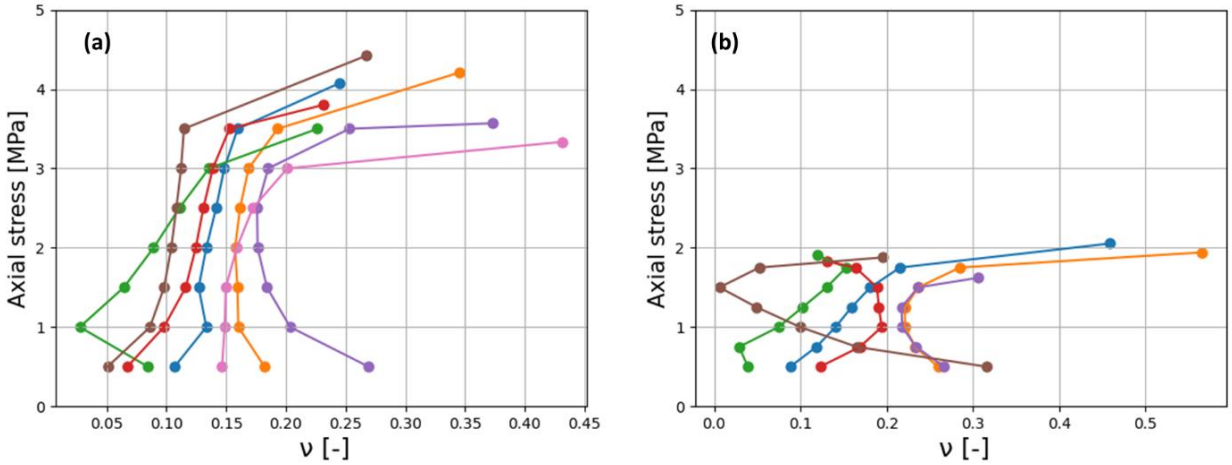

Figure 47: Axial stress – Poisson's ratio for MIX-1 **(a)** and MIX-2 **(b)**.

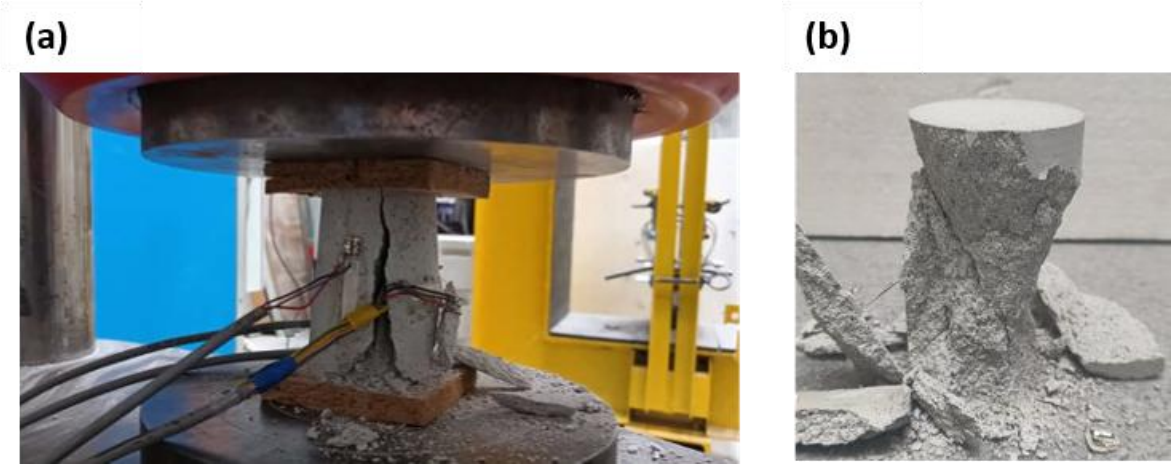

Figure 48: Failure modes evidenced for cylinders in compression: tensile cracks **(a)** and conical expulsion from the lateral surfaces **(b)**. From Zagaroli et al. [212].

Splitting compressive tests on series SCT_116 and SCT_129, consisting in cylinders with the same dimensions of the ones used for compression were carried out in line with ASTM C 496 [215] for concrete. This test was performed adopting a displacement-control test set-up with load rate of 0.01 mm/s pushing the load on the lateral surface of the sample by means of a plate steel bar (Fig. 49a-b). Measurements of the tensile strength and vertical displacement during the tests are plotted for both mortar mixes (Fig. 50a-b). Vales of the average peak splitting tensile strength are given in Table 12. Failure modes did not show any specific feature beyond the separation of the samples in two parts with no distinctions for the two mixes (Fig. 51).

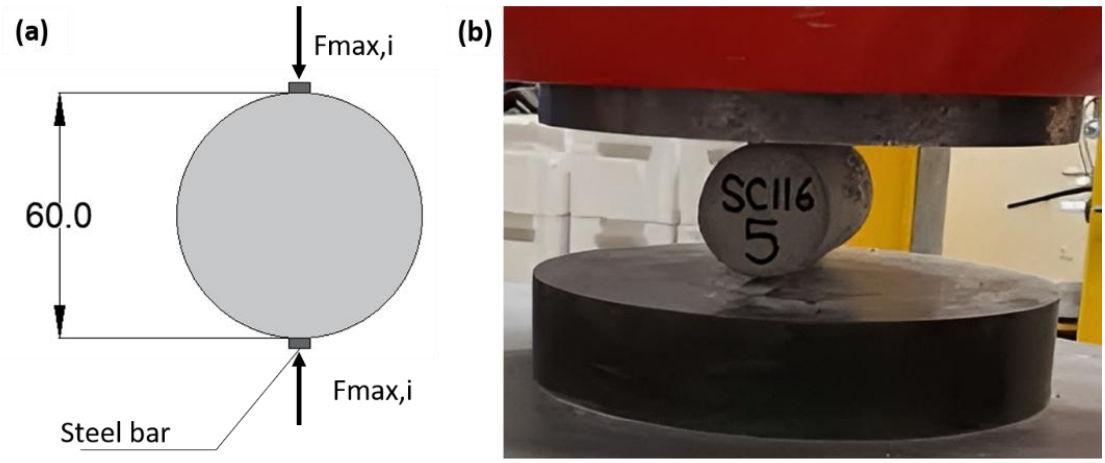

Figure 49: Scheme of the splitting tensile strength test **(a)** and typical sample ready to be tested in the test set up **(b)**. From Zagaroli et al. [212].

Table 12: Average peak tensile splitting strength for both mixes.

Mixes	Splitting tensile strength [MPa] (CoV%)
MIX-1 (1:1:6)	0.46 (19.1)
MIX-2 (1:2:9)	0.23 (11.0)

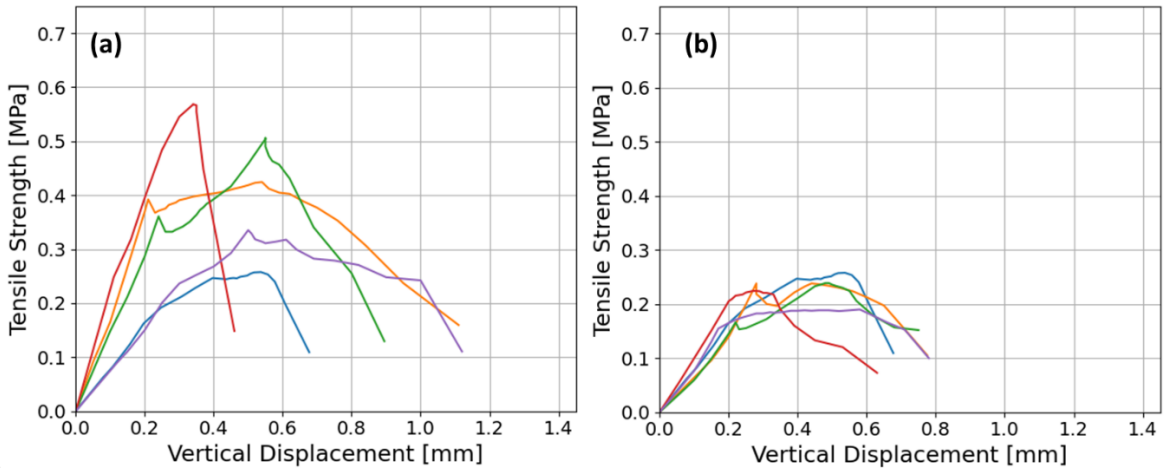

Figure 50: Tensile strength – vertical displacement relationships for MIX-1 **(a)** MIX-2 **(b)**. From Zagaroli et al. [212].

Figure 51: Typical failed sample after splitting load for both mortars. Adapted from Zagaroli et al. [212].

A detailed summary of all experimental results concerning standard flexural, compressive, and splitting tensile strength tests on mortar prisms is presented in the Appendix, as referenced in Section 8.2.

Finally, for the fracture energy tests on series FT_116 and FT_129, the standards RILEM FMC-50 [216] and JCI-S-001 [217] both based on three points bending tests, are applied. The main standard differences are related to the measurements of the deflection for the first and crack mouth opening displacement (CMOD) for the second standard in the formulation for evaluating the fracture energy. Specifically, notched beams measuring 100 × 100 × 500 mm where used. The notch dimensions are 5 mm in thickness and 30 mm in depth, with the depth chosen based on Hillerborg's recommendation [218], which suggests using a notch with dimensions ranging from 0.3 to 0.4 of the beam's depth. The load was applied in displacement control by means of a load actuator with maximum capacity of 5kN at a displacement speed of 0.1mm/min. Static scheme with test set-up details with measurements of both mid-deflection and CMOD were carried out with LVDTs (Fig. 52a-b). Load-deflection and load-CMOD curves are plotted in Fig. 53a-b for MIX-1 and in Fig. 54a-b for MIX-2.

Table 13 shows the values of the fracture energy evaluated according to RILEM FMC-50 [216] $G_{f\text{-}\delta}$ and JCI-S-001 [217] $G_{f\text{-}CMOD}$. The failure modes observed in the beams resembled those seen in standard prisms tested according to EN 1015-11 [53], with no distinction between the

two mixes. Occasionally, fracture development across the mid-span of the beam exhibited irregularities (Fig. 55).

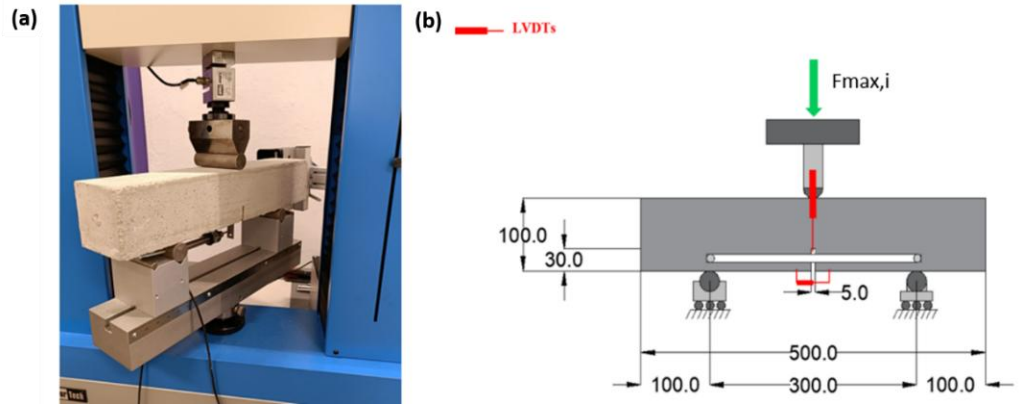

Figure 52: Test set-up for fracture energy evaluation **(a)** and sample specifics with dimensions in mm **(b)**. From Zagaroli et al. [212].

Table 13: Fracture energy results according two different approaches for both mixes. From Zagaroli et al. [212].

Mixes	$G_{f\text{-}\delta}$ [N/m] (CoV%)	$G_{f\text{-}CMOD}$ [N/m] (CoV%)
MIX-1 (1:1:6)	38.67 (28.6)	25.98 (8.0)
MIX-2 (1:2:9)	17.11 (22.8)	11.69 (24.5)

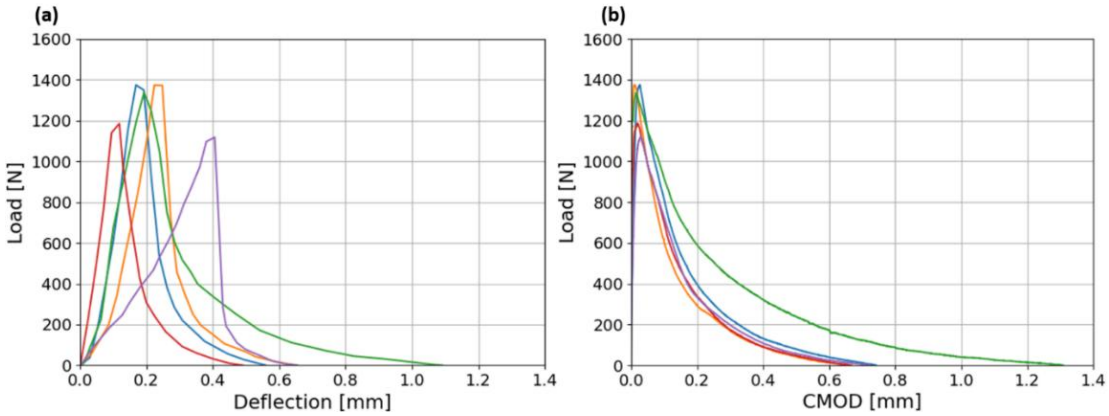

Figure 53: Load-deflection **(a)** and CMOD **(b)** for MIX-1. From Zagaroli et al. [212].

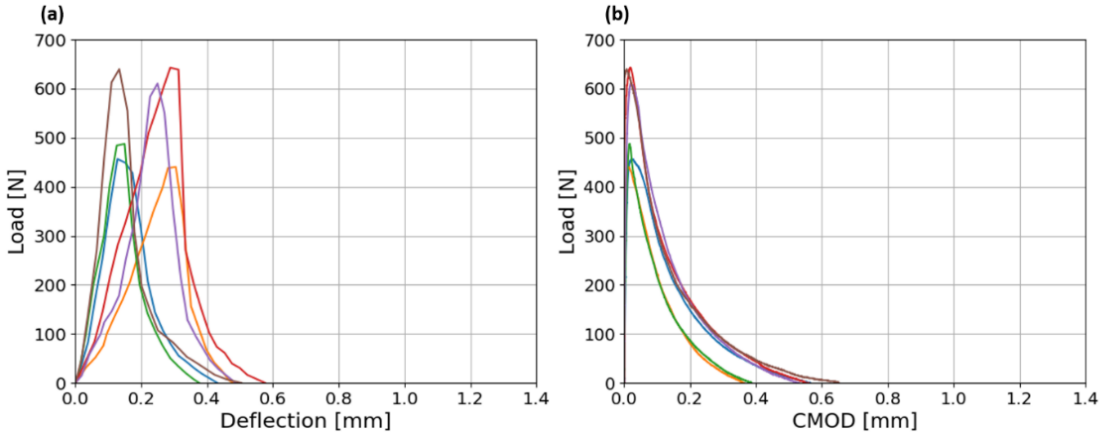

Figure 54: Load-deflection **(a)** and CMOD **(b)** for MIX-2. From Zagaroli et al. [212].

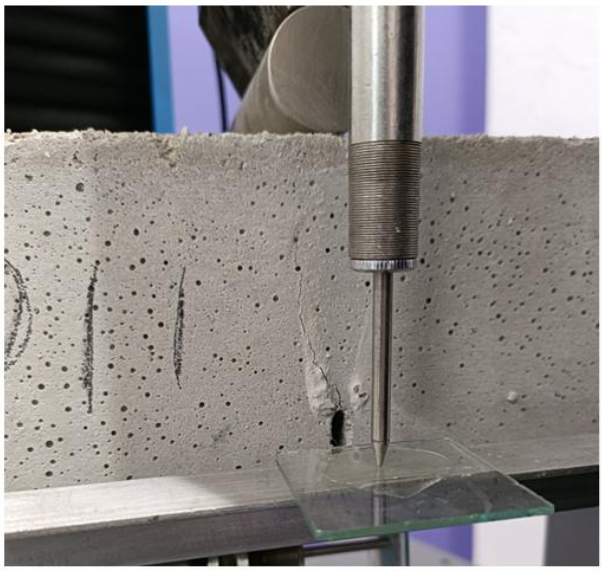

Figure 55: Typical failed sample after splitting load. Adapted from Zagaroli et al. [212].

3.3 Masonry behavior tests

For small masonry specimens, several tests are conducted to assess compressive strength, and diagonal tensile behavior. The tags for the testing series are as follows:

- CT - for compressive tests,
- ST - for shear triplet tests, and
- DCT - for diagonal compression tests.

Test programme and specification of the samples are presented in Table 14. Regarding the curing condition of the masonry, no specific treatment was applied; the samples were simply kept under standard laboratory conditions. These tests were performed using the mortar types MIX-1 and MIX-2 previously characterized, along with clay units that were prewetted before use. Determining the appropriate prewetting time for clay units remains a topic of debate in the scientific community, as this duration should be adjusted based on both the initial rate of absorption of the bricks and the water-retention properties of the mixtures. As per the British standard BS 4551 [219], water retentivity is defined as the capacity of fresh mortar to retain water when in contact with absorbent masonry units. This property is critical because water loss can hinder the proper curing of the mortar. In literature, Sahu et al. [220] have demonstrated that prewetting has a positive impact on the mechanical properties of masonry. However, using saturated bricks for masonry bricklaying can reduce the shear bond strength of triplets. Briceño et al. [221] recently identified an optimal solution by demonstrating that immersion for 30 minutes yielded the best shear bond properties for masonry triplets, regardless of several brick-mortar combinations studied. In this research, the indication from American standard ASTM C67 [222] where it is suggested to pre-wet clay units with initial rate of absorption superior to 1.6 kg/(m^2 min). This value was then considered as a limit and we adopted a time to submersion in order to decrease the initial rate of absorption of that limit. This resulted to be a time of approximately 1 minute.

Table 14: Test samples and series for small masonry assemblage.

Bricks	Mixes	Testing Series	Sample shape (mm)	Number of samples	Sample size (mm)
Clay bricks	MIX-1 (1:1:6)	ST_116	Triplets	9	219 × 215 × 102 mm
		CT_116	Wallettes	6	442 × 527 × 102 mm
		DCT_116	Wallettes	3	896 × 835 × 102 mm
Clay bricks	MIX-2 (1:2:9)	ST_129	Triplets	9	219 × 215 × 102 mm
		CT_129	Wallettes	6	442 × 527 × 102 mm
		DCT_129	Wallettes	3	896 × 835 × 102 mm

3.2.1 Shear triplet tests

Shear triplet tests (Fig. 56a) were conducted in accordance with EN 1052-3 [93] to assess internal friction and cohesion. These tests involved three distinct levels of pre-compression, corresponding to 0.2 MPa, 0.6 MPa, and 1.0 MPa, performed on a total of nine specimens. Throughout the test, a hydraulic pump was employed to apply and maintain the pre-compression at selected constant level. Then, a vertical actuator controlled the vertical shear load on the specimens with a loading rate of 0.15 kN/s. In order to measure displacements, two linear variable displacement transducers (LVDTs) were utilized on the same side of the specimens (Fig. 56b) and average relative displacements was calculated for each sample. Different failure modes were evidenced between triplets made of mortar MIX-1 and MIX-2. Triplets made of mortar containing more air lime showed principally failure modes with cracks in the unit/mortar bond area either on one or divided between two unit faces (described in the Appendix of the relative standard EN 1052-3 [93] as for failure type A.1-A.2). Triplet specimens constructed with mortar containing a lower lime content also exhibited failure by unit crushing and splitting, corresponding to failure mode A.4 as described in the Appendix of EN 1052-3 [93], particularly under high pre-compression levels P.

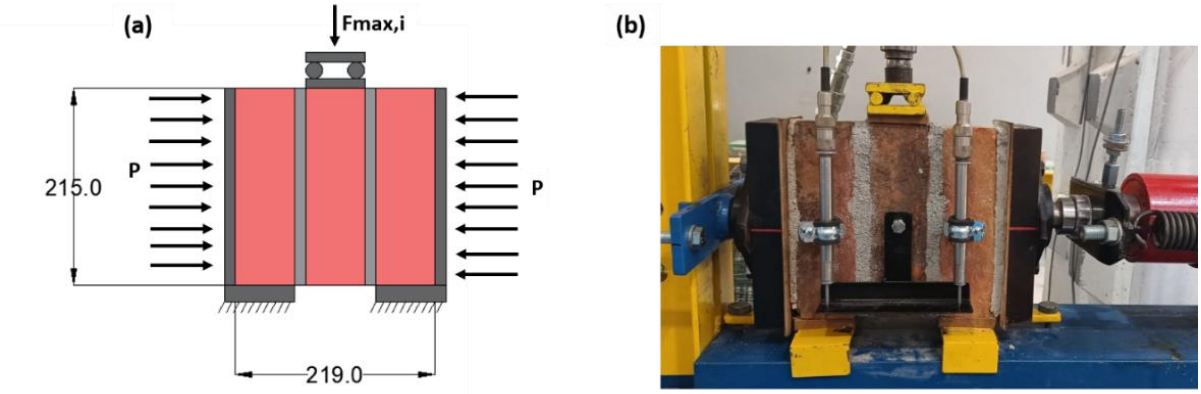

Figure 56: Static scheme for the shear triplet test **(a)** and typical triplet ready to be tested **(b)**.

Relationships between vertical load applied and relative vertical displacements for both mixes are plotted in Fig. 57a-b. The ultimate displacement being considered corresponds to the complete loss of vertical strength, even if the accuracy of load control setups after the post-peak softening behavior is not precise. Elevated levels of pre-compression lead to a higher vertical shear load. Moreover, test results reveal that the average shear strength of

triplets with mortar MIX-2, tested with the lowest level of pre-compression, is lower than that of triplets made of mortar MIX-1 with the equivalent level of pre-compression, as expected.

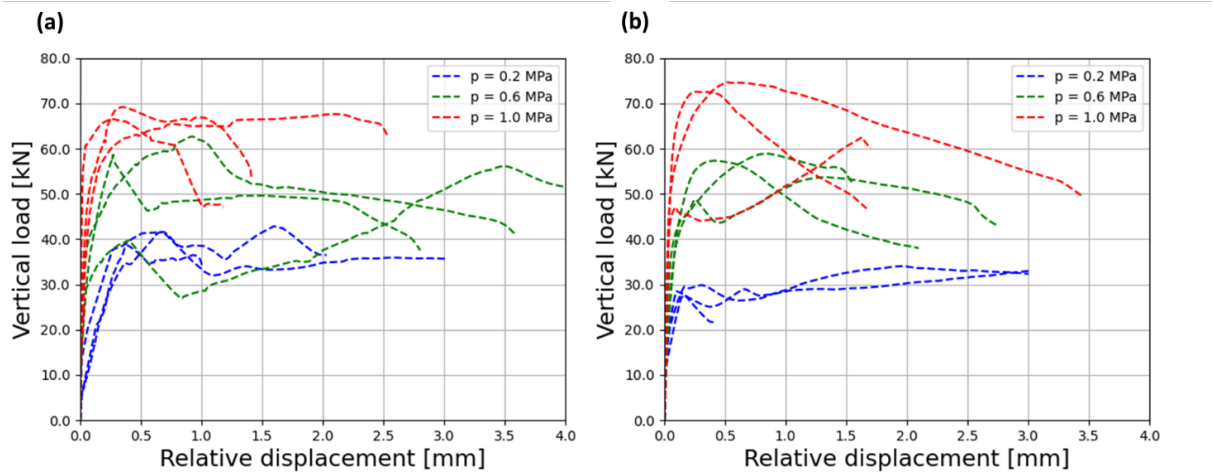

Figure 57: Vertical load F and vertical relative displacement for different level of pre-compression p of triplets made of mortar MIX-1 **(a)** and MIX-2 **(b)**.

This difference anyway is going to reduce by increasing level of vertical loads, showing a contrary trend for the highest level of pre-compression. This could be attributed to the variations in failure modes observed during testing, wherein failed samples made of mortar MIX-1 consistently exhibit shear cracks in the unit/mortar bond area (Fig. 58a), whereas triplets made of mortar MIX-2 display crushing and splitting failure of the units (Fig. 58b). In the last case, the coefficient of variation is also higher compared triplets of MIX-1 mortar. Values of the shear stress for each test together of the average values of the shear stresses associated with the different pre-compressive levels are given in Table 15.

Table 15: Shear stresses – normal pre-compression stress of masonry triplets.

Brick	Mixes	Pre-compression [MPa]	Shear stress [MPa]	Shear stress [MPa] (CoV %)
Clay bricks	MIX-1 (1:1: 6)	0.2	0.98	0.93 (5.2)
			0.88	
			0.95	
		0.6	1.34	1.35 (5.1)
			1.43	
			1.28	
		1.0	1.54	1.55 (2.0)
			1.57	
			1.52	
Clay bricks	MIX-2 (1:2:9)	0.2	0.75	0.72 (10.6)
			0.73	
			0.77	
		0.6	1.22	1.29 (4.7)
			1.31	
			1.34	
		1.0	1.42	1.59 (9.3)
			1.65	
			1.7	

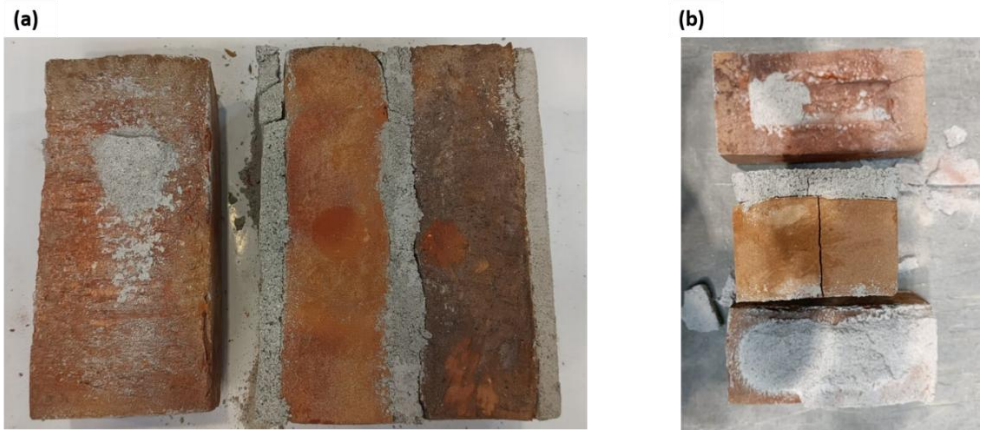

Figure 58: Typical failure mode for triplets made of mortar MIX-1 in correspondence of the highest level of p for mortar MIX-1 with failure at the interface mortar-brick (Type A.1) **(a)** and MIX-2 with shear failure along the brick (Type A.4) **(b)**.

3.2.2 Compressive tests

Compressive strength tests were conducted on six wall samples according to EN 1052-1 [97] standard. To comply with the European standard test protocol, a vertical load was applied at a displacement rate of 0.005 mm/s, controlled by a vertical actuator with maximum capacity of 1000 kN, thereby ensuring that failure occurred within 15 to 30 minutes. During this test, vertical and horizontal deformations were measured using four LVDTs positioned on both sides of the panels. The lengths of the vertical measuring bases were 175 mm, while the length of the horizontal ones were 221 mm. Geometry and measurement positions are given in figure Fig. 59a-b.

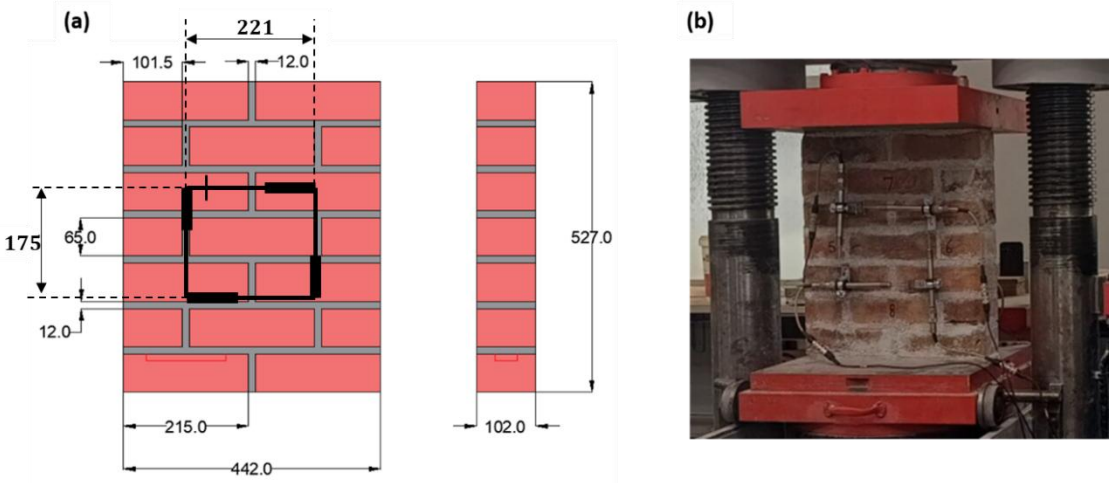

Figure 59: Dimensions of the chosen wallettes for masonry compressive testing align with the specifications outlined in EN 1052-1 [97] **(a)** and typical sample in the machine ready to be tested **(b)**.

Results in terms of axial stress-strain for both mixes are given in Fig. 60a-b. Experimental results revealed a peak compressive strength f_c of 8.40 MPa when testing masonry made of MIX-1 and 6.98 MPa for MIX-2, respectively. Elastic modulus E_c of the

wallettes was also calculated considering the stress and axial deformations corresponding to the range of one third of the peak compressive strength, as suggested by the relative standard. Values of the ductility μ is also calculated, considering the same bilinearization process used for mortar samples, accounting for the post-peak behavior of the samples. As expected, ductility and elastic modulus increases and decreases respectively for masonry made with the mixes containing a superior lime quantity. All the mechanical parameters analyzed are given in Table 16.

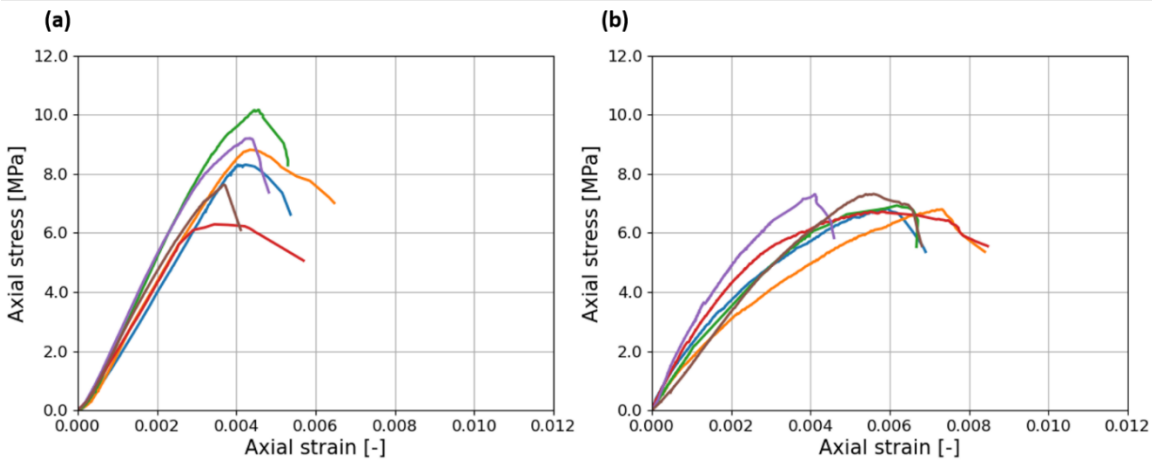

Figure 60: Experimental results in terms of compressive axial stress and strain for masonry made of MIX-1 **(a)** and MIX-2 **(b)**. Different color for each test performed.

Table 16: Mechanical parameters of masonry tested in compression. Adapted from [223].

Bricks	Mixes	fc [MPa] (CoV%)	Ec [MPa] (CoV%)	μ [-] (CoV%)
Clay bricks	MIX-1 (1:1:6)	8.40 (15.9)	2501.0 (11.6)	1.29 (3.6)
	MIX-2 (1:2:9)	6.98 (3.8)	2166.9 (26.6)	1.50 (4.2)

The crack patterns identified in various samples indicate that masonry constructed with mortar MIX-1 (116) and MIX-2 (129) did not exhibit any significant distinctions, with deformation initiating at the edge of the specimen before spreading towards the center of the panels. This crack development involved both bricks and head joints (Fig. 61a-b). A comparison of the experimental response of stack bonded prisms and wallettes made with the same material are given in literature [223].

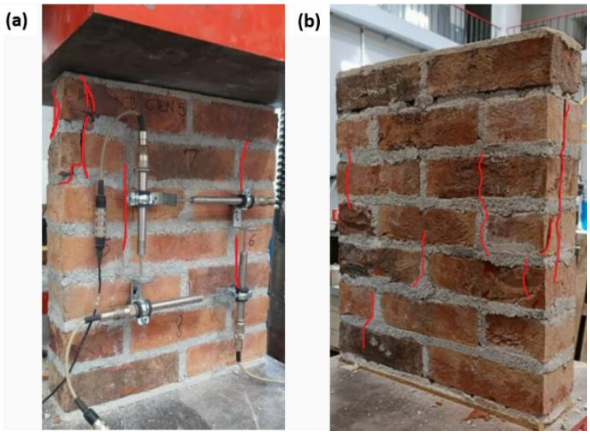

Figure 61: Crack development for masonry made of mortar MIX-1 **(a)** and MIX-2 **(b)**. Cracks evidenced with red lines. Adapted from [223].

The Appendix, specifically Section 8.3, presents a detailed overview of the experimental results related to the compressive behavior of masonry wallettes.

3.2.3 Diagonal compression tests

The diagonal shear capacity of masonry elements was assessed for determining masonry tensile properties in case of cracks agreed with the principal stress axis (diagonal direction) in accordance with RILEM [112] regulations. The analysis included the examination of three specimens for each investigated solution, associated here with two codes: MIX-1_DCT_x and MIX-2_DCT_x, where x ranges from 1 to 3 for each sample. Notably, MIX-1 and MIX-2 denote the two types of mixes previously defined.

Tests were conducted utilizing a load hydraulic jack with a maximum load capacity of 1000 kN. The load control setup operated at load speeds of 0.5 kN/s and 0.1 kN/s for masonry made of mortar MIX-1 and MIX-2, respectively. Load differences were adjusted based on the differences of expected strength of different masonry. The load was applied by means of steel loading shoes placed at the corner of the specimens with a proper design in order to avoid concentration of loads and local failure at the corners. The rigid connection between the wall and the steel shoes by the application of fast-setting cement mortar on the top and bottom of the walls and additional wood plate elements between the steel shoes and the walls. Selected dimensions for the wallettes and test set up details are given in Fig. 62a-b.

Two distinct measuring systems were employed on the two sides of the walls. On one side, displacements along the diagonals were measured using two linear variable displacement transducers (LVDTs) placed at a relative base distance of 900 mm. On the other side, a digital image correlation (DIC) system was employed to obtain a more detailed view of the crack patterns during the tests. In this case, the DIC system was specifically monitoring the relative displacements of the same points of the ones of the LVDTs but on the opposite side of the walls. At the same way of the bricks, the use of DIC required a surface treatment, which involved first creating a white background on which black dotted paint was randomly applied using a trowel. The camera was positioned at distance of 1.5 m from the walls. Both measurement systems are shown in Fig. 63a-b.

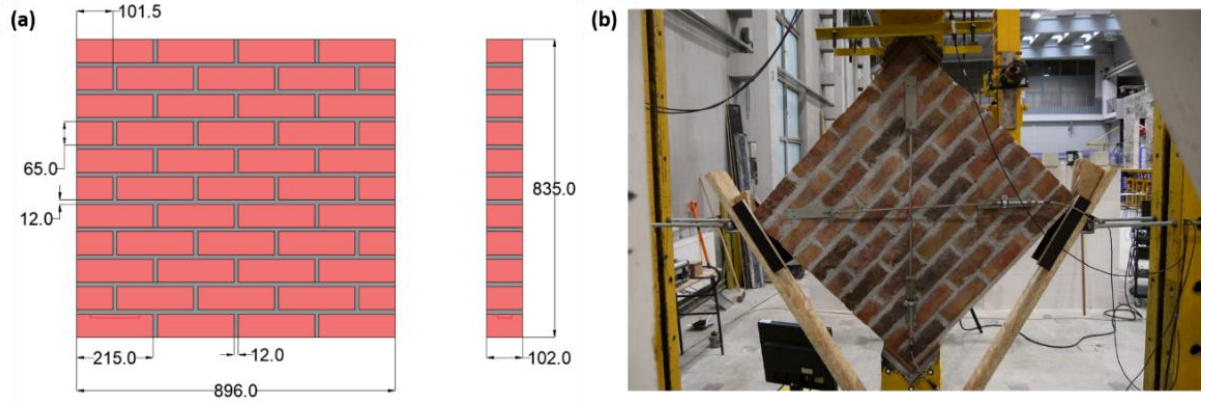

Figure 62: Dimensions of wallettes for diagonal compressive tests **(a)** and typical wallettes in the set-up before the tests **(b)**.

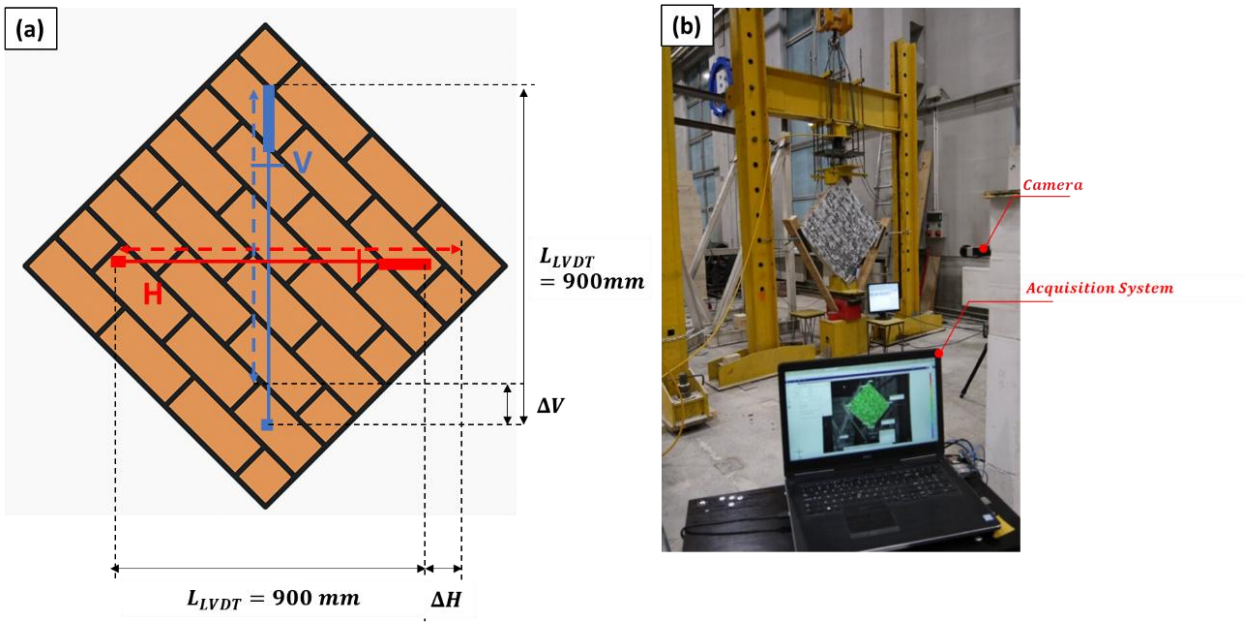

Figure 63: Configuration of the LVDT system: **(a)** Horizontal (H) and vertical (V) LVDTs showing the corresponding elongation (ΔH) and shortening (ΔV); **(b)** Setup of the DIC (Digital Image Correlation) measurement system.

The differences in the relative distances of the measurement points along the horizontal (H) and vertical (V) diagonals from the two systems, corresponding to the two different faces of the walls, were averaged. These averages were then used to calculate horizontal ε_h, vertical ε_v, and angular shear γ deformations relative to each wall. However, during the tests, minor variations between these measurement systems were observed, with sometimes more pronounced differences in the vertical relative displacements. In the following Fig. 64a-b and 65a-b, examples of different measurements highlighted during the tests for both mixes are shown.

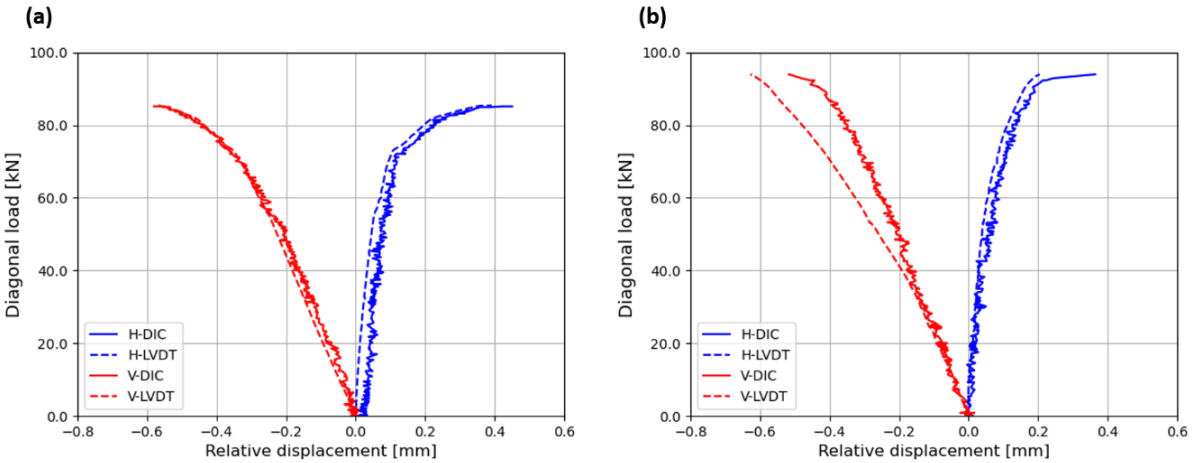

Figure 64: Minor differences between LVDT measurements on one side of the wall and DIC measurements on the other side for wall MIX-1_DCT_1 **(a)**, while pronounced differences in vertical displacements observed for wall MIX-1_DCT_2 **(b)**.

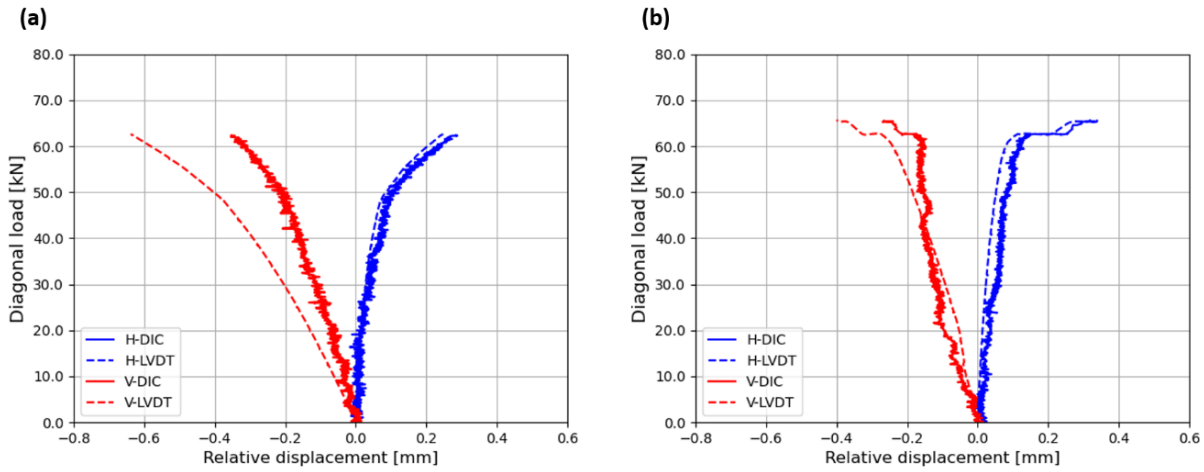

Figure 65: Pronounced differences between vertical LVDT measurements on one side of the wall and DIC measurements on the other side for wall MIX-2_DCT_1 **(a)**, while minor differences in vertical and horizontal displacements observed for wall MIX-2_DCT_2 **(b)**.

Table 17 shows the results of the mechanical properties at peak load in terms of shear and deformation properties from eq. (17-22) for all the samples. Furthermore, the shear stiffness from this test, G_{DCT} is determined by considering a range of shear stress (τ) to shear deformation (γ), spanning from 10% to 40% of the peak values. Considering the load control test set up, a pre-peak ductility μ_{DCT} factor is then calculated as the ratio of the shear deformation at peak (γ_{peak}) and 70% ($\gamma_{70\%}$) of shear stress in the monotonic branch.

$$\tau_{peak} = 0.707 \frac{P_{peak}}{A_n} \tag{17}$$

$$\varepsilon_v = \frac{\Delta V}{L_{LVDT}} \tag{18}$$

$$\varepsilon_h = \frac{\Delta \mathrm{H}}{L_{LVDT}} \tag{19}$$

$$\gamma = \varepsilon_v + \varepsilon_h \tag{20}$$

$$G_{DCT} = \frac{\tau_{40\%} - \tau_{10\%}}{\gamma_{40\%} - \gamma_{10\%}} \tag{21}$$

$$\mu_{DCT} = \frac{\gamma_{peak}}{\gamma_{70\%}} \tag{22}$$

Where τ_{peak} and P_{peak} are the peak shear stress and peak diagonal load applied respectively. A_n is the net cross section of the wallettes, determined as the average of its width

and height multiplied by its thickness. ε_v and ε_h are the axial deformations of the vertical and horizontal LVDT on masonry panel, defined as the ratio of the ΔV diagonal vertical shortening and ΔH diagonal horizontal elongation, divided for the length of the gauge L_{LVDT}, equal for both directions, in this case. $\tau_{40\%}$ and $\gamma_{40\%}$ are the shear stress and shear deformation in correspondence of the 40% of peak load. $\tau_{10\%}$ and $\gamma_{10\%}$ are the shear stress and shear deformation in correspondence of the 10% of peak load. Although no specific recommendations are currently available for the determination of shear stiffness, several Authors [224-225] proposes to calculate this value in this range as reasonably corresponding to a linear segment. Fig. 66a-b illustrates the relationship between shear stress and shear deformation for both mortar mixes. Within these plots, a clear linear range can be observed in the shear stress-strain behavior for the evaluation of the shear modulus.

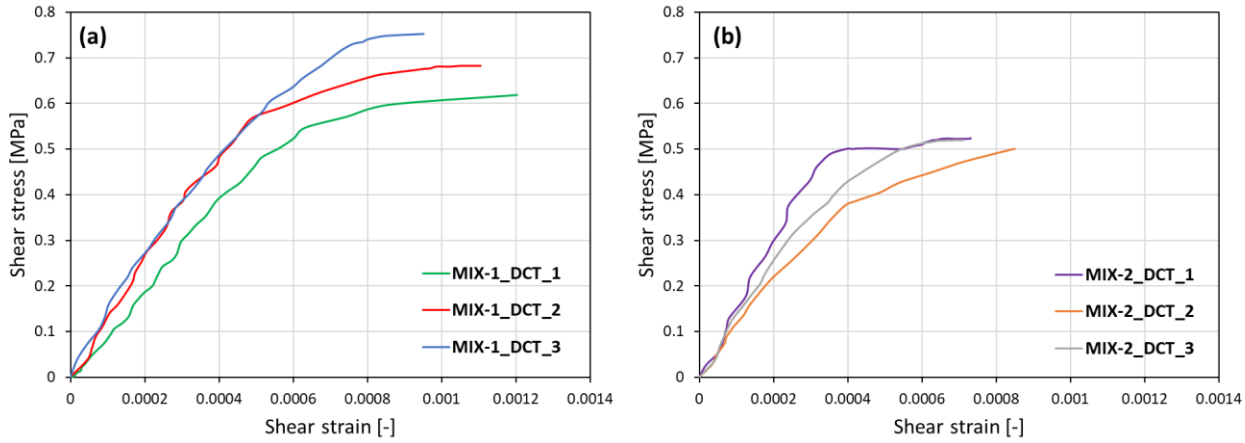

Figure 66: Experimental shear stress - shear strain relationships for masonry made of mortar MIX-1 **(a)** and MIX-2 **(b)**.

Results from the tests, in terms of failure mode, are presented in Fig. 67a-b. For both types of unreinforced masonry elements constructed with different mortar compositions, the cracks predominantly developed along the vertical diagonal, exhibiting a stepped failure pattern. This cracking behavior involved both the mortar bed-head joints and the brick units, highlighting the composite nature of the failure mechanism. In these cases, the walls exhibited a distinctly brittle failure mode, characterized by an abrupt loss of load-carrying capacity and sudden collapse.

Table 17: Mechanical parameters of masonry wallettes tested in diagonal compression.

Samples	P_{peak} [kN]	τ_{peak} [MPa]	ε_v [-]	ε_h [-]	γ [-]	G_{DCT} [MPa]	μ_{DCT} [-]
MIX-1_DCT_1	77.18	0.62	-0.00084	0.00037	0.0012	982.90	2.58
MIX-1_DCT_2	85.37	0.68	-0.00064	0.00047	0.0011	1422.23	2.78
MIX-1_DCT_3	93.94	0.75	-0.00064	0.00032	0.00095	1392.04	2.13
MIX-2_DCT_1	64.92	0.52	-0.00047	0.00024	0.00071	1560.20	2.27
MIX-2_DCT_2	62.37	0.50	-0.00055	0.00030	0.00085	1293.47	2.42
MIX-2_DCT_3	65.68	0.52	-0.00037	0.00036	0.00073	1407.60	3.05

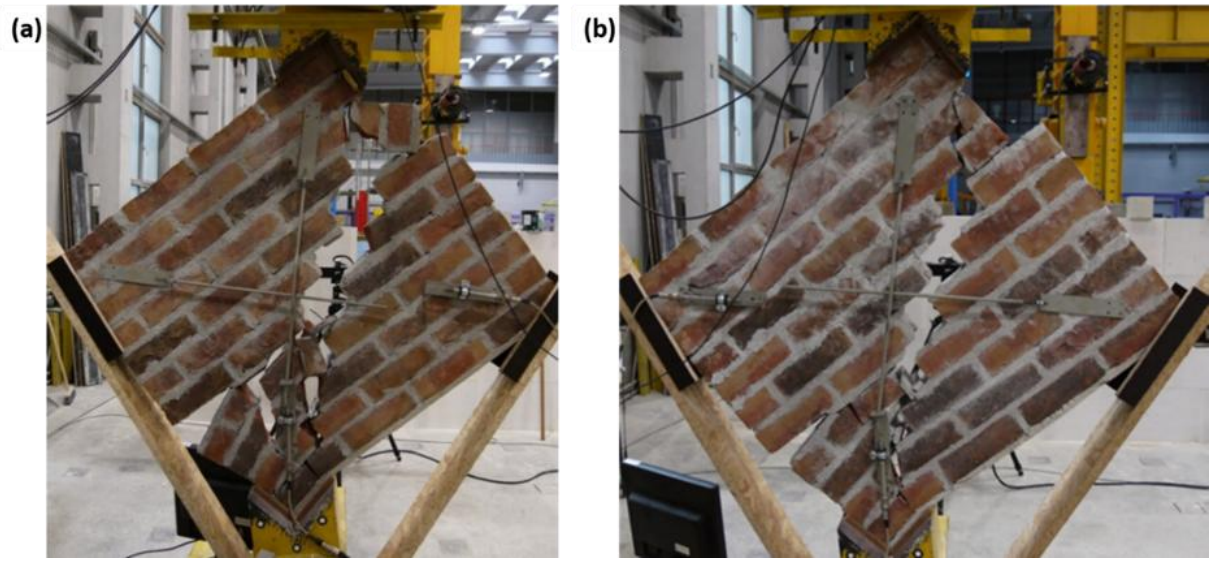

Figure 67: Failure mode of masonry specimens made of mortar type MIX-1 (116) **(a)** and made of mortar type MIX-2 (129) **(b)**.

3.3 Large scale tests

This section describes the test setups and main experimental outcomes from masonry testing of large-scale elements, highlighting the methodologies used and the key findings obtained. It aims to provide a comprehensive understanding of the testing procedures and the resulting data, offering insights into the behavior and performance of masonry under two conditions. The first relates to the vertical shear behavior of masonry walls supported by deflecting members when subjected to increasing vertical loads. The second is associated to the lateral shear behavior of masonry under cyclic loads. As for the previous tests, two masonry types are analyzed resulting from the two mortar types used.

3.3.1 URM walls under static vertical shearing

In this study, the vertical deformative behavior of masonry walls is examined using a simplified test setup designed to replicate the in-plane flexural behavior of masonry. This approach is similar to the tests conducted on the vertical response of deep concrete beam deflection, where testing literature is wider [226]. Masonry walls, constructed with the two previously described mortars and measuring approximately 1800 x 1300 mm, are considered for testing (Fig. 68). The primary focus, beyond the differences in materials, is also on the load application method and the static scheme. Specifically, the vertical load is applied at two distinct points, as shown in Fig. 69. In addition to the increasing actuator-induced vertical load P, the self-weight of the wall (app. 4 kN) and the instrumentation components, such as the load distribution beam (app. 1 kN), also act on the supports during the loading stages.

As a result, two walls are tested for each material type, using the same terminology as in the previous tests: VS_x_s, where x represents the material type (116 or 129 for the two mixes MIX-1 and MIX-2, respectively) and s indicates the load application distance, which can be either *s* = 600 mm or 350 mm. These walls are built on a thin steel beam with a thickness

of 20 mm and then positioned on two supports, allowing for vertical deformation with increasing vertical load applications. The load is precisely applied in load control at a load speed of 1 kN/s, utilizing an actuator with a maximum capacity of 1000 kN. Additionally, this increasing load is applied at the top of the wall through two steel plates, each with a thickness of 20 mm, positioned at two concentrated points. Test set up is shown in Fig. 70 and a review of the tests is given in Table 18.

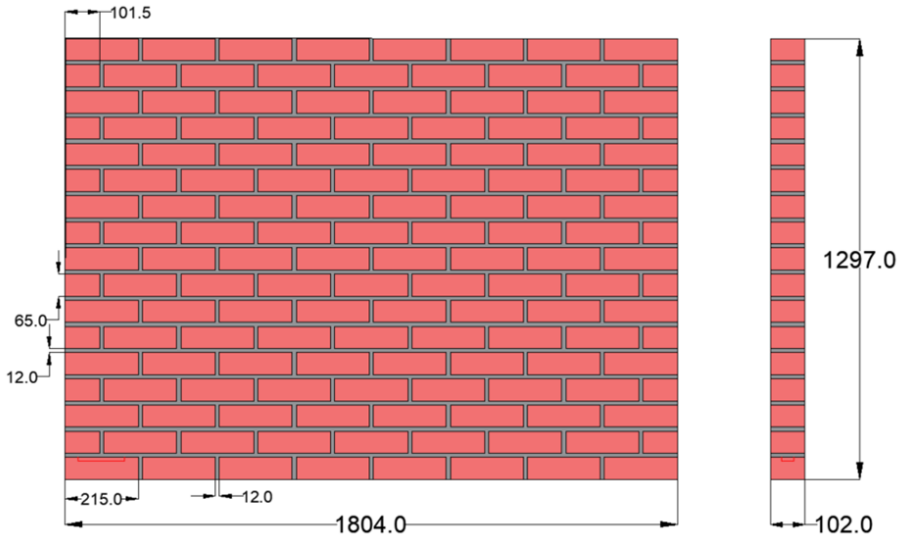

Figure 68: Dimensions (mm) of the walls subjected the in plane vertical loads.

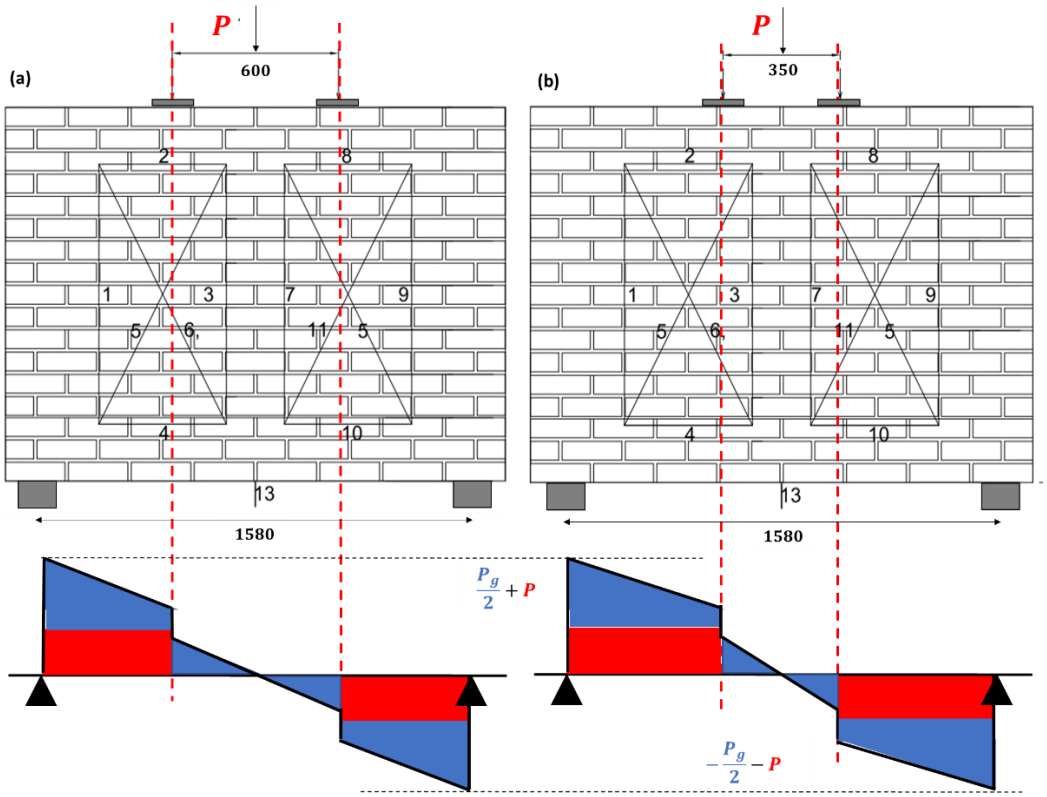

Figure 69: Static diagram showing the shear force distribution and load application method, where P represents the increasing vertical load applied by the actuator, and P_g corresponds to the load due to the self-weight of the wall and testing instrumentation.

Figure 70: Test set-up for in-plane vertical shearing quasi-static test adopted in this study.

Table 18: Programme of tests of masonry walls subjected to vertical shearing tests.

MASONRY TAG	MIX type	Brick type	B [mm]	H [mm]	t [mm]	s [mm]
VS_116_350	MIX-1	Clay	1804	1297	102	350
VS_116_600	MIX-1	Clay	1804	1297	102	600
VS_129_350	MIX-2	Clay	1804	1297	102	350
VS_129_600	MIX-2	Clay	1804	1297	102	600

Two different measuring systems were used on either side of the walls. On one side, displacements are measured using square-shaped LVDTs. Their positions on the walls are chosen on the basis of the simplified static scheme used to evaluate the global equilibrium of the external forces/reactions and recognizing areas where shear stresses are approximately constant. This results in two square frames arranged as shown in Fig. 71, identified as side A and side B. Specifically, the deformations are measured based on the changes in the axial deformations of each LVDT for each frame of the two sides. The rectangular measurement frames have dimensions of 500 x 900 mm. For each frame, four shear deformation angles θ_1, θ_2, θ_3 and θ_4 are associated with it, resulting from the relative displacements of each LVDT base from one load step to the next. Indicating with a, b, c, d, e and f the initial length of the bases and *a', b', c', d', e'* and *f'* the lengths of the bases after the application of the load, the measurements the angles (θ_1, θ_2, θ_3 and θ_4) can be calculated using the law of cosines (Fig. 72). The new lengths of the bases are then evaluated with (23-26):

$$e'^2 = a'^2 + d'^2 - 2a'd'\cos(90 + \theta_1) \qquad (23)$$

$$f'^2 = d'^2 + c'^2 - 2d'c'\cos(90 + \theta_3) \quad (24)$$

$$e'^2 = b'^2 + c'^2 - 2b'c'\cos(90 - \theta_4) \quad (25)$$

$$f'^2 = a'^2 + b'^2 - 2a'b'\cos(90 - \theta_2) \quad (26)$$

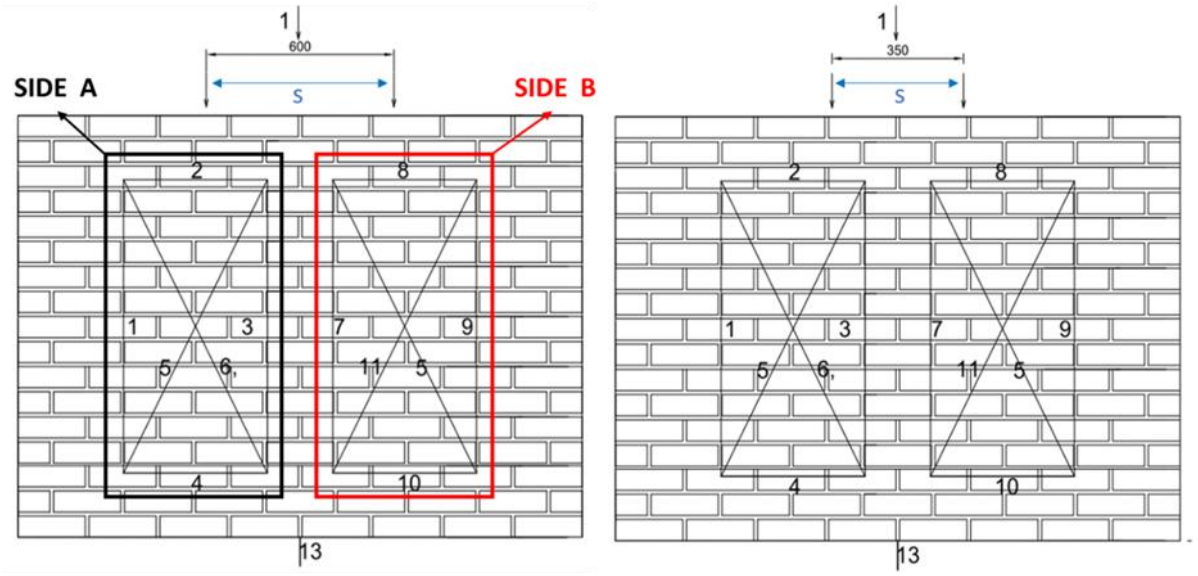

Figure 71: Measurement system for one side both masonry walls' type with different distance s.

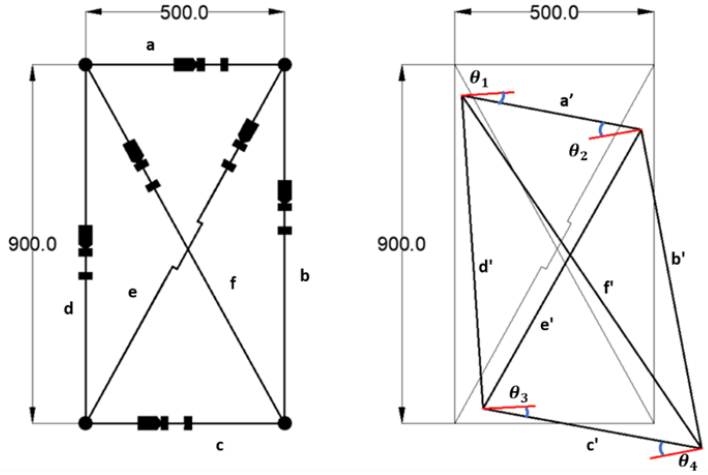

Figure 72: Rectangular measurement frames with dimensions of 500 x 900 mm. Frame dimensions and shear deformation angles θ_1, θ_2, θ_3 and θ_4 associated with the generic deformed shape.

Therefore, the deformation parameter as non-dilatational strain angles are evaluated using (27-30):

$$\theta_1 = arcsin\left(\frac{e'^2 - a'^2 - d'^2}{2a'd'}\right) \quad (27)$$

$$\theta_2 = arcsin\left(\frac{a'^2 + b'^2 - f'^2}{2a'b'}\right) \quad (28)$$

$$\theta_3 = arcsin\left(\frac{f'^2 - d'^2 - c'^2}{2d'c'}\right) \quad (29)$$

$$\theta_4 = arcsin\left(\frac{b'^2 + c'^2 - e'^2}{2b'c'}\right) \quad (30)$$

A global shear deformation angle θ (31) for each frame is then associated as the average of individual deformation angles θ_i, for each load step n:

$$\theta_n = \frac{1}{4}\sum_{i=1}^{4}|\theta_i| \quad (31)$$

Beyond local deformative measurements, shear stresses on both sides (32), calculated as the ratio of the load applied to a single plate (half of the total load *P* applied by the actuator) to the vertical wall cross-section A_v are also calculated with:

$$\tau_n = \frac{P_n}{2\,A_v} \quad (32)$$

And a shear modulus G_n (33) was calculated as the ratio of the shear stress τ_n to the corresponding deformation angle θ_n:

$$G_n = \frac{\tau_n}{\theta_n} \quad (33)$$

This system was also applied on the study of the lateral response of ACC blocks with and without bed joint reinforcement [227]. On the other side of the wall, a DIC system was employed to obtain measurements of the global displacements in particular the one at the middle span, that was also measured with an external LVDT and as for the diagonal test have a detailed overview of the crack patterns.

Wall VS_116_350 exhibited an asymmetrical damage pattern. In the initial loading phase, no cracking was observed. As the vertical load increased, lateral shear cracking developed on SIDE-B of the wall, with a shear crack propagating through both brick and mortar joints at a mid-vertical displacement of 1.1 mm and a vertical load of 160.35 kN. The crack pattern was sudden and visibly clear in both real observation and DIC command outputs (Fig. 73a). After this crack appeared, the vertical load continued to rise gradually, with no visible cracking on the opposite side of the wall. At a total vertical load of 188.86 kN, in addition to lateral cracking, a fracture appeared at the interface between the horizontal second and third brick layers from the bottom. This resulted from the masonry adjusting to the increased vertical deflection (Fig. 73b). This trend continued until testing ceased, reflecting

a gradual decrease in vertical load due to the load-controlled test setup. The final crack pattern observed at the end of the test for both sides is shown in Fig. 74.

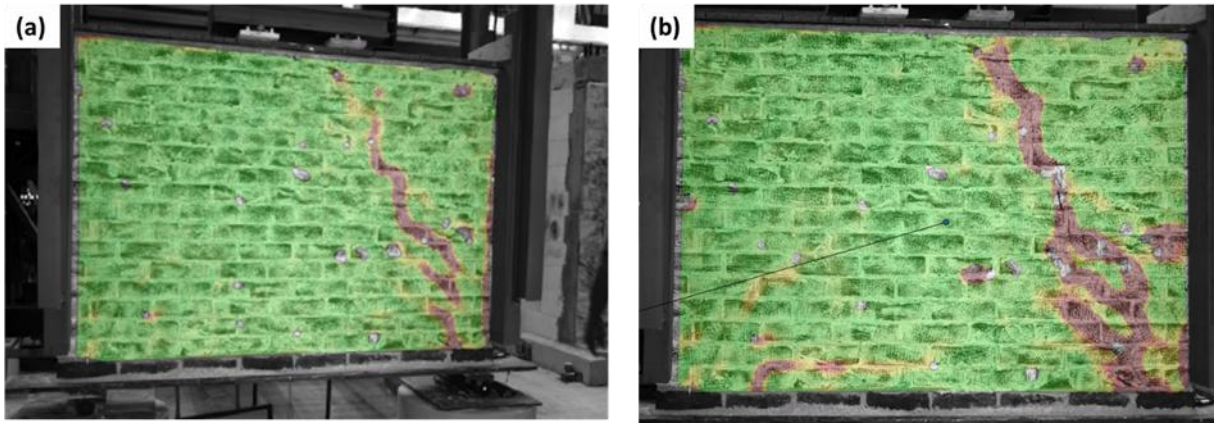

Figure 73: First crack formation **(a)** and additional crack propagation at the base layer due to increasing deflection **(b)** for VS_116_350.

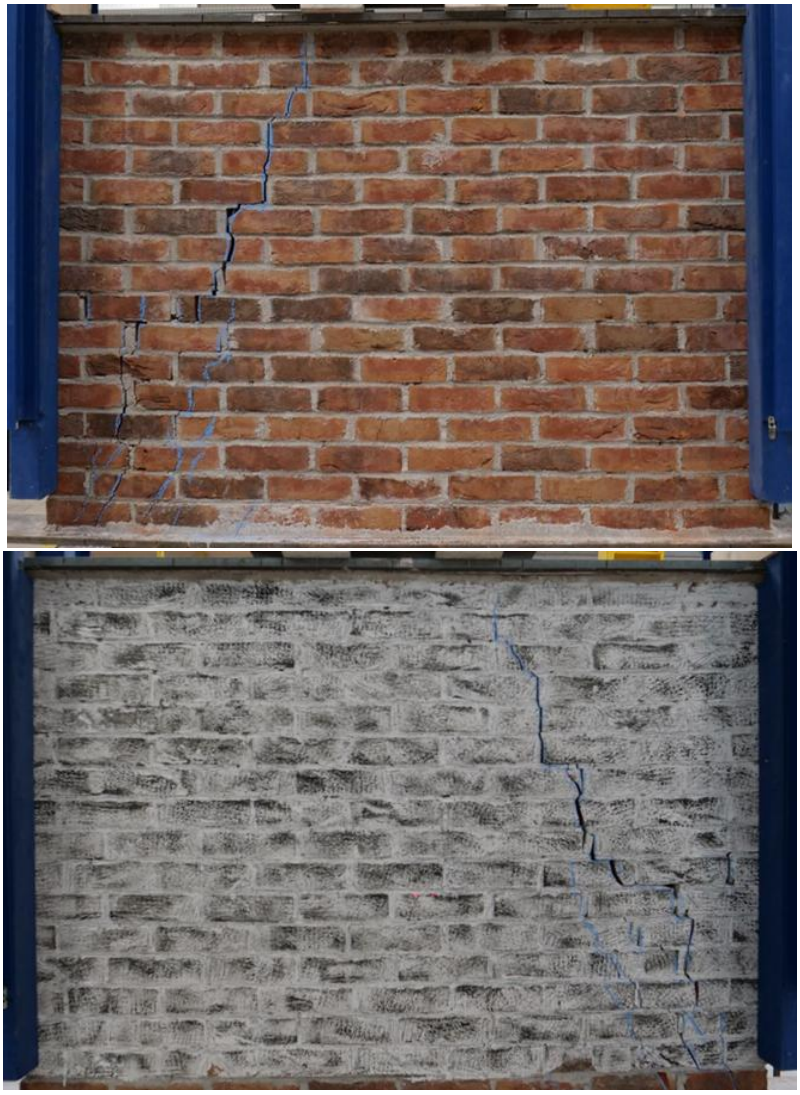

Figure 74: Crack patterns on back and front views of the wall made of mortar VS_116_350.

Fig. 75a-b shows the shear stress-angular strain response recorded on both sides of a masonry wall specimen subjected to vertical shear loading, considering all four θ_i angles for each side. The close agreement between the measured values supports the use of an average θ angle in subsequent calculations. The experimental test results for the masonry wall VS_116_350 reveal differing behaviors on each side: SIDE-A exhibited softening due to crack formation, while SIDE-A maintained elastic behavior throughout the test (Fig. 76a). This behavior is also reflected by the more rapid decreasing of the transverse stiffness modulus plotted against shear stresses in Fig. 76b). The global behavior, in terms of vertical displacements and applied vertical load, exhibits an elastic-plastic trend following the formation of the critical crack (Fig. 77).

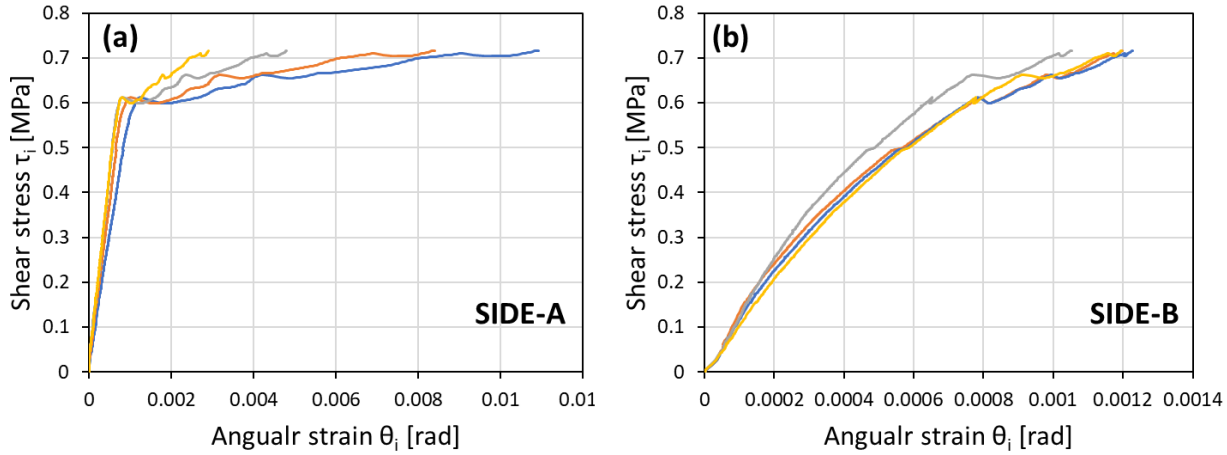

Figure 75: Shear stress-shear strain for all the θ_i angles evaluated for the **(a)** SIDE-A and **(b)** SIDE-B for masonry VS_116_350.

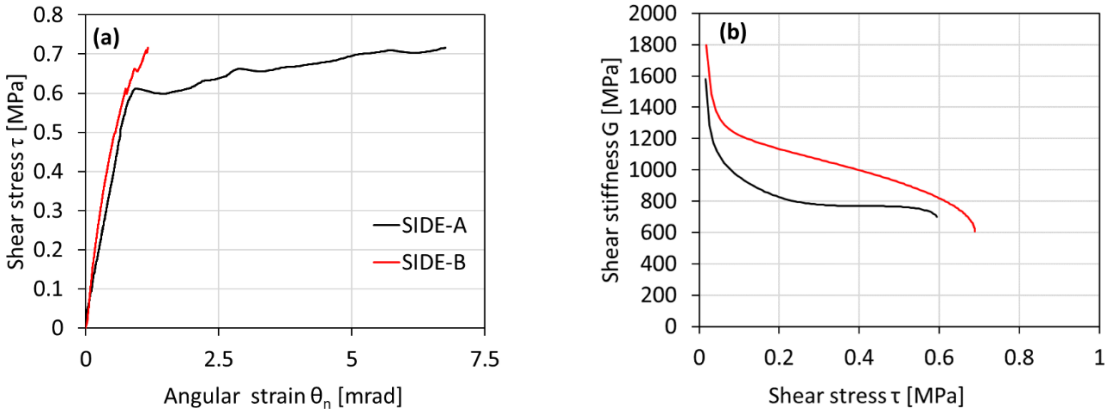

Figure 76: Shear stress-shear strain **(a)** and shear modulus-shear stress **(b)** relationships for the wall made with mortar VS_116_350.

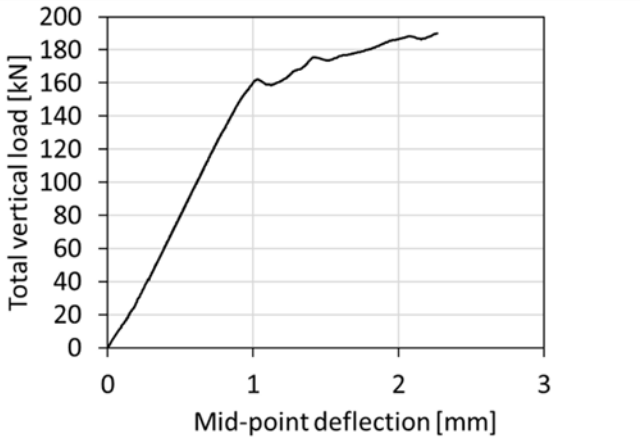

Figure 77: Total vertical load – deflection for the wall made with mortar VS_116_350.

Wall VS_116_600 exhibited a distinctly asymmetrical damage pattern during the vertical shear loading test. The initial formation of diagonal shear cracks was observed on one side of the wall (SIDE-B), occurring under a vertical external load of 263.88 kN and corresponding to a mid-span deflection of 1.32 mm. These first cracks indicated the onset of localized stress concentrations and progressive loss of stiffness on SIDE-B, while SIDE-A remained largely uncracked at this stage. As the vertical load increased, further propagation and widening of the existing cracks were recorded, leading to a critical state of damage. Under a total vertical load of 322.99 kN and a mid-span deflection of 4.48 mm, complete failure was observed through both the bricks and the mortar joints on SIDE-B. The failure mechanism included not only cracking but also the sliding of a portion of the wall along an inclined failure surface, clearly visible in the post-test observations (Fig. 78a-b). The final crack pattern developed across the entire wall surface is documented in Fig. 79, highlighting the dominance of the failure on SIDE-B compared to SIDE-A. The crack width measurements confirmed that the damage was more concentrated and severe on the initially cracked side. Also, here Fig. 80a-b show consistency between the responses on both sides justifying the use of an averaged angular strain value in the following analyses. The experimental results for the shear stress trend and transversal stiffness are presented in Fig. 81a-b, while the mid-deflection is shown in Fig. 82.

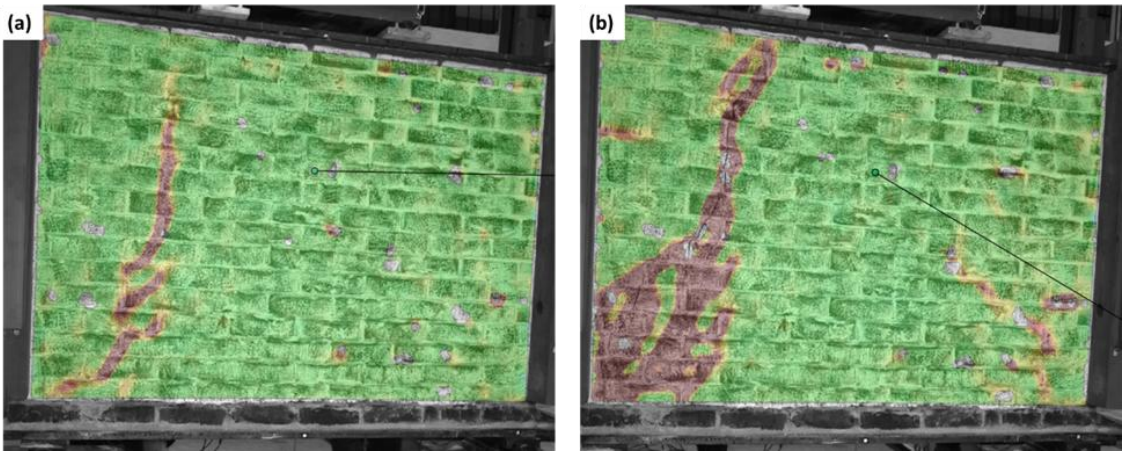

Figure 78: First crack formation **(a)** and crack pattern development at peak load **(b)** for VS_116_600.

Figure 79: Crack patterns on back and front views of the wall made of mortar VS_116_600.

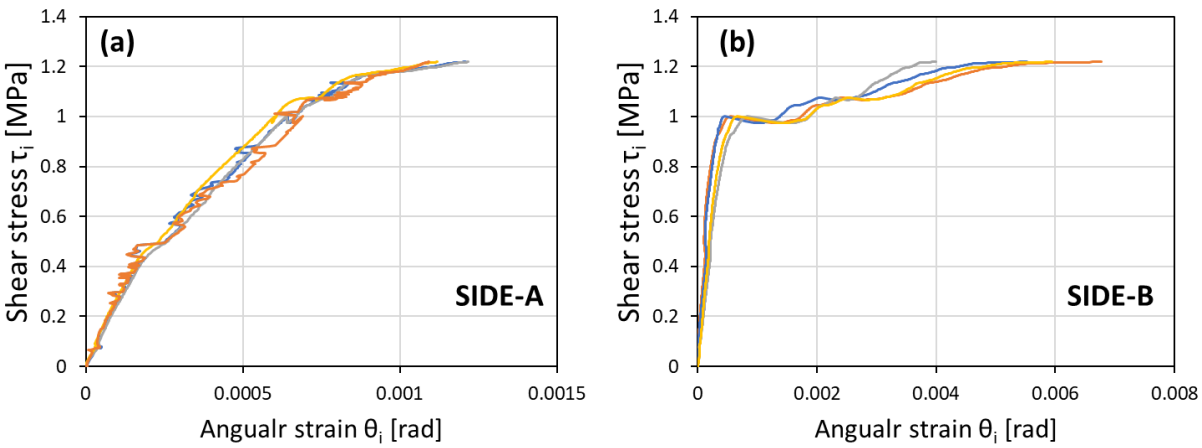

Figure 80: Shear stress-shear strain for all the θi angles evaluated for the **(a)** SIDE-A and **(b)** SIDE-B for masonry VS_116_600.

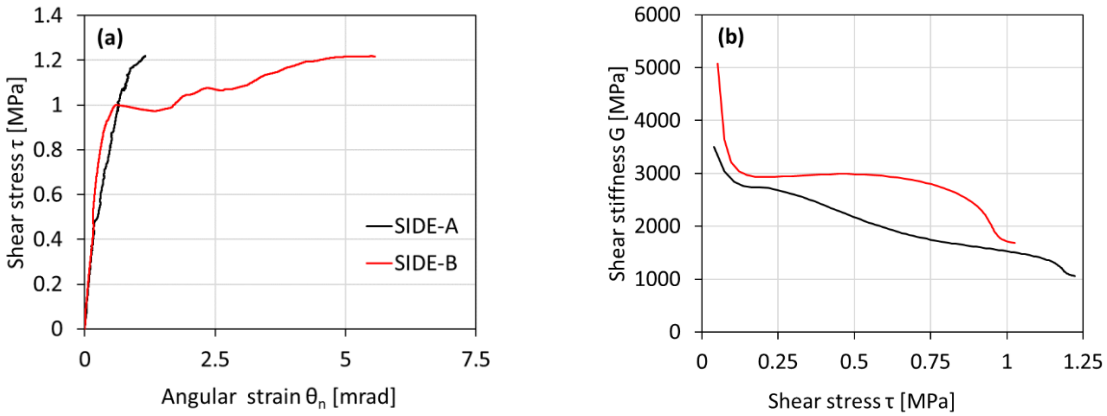

Figure 81: Shear stress-angular strain **(a)** and transversal stiffness shear stress **(b)** relationships for the wall made with mortar VS_116_600.

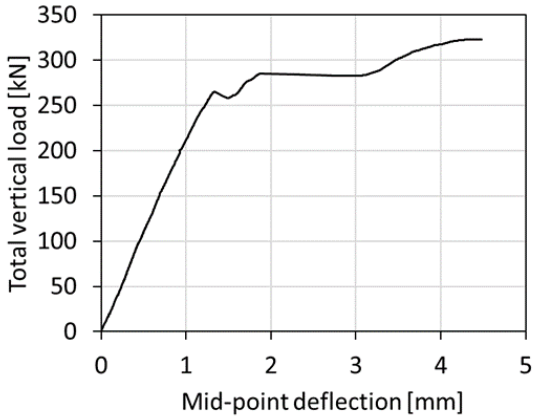

Figure 82: Total vertical load – deflection for the wall made with mortar VS_116_600.

Despite the symmetry of load application and boundary conditions, wall VS_129_350 displayed an asymmetrical progression of damage under increasing load. On the contrary of the latter tests, small cracks started to develop at for both parts of the walls, showing a more uniform behavior (Fig. 83a). As the vertical load increased, shear cracks concentrated on the SIDE-A of the wall, with visible cracks appearing at a total vertical load of 148.06 kN and a mid-vertical displacement of 1.71 mm. Subsequently, visible shear cracks were visible on the other side (SIDE-B) of the wall due to the redistribution of forces within the panel. Visible cracks on this side emerged at a total vertical load of 149.33 kN and a corresponding mid deflection of 1.78 mm. The pre-formed shear cracks then progressed together until the wall ultimately failed, displaying a stepped crack pattern that followed both the units and mortar joints, at a vertical load of 153.40 kN and an ultimate deflection of 4.32 mm (Fig. 83b). Definitely, SIDE-A showed crack opening wider than SIDE-B. Final crack patterns on both sides are evidenced in Fig. 84. Fig. 85a-b displays the shear stress versus angular strain behavior recorded on both faces of the masonry wall during vertical shear loading, considering all measured θi values. The strong correlation between the two sets of results supports the use of an average angular strain value in the subsequent evaluation. The local response of masonry wall VS_129_350, in terms of shear stress versus angular deformation for both sides, is shown in Fig. 86a. Fig. 86b presents the relationship between transverse stiffness and shear stress. An asymmetry

between the two sides is evident in Fig. 86a, where the critical shear stresses at crack initiation, identified by changes in initial stiffness, differ. The global behavior of the wall, represented by the total vertical load versus mid-span deflection, is reported in Fig. 87.

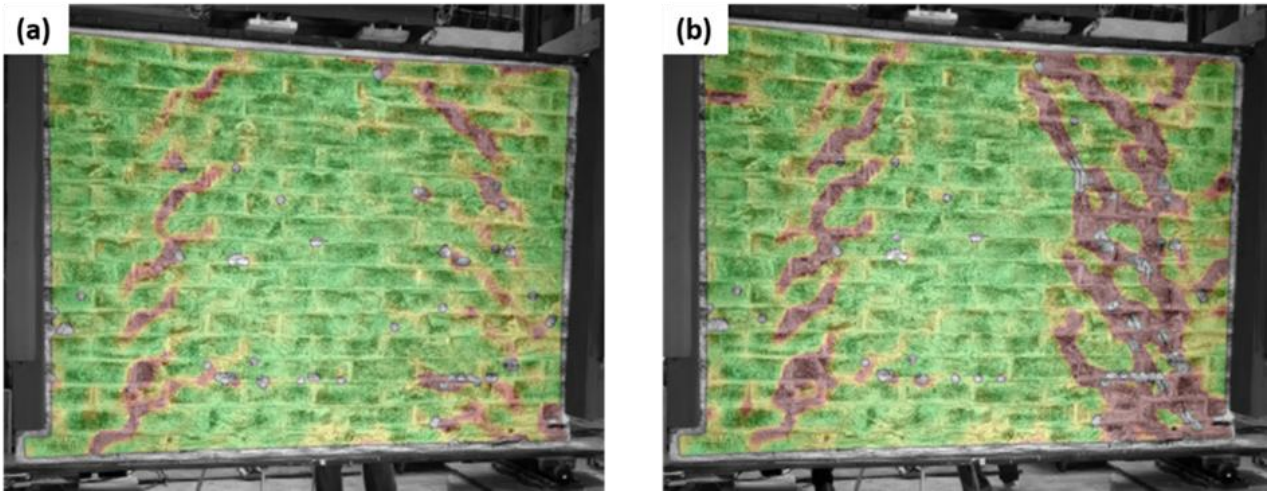

Figure 83: Symmetric response for initial loads **(a)** and development of cracking on both side of the wall for increasing loads **(b)** for VS_129_350.

Figure 84: Crack patterns on back and front views of the wall made of mortar VS_129_350.

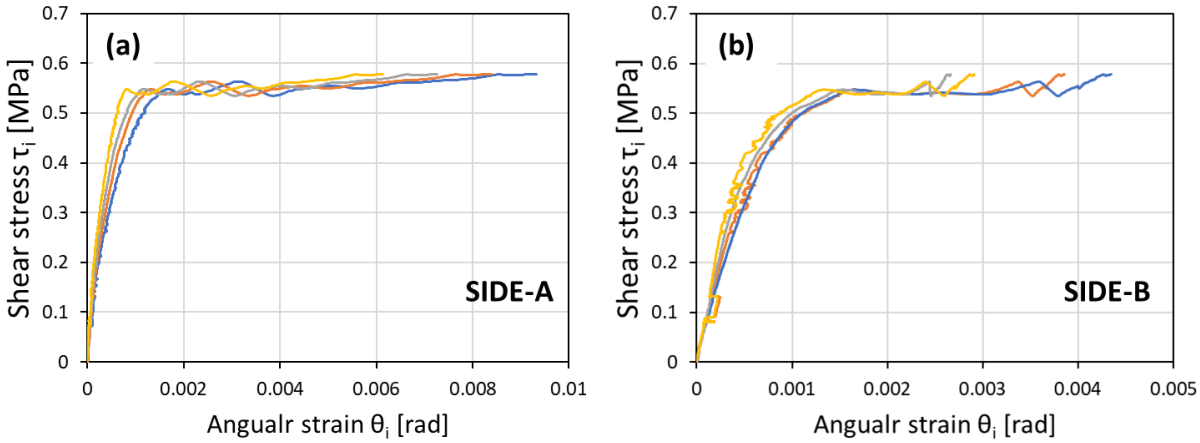

Figure 85: Shear stress-shear strain for all the θi angles evaluated for the **(a)** SIDE-A and **(b)** SIDE-B for masonry VS_129_350.

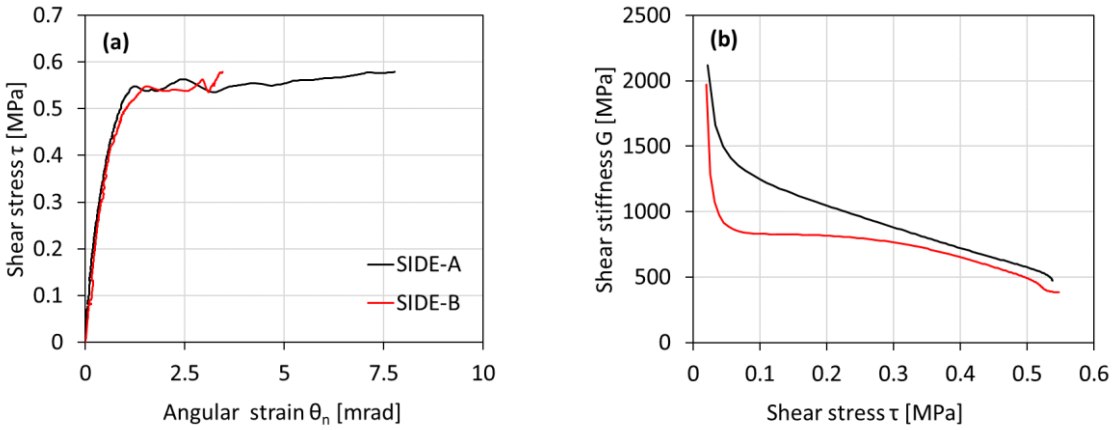

Figure 86: Shear stress-angular strain **(a)** and transversal stiffness shear stress **(b)** relationships for the wall made with mortar VS_129_350.

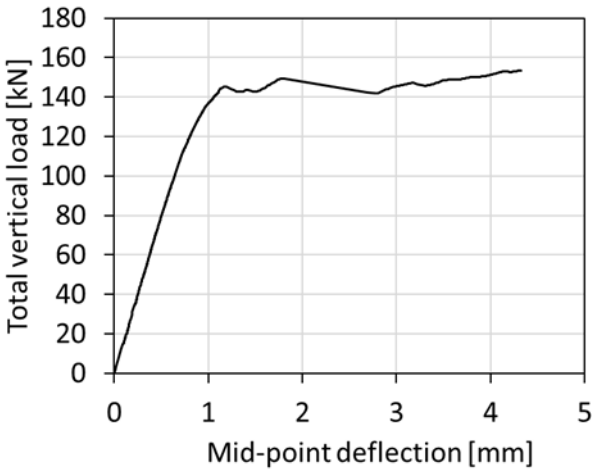

Figure 87: Total vertical load – deflection for the wall made with mortar VS_129_350.

The response of the masonry wall VS_129_600 showed similar behavior to its counterpart made of the same materials but with a lower spacing of external loading. The

response remained elastic until the first crack formed on SIDE-B of the wall at a vertical load of 208.28 kN, with a corresponding mid-deflection of 1.12 mm (Fig. 88a). As the load increased, a shear crack developed on the opposite side (SIDE-A) at a vertical load of 251.21 kN and a mid-deflection of 1.77 mm. From this point onward, both the load and displacement increased monotonically, with the previous cracks widening till the failure obtained with a maximum load of 300 kN. Additionally, deformation concentrations were observed at the top edge of the wall, horizontally and no-symmetrically, as seen in the previous test, continuing until the crack spread (Fig. 88b). Final crack pattern of the wall evidenced in the two sides is given in Fig. 89. All the measured θ_i angles on both sides of the masonry wall during vertical shear loading are represented in the shear stress-angular strain plots of Fig. 90a-b. Due to the close agreement between the two sets of data, an average θ value was considered appropriate for use in the subsequent analysis. The trends of shear stress versus angular deformations and transversal stiffness versus shear stress are presented in Fig. 91a-b, respectively, while the total applied load versus vertical displacement is shown in the following Fig. 92. Table 19 summarizes the experimental results for vertical load (P) and mid-deflection (δ) at crack initiation and ultimate failure. Table 20 reports shear stress, angular deformation, and transverse stiffness at critical and peak conditions for all walls, including the ratios of peak to critical shear stress and angular strain for both sides. As previously noted, the ratios between shear stresses and vertical loads remain consistent.

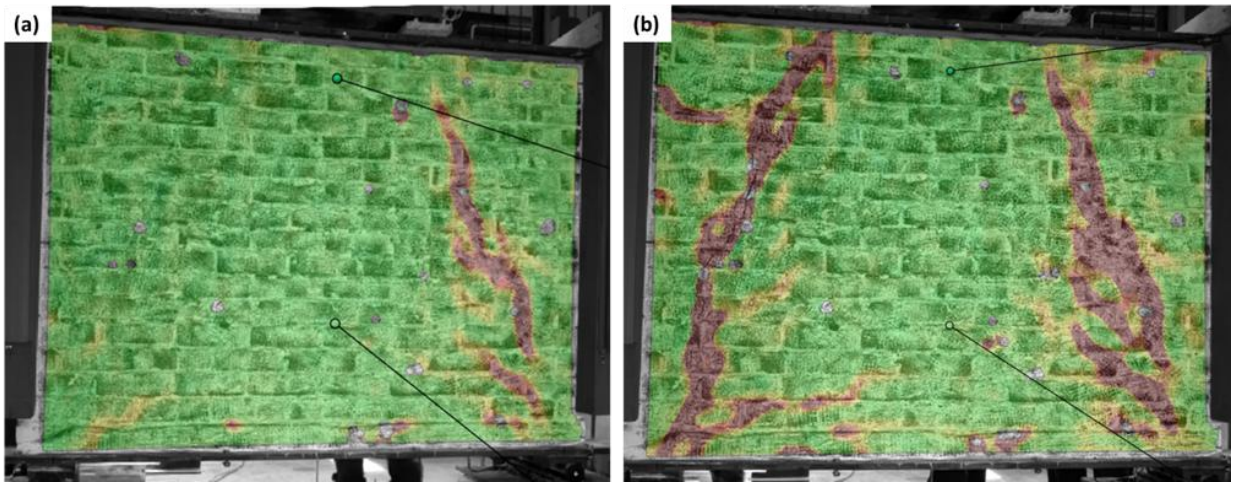

Figure 88: Initial crack formation **(a)** and concentration of deformation at both sides of the wall for increasing loads **(b)** for VS_129_600.

Table 19: Summary of critical and peak load values, along with the corresponding critical mid-deflection, ultimate deflection and relative ratios, for both tested masonry walls.

Samples	P_{cr} [kN]	P_{max} [kN]	δ_{cr} [mm]	δ_{max} [mm]	P_{max}/P_{cr} [-]	δ_{max}/δ_{cr} [-]
VS_116_350	158.24	189.83	0.98	2.27	1.20	2.32
VS_116_600	263.88	323.08	1.32	4.48	1.22	3.41
VS_129_350	144.18	153.40	1.13	4.32	1.06	3.83
VS_129_600	208.28	299.99	1.12	4.41	1.44	3.93

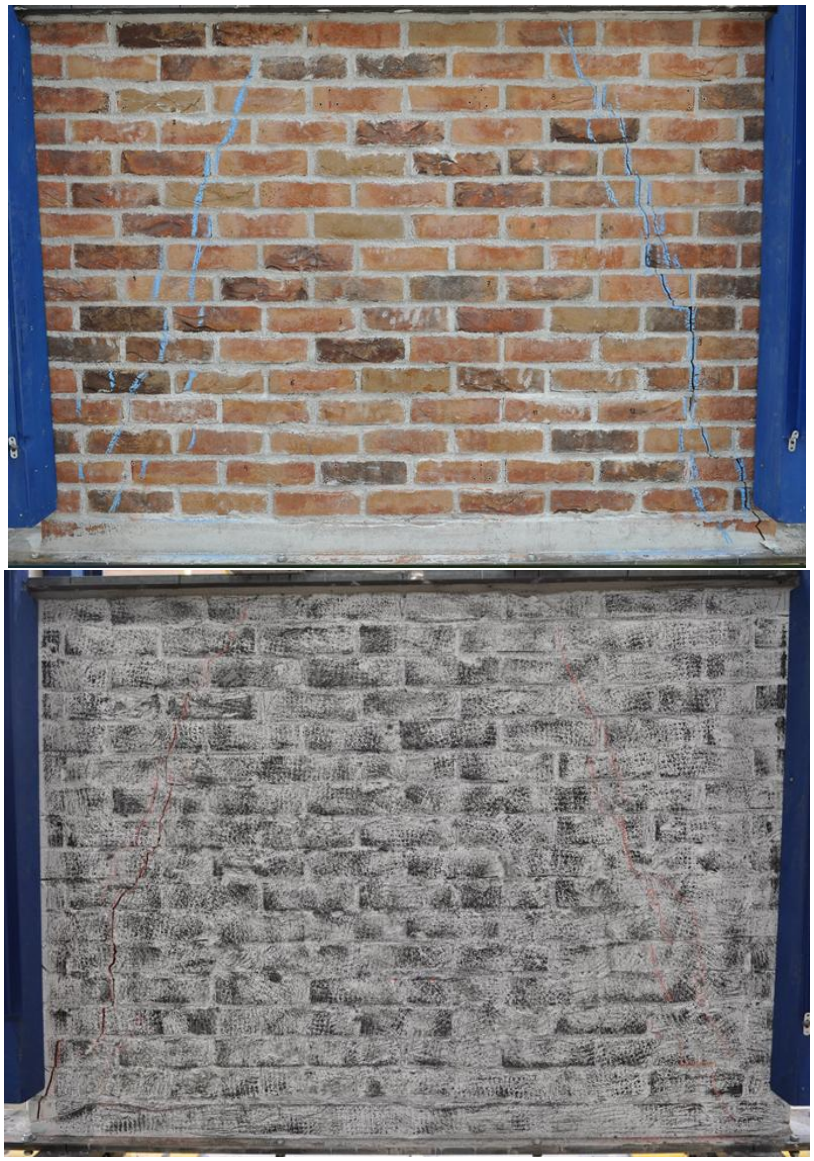

Figure 89: Crack patterns on back and front views of the wall made of mortar VS_129_600.

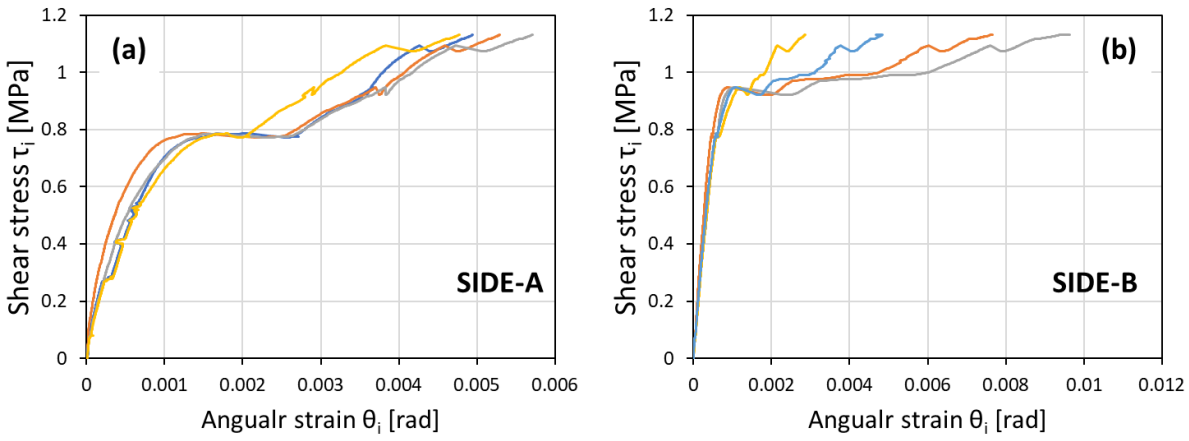

Figure 90: Shear stress-shear strain for all the θ_i angles evaluated for the **(a)** SIDE-A and **(b)** SIDE-B for masonry VS_129_600.

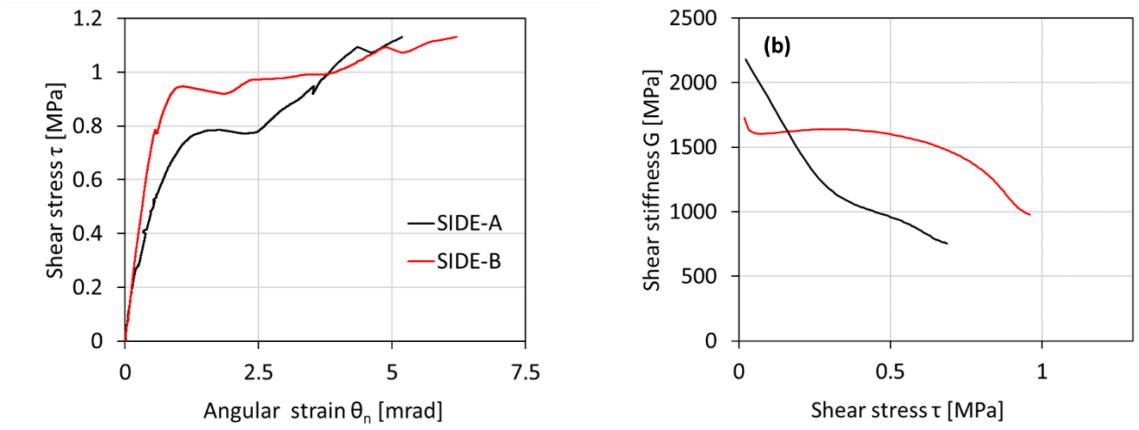

Figure 91: Shear stress-angular strain **(a)** and transversal stiffness shear stress **(b)** relationships for the wall made with mortar VS_129_600.

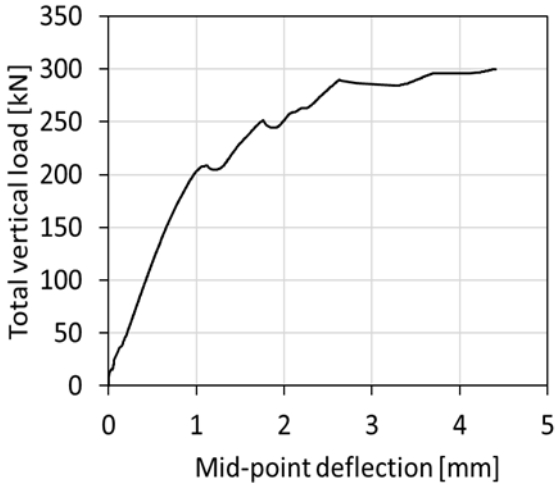

Figure 92: Total vertical load – deflection for the wall made with mortar VS_129_600.

Table 20: Summary of critical and peak shear stresses, angular deformation for both masonries tested for both sides.

Samples (side)	τ_{cr} [MPa]	τ_{max} [MPa]	θ_{cr} [mrad]	θ_{max} [mrad]	τ_{max}/τ_{cr} [-]	θ_{max}/θ_{cr} [-]
VS_116_350 (A)	0.60	0.72	0.85	6.76	1.20	7.95
VS_116_350 (B)	-	0.72	-	1.17	-	-
VS_116_600 (A)	1.00	1.22	0.64	1.16	1.22	1.82
VS_116_600 (B)	1.00	1.22	0.57	5.56	1.22	9.75
VS_129_350 (A)	0.54	0.58	1.15	7.78	1.06	6.79
VS_129_350 (B)	0.54	0.58	1.44	3.45	1.06	2.40
VS_129_600 (A)	0.79	1.13	1.72	5.18	1.44	3.01
VS_129_600 (B)	0.79	1.13	0.56	6.21	1.44	11.13

3.3.2 URM walls under horizontal cyclic loading

Lateral cyclic pushover tests were performed on single-leaf masonry walls with dimensions of 1350 × 1759 mm (Fig. 93) and 1350 × 1297 mm (Fig. 94), designated as Type A and Type B, respectively, to examine differences in shape response. The tests were conducted

after a 28-day curing period for the samples in the lab, consistent with all previous tests. The test set-up was realized in order to reproduce the boundary conditions of double-bending. In this case, the top of the wall is able to move horizontally but the top rotation is constrained. Image of the test setup is given in Fig. 95. The walls were constructed directly on concrete beams measuring 250 x 250 mm. A second concrete beam was then attached to the top of the wall using fast-setting cement mortar. This upper beam was connected to a steel frame with a hinge system, linking it to a lateral actuator for applying lateral loads. Additionally, steel rollers were incorporated to facilitate horizontal movement, along with a steel redistribution beam to enable vertical load application in the model.

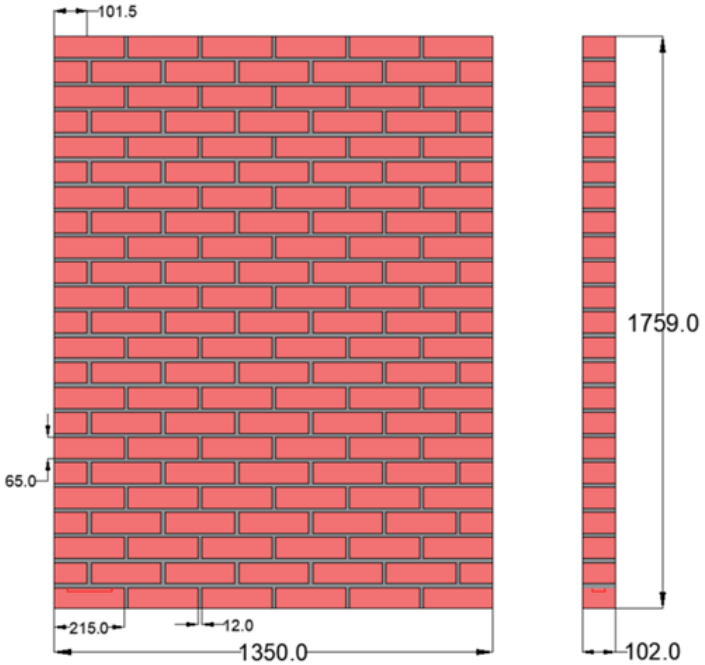

Figure 93: Dimensions (mm) of the walls type A subjected the in plane lateral cyclic loads.

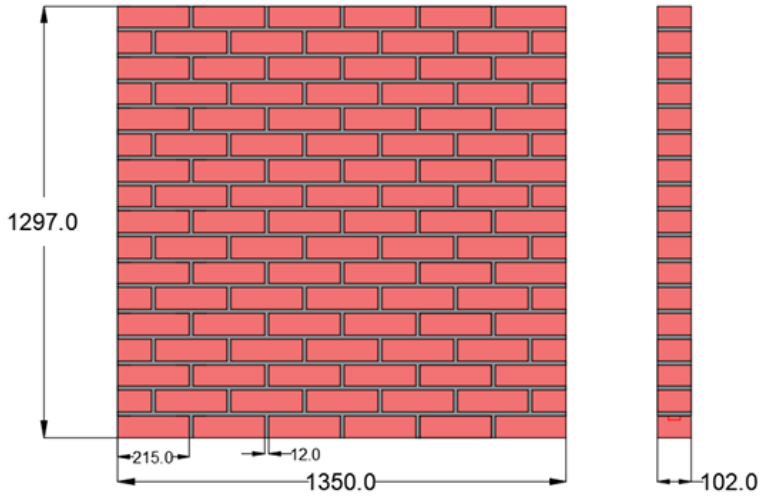

Figure 94: Dimensions (mm) of the walls type B subjected the in plane lateral cyclic loads.

Figure 95: Test set-up for the lateral cyclic response with wall ready to be tested.

Two different levels of pre-compression were selected to investigate their impact on the response, alongside the aspect ratio as a key parameter. Literature level of pre-compression vary from 10% to 30% of the compressive strength of masonry tested. In this study, the pre-compression levels were set at 15% and 30% of the maximum compressive strength to account differently according to the materials of the wall. Each wall is then identified with a code HC_mat_type_p, where mat is 116 or 129 recalling the proportions of MIX-1 and MIX-2, type is the dimensions type of the wall (A or B) and p is the percentage of pre-compression (15% or 30%). One wall for each parameter was tested with a total of 8 walls. Summary of the test designation is given in Table 21.

Table 21: Designation of the test specimens for the lateral cyclic pushover tests.

MASONRY TAG	MIX type	B [mm]	H [mm]	t [mm]	p [%]
HC_116_A_15	MIX-1	1350	1759	102	15
HC_116_A_30	MIX-1	1350	1759	102	30
HC_116_B_15	MIX-1	1350	1297	102	15
HC_116_B_30	MIX-1	1350	1297	102	30
HC_129_A_15	MIX-2	1350	1759	102	15
HC_129_A_30	MIX-2	1350	1759	102	30
HC_129_B_15	MIX-2	1350	1297	102	15
HC_129_B_30	MIX-2	1350	1297	102	30

The tests procedure is described as follow. First the pre-compression was applied and kept constant during all the test, then the lateral cyclic displacements are imposed through a cyclic load actuator with maximum capacity of 1000 kN. Specifically, the displacement history imposed is based on the FEMA-461 [228] recommendations suggesting drift proportional to

the heights of the walls with increasing amplitude of 1.4 times (Fig. 96a-b), starting with a drift of 0.05% till failure. Anyway, displacement control was performed manually due to the limitations of the lab equipment operating in load control for lateral loads, resulting in acceptable differences in lateral drifts observed across different walls. For each amplitude only one cycle was repeated with a displacement-controlled system in order to keep the testing time within a maximum of 3 hours. On one side of the wall, a DIC system was used, allowing the open-source software GOM Correlate to provide a qualitative indication of crack development and principal strains in the masonry. Measurements of the global top lateral displacements were carried out using LVDTs.

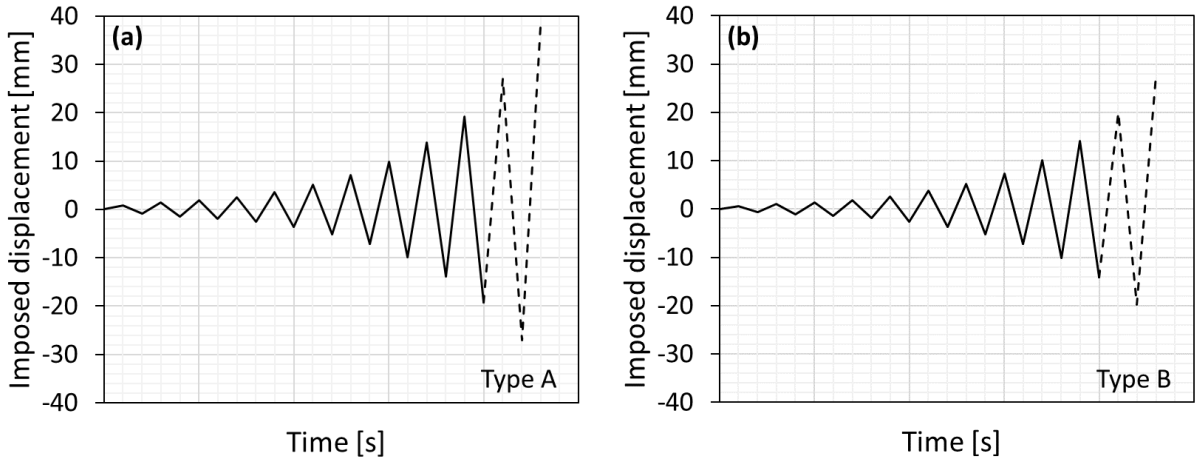

Figure 96: History of lateral displacements imposed for the cyclic test for walls type A **(a)** and type B **(b)**.

From the hysteresis loops, the secant stiffness values are determined as the slope of the line connecting the peak shear loads of each cycle [229] (Fig. 97). This allows for the subsequent evaluation of the secant stiffness changes for each cycle. Specifically, the secant stiffness can be evaluated as per equation (34), where $\pm V_i$ and $\pm \delta_i$ are the positive and negative peak base shears and the relative displacements, respectively.

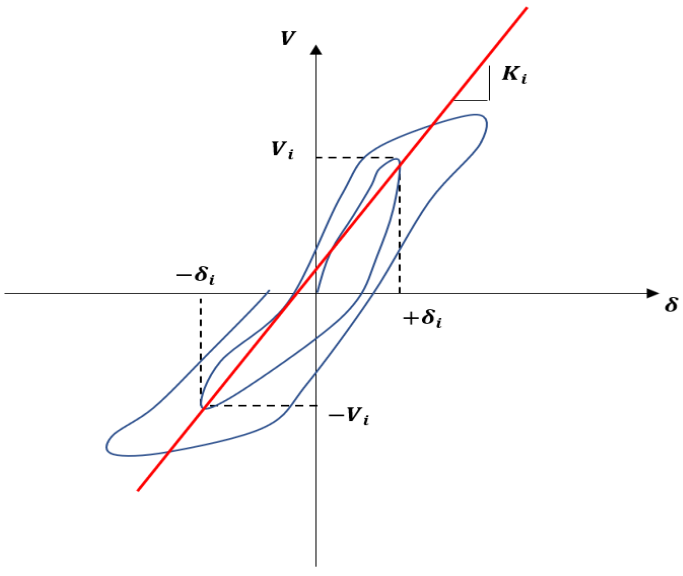

Figure 97: Quantities for secant stiffness evaluation.

$$K_i = \frac{(|+V_i| + |-V_i|)}{(|+\delta_i| + |-\delta_i|)} \quad (34)$$

The energy dissipation of walls is also a crucial parameter, especially in the context of displacement-based methods for seismic assessment of structures [230]. The quantification of energy dissipation during cyclic loading can be expressed in terms of equivalent viscous damping ξ_{eq} as per equation (35). This is determined by considering the lateral load-displacement curves for each cycle, along with the corresponding energy dissipation W_d and the positive W^+_e and negative W^-_e peak elastic energy dissipations [141] (Fig 98).

$$\xi_{eq} = \frac{W_d}{2\,\pi\,(W_e^+ + W_e^-)} \quad (35)$$

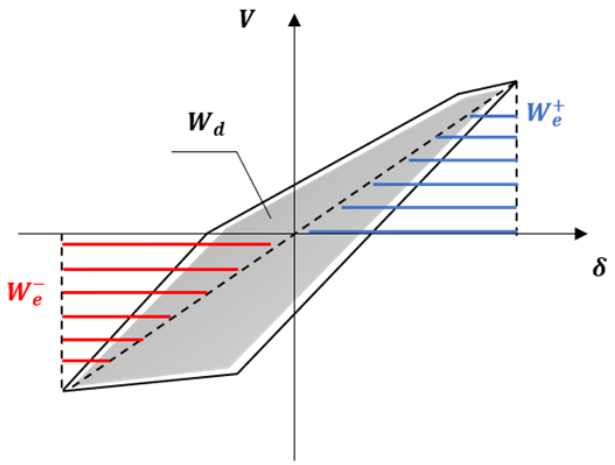

Figure 98: Quantities for hysteretic dissipation evaluation.

To subsequently compare the results of the lateral cyclic response of masonry walls, the hysteresis curves are modified. First, the envelopes for the positive and negative directions are obtained, followed by the creation of a bilinear approximation based on the studies [141]. In this study, the latter approach [141] has been adopted for the positive and negative push directions. Starting from the envelopes, values of the experimental peak base shear and experimental ultimate displacements are determined. Then, the elastic stiffness K_e of the bilinear curve is determined considering a secant from zero to the correspondence of the 70% of the peak experimental base shear for both positive and negative direction. At the same way, the ultimate displacement δ_u of the bilinear curve is obtained in correspondence of the decrement of 20% of the experimental peak shear strength on the softening branch. Knowing these two points on the curves, the determination of the peak shear strength of the bilinear curve Vu is finally obtained imposing equivalence of the area of the bilinear curve with the cyclic envelope for all cyclic tests for all the respective directions (Fig. 99). This process permits also the determine the elastic displacement δ_e. At this point, a value of the ductility is evaluated as the ratio of the previous displacements so determined.

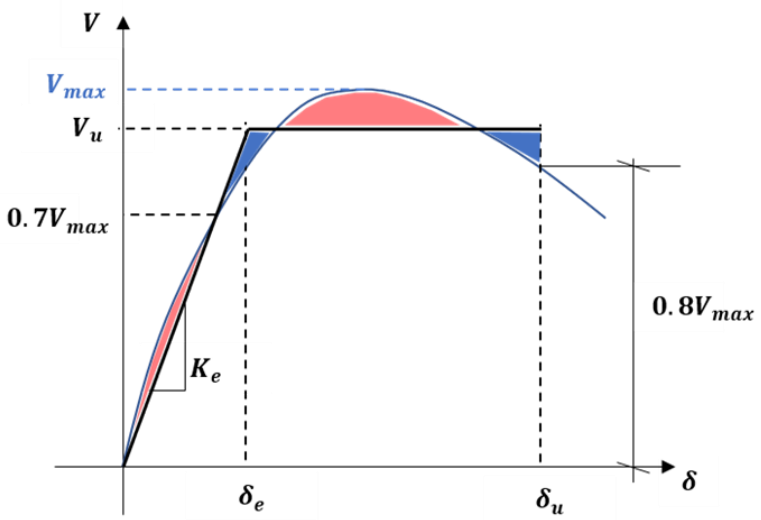

Figure 99: Bilinearization adopted for negative and positive cyclic direction.

For the Type A wall specimens, HC_116_A_15 exhibited a flexural/rocking behavior under lateral loading throughout the entire test. Given the relatively low compressive strength, which resulted in a maximum load of 174 kN, a flexural response was anticipated. Failure initiated at the base of the wall in the tension (pulling) direction during the fifth loading cycle, at a horizontal displacement of 3.54 mm, indicating a flexural mechanism and subsequent base rotation (Fig. 100a). From this point, the response transitioned into a nonlinear plastic behavior that was nearly symmetrical in both the pushing and pulling directions. In the following cycles, the wall experienced only minor damage until the eleventh cycle, when visible tensile cracking began to localize at the base (Fig. 100b). This occurred at a horizontal displacement of approximately 27 mm, accompanied by larger base rotations. By the start of the twelfth loading cycle, the final crack pattern had developed, characterized by shear cracks along the brick-mortar interfaces. These were attributed to the restriction of flexural movement imposed by the double-bending configuration (Fig. 100c).

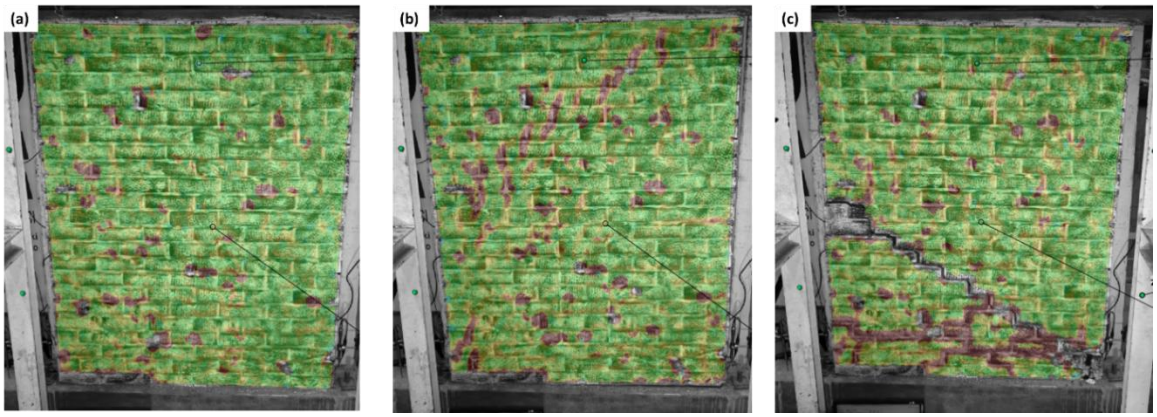

Figure 100: Initial crack at the base with consequent rocking movement **(a)**, concentration of cracks at the base **(b)**, and final crack pattern in correspondence of failure for masonry wall HC_116_A_15 **(c)**.

The masonry wall HC_116_A_30, constructed with mortar MIX-1, displays a diagonal shear failure response, as supposed due to the elevated pre-compressive load. This load, based on an assumed average compressive strength of 8.4 MPa for the masonry,

corresponded to 30% of the applied vertical load, totaling 347.01 kN. The first cracks appeared at the center of the panel during the top displacement cycle of 1.5 mm, consisting of small vertical and diagonal cracks (Fig. 101a). By the fourth cycle, as the response shifted from elastic to more plastic behavior, critical diagonal cracks formed, opening in the central area and extending diagonally toward the wall's edges (Fig. 101b). This trend continued in the following cycles, with further widening of the central and diagonal cracks. Fig. 101c shows the DIC crack displacements for the previous cycle before the failure of the panel.

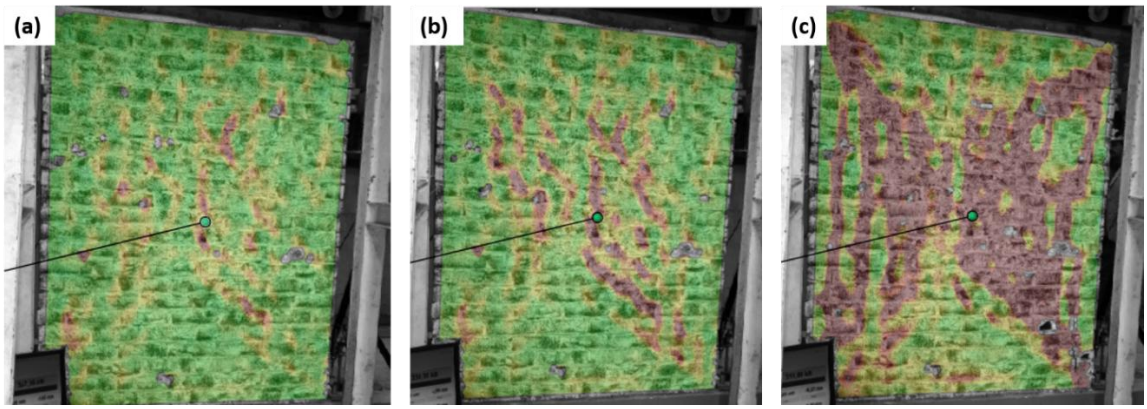

Figure 101: Initial crack formation **(a)**, development of cracks at the center of the panel **(b)**, and crack pattern one cycle prior to failure for masonry wall HC_116_A_30 **(c)**.

The masonry wall HC_129_A_15, built using mortar MIX-2, exhibited a flexural/rocking behavior similar to its counterpart constructed with mortar MIX-1 under the same percentage level of vertical loading. In this case, the pre-compressive load was 143 kN, reflecting the lower compressive strength of MIX-2. The response of the wall remained within the elastic range up to the fifth loading cycle, corresponding to a horizontal displacement of approximately 3.5 mm (Fig. 102a). With further loading cycles, increased base rotations were observed, accompanied by only minor damage to the wall (Fig. 102b). Fig. 102c shows the DIC visualization of the final crack development, which, like in the MIX-1 counterpart, consists of a diagonal crack propagating along the mortar–brick bed head joints.

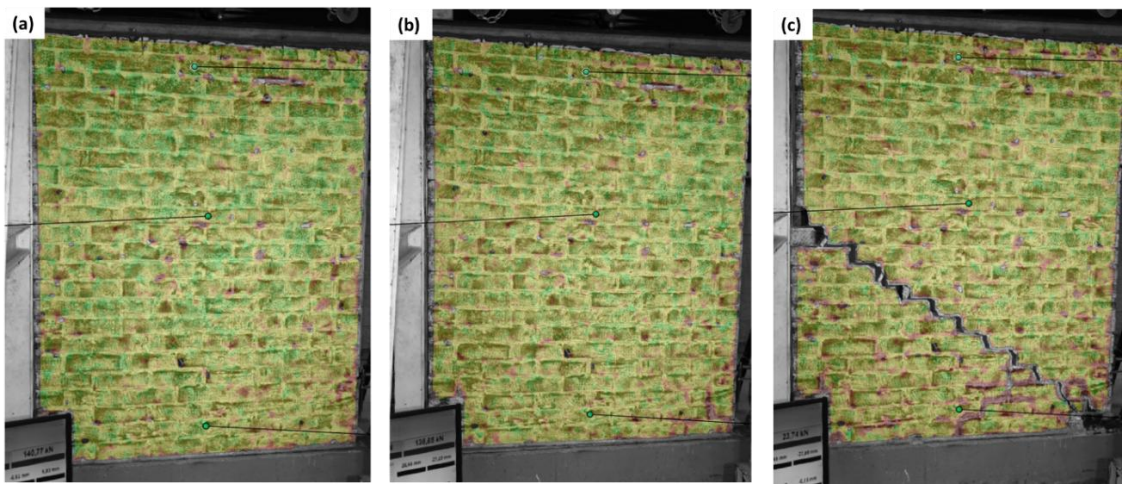

Figure 102 Initial crack at the base with consequent rocking movement **(a)**, minor crack development after rocking movement **(b)**, and **(c)** failure crack pattern for masonry wall HC_129_A_15.

For masonry wall HC_129_A_30 made with mortar MIX-2 a compressive strength of 6.9 MPa resulted in an applied vertical load of 285.04 kN. The first visible cracks on the panel appeared at the peak load of the third cycle, corresponding to a displacement of 2.05 mm and a peak load of 68.34 kN (Fig. 103a). In the following 4th cycle, cracks also developed on the opposite base of the wall, showing horizontal and vertical cracks due to the opposing tensile and compressive stresses at the opposite base of the wall (Fig. 103b). The crack pattern then developed with concentration of diagonal cracks in both positive and negative peak lateral displacements where the Fig. 103c shows the crack concentration in the wall in the previous negative peak cycle before failure at 12.42 mm and 86.88 kN.

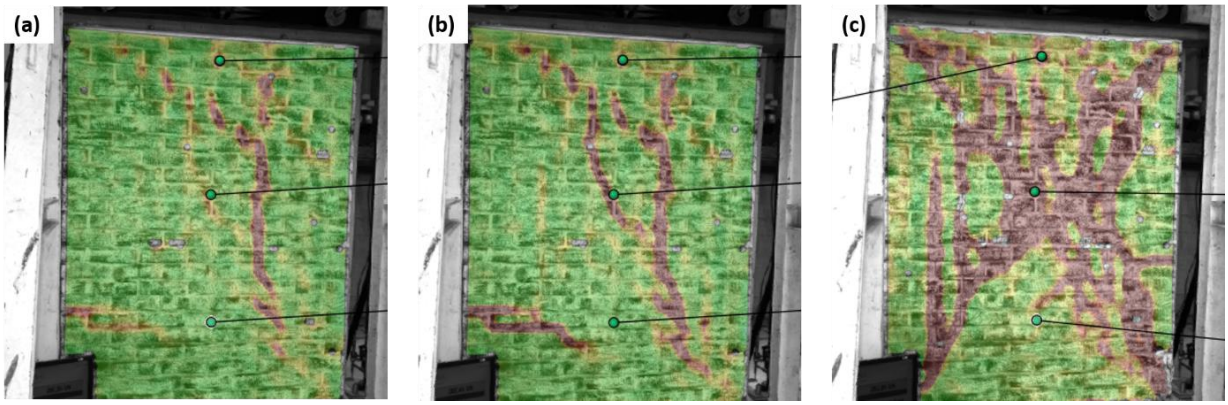

Figure 103: Initial crack formation **(a)**, development of cracks at the base due to corner tension **(b)**, and **(c)** crack pattern one cycle prior to failure for masonry wall HC_129_A_30.

The experimental cyclic responses, expressed in terms of horizontal load versus displacement hysteresis loops, are presented in Fig. 104a-d. These figures also include the corresponding backbone curves derived from the experimental data, along with the linearization approach adopted to characterize the global lateral behavior of the walls. Furthermore, Fig. 105a-d shows the evolution of the secant stiffness throughout the cyclic loading history, highlighting the progressive stiffness degradation with increasing displacement amplitudes. In addition, Fig. 106a-d illustrates the equivalent viscous damping values calculated for each cycle, providing insights into the energy dissipation capacity of the walls under repeated loading. Together, these results offer a comprehensive overview of the cyclic performance of the tested masonry specimens.

Among the Type B masonry walls, HC_116_B_15 is the only specimen of this size that exhibits a mixed failure mode, combining diagonal shear and rocking behavior. Initially, the wall displays a shear-dominated response up to the seventh cycle, corresponding to a horizontal displacement of 5.18 mm, with no significant visible damage (Fig. 107a). During this cycle, under a lateral pulling (negative) load of 109.21 kN and a displacement of 3.03 mm, a reduction in base shear becomes apparent. From this point onward, the response transitions toward a flexural/rocking mechanism, marked by the formation of new cracks at the base due to tensile stresses, particularly at a lateral displacement of 10.12 mm (Fig. 107b). Final failure occurs in the eleventh cycle, with diagonal cracking forming in both the pushing and pulling directions (Fig. 107c).

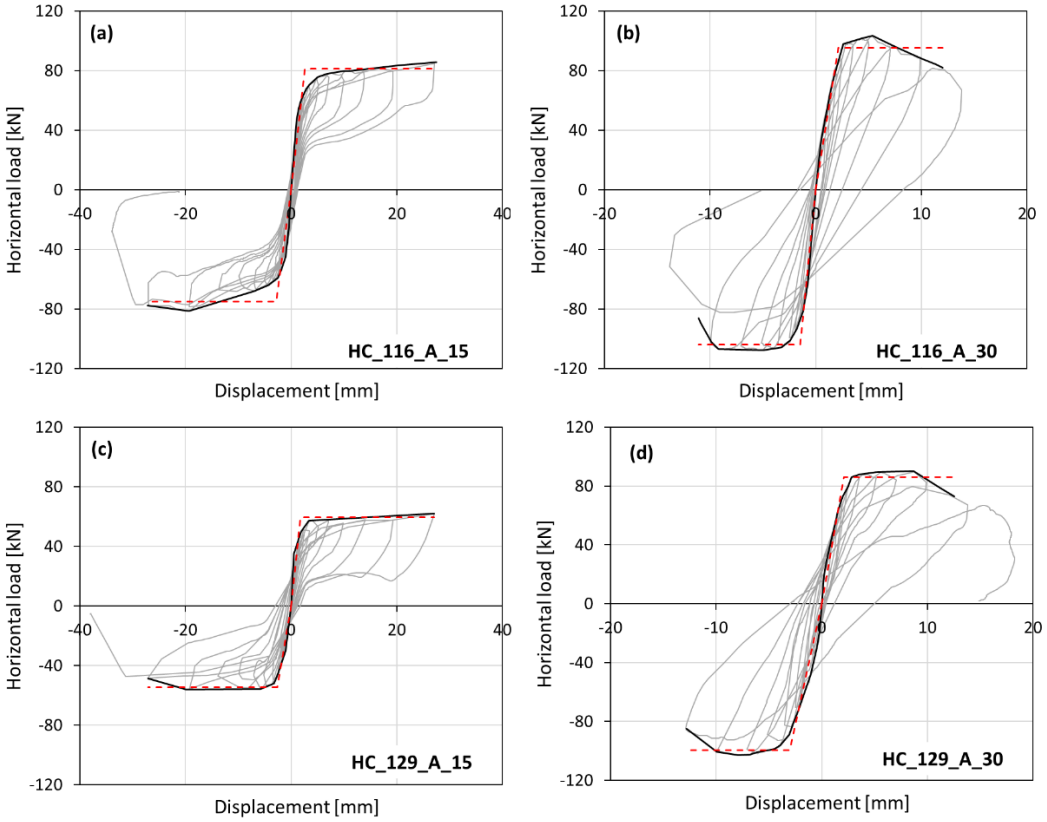

Figure 104: Experimental cycles (gray), backbone (black) and bilinear curve (red) for **(a)** HC_116_A_15, **(b)** HC_116_A_30, **(c)** HC_129_A_15 and **(d)** HC_116_A_30.

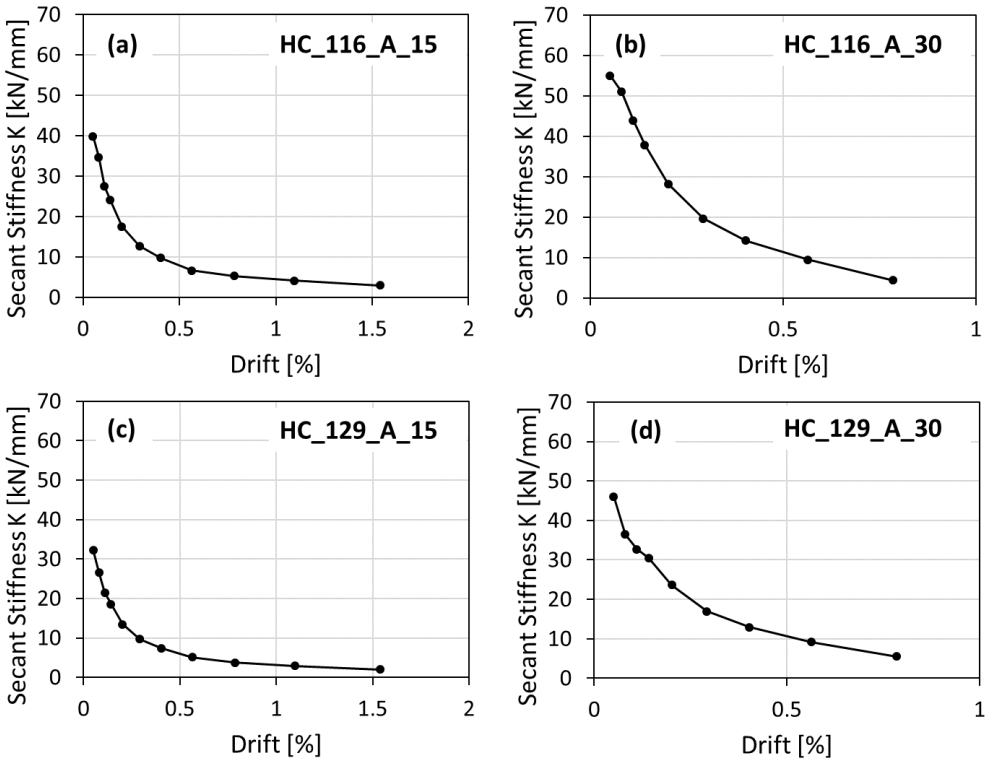

Figure 105: Secant stiffness decay vs drift for **(a)** HC_116_A_15, **(b)** HC_116_A_30, **(c)** HC_129_A_15 and **(d)** HC_116_A_30.

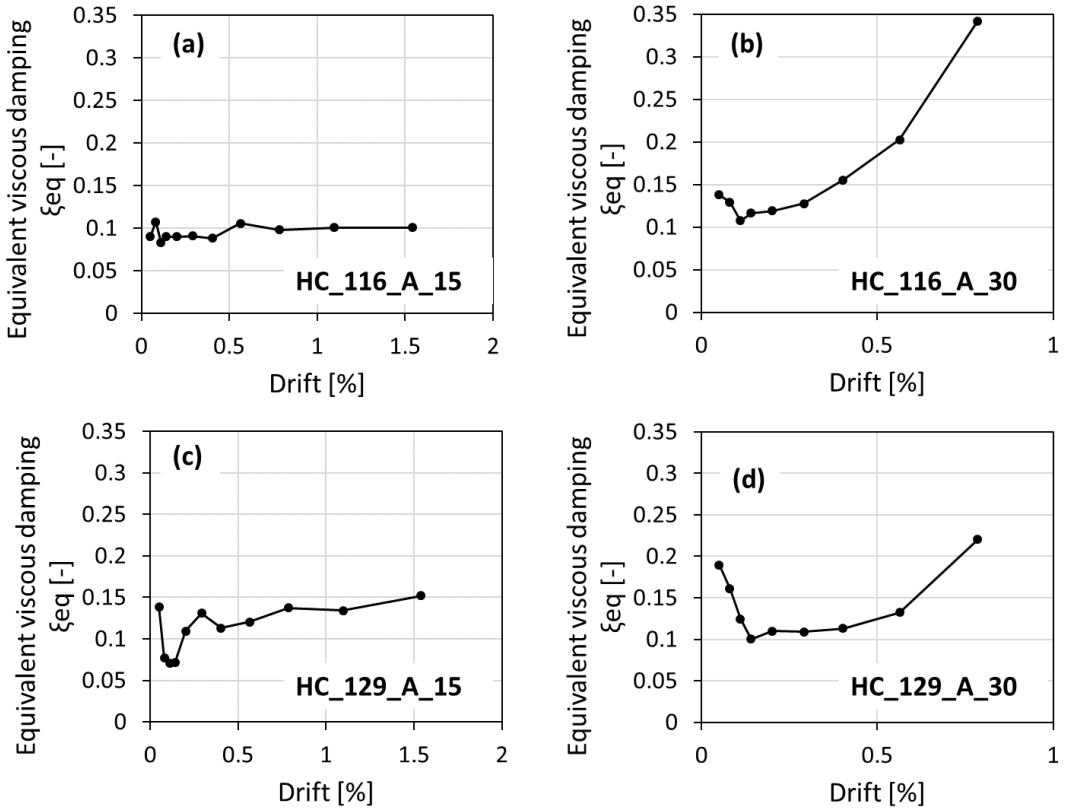

Figure 106: Equivalent viscous damping vs drift for **(a)** HC_116_A_15, **(b)** HC_116_A_30, **(c)** HC_129_A_15 and **(d)** HC_116_A_30.

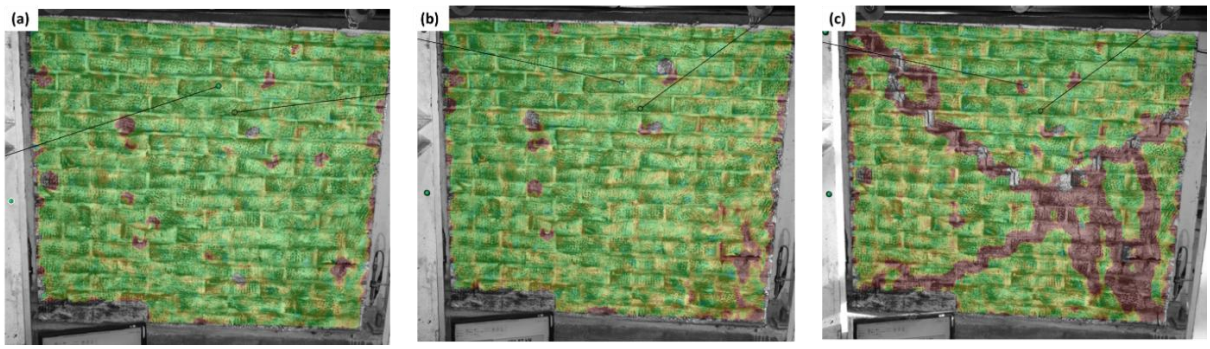

Figure 107: Initial shear response with limited damage **(a)**, reduction in base shear due to rocking and concentration of cracks at the corner **(b)**, and **(c)** crack pattern in correspondence of the failure for masonry wall HC_116_B_15.

HC_116_B_30, as expected due to its high compressive strength and small slenderness ratio, exhibited a shear failure mode. Shear deformation began to manifest as early as the fifth cycle, with a peak displacement of 2.59 mm (Fig. 108a). At this point, the wall transitioned from the elastic to the plastic phase. By the seventh cycle, with a displacement of 5.19 mm and a peak load of 174.79 kN, a distinct crack pattern had developed, characterized by the formation of diagonal cracks (Fig. 108b). In the final cycle, with a displacement of 7.26 mm, the wall exhibited a decrease in peak base shear of over 15% in both pushing and pulling directions. This was accompanied by the widening of the diagonal cracks, which propagated through both mortar joints and brick units (Fig. 108c).

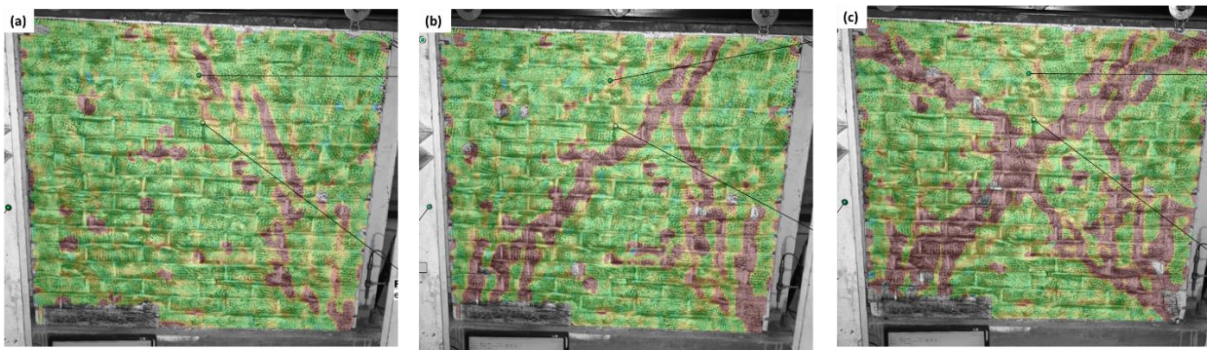

Figure 108: Initial crack formation **(a)**, development of diagonal cracking **(b)**, and **(c)** final crack pattern for masonry wall HC_116_B_30.

HC_129_B_15 exhibited a shear-dominated response. The first visible cracks appeared at the peak load of the fourth cycle, corresponding to a displacement of 1.94 mm and a peak load of 126.11 kN (Fig. 109a). By the eighth cycle, under a pulling displacement of 6.03 mm and a lateral load of 75.05 kN, diagonal cracks began to propagate from the previously formed cracks (Fig. 109b). At the ultimate displacement of the eighth cycle with 7.26 mm, the development of a clear diagonal cracking pattern was observed, with the reduction of the peak lateral load and increased dissipation (Fig. 109c).

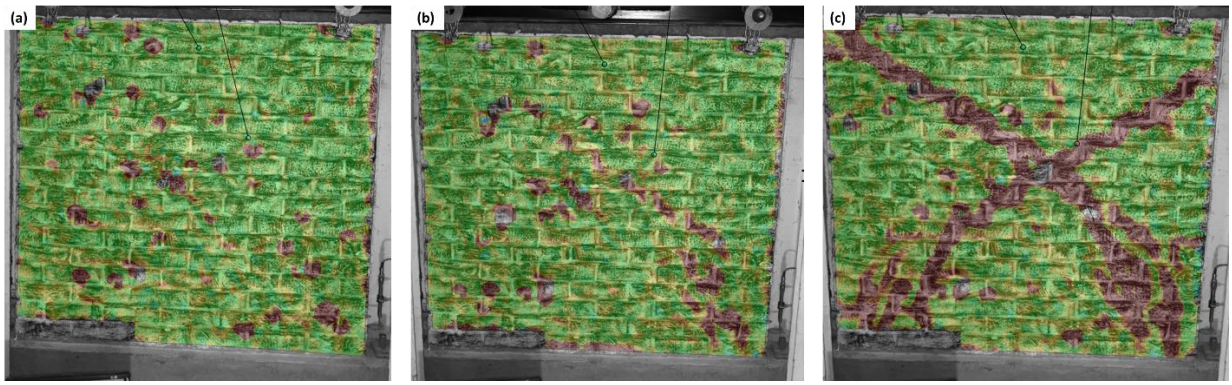

Figure 109: First visible crack formation **(a)**, propagation of previous cracking **(b)**, and **(c)** final diagonal cracking for masonry wall HC_129_B_15.

HC_129_B_30 also exhibits a shear failure mode, with diagonal cracks developing along the mortar and joints at the center of the panel. In the negative pulling direction, at the displacement of 2.60 mm and a base shear of 121.09 kN, the initial formation of a diagonal crack is observed (Fig. 110a). As the lateral load increases, at a positive pushing displacement of 3.56 mm and a lateral load of 123.19 kN, diagonal cracks form in both diagonal directions, intersecting at the center of the panel vertically due to high vertical loads (Fig. 110b). Fig. 110c shows the final crack pattern at the ninth cycle, where wall failure is evident due to both diagonal and vertical cracking system.

Similarly, for type B walls, the experimental cyclic responses, backbone curves, and corresponding linearized curves are plotted in Fig. 111a-d. These figures provide a detailed view of the hysteretic behavior, peak responses, and the adopted linearization approach for characterizing the global performance of the specimens. Additionally, the evolution of secant stiffness and equivalent viscous damping throughout the loading cycles, previously described,

is illustrated in Fig. 112a-d and Fig. 113a-d, respectively. The experimental peak loads and the corresponding displacements in both positive and negative loading directions are reported in Table 22, allowing for a comparative evaluation of the maximum capacities of the tested walls. Furthermore, Table 23 summarizes key parameters derived from the cyclic tests, including positive and negative initial elastic stiffness, linearized peak horizontal loads, elastic displacement limits, ultimate displacements, and calculated ductility values for all tested masonry specimens. These results contribute to a comprehensive understanding of the mechanical behavior and deformation capacity of type B walls under cyclic loading conditions.

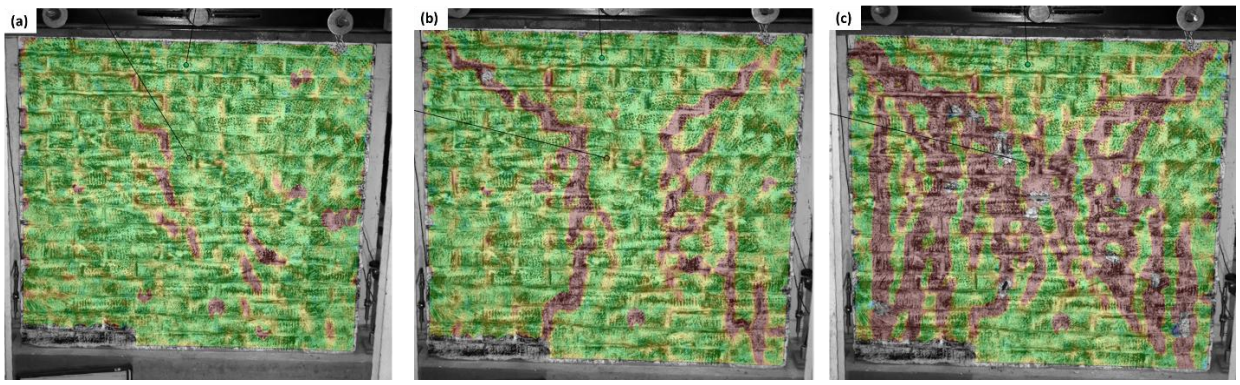

Figure 110: Initial crack formation **(a)**, development of shear/crushing cracks at the center of the panel **(b)**, and **(c)** crack pattern in correspondence of the failure for masonry wall HC_129_B_30.

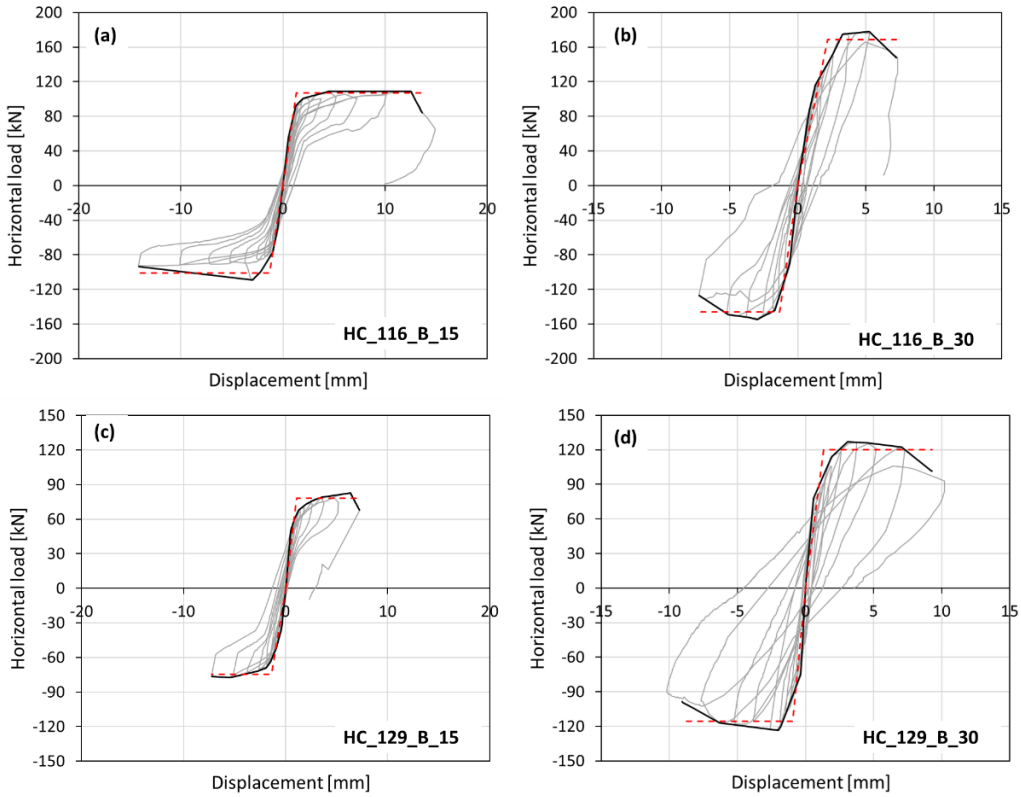

Figure 111: Experimental cycles (gray), backbone (black) and bilinear curve (red) for **(a)** HC_116_B_15, **(b)** HC_116_B_30, **(c)** HC_129_B_15 and **(d)** HC_116_B_30.

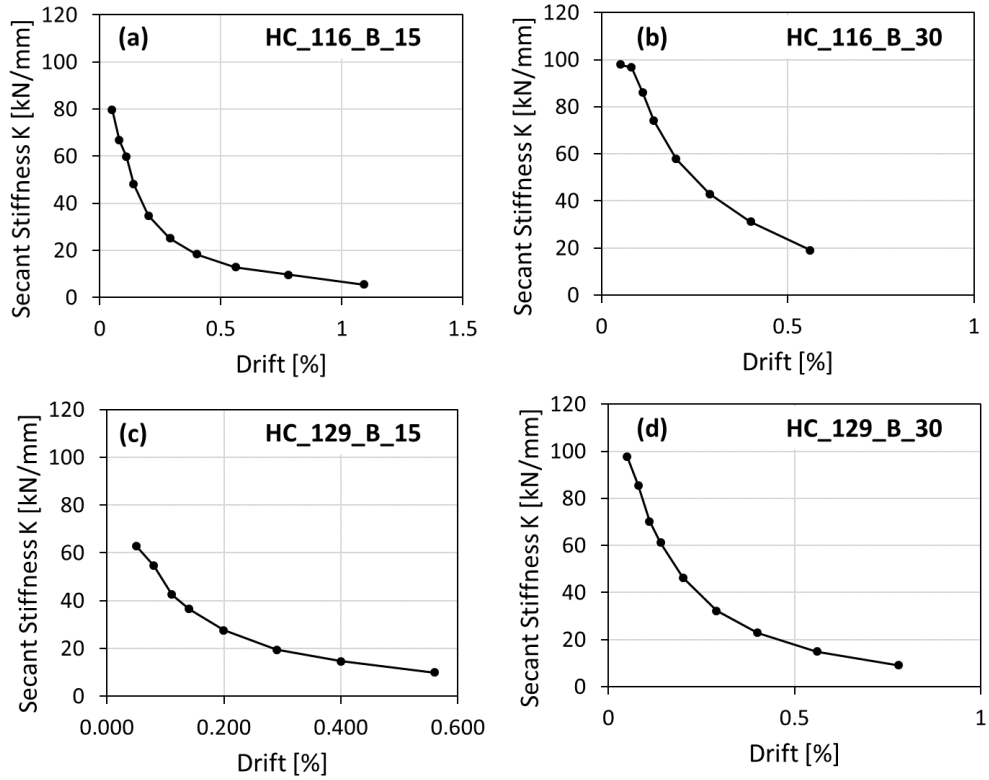

Figure 112: Secant stiffness decay vs drift for **(a)** HC_116_B_15, **(b)** HC_116_B_30, **(c)** HC_129_B_15 and **(d)** HC_116_B_30.

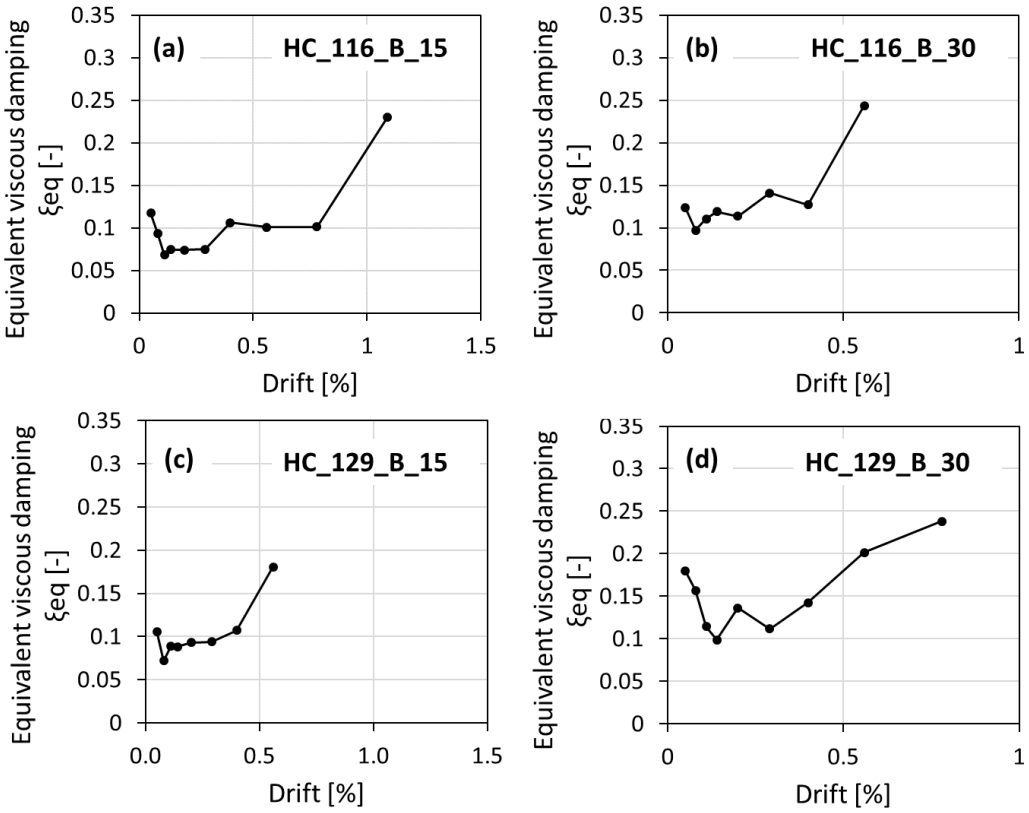

Figure 113: Equivalent viscous damping vs drift for **(a)** HC_116_B_15, **(b)** HC_116_B_30, **(c)** HC_129_B_15 and **(d)** HC_116_B_30.

Table 22: Peak positive/negative (+/-) lateral loads and corresponding displacements.

Samples	$V_{peak}^{(+)}$ [kN]	$\delta_{peak}^{(+)}$ [mm]	$V_{peak}^{(-)}$ [kN]	$\delta_{peak}^{(-)}$ [mm]
HC_116_A_15	84.76	27.08	-81.48	-19.32
HC_116_A_30	103.31	5.38	-107.54	-5.38
HC_129_A_15	62.00	27.08	-55.72	-19.29
HC_129_A_30	89.53	8.75	-103.13	-6.94
HC_116_B_15	109.09	11.65	-109.21	-3.02
HC_116_B_30	177.67	4.86	-154.72	-2.99
HC_129_B_15	82.85	6.36	-77.37	-5.46
HC_129_B_30	126.82	3.75	-123.32	-2.14

Table 23: Linearized quantities (Elastic modulus K_e, elastic displacement Δ_e, ultimate displacement Δ_u, lateral load V and ductility μ) for positive and negative direction.

Samples (load direction)	V [kN]	K_e [kN/mm]	Δ_e [mm]	Δ_u [mm]	μ [-]
HC_116_A_15(+)	81.11	31.50	2.57	27.50	10.68
HC_116_A_15(-)	75.25	25.93	2.90	27.24	9.39
HC_116_A_30(+)	95.40	45.06	2.12	12.03	5.68
HC_116_A_30(-)	103.94	71.69	1.45	11.11	7.66
HC_129_A_15(+)	59.53	33.71	1.77	27.08	15.34
HC_129_A_15(-)	54.65	20.98	2.61	27.08	10.39
HC_129_A_30(+)	86.23	41.45	2.08	12.53	6.02
HC_129_A_30(-)	99.45	32.62	3.05	12.82	4.21
HC_116_B_15(+)	106.96	81.78	1.31	13.51	10.33
HC_116_B_15(-)	101.14	76.45	1.32	14.13	10.68
HC_116_B_30(+)	168.73	77.50	2.18	7.26	3.33
HC_116_B_30(-)	146.37	110.73	1.32	7.26	5.49
HC_129_B_15(+)	77.91	71.71	1.09	7.26	6.68
HC_129_B_15(-)	74.86	53.48	1.40	7.26	5.19
HC_129_B_30(+)	120.23	90.04	1.34	9.29	6.96
HC_129_B_30(-)	115.70	121.16	0.95	9.08	9.50

3.4 Elaboration and analysis of the results

3.4.1 Mortar behavior

Different mortar mixes incorporating various proportions of air lime in the binder were subjected to mechanical testing, with the experimental findings presented in preceding sections. Full mechanical investigation of mortar is also furnished in the own Author contribution Zagaroli et al. [212]. For the mixes analyzed, the increment of lime in the binder generally leads to a decrease of the mechanical properties of approximately 50 % (Fig. 114). Regardless, the post-peak behavior of mortars indicates a benefit from the addition of lime, particularly in mortar MIX-2, which, possessing the highest lime content, demonstrates an ability to sustain wider deformations after reaching the peak. Kaushik et al. [101] and Lumantarna et al. [102] observed that the compressive strength of masonry prisms tends to increase alongside the compressive strength of bricks and mortars. However, this phenomenon holds true only when mortars are weaker than bricks. In this regard, employing

weaker mortars could be perceived positively in masonry construction compared to using strong cement mortars without lime.

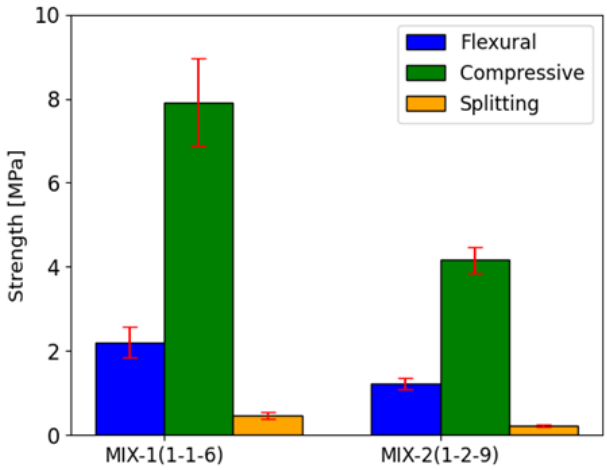

Figure 114: Comparisons strength of mortar mixes. From Zagaroli et al. [212].

The ratios of the average peak flexural strength (f_l), half prism compressive strength (f_c), and cylindric splitting tensile strength (f_t) are provided in Table 24 relative to the lime content in the binder composition (33.8% for MIX-1 and 50.5% for MIX-2 by mass). It is possible to notice how the ratio of the tensile to compressive strength remains constant between the mortars with values typical of masonry components. As the lime content in the binder increases, there is an observed rise in the flexural strength relative to the compressive and tensile strength. However, it is important to note that this trend should be viewed as indicative, and further investigations involving higher lime contents should be taken into account. From a code perspective point of view, these mortars can be classified as an M5 and a M2.5 almost reaching at 28 days the minimum compressive strength of 5 MPa. Effectively, according to the Eurocode 8 [159], the use of mortars with compressive strength inferior of 5 MPa is not recommend in seismic zone and always evaluated with suggestions based on the several national annexes. The compressive strength of mortars significantly depends on the type and granulometric distribution of the aggregates used in the mix. In this study, only one distribution was considered, whereas Lana et al. [48] demonstrated that modifying the granulometric distribution can substantially influence the compressive behavior of mortars.

Table 24: Mechanical parameters of masonry tested in compression.

Mixes	f_l/f_c [-]	f_t/f_c [-]	f_t/f_l [-]
MIX-1 (1:1:6)	0.28	0.06	0.21
MIX-2 (1:2:9)	0.30	0.06	0.19

Another finding from the experimental investigation at the mortar level is the ratio of cylindrical compressive strength to prism compressive strength, which averages 0.49 for MIX-1 and 0.45 for MIX-2 across the analyzed shapes. These values are notably low when compared to the shape factor analysis of concrete samples in cube and cylinder forms [231].

These differences are reconducted to the integration of soft plywood plates between the bases of cylinders during the testing after the rectification process.

The observed Poisson's ratios align with the values commonly reported in the literature for lime, cement, or blended mortars, falling within the range of 0.15 to 0.25 [49]. The same consideration can be done for the Elastic modulus showing respect to literature values from similar investigations [232]. Similarly, the open porosity values of the mortar are expected to align with those tested by Ramesh et al. [233], ranging from 27% to 24% for a volumetric mix ratio of 1:1:6 (cement:lime:sand) and from 27.4% to 25.8% for a volumetric mix ratio of 1:2:9. Concerning fracture energy, the values obtained using the RILEM approach are consistent with those obtained by Ramesh et al. [232]. In their study, Ramesh et al. [232] tested mortar mixes containing cement CEM I 42.5 R and air lime in identical proportions to those analyzed in this study, but with samples measuring 40 x 40 x 160 mm. In this scenario, the elevated fracture energy values noted in our research compared to the ones from Ramesh et al. [232] might be also associated with the specimen size issues of the 3-point bending test, already noted in several studies [234-236]. Moreover, larger beam dimensions result in a higher level of fracture energy due to the increased extent of crack development along the middle cross-section [237]. Naturally, due to the convenience of testing and handling in climatic chambers, several Authors [232,238] investigated fracture energy using small prisms with a modified RILEM formulation to achieve a more size-independent measurement [239]. Finally, the differences in fracture energy values obtained through various measurement methods, such as deflection and crack mouth opening displacement (CMOD), as suggested by different standards, indicate an average reduction of approximately 30% for both mixes when using the CMOD to calculate fracture energy.

3.4.2 Masonry specimen's behavior

Based on the results of the shear triplet tests, it is possible to characterize the Mohr-Coulomb criterion features for both mixes (Fig. 115). This criterion is defined by two parameters: cohesion or initial shear strength (c) and the angle of friction (ϕ). The latter parameter is commonly expressed in terms of its tangent ($\tan \phi$), representing the coefficient of friction, with the full expression of the Mohr-Coulomb criterion as $\tau = c + (\tan \phi)\, \sigma$. Employing linear regression on the experimental results of normal and shear stresses obtained, these values can be specifically determined for the two types of mortar analyzed (Table 25), where the R^2 values obtained are 0.96 and 0.97 for mortar type MIX-1 and type MIX-2, respectively, with reliability of the prediction. The cohesion values of the mortar with lower air lime content are higher compared to those of the mortar with higher lime content, aligning with the Eurocode 6 [13] interpretation of the tests. This indicates a relationship between the compressive strength and cohesion of the mortar, demonstrating an inverse proportionality. The intersection of the two criterions and the differences in the angle of frictions can be connected with the modification of the failure modes that were different for higher level of pre-compression for the mixes. In order to be clearer in terms of this parameter, additional tests using superior level of pre-compression to 1.0 MPa, not contemplated by actual standards, should be considered for understanding the real shape of the domain. It is

also worth mentioning that the tests conducted here were done at 28 days. However, given the carbonation process affecting these types of mortars, it is advisable to extend the testing period to observe the time-dependent evolution of the parameters in order to model more realistic scenarios.

Table 25: Mohr-Coulomb bond properties evaluated from the tests.

Mixes	c [MPa]	ϕ [-]	tan ϕ [-]
MIX-1 (116)	0.81	0.65	0.76
MIX-2 (129)	0.54	0.83	1.09

From a code perspective, the characteristic value of the initial shear strength can be obtained by multiplying for 0.8 the relative average value obtained from the tests. When considering both the characteristic values of initial shear strength and friction coefficient, it is evident that both mortars mixes analyzed meet the minimum recommended standard for the cohesion, to be assumed in absence of additional tests. Specifically, for our mortar strength class, which spans from 2.5 MPa to 9 MPa, this coefficient of friction remains at 0.2 MPa, significantly lower than the one derived from our testing. Although the materials and testing conditions in the present study were generally comparable to those reported in previous works [240], certain differences in experimental procedures may account for the higher cohesion and friction angle values observed. In particular, the cohesion values obtained in this study are approximately two to three times greater than those reported for triplets made with similar materials [240]. Minor variations in the testing protocol, such as the use of load control instead of displacement control, differences in loading rates, or variations in data acquisition procedures, can significantly influence the measured bond parameters. Additionally, meticulous specimen preparation and stricter quality control during the testing phase may have contributed to improved mortar-brick interface performance. Although these differences may appear subtle, they are known to significantly affect the mobilization of bond strength and frictional resistance in masonry interfaces.

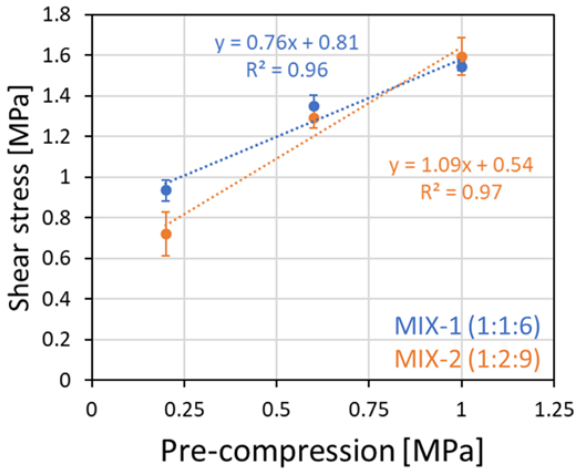

Figure 115: Coulomb-Mohr criterion in terms of shear-normal stress for mixes MIX-1 and MIX-2.

The compressive strength findings show the distinctions between masonry constructed with lime mortars and those with stronger mortars, a trend observed in numerous

prior studies [241, 101-102]. For a better visualization of the differences between the compressive stress-strain relationships, the average stress-stain results for both mixes are plotted together in Fig. 116. Increasing the air lime percentage in the mortar for masonry evidently reduces its compressive strength, yet simultaneously enhances the deformation capacity of the masonry. With a mean peak compressive stress of 8.40 MPa and 6.98 MPa for masonry comprising mortar MIX-1 and MIX-2 respectively, there is a noticeable reduction of 16.90 % in compressive strength. Conversely, the peak compressive strength is achieved at a peak axial deformation of 0.0041 and 0.0058 for masonry using mortar MIX-1 and MIX-2, indicating a 41.46 % increase in peak axial deformation for MIX-2 compared to MIX-1.

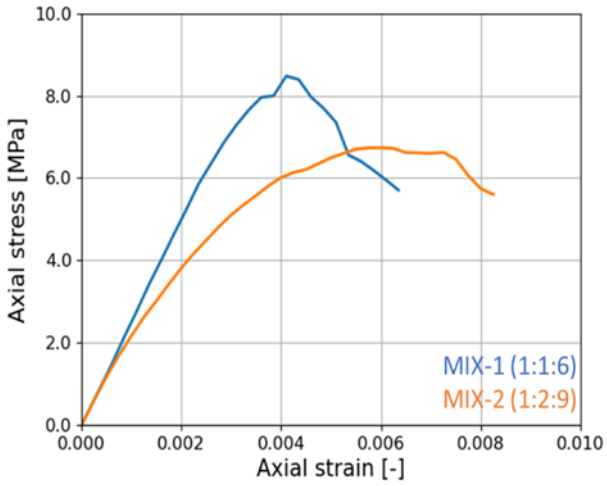

Figure 116: Average experimental compressive stress-strain comparison for masonry made of mortar MIX-1 and MIX-2.

At this stage, a 47% reduction in mortar compressive strength with increasing lime content (Table 10) corresponds to a 16.9% decrease in the relative masonry strength, as previously noted, which remains significantly lower than the reduction observed in the mortars. Similarly, Ramesh et al. [242] observed a comparable trend in the mechanical characterization of air lime-based masonry elements, reporting an approximate 11% increase in compressive strength when the binder composition changed from a 1:2:9 to a 1:1:6 ratio of cement, lime, and sand. To predict the compressive strength, power models are employed to estimate the experimental compressive strength of both mixes listed in Table 26, directly applying the regression formulation derived from their studies. Specifically, the Eurocode 6 [13] formulation is based on the characteristic values of the compressive strength that in this case, is calculated dividing the average compressive strength for 1.2 for both masonries, according to the relative standard for the compressive strength evaluation of masonry EN 1052-1 [97].

Eurocode 6 [13] formulation overestimate the characteristic peak compressive strength obtained from experimental test of about 10% for both types of masonries. The relationships found in the literature by Kaushik et al. [101] and Lumantarna et al. [102] represent two extremes regarding the experimental compressive strength obtained from our testing. The former underestimates by approximately half of the experimental value, while the latter overestimates by about 33% of the experimental value.

Table 26: Prediction of the peak compressive strength (*Characteristic value).

Mixes	Eq.	K	α	β	f [MPa] – pred.	f [MPa] – exp.	Diff [%]
MIX-1 (1:1: 6)	EC6 [13]	0.55	0.7	0.3	7.9	7.0*	-11.03
	Kaushik et al. [101]	0.63	0.42	0.32	4.2	8.4	102.26
	Lumantarna et al. [102]	0.75	0.75	0.31	12.7	8.4	-33.71
MIX-2 (1:2:9)	EC6 [13]	0.55	0.7	0.3	6.5	5.8*	-10.30
	Kaushik et al. [101]	0.63	0.42	0.32	3.4	6.98	104.07
	Lumantarna et al. [102]	0.75	0.75	0.31	10.4	6.98	-33.54

The relationship between the elastic modulus and the peak compressive strength, as outlined in Eurocode 6 [13], is assumed to be normalized to 1000 without specific details. For masonry constructed from MIX-1 and MIX-2, the ranges indicated in Fig. 117a-b are consistent with earlier studies, but not in line with the current standard prescriptions. Specifically, Segura et al. [243], through their study on the static and cyclic compressive response of brick masonry made with solid clay bricks and hydraulic lime-based mortar, found that the strengths measured experimentally were satisfactorily estimated by Eurocode 6 [13]. However, the stiffness obtained was significantly lower than the value proposed by the building code. Also, Drougkas et al. [244] highlighted discrepancies in evaluating the compressive strength and elastic modulus of six wallets with lime-based masonry. For masonry constructed with mortar MIX-1, the elastic modulus ranges from a minimum of 245 to a maximum of 363 times the compressive strength, averaging around 294 times the elastic modulus. In contrast, for masonry made with mortar MIX-2, these ranges extend from 233 to 430 times, averaging about 310 times the elastic modulus. There is a higher dispersion observed in the masonry with a higher lime content compared to those with lower lime content. Definitely, the difference between the recommended values from the code and the experimental results is primarily due to the high safety factors used in current masonry building codes for designing new structures in the elastic phase, which prescribe a higher stiffness.

For the diagonal compression test results, the comparison in terms of shear stress and shear strain on average is given in Fig. 118. Not relevant differences in the shear stiffness on average are evidenced. Considering the average values of the peak shear stresses for both masonry there is a reduction of the peak shear stress of 24.71% for masonry made of mortar MIX-2. In contrast to the compressive stress-strain curves, the peak shear deformation, representing the ultimate deformation due to the load control test setup, is about 30% lower for masonry composed of mortar MIX-2. Effectively, there is a notable absence of information regarding the post-peak behavior of these curves, which could be particularly relevant for assessing post-peak ductility in life safety checks. This information could modify the trend here observed for the pre-peak ductility, where the differences for the deformation capacity in terms of ratio between ultimate and elastic angular strain is very low between the two masonry types analyzed.

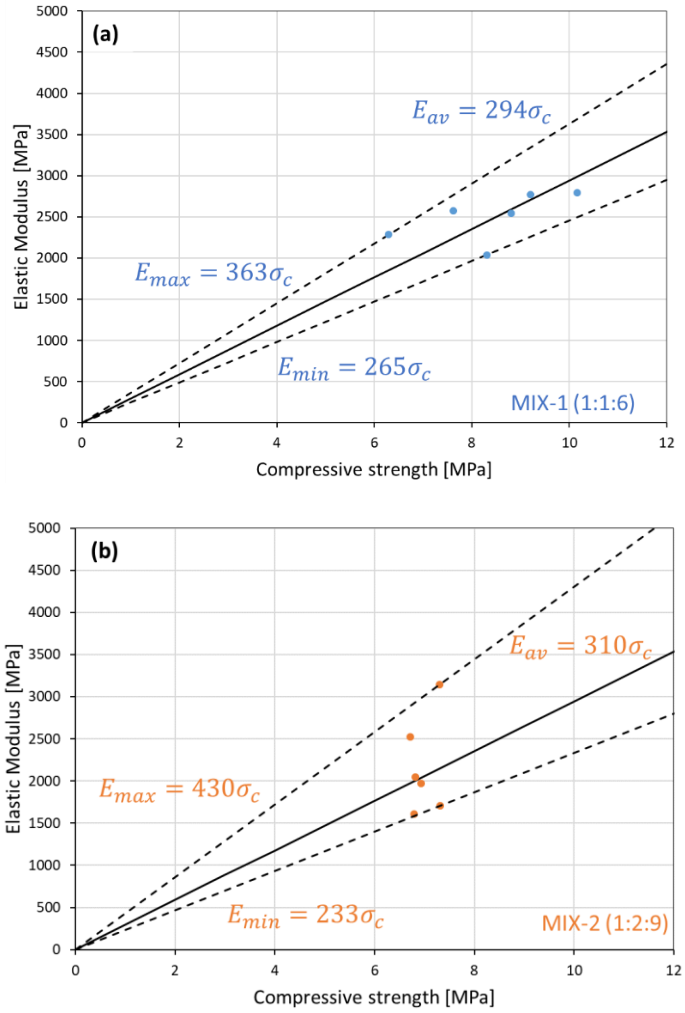

Figure 117: Elastic modulus versus compressive strength from experimental tests for masonry made of mortar MIX-1 **(a)** and MIX-2 **(b)** with relative minimum (E_{min}), maximum (E_{max}) and average (E_{av}) values.

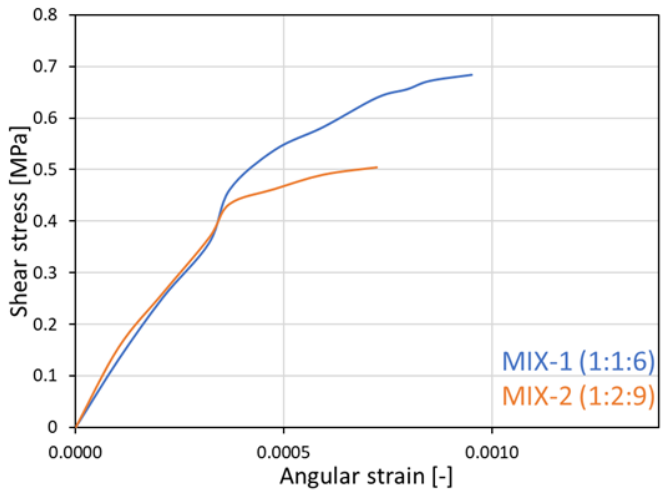

Figure 118: Average shear stress - shear strain relations for masonry made of mortar MIX-1 and MIX-2 in diagonal compression test.

3.4.2 URM walls under static vertical shearing

The comparison of the peak vertical load and mid-span deflection of masonry walls built using mortars MIX-1 and MIX-2 (labeled as 116 and 129, respectively), under two different load spacings (350 mm and 600 mm) is shown in Fig. 119a-b. As expected, masonry constructed with MIX-1 mortar (VS_116_350 and VS_116_600) generally sustains higher vertical loads. This is particularly evident at critical points, where MIX-2 masonry (VS_129_350 and VS_129_600) shows a reduction in vertical load of 9.75% and 26.69%, respectively. A similar trend is observed in terms of ultimate peak load, with reductions of 23.75% and 7.7% for VT_129_350 and VS_129_600, respectively.

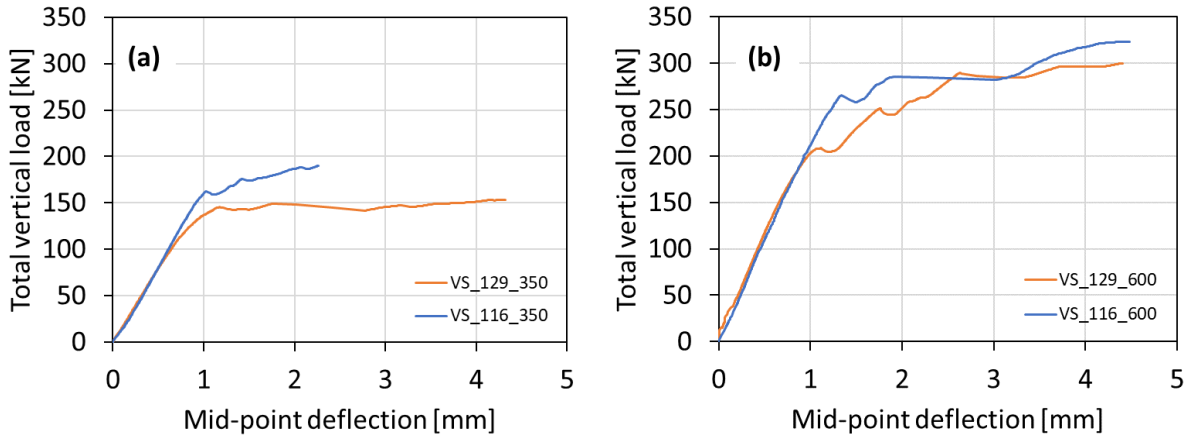

Figure 119: Total vertical load vs mid-displacement comparisons of MIX-1(116) and MIX-2(129) for the spacing of **(a)** 350 mm and of **(b)** 600 mm.

However, the displacement behavior reveals a different pattern. For tests with 350 mm load spacing (Fig. 119a), the MIX-2 masonry exhibits higher crack and ultimate displacements compared to MIX-1, with increases of 13.27% and 47.45%, respectively. Conversely, for the 600 mm load spacing (Fig. 119b), the MIX-2 specimens show lower crack and ultimate displacements, with decreases of 17.86% and 1.59%, respectively, compared to MIX-1.
When comparing different load spacings for the same wall material, walls with a 600 mm spacing demonstrate superior critical and ultimate load capacities. Specifically, for MIX-1, the increase from 350 mm to 600 mm spacing results in a rise of 40.03% in critical load and 41.24% in ultimate load. For MIX-2, the corresponding increases are 30.78% and 48.86%, respectively. The displacement behavior does not follow a clear trend. However, it is noteworthy that the critical displacements for the same materials under different loading conditions are quite similar, showing a difference of approximately 26% for MIX-1 and only 1% for MIX-2.

A similar pattern can be noticed in the shear strength and angular deformations evaluated for the different sides of the walls for both masonry types (Fig. 120a-b). Specifically, the shear strength, calculated as a ratio of the peak load to the cross-section area, is used here only for comparative purposes in simplified assumption. Indeed, this approach does not consider the distribution along a rectangular cross-section as parabolic with a maximum, rather than constant, as would be suggested by simply dividing the peak load by the

rectangular area. In this sense the variation of the shear stress, derived from the external load applied are the same previously analyzed.

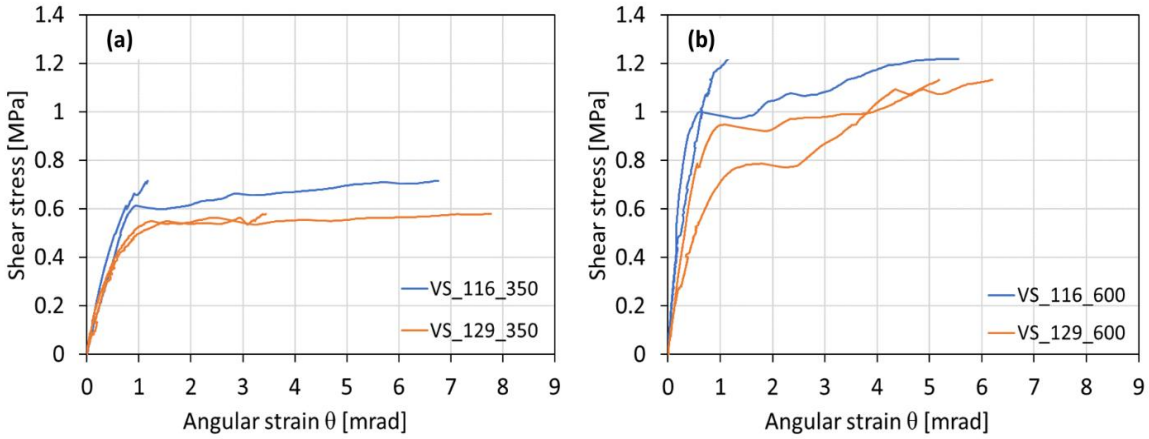

Figure 120: Shear stress vs angular strain comparisons of MIX-1(116) and MIX-2(129) for the spacing of **(a)** 350 mm and of **(b)** 600 mm.

In contrast to the behavior observed in vertical displacements, the angular strains at the critical point are consistently higher for walls constructed with MIX-2 mortar across both load spacing conditions (Fig 120a-b). Averaging the values from both sides, the critical angular strain for MIX-2 (129) exceeds that of MIX-1 (116) by 34.36% in the 350 mm spacing case. For the 600 mm spacing, this difference increases to 46.93%. A similar trend is observed in the ultimate angular strains, with MIX-2 showing increases of 29.39% and 41.0% for the 350 mm and 600 mm spacings, respectively. This behavior is likely due to the fact that MIX-1 (116) wall specimens exhibited limited damage on one side (Fig. 74 and Fig. 79), resulting in less uniform deformation and crack development primarily concentrated on a single face. Additional testing is recommended to further investigate this phenomenon. In this sense, it can be concluded that masonry with more air lime content in the binder allow for a better redistribution of the deformation within the walls and a potentially beneficial aspect for seismic resilience, although at the cost of reduced strength.

Considering the effect of load spacing on the same wall materials, MIX-1 shows higher angular strain values, both at the critical and ultimate stages, when the load spacing is 350 mm. Specifically, there is a reduction of 40.5% in critical angular strain and 18.0% in ultimate angular strain when increasing the spacing from 350 mm to 600 mm. A similar trend is observed for MIX-2 at the critical stage, with a 13.56% reduction. However, the ultimate angular strain for MIX-2 behaves differently, showing a slight increase of 1.40% with the larger 600 mm spacing.

Fig. 121a-b illustrate the variation of shear stiffness G as a function of shear stress τ for masonry walls constructed with mortars MIX-1 and MIX-2, under two different load spacing conditions (350 mm and 600 mm, respectively). In both cases, the stiffness-shear stress relationship displays a nonlinear decreasing trend, indicative of progressive damage and stiffness degradation under increasing shear loads. A consistent observation across both load configurations is the superior transversal stiffness of walls made with MIX-1 mortar (VS_116),

which maintain significantly higher stiffness values throughout the loading range when compared to MIX-2 specimens (VS_129). This indicates a higher resistance to shear-induced deformation for MIX-1 masonry. Notably, the difference in stiffness between the two mortar types becomes even more pronounced under the 600 mm spacing condition, where the initial and residual stiffness of MIX-1 walls exceeds that of MIX-2 by a substantial margin. These results confirm the enhanced mechanical performance of MIX-1 mortar, independent of the load application scheme.

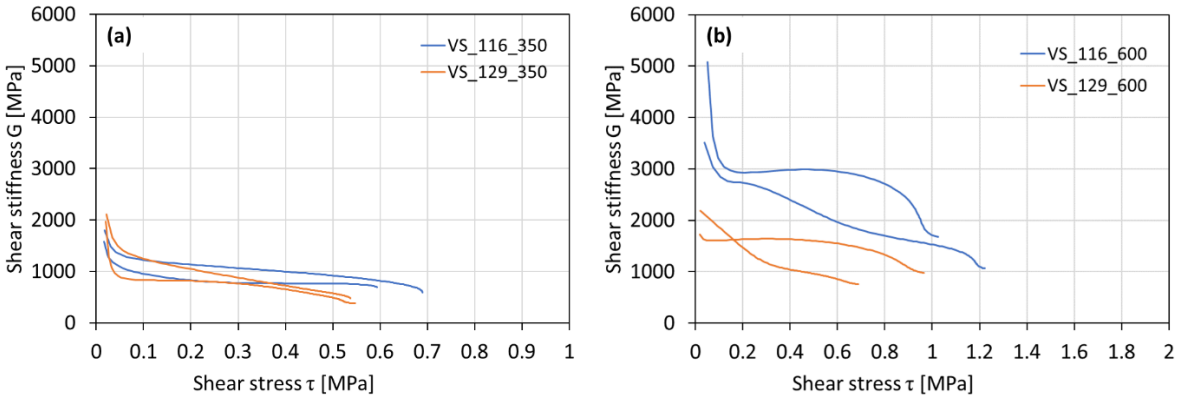

Figure 121: Shear stiffness vs shear stress comparisons of MIX-1(116) and MIX-2(129) for the spacing of **(a)** 350 mm and of **(b)** 600 mm.

In Table 27 is shown a comparative analysis between the critical shear stresses (τ_{cr}) obtained from the VS test series with 350 mm and 600 mm of load spacing and the maximum shear stresses (τ_{max}) from the DCT test series, specifically referring to materials 116 (MIX-1) and 129 (MIX-2).

Table 27: Comparison between critical shear stresses (τ_{cr}) from VS tests and maximum shear stresses (τ_{max}) from DCT tests for materials 116 (MIX-1) and 129 (MIX-2), including the τ_{cr}/τ_{max} ratio.

Test	τ_{cr} [MPa]	Test	τ_{max} [MPa]	τ_{cr}/τ_{max} [-]
VS_116_350	0.6	MIX-1_DCT	0.68	0.88
VS_116_600	1.0	MIX-1_DCT	0.68	1.47
VS_129_350	0.54	MIX-2_DCT	0.51	1.06
VS_129_600	0.79	MIX-2_DCT	0.51	1.55

It is evident that the ratio τ_{cr}/τ_{max} ranges approximately between 0.88 and 1.55, with increasing ratio corresponding to the superior load spacing. This suggests that the vertical shear tests conducted in this study tend to yield higher shear stress values at the onset of cracking compared to those observed in diagonal compression test configurations. This outcome is not unexpected, as the diagonal compression test induces a combined state of shear and diagonal tension, often leading to premature cracking governed by the tensile strength of the masonry. In contrast, the vertical shear test produces a more uniform shear stress distribution without significant tensile components, which delays crack initiation and allows for a higher load-bearing capacity prior to failure. Additionally, the ratio corresponding to the material MIX-2 (129) are superior to the ones of material MIX-1 (116) considering the respective load span application, this suggests that diagonal compression tests are more

sensitive to reductions in mortar strength with a superior reduction in tensile strength. In contrast, vertical shear tests, governed primarily by frictional and cohesive mechanisms along bed joints, exhibit a more stable response with inferior differences.

3.4.3 URM walls under horizontal cyclic loading

This section compares the experimental results of the lateral cyclic behavior of the tested walls. Initially, Fig. 122a-b illustrates the bilinear curves for both positive and negative loading directions, considering different masonry types and levels of pre-compression.
As previously reported in the literature [145], increasing the level of pre-compression enhances the peak shear strength while reducing the displacement capacity in both masonry types. Furthermore, walls with a lower aspect ratio tend to exhibit higher shear strength but lower displacement capacities.

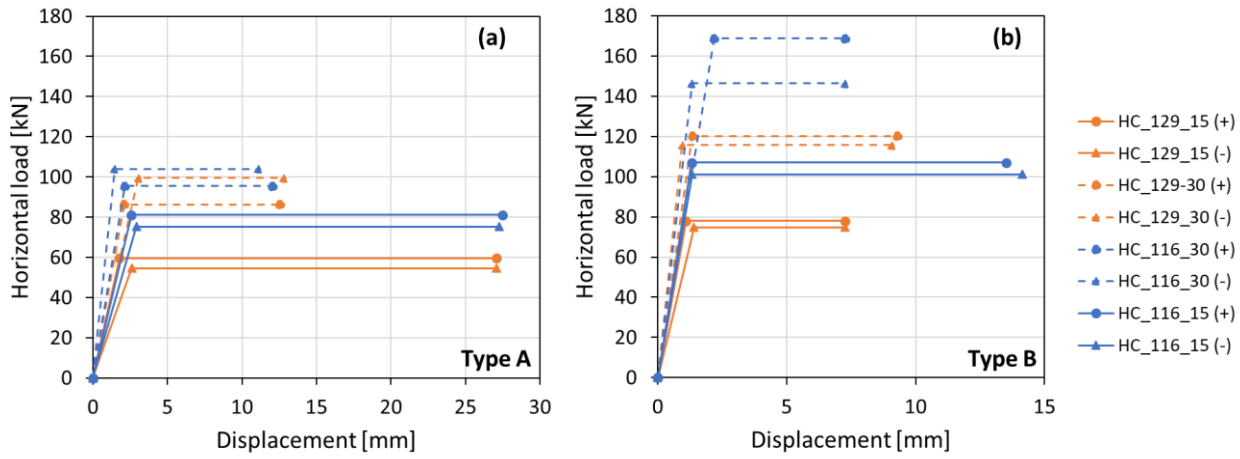

Figure 122: Bilinear curves positive (+) and negative (-) for masonry walls made of MIX-1(116) and MIX-2(129) for **(a)** type A and **(b)** type B walls.

For the type A higher masonry panels (Fig. 122a), considering the average response between positive and negative loading directions, the increase in base shear for masonry MIX-1 (116) and MIX-2 (129) from 15% to 30% pre-compression is 27.48% and 62.62%, respectively. Concurrently, this increase in pre-compression results in a reduction of ultimate displacement by 57.72% for MIX-1 (116) and 53.20% for MIX-2 (129). Similarly, the displacement trend mirrors the ductility trend, showing a reduction of 35% for masonry made of mortar MIX-1 and 60% for using of mortar type MIX-2.

A similar trend is observed in Fig. 122b, where base shear increases by approximately 50% for both MIX-1 and MIX-2 as pre-compression levels rise. While MIX-1 specimens (HC_116_15 and HC_116_30) follow the expected pattern, the MIX-2 specimens (HC_129_15 and HC_129_30) exhibit a 26.48% increase in ultimate displacement with higher pre-compression. This divergence from the general trend may be attributed to the shear-dominant failure mode observed in MIX-2 walls at both pre-compression levels, with no evidence of flexural failure. Additionally, the more distributed cracking pattern at higher pre-compression levels may have enhanced energy dissipation and deformation capacity. This

deviation is also reflected in the displacement ductility: MIX-1 shows a reduction of about 60% from HC_116_30 to HC_116_15, whereas MIX-2 shows an improvement of approximately 35% from HC_129_30 to HC_129_15.

From a material comparison standpoint, for type A piers (Fig. 122a), masonry MIX-1 (HC_116_15 and HC_116_30) demonstrates peak load increases of 36.94% and 7.35%, respectively, when compared to MIX-2 (HC_129_15 and HC_129_30) under the same pre-compression levels. Although the difference in ultimate displacement between HC_116_15 and HC_129_15 is minimal, at 30% pre-compression, the masonry with higher lime content (HC_129_30) exhibits a noticeably greater ultimate displacement of 9.55% compared to HC_116_30. However, the ductility trend reveals an opposite behavior. Specifically, at 15% pre-compression, HC_129_15 shows an increase in ductility of approximately 24% compared to the lower lime content masonry HC_116_15. Conversely, at 30% pre-compression, HC_116_30 exhibits about 30% higher ductility than HC_129_30.

Similar conclusions can be drawn for masonry type B (Fig. 122b). MIX-1 masonry (HC_116_15) exhibits a 36.21% higher peak load and nearly twice the ultimate displacement compared to MIX-2 (HC_129_15). Additionally, HC_116_15 shows nearly double the displacement ductility of HC_129_15. As seen with type A piers, the peak base shear for MIX-1 (HC_116_30) is 33.55% greater than that of MIX-2 (HC_129_30); however, this is accompanied by a 20.93% reduction in ultimate displacement. Interestingly, at 30% pre-compression, HC_129_30 demonstrates nearly twice the ductility of HC_116_30.

In terms of response differences between wall types, type B generally exhibits higher lateral load capacity approximately 30% greater than type A, for all masonry types under the same material and pre-compression conditions, with the exception of masonry HC_116_30. In this case, type B shows an increase of about 60% in peak load compared to its type A counterpart. While no consistent trend is observed for ultimate displacements and ductility, type B walls consistently exhibit lower ultimate displacement values than type A walls, as expected. Review bar charts of the average values of lateral shear strength, ultimate displacements and ductility from the different types are given in the Figs. 123-124-125.

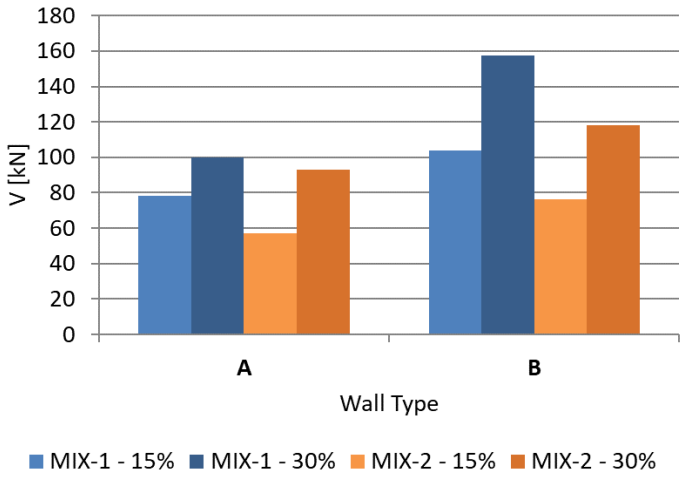

Figure 123: Comparison average positive/negative bilinear shear load V for all tested masonry.

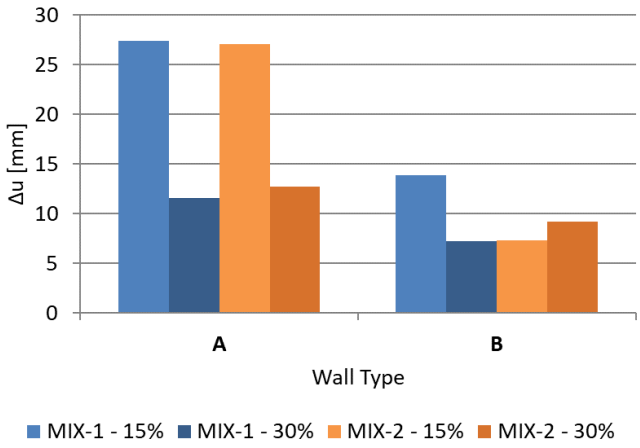

Figure 124: Comparison average positive/negative bilinear ultimate displacements *Δu* for all tested masonry.

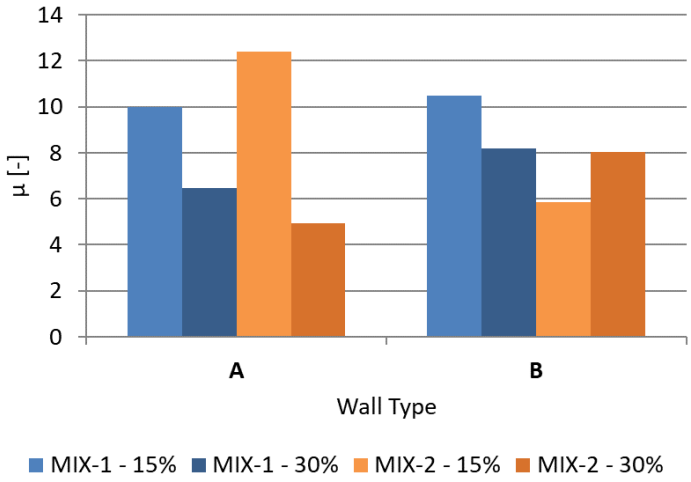

Figure 125: Comparison average positive/negative bilinear ductility μ for all tested masonry.

The comparative analysis of masonry MIX-1 (116) and MIX-2 (129) highlights distinct performance trends under lateral loading. MIX-1 demonstrates superior mechanical behavior, achieving higher peak loads and greater displacement capacity, particularly in Type B walls, indicating enhanced strength and ductility. However, MIX-2 shows a more symmetric and stable response between loading directions, which may be beneficial in seismic applications requiring cyclic stability. Despite this, its lower load capacity and reduced displacement limit its effectiveness compared to MIX-1. Overall, MIX-1 offers a more robust seismic performance, while MIX-2 provides a more controlled but less resistant response.

The variation of secant stiffness with drift for both Type A and Type B walls is illustrated in Fig. 126a-b. As expected, all configurations exhibit a progressive reduction in secant stiffness with increasing drift, reflecting the typical degradation of stiffness due to damage accumulation and crack propagation under lateral cyclic loading. A comparison between pre-compression levels shows that higher pre-compression (30%) results in increased initial stiffness for both masonry MIX-1 and MIX-2, confirming the role of axial loading in enhancing wall rigidity. However, despite this initial advantage, the stiffness degradation trend remains similar across all pre-compression levels, indicating that higher axial load does not significantly delay the loss of stiffness at large drift demands.

A distinct difference is observed between the two masonry mixes. Walls constructed with masonry MIX-1 (HC_116_15 and HC_116_30) generally display higher secant stiffness than their MIX-2 counterparts, particularly in Type B configurations (Fig. 126b). This behavior suggests superior mechanical performance of MIX-1, likely due to differences in material composition or bonding quality. Additionally, Type B walls consistently show greater secant stiffness than Type A walls under the same material and loading conditions, with a particularly notable increase for the HC_116_30 configuration, where stiffness in Type B exceeds that of Type A by approximately 60%. This enhanced stiffness in Type B walls may be attributed to their geometry or boundary conditions, which provide better lateral resistance and stiffness retention throughout the loading process.

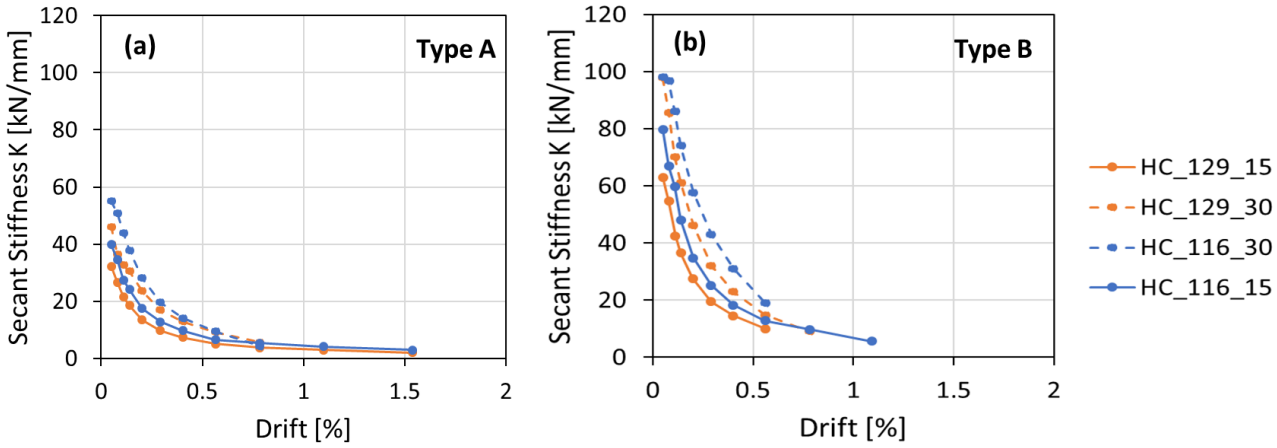

Figure 126: Secant stiffness decay vs drift for masonry walls made of MIX-1(116) and MIX-2(129) for **(a)** type A and **(b)** type B walls.

The Fig. 127a-b illustrates the relationship between equivalent viscous damping ξ_{eq} and drift percentage for various conditions represented by HC_129_15, HC_129_30, HC_116_15, and HC_116_30.

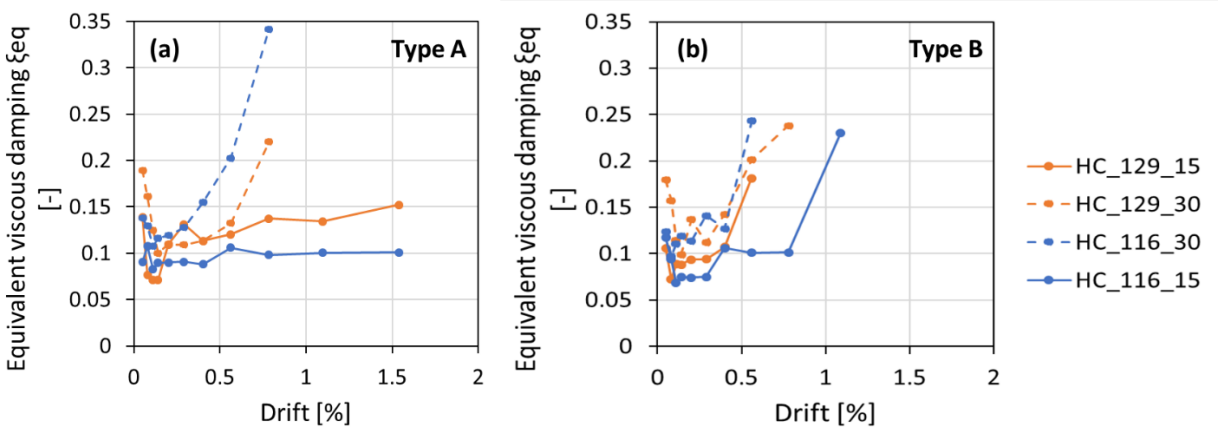

Figure 127: Equivalent viscous damping vs drift for masonry walls made of MIX-1(116) and MIX-2(129) for **(a)** type A and **(b)** type B walls.

In Type A walls (Fig. 127a), the equivalent viscous damping for both HC_129_15 and HC_116_15 slowly increases as the drift percentage rises. However, the rate of increase varies

between the two conditions. HC_129_15 experiences a significant rise in damping at higher drift percentages, particularly beyond 1%, while HC_116_15 shows a more gradual increase. For walls subjected to 30% pre-compressive loads, the increase in damping with lateral drift is even more pronounced.

In Type B (Fig. 127b), a similar upward trend in damping with increasing drift is observed. HC_129_15 shows a noticeable increase in damping as the drift percentage exceeds around 0.2%, with a sharp rise especially after 0.3%. The damping for HC_129_30 follows a similar trend but with a more gradual increase compared to HC_129_15. HC_116_15 and HC_116_30 exhibits both an increase in damping but with abrupt increase when the drift exceeds 0.3%.

As noted by Magenes and Calvi [148], dissipated energy increases with damage and is linked to the failure mechanism. Notably, all walls that exhibited diagonal shear crack failure (HC_116_30 and HC_129_30, both in Type A and B) by the end of testing showed damping values exceeding 20%, which aligns with similar investigations [154] and indicates a clear increase in viscous damping. In contrast, masonry walls that experienced flexural failure mode (HC_116_15_A and HC_129_15_A) maintained nearly constant viscous damping throughout the testing cycles. HC_116_15_B, for example, shows a mixed behavior, with damping remaining almost constant but following a stepped function pattern.

Although MIX-2 shows a significant reduction in compressive strength (approximately 47%) compared to MIX-1, the masonry made with MIX-1 experiences a reduction of only around 25%, with a minimum decrease of just 6% when compared to MIX-2. This suggests that despite the notable decrease in compressive strength of the mortar, the impact on lateral load-bearing capacity is relatively modest (Table 28). This observation warrants further investigation, as it implies that using mortars with a higher lime content in the binder may still be a viable option, considering the relatively smaller reduction in lateral load-bearing capacity compared to the more significant drop in compressive strength. Ramesh et al. [245] observed, after testing nine masonry walls with varying air lime contents in the mortar, that the inclusion of lime moderately enhances drift capacity and ductility as for part of our testing series. Furthermore, a mix with a volumetric proportion of 1:1:6 of (cement:lime:sand) demonstrated the highest lateral capacity compared to a cement-only mix with a 1:5 proportion relative to the aggregate. Anyway, these considerations should stem for the testing of other walls with different boundary conditions, involving different failure mechanisms and the modification of other parameters.

Table 28: Difference in mortar and lateral base shear strength for masonry walls made with difference mixes.

	MIX-1 (1:1:6)	**MIX-2 (1:2:9)**	**Diff. [%]**
Mortar compressive strength	7.91	4.16	-47.41
Base shear HC_15_A	78.18	57.09	-26.98
Base shear HC_30_A	99.67	92.84	-6.85
Base shear HC_15_B	104.05	76.39	-26.59
Base shear HC_30_B	157.55	117.96	-25.13

CHAPTER 4 - NUMERICAL SIMULATIONS

4.1 Adopted numerical strategy

The experimental tests discussed in the previous section regarding the walls subjected to increasing vertical load on deflecting members and cyclic in-plane lateral shear force are taken into consideration for fem modelling. Specifically, one modeling approach is considered hereafter in the context of macro modelling, aimed at achieving global structural results with limited mechanical information and analysis time. The primary objective of the numerical analysis outlined in this section is to assess the shear base-displacement curve in lateral cyclic testing, the vertical load-mid deflection in vertical testing, and the associated failure modes. This evaluation will be conducted utilizing a macro-mechanical total strain crack modeling approach.

Regarding the mechanical properties analyzed, the values from experimentation of compressive and diagonal compressive tests on wallettes are used as input for describing the response of the larger scale tests. The parameters of the properties that have not been determined directly from the previous experimentation i.e. masonry compressive and tensile fracture energies are first deducted by the recommendations available in Lourenco and Gaetani [246] and then parametrically adjusted for a reasonable fitting with the experimental results from the wallettes. In particular, this final stage necessitated macro-modeling of compressive and diagonal compressive tests, a process typically conducted using simplified or detailed micro-modeling approaches based on experimental data from mortar, bricks, and interfaces. However, in this instance, the primary aim is only to reasonably calibrate the total strain crack models for larger scale tests and visualize its response in relation to experimental tests. A description of these models is given subsequently. A review of the final mechanical parameters is given in Table 29.

Table 29: Parameters for the TSC model adopted.

Parameters	MIX-1 (1:1:6)	MIX-2 (1:2:9)
Compressive strength [MPa]	8.4	6.9
Elastic modulus [MPa]	2500	2170
Poisson's ratio	0.19	0.21
Comp. fracture energy [N/m]	11700	13200
Tensile strength [MPa]	0.42	0.28
Tensile fracture energy [N/m]	10	20

For the compressive tests of both masonry types (made of mortar MIX-1 and MIX-2), a finite element model with plane stress shell elements of 4 nodes is chosen with a final mesh size of dimensions 14.5 x 11.95 mm. No interfaces in correspondence of the top and bottom of the wall is introduced. The boundary conditions tried to reproduce the real conditions of the experimental tests where from the crack patters is possible to notice a certain confinement effect of the platens. As a result, the vertical and horizontal displacements at the bottom, as well as the horizontal displacements at the top of the walls, were fixed. The load is applied at the top in terms of displacements applying a displacement control integrator with

regular Newton–Raphson method for equilibrium iteration. Convergence criteria based on energy is selected with 10^{-3} tolerance. Naturally, imposed displacements were scaled during the analysis to comply with the complexity of the analysis in particular way in correspondence of softening phase, keeping anyway a control of the number of the iteration to convergence always inferior to 100. An image of the model is given in Fig. 128.

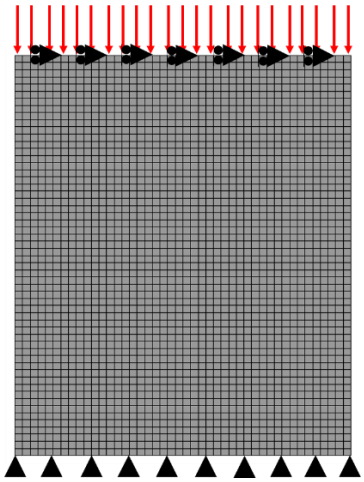

Figure 128: Macro-mechanical fem model for the compressive test adopted for both masonry types.

Based on the mechanical parameters of Table 29, the comparison of the experimental minimum and maximum with the results of the models for both masonry types is shown in Fig. 129a-b. The results showed a good alignment with those obtained for masonry composed of mortar MIX-2 and MIX-1, although there was a variation in the post-peak behavior observed in the latter type of masonry with more ductility for the model compared to the tests.

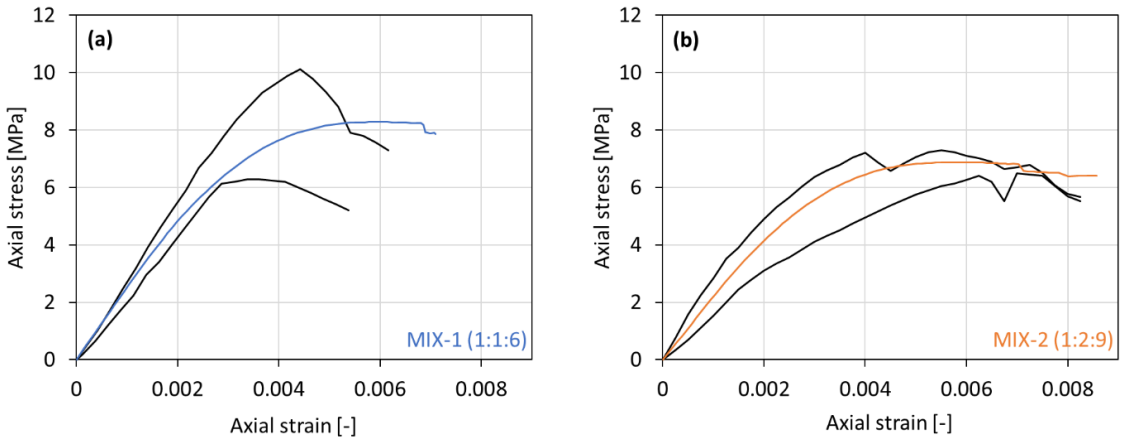

Figure 129: Comparison of uniaxial compression stress-strain curves for masonry made of MIX-1 **(a)** and MIX-2 **(b)**, showing experimental data (black lines) at minimum and maximum values alongside numerical results (blue line for MIX-1 and orange line for MIX-2).

For the diagonal compression tests, a finite element model with plane stress elements of 4 nodes is also chosen with mesh size of dimensions 8.96 x 8.65 mm. No interfaces are employed at the points of contact with the steel shoes, thereby eliminating the need to model the steel shoes subsequently. The boundary conditions were set to replicate fixed contact at

the base edge in contact with the steel shoes, with vertical and horizontal displacements restricted. Additionally, at the top, nodes were tied within the square area corresponding to the top steel shoe to simulate a rigid portion of masonry where the load is applied. Consequently, only a vertical load without horizontal displacements is applied to this area. This modeling choice was informed by experimental evidence indicating no damage in the area corresponding to the top steel shoes across all analyzed samples. Also, this modeling technique, employed for similar tests, was also utilized by Basili et al. [179-180]. For the nonlinear static analysis, the same displacement control and convergence criterion of the previous test is adopted. Image of the FEM model is given in Fig. 130.

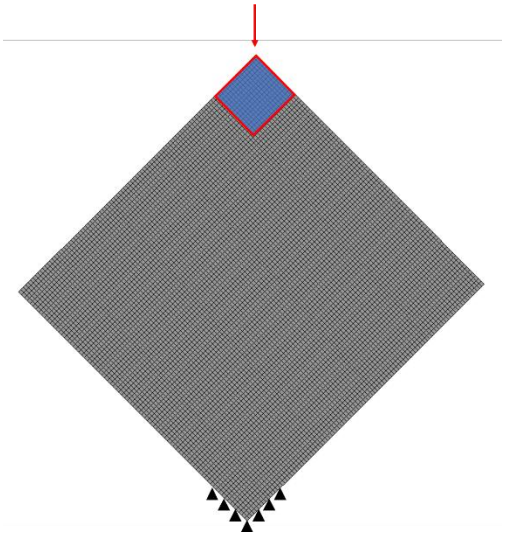

Figure 130: Macro-mechanical fem model for the diagonal compressive test adopted for both masonry types.

The experimental and numerical results are compared based on the relative displacements of the measurement points on the two diagonals of the wallettes in the experimental tests, specifically focusing on their relative horizontal and vertical displacements. In order to carry out this comparison, the corresponding mesh points in the finite element model are identified, and relative displacements are computed at each incremental load step. The results are given in Fig. 131a-b with maximum and minimum experimental values.

The results indicate strong correspondence in relative vertical displacements but less so in horizontal displacements. This discrepancy likely stems from the simplicity of the model, which does not fully capture the orthotropic nature of masonry response. Nonetheless, the model still offers a solid approximation, particularly regarding peak load, which in this case is primarily influenced by masonry tensile strength. Regarding the response in the plastic phase of the model, only a few load steps reached convergence, indicating a decrease in load immediately after the post-peak with a “broken line” pattern. This observation aligns with findings from previous studies on the modeling of diagonal wallettes using total strain crack models [181]. Improving the fit of numerical curves for the diagonal compressive tests could be achieved by adjusting the Poisson’s ratio, but this would require using values that significantly deviate from the experimental ones. Therefore, the choice was made to adhere

more closely to the experimental values, acknowledging the limitations of the numerical model. Using these calibrated parameters, the next paragraph will focus on predicting the stiffness and lateral shear base reaction of large-scale masonry walls subjected to vertical and lateral cyclic loads with total strain crack models.

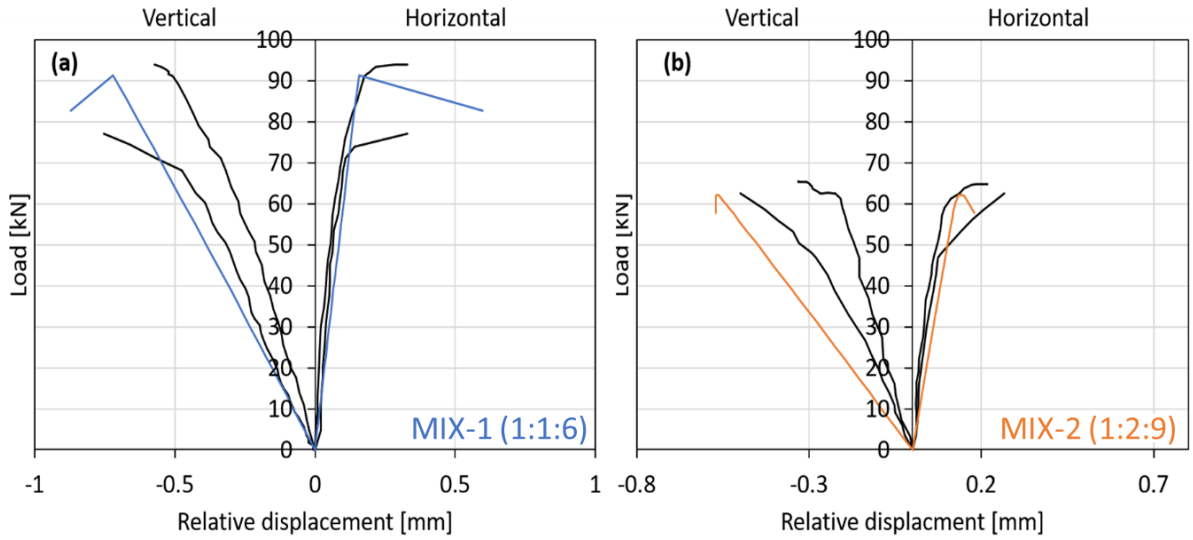

Figure 131: Comparison of vertical load-relative horizontal and vertical displacements for masonry made of MIX-1 **(a)** and MIX-2 **(b)**, showing experimental data (black lines) at minimum and maximum values alongside numerical results (blue line for MIX-1 and orange line for MIX-2).

4.2 Prediction of behavior of masonry larger scale masonry wallettes

This section focuses on the finite element modeling of masonry walls subjected to both vertical and horizontal loads, employing macro modeling techniques to simulate their response under various conditions. In the case of walls subjected to vertical and horizontal loads, the modeling approach incorporates material properties discussed previously. By integrating these modeling techniques, this section provides the comprehensive description of the models adopted for the comparison with experimental tests of masonry walls under varying load conditions, contributing to the next chapter to their comparison and validation.

4.2.1 Masonry walls subjected to statically vertical shearing

For the walls on deflecting members subjected to vertical loads, macro modelling technique is based on the same material properties previously discussed. In this case, for the bottom steel beam, a model that also accounts for the additional height of the support is used, employing a linear elastic model with a Young's modulus of 200 GPa and a Poisson's ratio of 0.3. Additionally, a redistribution top beam and top steel plates are introduced at the actual load application points. For all analyses involving models with different load application spacings, the interface between the steel elements and the masonry was assumed to be perfectly rigid, consistent with the imposed boundary conditions. The finite model is shown in Fig. 132, where a mesh of plane stress elements with linear quadrilateral elements with four-point integration scheme is chosen, with a maximum element size of 10 x 10 mm. The

boundary conditions at the bottom part of wall essentially consists on vertical and horizontal displacement constrained in correspondence of the support plates.

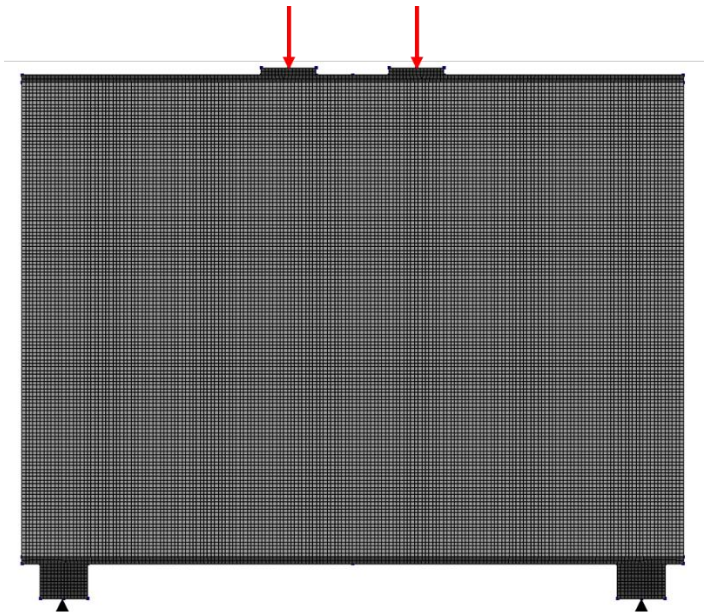

Figure 132: Macro fem model for the wall subjected to vertical loads.

In this case as well, the analysis was performed by scaling the load multiplier from a maximum load value of 1 kN to smaller load steps. Similarly, different load steps were used to address the complexity of the analysis. Arc-length control was set to monitor the vertical displacements of the top central nodes where the load is applied. Also, for this analysis, the Newton–Raphson method was selected for equilibrium iteration with satisfaction of energy and force criteria with tolerance of 10^{-4} and 10^{-3}.

4.2.2 Masonry walls under horizontal cyclic loads

For the cyclic tests, top and bottom concrete beams are considered in correspondence of the supports, a linear elastic model was considered with Young's modulus equal to 30 GPa and Poisson's ratio equal to 0.2. The finite model is shown in Fig. 133, where a mesh with linear quadrilateral elements with 2 × 2 integration scheme is chosen, with element size of 10 x 10 mm.

The boundary conditions at the bottom of the concrete element are also shown, together with the distributed load on top and the horizontal force. Specifically, for the latter, the bottom side of the wall was fixed in both the vertical and horizontal directions, while at the top edge, constraints were applied to the vertical and horizontal displacements to maintain the top of the wall horizontal during the pushover analysis by means of a tying in correspondence of the node where the lateral force is applied.

While no significant differences were noted for the modelling of the tests under vertical loads, this time, the TSC model incorporated a damage-based reduction of the Poisson's ratio to simulate the phenomenon where stretching in the direction orthogonal to the crack does not cause expansion. This approach allows for a more realistic force redistribution, as previously noted by Parisse et al. [247] in the modeling of the lateral cyclic response of stone masonry

piers. The analysis proceeded in line with the previous one, the arc-length control was set to monitor the horizontal displacement of the node where the horizontal force is applied. Finally, the regular Newton–Raphson method was selected for equilibrium iteration, checked according to the simultaneous satisfaction of energy and force criteria (10^{-4} and 10^{-2}, respectively), with line search control activated.

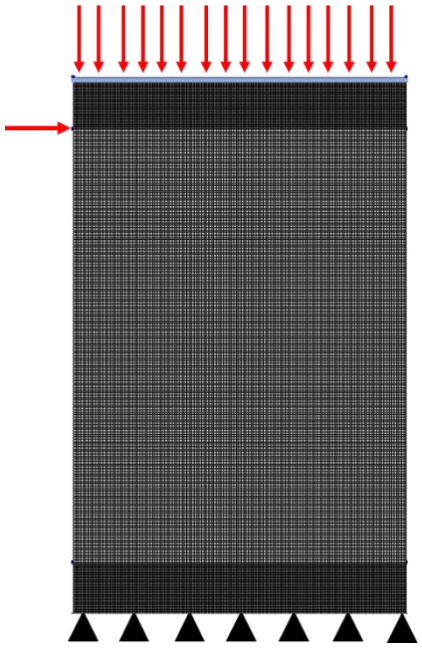

Figure 133: Macro-mechanical fem model for the wall subjected to lateral loads (light blue line representing the tying).

4.3 Validation of prediction methods by experimental data

4.3.1 Masonry walls subjected to static vertical shearing

The comparison between the vertical load–deflection relationships obtained from experimental tests and numerical models for masonry constructed with mortar types MIX-1 (116) and MIX-2 (129), with a spacing of 600 mm is presenting in Figures 134a-b.

For masonry walls with 600 mm spacing, as the applied load increases, the numerical model tends to overestimate the stiffness compared to the experimental results; however, the predictions remain reasonably accurate. At a certain stage, diagonal cracks begin to form in the models near point A (Fig. 135a-b), causing a temporary reduction in load-bearing capacity. Subsequently, the load-bearing capacity increases again. This behavior has been seen in similar investigations with the same modelling approaches when crack is formed [248-249]. Moreover, the crack patterns derived from principal stress analysis in the models show the presence of symmetrical horizontal cracks. These cracks, however, were only observed asymmetrically and at the final stage of the experiments, right before failure, in the test specimens (Fig. 78b and Fig. 88b).

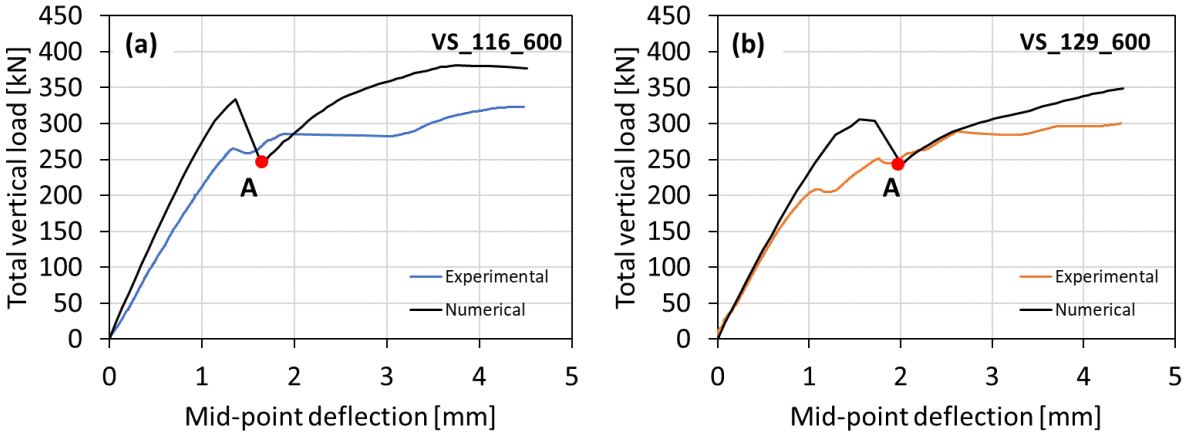

Figure 134: Experimental vs numerical vertical load-mid-point deflection for wall **(a)** VS_116_600 and **(b)** VS_129_600.

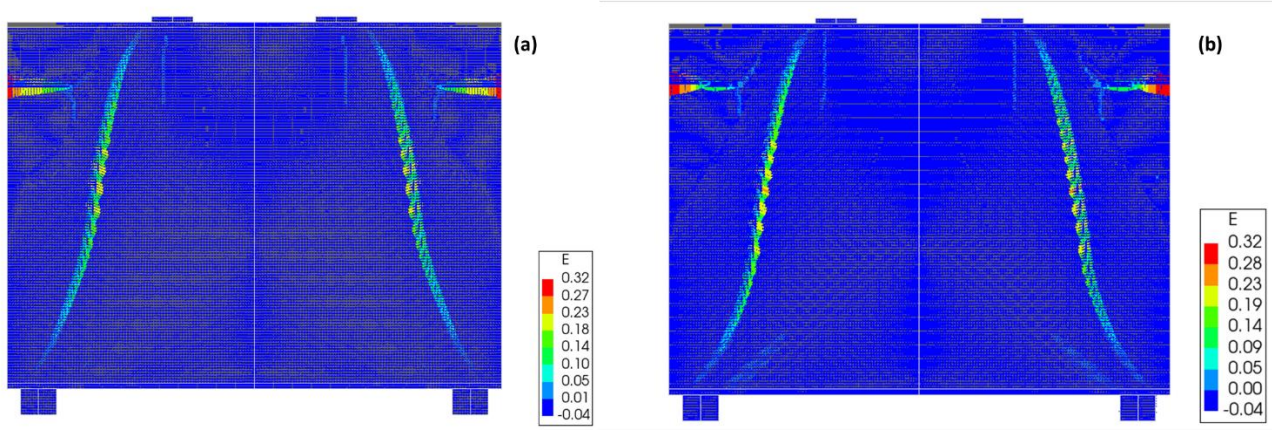

Figure 135: Modelling results of the crack patterns in correspondence of crack formation at point A for **(a)** VS_116_600 and **(b)** VS_129_600.

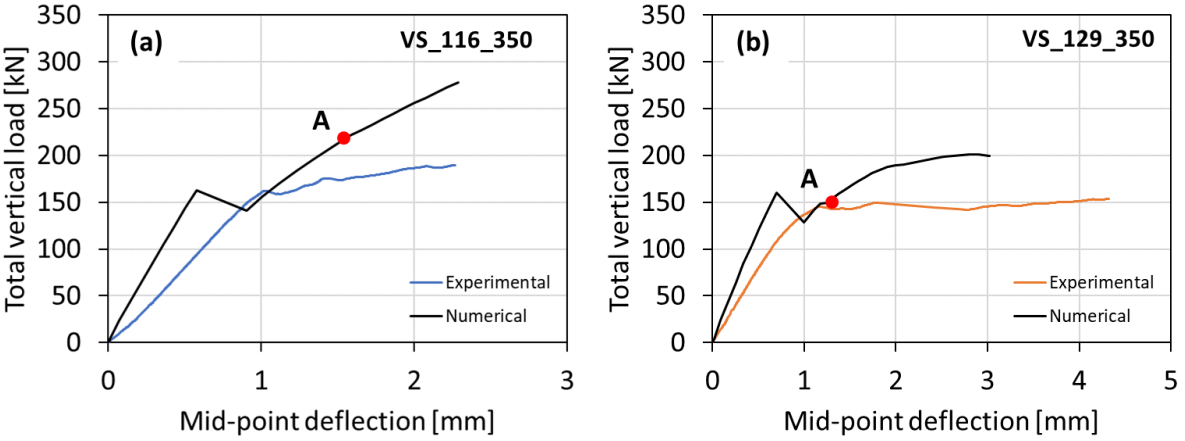

Figure 136: Experimental vs numerical vertical load-mid-point deflection for wall **(a)** VS_116_350 and **(b)** VS_129_350.

Similar trend is observed for the masonry walls subjected to loading at 350 mm, specifically for specimens VS_116_350 and VS_129_350 (Fig. 136a-b). As in the previous analysis, the numerical model generally overestimates both the stiffness and the ultimate

load. In this case, horizontal cracks in the model appear near the point of sudden reduction in load-bearing capacity, which corresponds to the development of diagonal shear cracks. This could be due to the different load steps used in these analyses requiring additional reduction for the convergence. However, horizontal cracking at point A (Fig. 137a-b) is only visible in the experimental test of the masonry built with MIX-2 (129) mortar (Fig. 83b). In contrast, the experimental specimen with MIX-1 (116) mortar (Fig. 73b) exhibits immediate failure characterized solely by diagonal cracking.

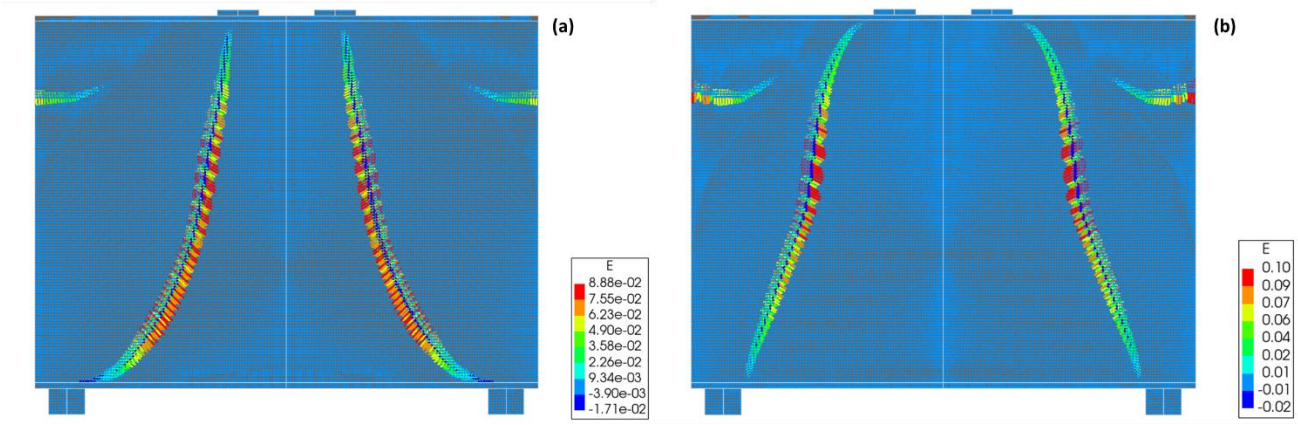

Figure 137: Modelling results of the crack patterns in correspondence of crack formation at point A for **(a)** VS_116_350 and **(b)** VS_129_350.

The discrepancies observed between the experimental and numerical responses for both masonry types can be attributed to several factors, most notably the simplicity of the numerical model and its assumption of continuous isotropic material behavior. Additionally, differences in stiffness may result from the inherent heterogeneity of masonry materials, which the model does not fully capture. In the experimental tests, not all walls exhibited symmetric behavior with crack development more prominently on one side, whereas the model inherently assumes a symmetric response. This contrast is especially evident in masonry constructed with MIX-1 mortar, where the failure response was clearly localized on one side, unlike the more balanced behavior seen in MIX-2 masonry. Moreover, the modeling of contact interfaces between masonry and steel components may also influence the divergence between numerical and experimental results. Accurately representing these interfaces would require the definition of additional parameters and dedicated testing. As highlighted by Giardina et al. [120-121], modeling such interfaces remains a considerable challenge in numerical analysis.

Table 30 highlights the differences in load and deflection at the onset of the first crack for both masonry types, along with the corresponding critical values. While a closer alignment with the experimental response could improve the numerical trend, the predicted deflection at first crack is generally lower by approximately 8% for masonry with mortar MIX-1 (116) and 13% for MIX-2 (129), in the case of 350 mm spacing. For masonry with 600 mm spacing, the numerical predictions exceed the experimental values: by around 20% for masonry made using mortar MIX-1, and approximately 44% for mortar type MIX-2. The latter discrepancy can be attributed to the broader transition from the elastic to the plastic phase observed in the experimental results for masonry made of mortar MIX-2, which contributes significantly to the

higher deviation and in this case has been selected as the lowest. Regarding the critical vertical loads, the numerical predictions demonstrated a reasonably good level of accuracy, with differences ranging between approximately 8% and 14% when compared to the experimental results. Such deviations are considered acceptable within the context of masonry modeling, given the inherent variability of material properties and the simplifications adopted in the macro-modelling approach. Overall, the results confirm the capability of the numerical models to reliably capture the initial cracking and failure conditions under vertical shear loading.

Table 30: Masonry deflection δ and vertical load Fv prediction in correspondence of crack first cracking and critical value from experimental tests with relative differences.

Samples	δ-num	δ-exp	Diff [%]	Fv-num	Fv-exp	Diff. [%]
VS_116_600	1.65	1.32	20.00	243.67	263.88	-8.29
VS_129_600	2.01	1.12	44.28	242.91	208.28	14.26
VS_116_350	0.905	0.98	-8.29	140.99	158.24	-12.23
VS_129_350	0.997	1.13	-13.34	128.69	144.18	-12.04

4.3.2 Masonry walls under horizontal cyclic loads

The comparison of the experimental and numerical results in load-displacement diagrams for both positive and negative push directions for type A of tested wall was presented in Figures 138a-b, 139a-b, 141a-b and 142a-b.

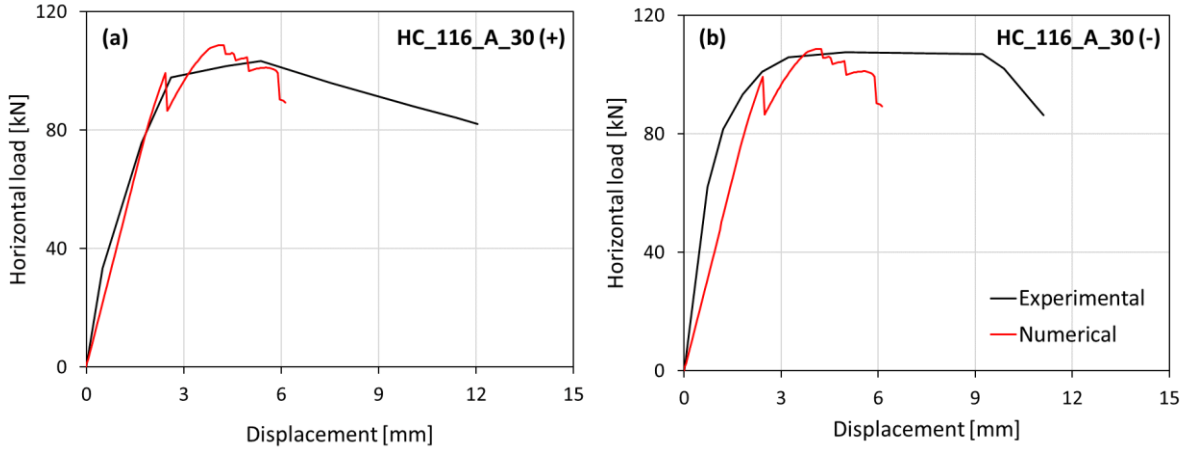

Figure 138: Experimental vs numerical lateral test results for **(a)** positive and **(b)** negative load direction for masonry HC_116_A_30.

Across specimens subjected to 30% of vertical pre-compression, HC_116_A_30 and HC_129_A_30 (Fig. 138a-b and Fig. 139a-b), the numerical models generally show good agreement with the experimental data in terms of stiffness. With small underestimations more evident in the case of the negative direction for masonry wall HC_116_A_30. As for the peak load, the numerical results show small but noticeable differences. For HC_116_A_30 and HC_129_A_30, the model slightly overestimates the peak in the positive direction and slightly underestimates it in the negative direction. The cracks observed at peak load in the numerical models (Fig. 140a-b) are consistent with the experimental results, showing a diagonal crack pattern similar to that captured by the DIC analysis.

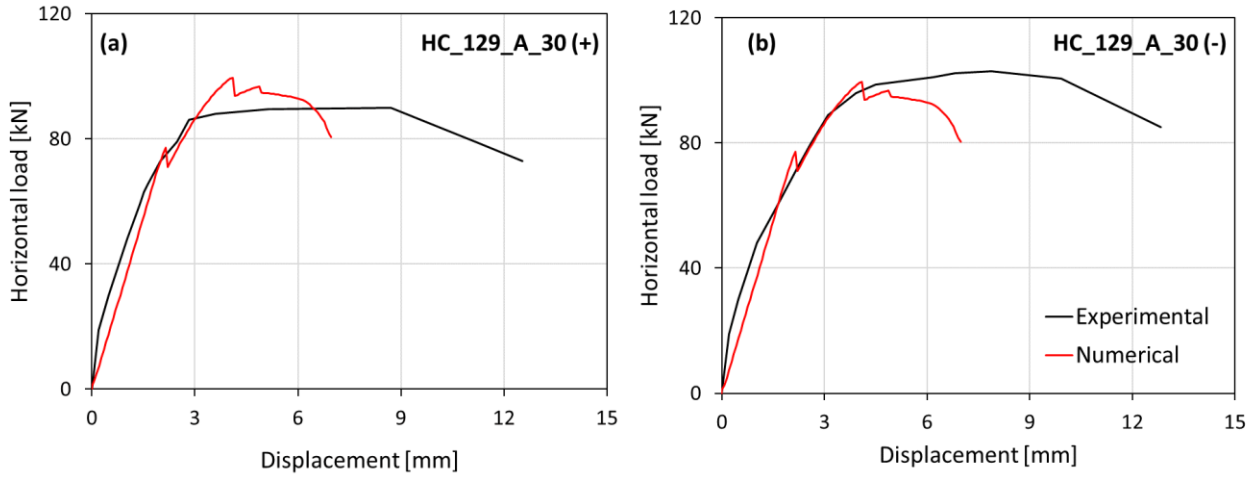

Figure 139: Experimental vs numerical lateral test results for **(a)** positive and **(b)** negative load direction for masonry HC_129_A_30.

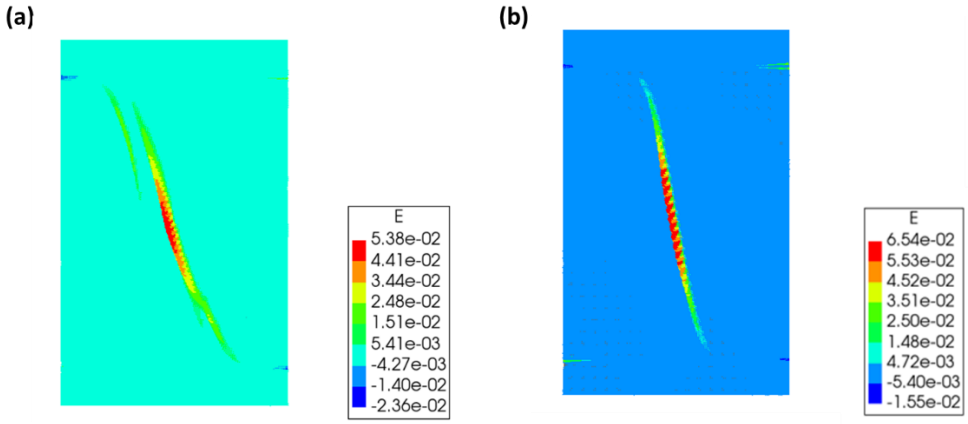

Figure 140: Principal crack strains at peak load for **(a)** HC_116_A_30 and **(b)** HC_129_A_30.

For the tests carried out on masonry type A with 15% pre-compressive load (Fig. 141a-b and Fig. 142a-b), the numerical models accurately reproduce the initial stiffness and tend to overestimate the peak load in both loading directions. However, in both cases, whether the walls were built with MIX-1 or MIX-2 mortars, the models fail to fully capture the post-peak behavior observed experimentally, which is more stable and ductile. This discrepancy arises because, after the initial elastic phase, failure at the base of the wall triggered a rocking mechanism. Our test setup was not fully able to restrain this rocking, and although it limited the vertical uplift at the top, it did not maintain ideal double-bending boundary conditions.

In contrast, the numerical model assumes ideal double-bending boundary conditions with fully restrained supports, resulting in a shear-dominated response, during all the analysis. This leads to lower displacements in the model, higher peak loads, and the formation of shear cracks at peak load (Fig. 143a-b). In the experimental tests, however, the occurrence of shear damage was influenced by the limited rotational restraint provided by the test frame. Additionally, the relatively low bond strength of the masonry contributed to the detachment of a portion of the wall, with failure propagating along both head and bed joints.

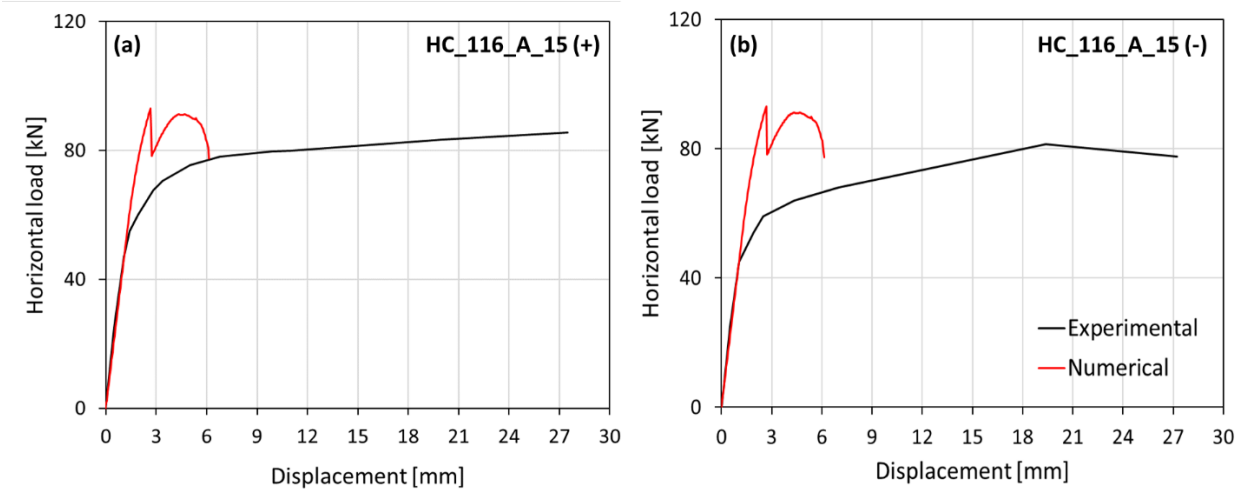

Figure 141: Experimental vs numerical lateral test results for **(a)** positive and **(b)** negative load direction for masonry HC_116_A_15.

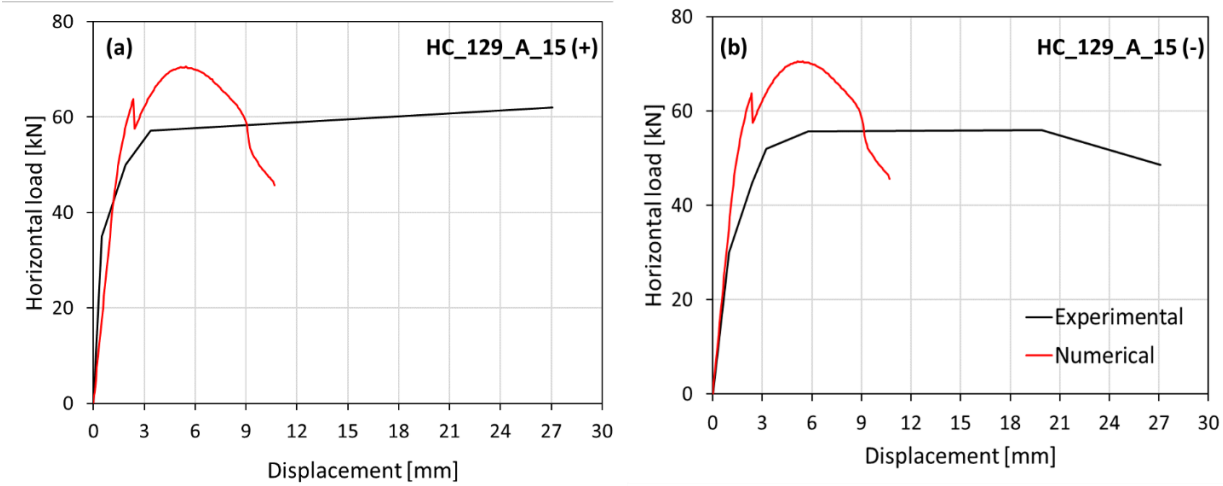

Figure 142: Experimental vs numerical lateral test results for **(a)** positive and **(b)** negative load direction for masonry HC_129_A_15.

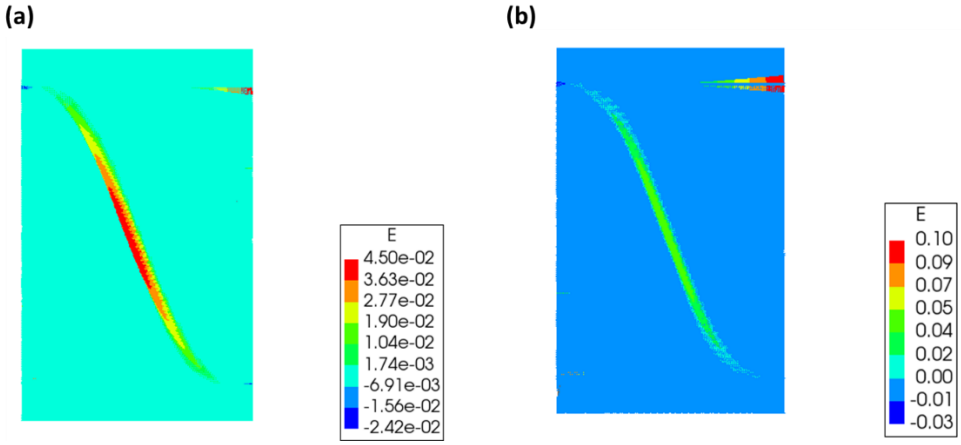

Figure 143: Principal crack strains at peak load for **(a)** HC_116_A_15 and **(b)** HC_129_A_15.

A comparable assessment for masonry type B, based on capacity curves, is presented in the following plots. In the analogous tests, conducted on specimens with different

dimensions but the same vertical pre-compression level of 30%, a clear underestimation of the initial stiffness is observed (Fig. 144a-b and Fig. 145a-b), for both masonry types constructed with MIX-1 and MIX-2 mortars. This time, however, the discrepancy is more pronounced, with the numerical models exhibiting a noticeably more flexible response. As for the peak shear load, the models perform reasonably well, similarly to the type A specimens, and are able to predict the experimental peak load with fair accuracy. In terms of crack pattern, the model successfully captures the diagonal cracking observed at peak load in this case as well (Fig. 146a-b).

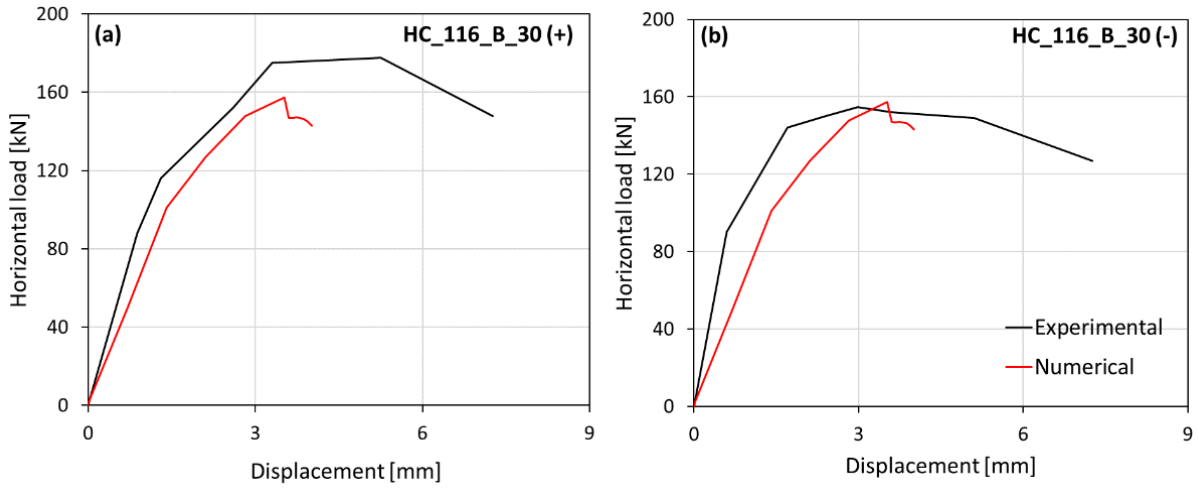

Figure 144: Experimental vs numerical lateral test results for **(a)** positive and **(b)** negative load direction for masonry HC_116_B_30.

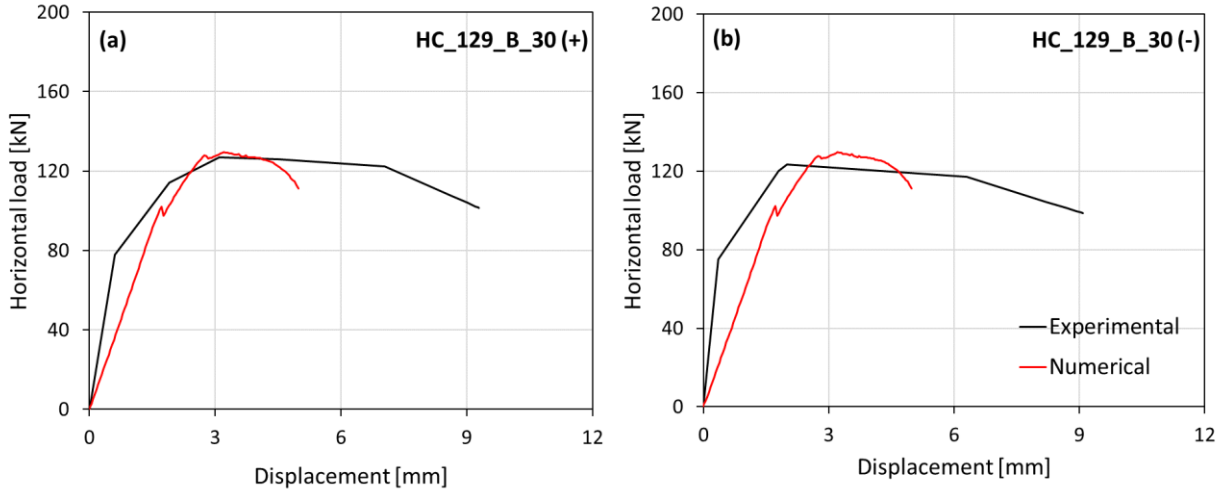

Figure 145: Experimental vs numerical lateral test results for **(a)** positive and **(b)** negative load direction for masonry HC_129_B_30.

For the type B models with a low level of pre-compression, specimen HC_116_B_15 shows a good overall agreement between the numerical and experimental responses in both loading directions (Fig. 147a-b). During the test, a mixed failure mode was observed, with minor damage at the base; however, base rotation was largely restrained, and the response was primarily governed by shear dissipation. This is also reflected in the numerical model,

which reproduces the experimental behavior more accurately than the corresponding type A masonry with the same pre-compression level, showing only a slight overestimation of the peak shear load. Nevertheless, the test results also reveal an overestimation of lateral displacements, likely due to additional base rotation not captured in the model. This leads to horizontal displacements even greater than those observed in the corresponding wall constructed with mortar MIX-2, characterized only by shear response (Fig. 148a-b).

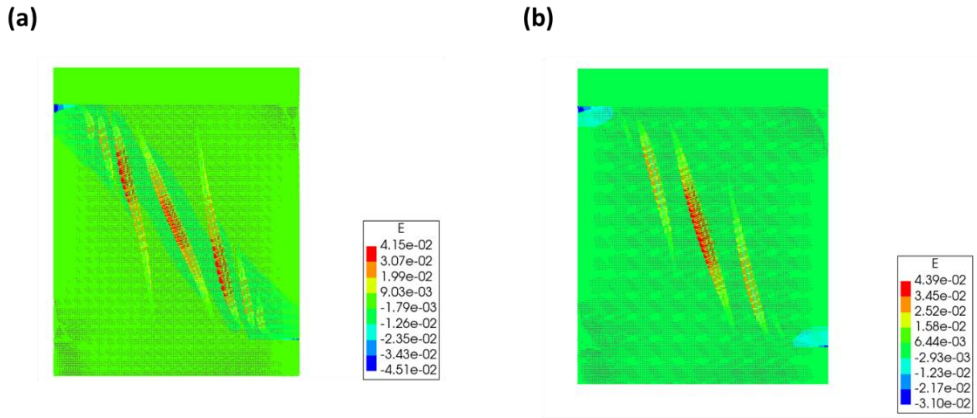

Figure 146: Principal crack strains at peak load for **(a)** HC_116_B_30 and **(b)** HC_129_B_30.

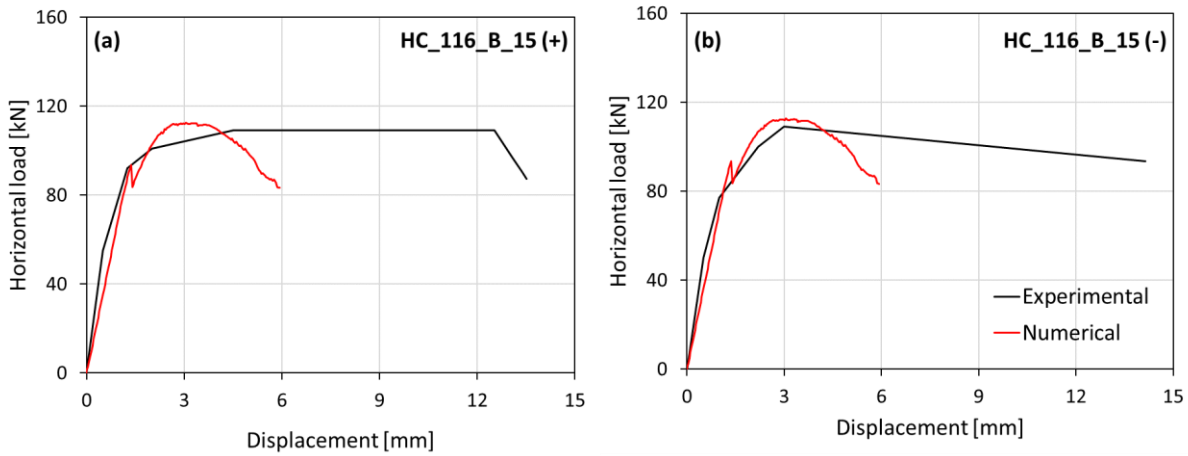

Figure 147: Experimental vs numerical lateral test results for **(a)** positive and **(b)** negative load direction for masonry HC_116_B_15.

The latter (Fig. 148a-b) shows the numerical results closely follow the experimental data, particularly in the initial elastic range and around the peak load. The numerical model slightly overestimates the post-peak response, indicating a higher residual capacity compared to the experimental results. Nonetheless, the overall agreement between the curves suggests that the numerical model provides a reliable representation of the structural behavior in both loading directions.

As anticipated, none of the models are able to fully reproduce the softening behavior observed in the experimental tests. This limitation, especially in predicting ultimate displacements associated with diagonal shear cracking, is well-documented in the literature [246]. It stems from the simplicity of the modeling approach, which assumes a homogenized material calibrated based on experimental results. While more advanced modeling techniques

can offer improved accuracy, they typically require a greater number of input parameters and increased computational effort.

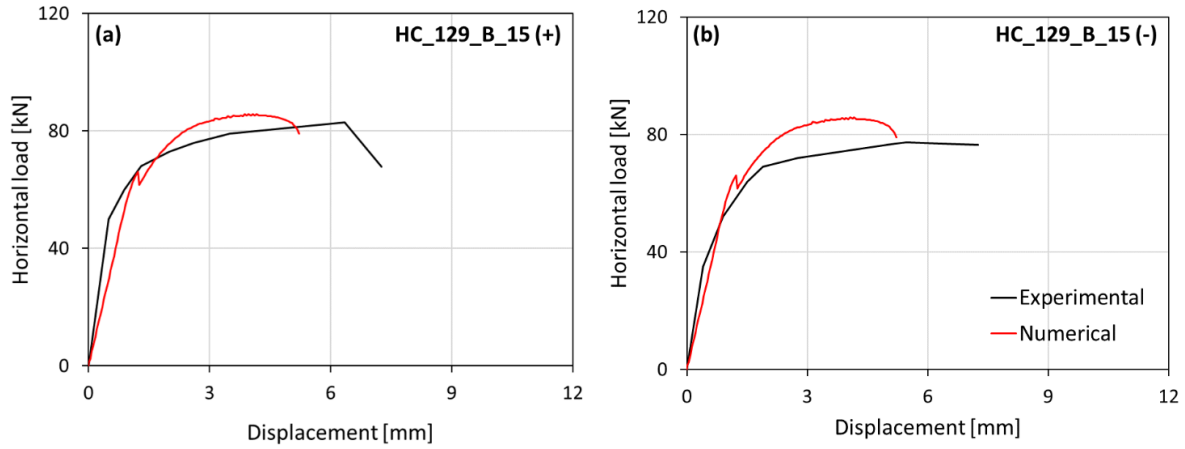

Figure 148: Experimental vs numerical lateral test results for **(a)** positive and **(b)** negative load direction for masonry HC_129_B_15.

Similarly to the type A models, the numerical calculations performed for the type B models and precompression corresponding to 15% of the compressive strength of the wall also showed the influence of partial rotation of the tested model for loads close to state of failure. This was manifested in the form of horizontal cracks in the corners of the test models just below the reinforced concrete cap beam and concerns both the models made using MIX-1 and MIX-2 mortars (Fig. 149a-b).

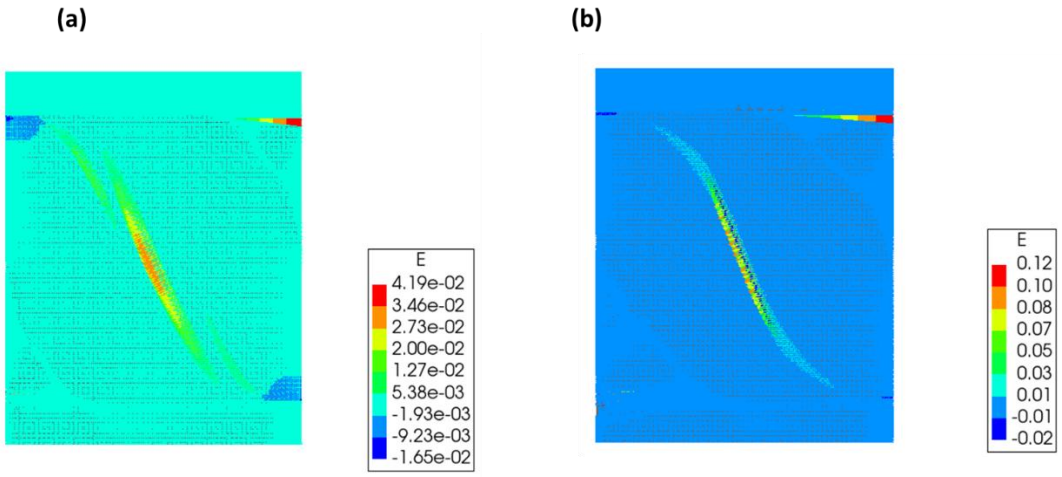

Figure 149: Principal crack strains at peak load for **(a)** HC_116_B_15 and **(b)** HC_129_B_15.

Analyzing the values given in Table 31, it can be seen how the peak load in numerical models is generally overestimated. Nevertheless, the difference between numerical and experimental values ranges from a minimum of 2.73% to a maximum of 26.71%. It is worth noting that the greater discrepancy is related to the tests under the influence of base rotation, which from the very beginning reduces the reliability of the forecast. In this sense, the accuracy of the forecast of series B is also better compared to series A.

Table 31: Prediction of the masonry peak horizontal load (Fh-num) by numerical models and the corresponding peak experimental strength, along with the relative differences in both positive and negative directions.

Specimens	Fh-num [kN]	Fh^{+}-exp [kN]	Fh^{-}exp [kN]	$Diff^{+}$ [%]	$Diff^{-}$ [%]
HC_116_A_30	108.67	103.31	107.54	5.19	1.05
HC_129_A_30	99.57	90.32	102.36	10.24	-2.73
HC_116_A_15	93.09	85.50	81.50	8.88	14.23
HC_129_A_15	70.60	62.00	55.72	13.87	26.71
HC_116_B_30	157.25	177.67	154.72	-11.49	1.64
HC_129_B_30	129.61	126.82	123.32	2.20	5.10
HC_116_B_15	112.66	109.00	109.21	3.35	3.15
HC_129_B_15	85.78	82.85	77.36	3.54	10.89

From a material-based comparative perspective, the peak load predictions for masonry constructed with mortar MIX-1 (116) generally exhibit a more consistent and accurate alignment with the numerical simulation results across all configurations. This suggests a good calibration of the model parameters for this specific mortar type. Nevertheless, even for masonry walls constructed with mortar MIX-2 (129), particularly specimens HC_129_B_30 and HC_129_B_15, the differences between numerical predictions and experimental peak loads remain relatively low, with discrepancies ranging from 2.2% to 10.89%. Such deviations fall within acceptable margins for macro-modelling approaches typically applied to masonry structures, confirming the robustness of the adopted modeling strategy.

These results highlight the capability of the numerical model to adequately capture the influence of material properties on the global behavior of masonry walls. In particular, for the B-type configuration, which features a squatter geometry and different failure mechanisms compared to slender walls, the model demonstrates good predictive reliability for the performance of the 129 series specimens. The observed agreement between experimental and numerical outcomes supports the validity of the model assumptions and parameter calibrations, providing confidence in its application for further analyses or parametric studies.

Although the macro-modelling approach captured the global behavior with good accuracy, it inherently simplifies localized cracking and post-peak degradation mechanisms. Future studies incorporating refined micro-modelling could provide further insights into damage evolution and crack development.

CHAPTER 5 - ANALYTICAL OR SEMI-ANALYTICAL METHODS AND PROCEDURES

The analytical and semi-analytical procedures available for estimating peak lateral loads and displacements in masonry elements have been thoroughly reviewed in the literature chapter. This section now focuses on applying part of those methods to the tested specimens and evaluating their accuracy in predicting the experimental behavior.

5.1 Existing calculating methods and procedures

It is important to distinguish between the primary effects induced by vertical loads on deflecting members and those resulting from the lateral cyclic response of masonry walls.

In the case of the former, there is no standardized test setup currently available; in fact, the tests we conducted on masonry under vertical loading were based on a non-standardized experimental procedure. From a code perspective, deflection in masonry walls is a crucial aspect of structural performance, primarily influencing the serviceability of masonry structures. In this context, not specific recommendations are furnished for masonry structures. Earlier European building design codes focused on limiting stresses within the elastic phase. However, with recent code updates, serviceability limit states are now predominantly verified in terms of the maximum allowable displacements or deflections for specific structural elements. Kania et al. [137] provided a review of the existing limits from various codes, primarily concerning non-structural masonry elements and infill masonry in reinforced concrete structures. This review is fully presented here for ease of reference, with the relevant sources listed in Table 32, focusing mainly on the ratio of deflection to the span (S) or the maximum allowable deflection (δ). The limits provided by various standards are then compared, in the following paragraph, with the critical values obtained in this study for masonry constructed with different mortar types and subjected to varying load spacings as part of our experimental campaign.

Table 32: Several codes reviewed by Kania et al. [137] for masonry subjected to vertical deflection.

Standard	δ/S
ACI 318-08 [250]	1/450
ACI-530-08 / ASCE 5-08 / TMS 402-08 [251]	1/600
BS 5628 [252]	1/500
DIN 1045-1 [253]	1/500
NBN B 03-003 [254]	1/1000
EN 13747: 2005 [255]	1/500
PN-B-03264: 2002 [256]	1/250

Another approach is presented in the Polish National Annex to Eurocode 6 [13] and previous national Masonry Code PN-B-03002:2006 [257], which introduces a deformation-based verification criterion. This method follows the tradition of earlier national codes that imposed limits on both stress and strain states. The criterion, developed based on

experimental research by Kubica [127], limits the angular deformation (Θ_{sd}) of masonry walls to an admissible value (Θ_{adm}) as per equation (36). The recommended admissible values of the non-dilatational strain angle for use in Poland are derived from various experimental studies, including the research conducted by Kubica [127]. These values, which have been normatively adopted, vary depending on the masonry unit group and the type of mortar used. The corresponding values are presented in Table 33.

$$\Theta_{sd} \leq \Theta_{adm} \tag{36}$$

Table 33: Admissible values of non-dilatational strain angle Θ_{adm} [miliradians] given in [257].

Type of masonry units	Cement mortar	Cement-lime mortar
Group 1 excluding AAC blocks	0.4	0.5
Group 2, 3 and 4	0.3	0.4
Autoclaved aerated concrete blocks (AAC)	0.2	0.3

The determination of Θ_{sd} can be performed using finite element models (FEM) or, as in this case, based on experimental testing of masonry elements. Alternatively, an approximate value can be obtained through a simplified approach, treating the masonry structures as a frame structure and determining the angular deformation on the base of the deformation of the deformed panel (Fig. 150), where Δa is the difference of the vertical displacement of the extremes of masonry panel and L the length of the panel itself (37).

$$\Theta_{sd} = \frac{\Delta a}{L} \tag{37}$$

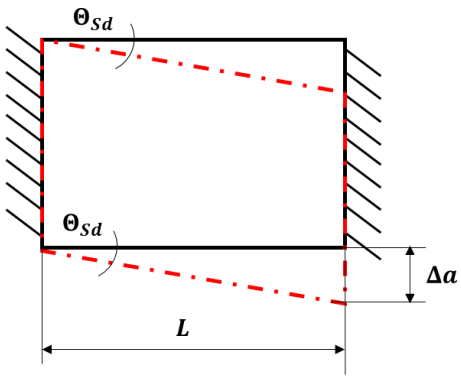

Figure 150: Simplified static scheme for the determination of the non-dilatational strain angle Θ_{sd}. Adapted from Kubica [127].

Effectively, this approach based on the frame structure hypothesis leads the question of the representativity of these values of deformation due to the soil-structure interaction, the variation of the stiffness of masonry elements and complex deformation of the panels. In this case, it is recommended the determination of a global shear deformation angle $\Theta_{sd,G}$ and a local deformation angle $\Theta_{sd,,L}$, assuming the first associated to the length of the entire panel or lintel L_i and the second assumed to the segment of concentration of deformation L'_i (approximately equal to 40 % of L_i), based on the deformed shape (Fig. 151).

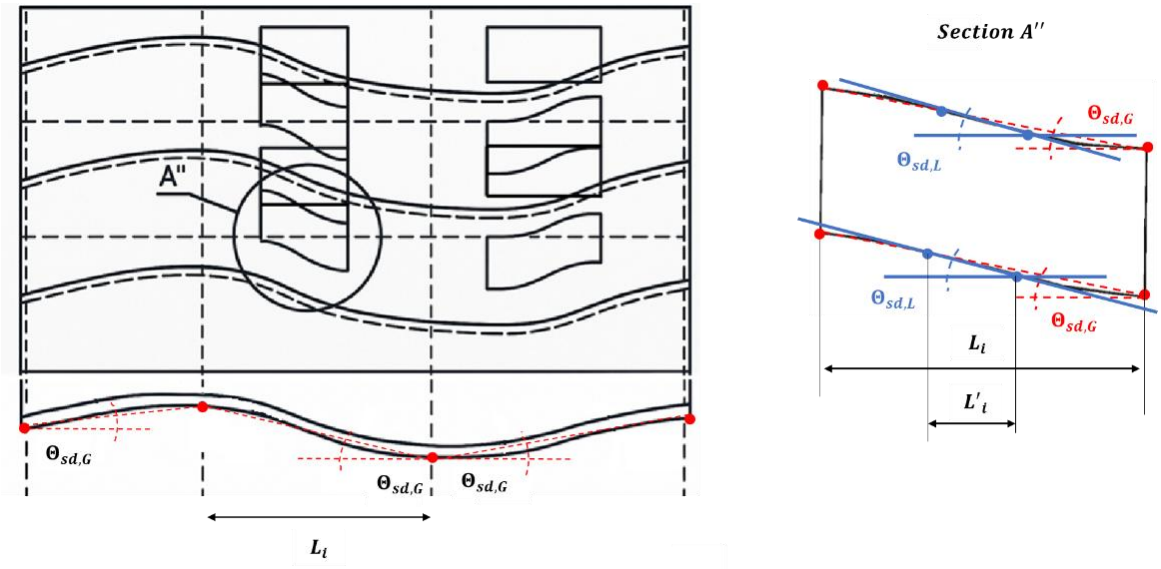

Figure 151: Scheme of deformed wall subjected to irregular settlements for panel-scale elements for local $\Theta_{sd,L}$ and global non-dilatational strain angle $\Theta_{sd,G}$. Adapted by Kubica [127].

Regarding the prediction of lateral cyclic behavior, several formulations are available in literature [258]. Generally, the code formulations for predicting shear strength at the macro level are differentiated based on the wall failure mode mechanism. Among the various formulations, those used to compare lateral strength with experimental values are presented below, referring to Eurocode 6 [13] and Eurocode 8 [159]. Even though some modifications of these formulations are available in the literature, such as those proposed by Magenes and Calvi [148] based on experimental campaigns aimed at improving prediction accuracy by adding some parameters, the decision was made to adopt the standard code formulations in their original form in order to ensure consistency, simplicity, and broader applicability. Using the unmodified code provisions allows for a more direct comparison with common design practices and facilitates a clearer assessment of their predictive capabilities within the scope of this study. These formulations (38-40) are arranged without considering the γ design coefficients but including only parameters determined experimentally for effective comparison, expressing the flexural, diagonal cracking and shear sliding domains:

$$V_{tc} = A_w \frac{\alpha\, f_a B}{2\, H}\left(1 - \frac{f_a}{0.87 f_m}\right) \tag{38}$$

$$V_{dc} = \frac{f_t\, A_w}{b}\sqrt{1 + \frac{f_a}{f_t}} \tag{39}$$

$$V_s = \left(f_{v0} + \frac{P_D}{t\, l_c}\right) t\, l_c \tag{40}$$

where:

- A_w is the base area of the wall, f_a is the axial compressive strength acting on the top of the wall;
- B is the base of the wall;

- H is the height of the wall;
- f_m is the maximum compressive strength of the wall;
- f_t is the masonry tensile strength determined by means of diagonal compressive strength;
- b is the factor for the redistribution of shear stresses (1 for $H/B < 1$, 1.5 for $H/B > 1.5$);
- f_{v0} is the initial shear strength;
- P_D is the vertical load applied;
- t is the thickness of the wall;
- l_c is the length of the compressed part of the wall that is not cracked and then reacting again the sliding.

For the last parameter, the equation provided by Eurocode 6 [13] for shear strength due to sliding depends on l_c, which itself is a function of shear strength [161]. Given this, the code recommends calculating the compressed part l_c by assuming a linear stress distribution at the base of the wall. To provide a broader overview of the failure mechanisms in the tested masonry walls, a comparison is presented in the next paragraph in terms of the shear strength domains.

Displacements also play a key role in modern displacement-based design approaches and have become increasingly important in the context of seismic design [259]. Regarding the displacement capacity, codes only furnish values based on limit states as shown in section 2.2.1. In this part, the focus is given to the Eurocode 8 formulations [159]. Specifically, Eurocode 8 – Part 3 defines lateral drifts for various limit states based on the governing failure mode. For Life Safety/Severe Damage limit state (SDLS), the shear mode exhibits a drift of 0.4%. In the case of Near Collapse limit conditions (NCLS), this value is increased of a factor of 4/3. Specifically, for experimental and comparative purposes, the first drift can be associated with the experimental drift value at 0.8 times the peak lateral force in the softening branch. The second drift can be considered as the maximum experimental drift reached during the test or the maximum attained in the last complete cycle [141]. For walls failing in flexure, the drift at the Serviceability Damage Limit State (SDLS) is considered to be the maximum displacement just before the loss of bearing capacity, due to the low drop of lateral load associated to this mechanism. According to the code, this drift is proportional to the wall's height-to-base ratio. The load-controlled test setup for lateral loading did not allow, in some cases, a clear identification of drift values in the softening branch. Additionally, some tests were interrupted before reaching failures of the wall, evidencing reduction of the lateral load capacity superior of the 20 %. As a result, these drift values are, at times, conservatively assumed to be the same.

5.2 Verification of existing methods by experimental results

In our study, a comparison between the experimental results and the recommended ratios revealed that the experimental deflections were consistently lower than those suggested by various codes (Table 34 and Table 35). However, the degree of discrepancy differs based on the type of masonry being analyzed. For example, the NBN B 03-003 [254] code indicated a minimum difference of approximately 19.70% for masonry made with mortar

MIX-1(116) when subjected to a loading distance of 600 mm. Similarly, the same code showed the minimum discrepancy for masonry made with MIX-2 (129) in both load application configurations of 350 mm and 600 mm. Polish national concrete code PN-B-03264: 2002 [256] is the code that most significantly overestimates the ratio, exceeding 300%. This suggests that codes designed for concrete structures may not be suitable for non-structural masonry elements, as they are not tailored to account for the unique properties of masonry. In this context, the results are limited and quite scattered due to the variety of test setups available, making it challenging to draw comparative conclusions with values from the literature. Naturally, this comparative analysis is just a starting point for the development of more refined and accurate design guidelines, as it highlights the need for further research and a deeper understanding of the behavior of different masonry types under subsoils settlements.

Table 34: Comparison vertical displacement limits according to several codes reviewed by Kania et al. [137] for masonry made with MIX-1 (116).

Test		**VS_116_350**	**VS_116_600**	**VS_116_350**	**VS_116_600**
Standard	**δ/S**	**δ/S**	**δ/S**	**Diff [%]**	**Diff [%]**
ACI 318-08 [250]	0.0022	0.00062	0.00084	258.28	165.99
ACI-530-08 / ASCE 5-08 / TMS 402-08 [251]	0.0017	0.00062	0.00084	168.71	99.49
BS 5628 [252]	0.0020	0.00062	0.00084	222.45	139.39
DIN 1045-1 [253]	0.0020	0.00062	0.00084	222.45	139.39
NBN B 03-003 [254]	0.0010	0.00062	0.00084	61.22	19.70
EN 13747: 2005 [255]	0.0020	0.00062	0.00084	222.45	139.39
PN-B-03264: 2002 [256]	0.0040	0.00062	0.00084	544.90	378.79

Table 35: Comparison vertical displacement limits according to several codes reviewed by Kania et al. [137] for masonry made with MIX-2 (129).

Test		**VS_129_350**	**VS_129_600**	**VS_129_350**	**VS_129_600**
Standard	**δ/S**	**δ/S**	**δ/S**	**Diff [%]**	**Diff [%]**
ACI 318-08 [250]	0.0022	0.00072	0.00071	210.72	213.49
ACI-530-08 / ASCE 5-08 / TMS 402-08 [251]	0.0017	0.00072	0.00071	133.04	135.12
BS 5628 [252]	0.0020	0.00072	0.00071	179.65	182.14
DIN 1045-1 [253]	0.0020	0.00072	0.00071	179.65	182.14
NBN B 03-003 [254]	0.0010	0.00072	0.00071	39.82	41.07
EN 13747: 2005 [255]	0.0020	0.00072	0.00071	179.65	182.14
PN-B-03264: 2002 [256]	0.0040	0.00072	0.00071	459.29	464.29

A comparison of the non-dilatational strain angle Θ_{sd} with the admissible values specified in Polish PN-B-03002:2006 [257] is presented in Table 36. The comparison assumes the brick category of Group 1, for which the recommended limit is Θ_{adm} equal to 0.5 mrad for cement-lime mortar walls. In this analysis, Θ_{sd} corresponds to the critical angular deformation measured on each side of the panel. Experimental results consistently exceed the code-

prescribed limit, with overages ranging from about 12% to 71%, highlighting the underestimation of deformation capacity in walls built with air lime mortar. This trend is even more pronounced in specimens with higher lime content, where most values exceed the standard limit by a substantial margin. This underscores the fact that lime-based masonry possesses a significantly greater deformation capacity than currently recognized by existing code provisions, which tend to conservatively underestimate its ductility for safety and design reliability reasons. Masonry constructed using mortars with higher amounts of lime in the binder exhibit significantly improved crack resistance.

Table 36: Comparison non-dilatational strain angles according to PN-B-03002:2006 [257] and experimental ones for both masonry types and sides.

Samples (side)	θ_{adm} [mrad]	θ_{cr} [mrad]	Diff. [%]
VS_116_350 (A)	0.5	0.85	-41.18
VS_116_350 (B)	0.5	-	-
VS_116_600 (A)	0.5	0.64	-21.88
VS_116_600 (B)	0.5	0.57	-12.28
VS_129_350 (A)	0.5	1.15	-56.52
VS_129_350 (B)	0.5	1.44	-65.28
VS_129_600 (A)	0.5	1.72	-70.93
VS_129_600 (B)	0.5	0.56	-10.71

Regarding the lateral cyclic response, the plots of relationships (38-40) under varying levels of pre-compressive load (N) applied to the top of the wall effectively illustrate the hierarchy of resistance.

Fig. 152 shows that for a 30% compressive load, the lower domain is the diagonal shear domain, while for 15%, the lower domain is the flexural domain, which accurately predicts the types of failure modes of the piers, typically represented by the lowest strength mechanism. Beyond this, the experimental values are generally overestimated by the prediction, based on the relative intersection with the domains and the level of pre-compression.

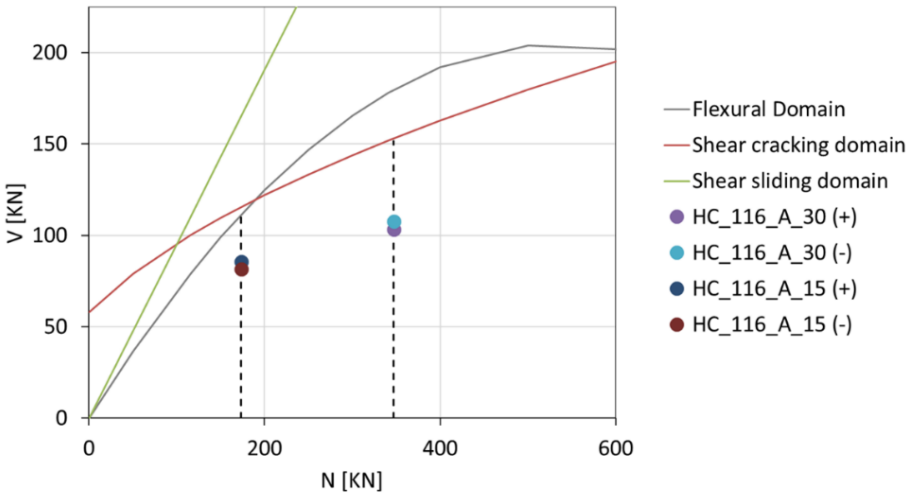

Figure 152: Strength domains for the tested masonry walls of series HC_116_A with dots indicating the experimental values of peak lateral shear load V in relation to the corresponding pre-compression load N.

Whereas Fig.153 displays the same quantities for the series of walls made with mortar type MIX-1(116), but with smaller dimensions. In this case, the prediction of the failure mode, primarily related to diagonal shear cracking, holds true for both masonry types with different levels of pre-compression. The prediction is particularly accurate for the 15% pre-compression case, but for the HC_116_B_30 masonry, the model overestimates the experimental value.

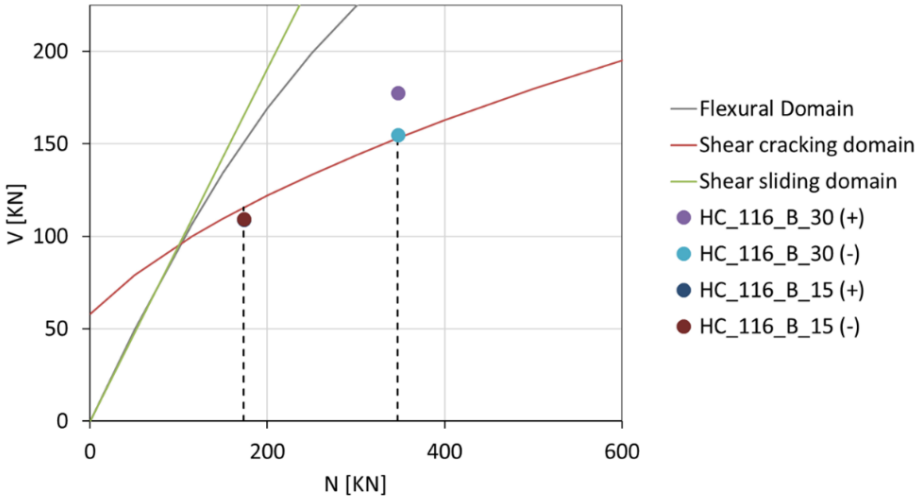

Figure 153: Strength domains for the tested masonry walls of series HC_116_B with dots indicating the experimental values of peak lateral shear load V in relation to the corresponding pre-compression load N.

A similar analysis to the previous one, illustrating the relationship between shear and normal force for a series of walls, but this time using a different mortar, MIX-2 (129) presents Fig. 154. In this case, the failure mode is predicted for masonry subjected to 30% pre-compression, but not for 15%. However, for the latter case, we are very close to the intersection between the flexural and shear domains, suggesting some interaction. Once again, for both vertical load cases, the experimental values are overestimated by the prediction.

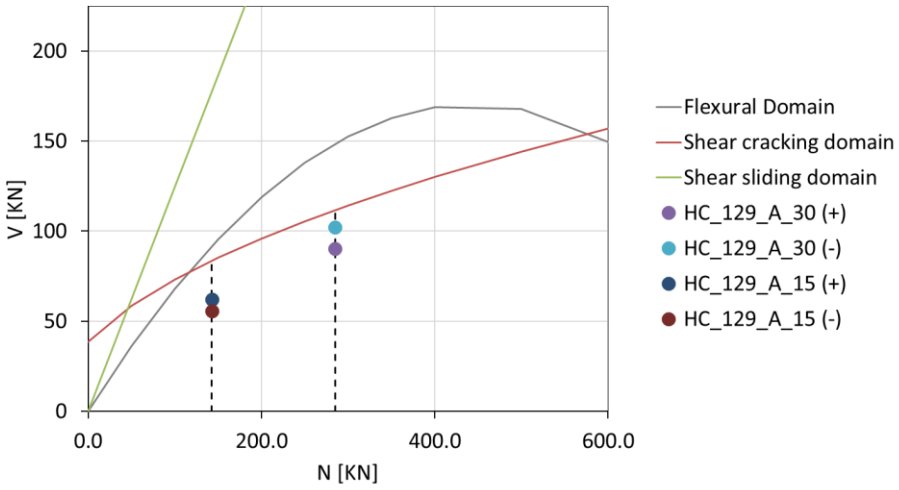

Figure 154: Strength domains for the tested masonry walls of series HC_129_A with dots indicating the experimental values of peak lateral shear load V in relation to the corresponding pre-compression load N.

Finally, Fig. 155 represents the domain for the series of masonry MIX-2 (129) with B dimensions. The graph shows that for both 30% and 15% pre-compression, the failure mode is predicted to be related to shear cracking, as indicated by the data points falling within the shear cracking domain. Additionally, the negative pre-compression case also aligns within the shear cracking domain, suggesting that shear cracking remains the dominant failure mechanism even under low pre-compression. However, as with the previous cases, there is an overestimation of the experimental values for masonry subjected to the highest pre-compressive load.

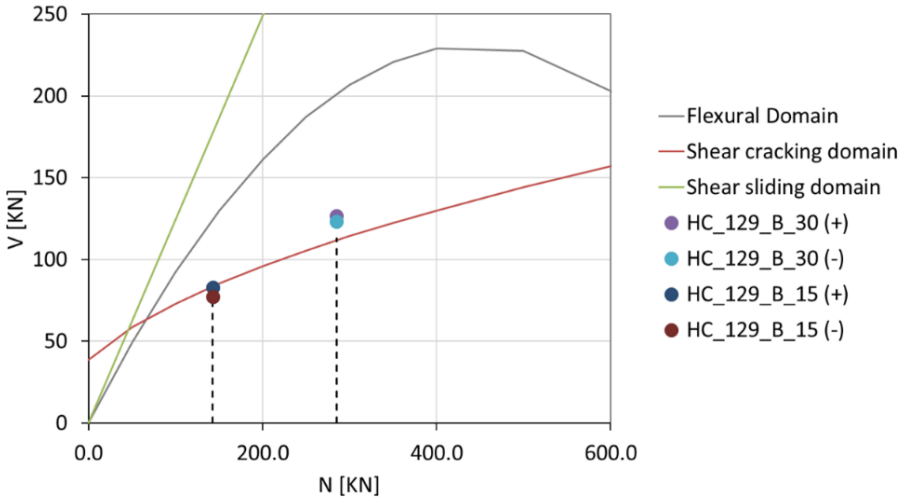

Figure 155: Strength domains for the tested masonry walls of series HC_129_B with dots indicating the experimental values of peak lateral shear load V in relation to the corresponding pre-compression load N.

The difference between the experimental and analytical shear strength values obtained using existing methods is shown in Table 37.

Table 37: Prediction of the masonry peak horizontal load (Fh) by existing methods and the corresponding peak experimental strength, along with the relative differences in both positive and negative directions.

Specimens	Fh [kN]	Fh^{+}-exp [kN]	Fh^{-}exp [kN]	$Diff^{+}$ [%]	$Diff^{-}$ [%]
HC_116_A_30	151.45	103.31	107.54	46.60	40.83
HC_129_A_30	111.43	90.32	102.36	23.37	8.86
HC_116_A_15	110.01	85.50	81.50	28.66	34.98
HC_129_A_15	83.00	62.00	55.72	33.87	48.96
HC_116_B_30	153.43	177.67	154.72	-13.64	-0.83
HC_129_B_30	112.95	126.82	123.32	-10.93	-8.41
HC_116_B_15	115.65	109.00	109.21	6.10	5.90
HC_129_B_15	84.04	82.85	77.36	1.44	8.64

The predictions for the type A walls, for both mortar mixes, are significantly less accurate compared to those for type B walls. Additionally, for type B walls, masonry made with mortar MIX-2 (129) is the one with providing more consistent and reasonable prediction with differences ranging from a minimum of 1.44 % to a maximum of 10.93 %. Since most of the failures are described by the Turnšek and Čačovič shear domain, which depends on a factor *b* for the redistribution of shear stresses, this factor was set to 1 as recommended by the code, assuming a double bending condition and a ratio between the height of inflection and the

base of the walls less than one. These results, as previously pointed out by Celano et al. [118], suggest the possibility of using different values for *b*, depending on the aspect ratio of the walls, which may be more complex than the one currently suggested by the codes. Calculating *b* from equation (39) considering the values of shear strength and relative pre-compressive strength, we obtain for the series HC_116_A and HC_129_A average *b* values of 1.42 (3.70%) and 1.29 (13.35%) superior to one. While for HC_116_B and HC_129_B we have 0.99 (9.45%) and 0.97 (9.55%) respectively in line with the code recommendations. A linear regression on the values obtained for *b* and their respective ratio of the inflection height (H_f) and base of the walls (*B*) is given in Fig. 156 with the relative fitting equation with our data. From the linear regression analysis, setting the resulting value of b to 1.35 for both Series A with materials MIX-1 (116) and MIX-2 (129) would help minimize the discrepancies between the experimental shear values and those predicted by the proposed formulation for masonry type A (Fig. 157 and Fig. 158). This adjustment significantly improves the alignment between predicted and observed peak shear stresses, suggesting that a calibrated *b* value could enhance the reliability of simplified design approaches when applied to air lime-based mortars.

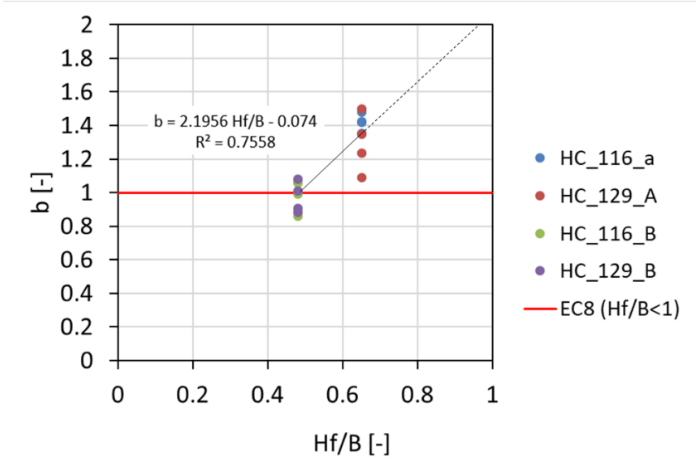

Figure 156: Evaluation of b based on experimental data from this study.

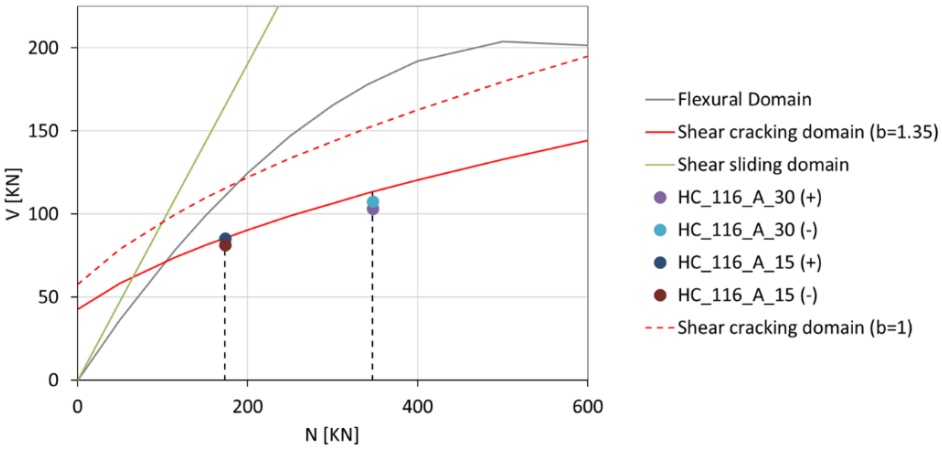

Figure 157: Shear strength domains modification for tested masonry walls of series HC_116_A with dots indicating the experimental values of peak lateral shear load V in relation to the corresponding pre-compression load N.

However, it must be emphasized that this conclusion is based solely on the materials tested within the scope of this study and under a specific boundary condition. Therefore, further experimental campaigns, involving a broader range of material compositions, different mortar strength classes, and alternative loading and boundary conditions, are necessary to validate the general applicability of this proposed adjustment. In addition, complementary numerical simulations incorporating different geometries would be beneficial to confirm the robustness of the modified parameter across a wider range of masonry typologies.

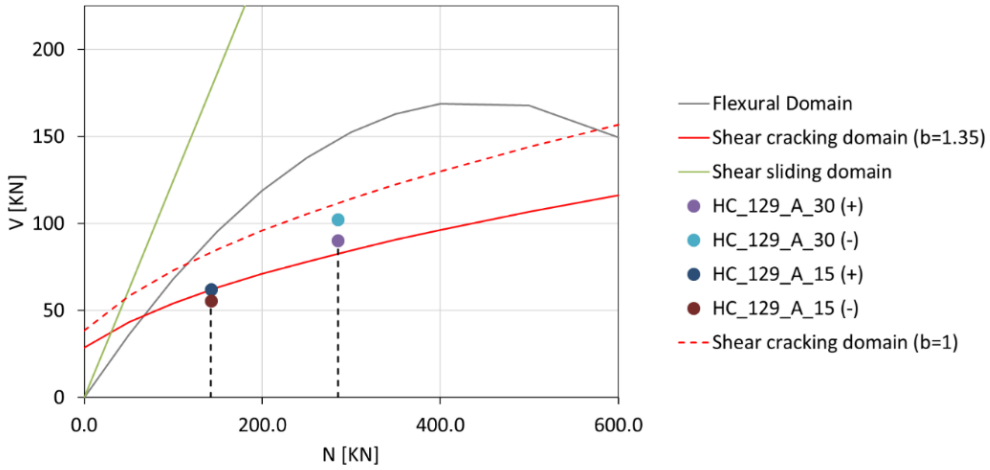

Figure 158: Shear strength domains modification for tested masonry walls of series HC_126_A with dots indicating the experimental values of peak lateral shear load V in relation to the corresponding pre-compression load N.

The Tables 38-39 report the drift values for the tested walls in both positive and negative loading directions, along with the corresponding deviations from the code-prescribed limits.

Table 38: Drift ratios for all masonry specimens in positive (+) and negative (-) load directions at SDLS.

Specimens	SDLS limit	Drift^{+}-exp	Drift^{-}-exp	Diff $^{+}$[%]	Diff $^{-}$[%]
HC_116_A_30	0.40%	1.37%	1.26%	-70.76	-68.33
HC_129_A_30	0.40%	1.42%	1.46%	-71.92	-72.56
HC_116_A_15	0.52%	3.13%	2.21%	-83.33	-76.37
HC_129_A_15	0.52%	3.08%	2.26%	-83.07	-76.97
HC_116_B_30	0.40%	0.83%	0.83%	-51.54	-51.54
HC_129_B_30	0.40%	1.06%	1.03%	-62.13	-61.13
HC_116_B_15	0.40%	1.42%	1.61%	-71.86	-75.10
HC_129_B_15	0.40%	0.72%	0.83%	-44.60	-51.54

For both types of masonry elements, the code-based calculations did not accurately predict the experimental drift capacities. This issue has also been widely recognized in the literature [140-141, 260], where several authors reported significant discrepancies between code predictions and observed experimental results, particularly in cases dominated by diagonal shear cracking mechanisms. Notably, in several tests, the lateral load remained relatively stable over an extended displacement range without significant softening, with large

displacement values occurring primarily during the final, incomplete loading cycles. This behavior led to the practical assumption of equivalent drift values for both SDLS and NCLS, effectively reducing the observed difference between the wall drifts and those predicted by the code, particularly for NCLS values (Table 38). Despite these considerations, it is important to highlight that the drift limits specified by the current codes appear to be generally conservative when compared to the experimental drift capacities achieved by masonry constructed with both MIX-1 (116) and MIX-2 (129) mortars. This aspect, while ensuring safety margins, could potentially lead to an underestimation of the actual deformation capacity of air lime-based masonry elements, thereby penalizing their performance evaluation in design practice.

Table 39: Drift ratios for all masonry specimens in positive (+) and negative (-) load directions at NCLS.

Specimens	NCLS limit	Drift^{+}-exp	Drift^{-}-exp	Diff $^{+}$[%]	Diff $^{-}$[%]
HC_116_A_30	0.53%	1.57%	1.57%	-66.25	-66.25
HC_129_A_30	0.53%	2.08%	1.46%	-74.50	-63.64
HC_116_A_15	0.70%	3.13%	3.24%	-77.71	-78.50
HC_129_A_15	0.70%	3.08%	3.56%	-77.36	-80.41
HC_116_B_30	0.53%	0.91%	0.83%	-41.73	-35.79
HC_129_B_30	0.53%	1.16%	1.16%	-54.39	-54.12
HC_116_B_15	0.53%	1.70%	1.61%	-68.76	-67.01
HC_129_B_15	0.53%	0.83%	0.83%	-35.79	-35.79

CHAPTER 6 - SUMMARY AND CONCLUSIONS

This research focused on investigating the behavior of unreinforced masonry walls built with air lime-based mortars under vertical shearing and lateral cyclic loads. The work addressed the necessity of developing more sustainable construction materials while maintaining structural performance standards. Through a combined experimental, numerical, and analytical approach, the thesis offered new insights into the potential application of lime-based mortars in modern masonry construction, contributing toward a more sustainable building practice.
The research hypotheses outlined in Chapter 1 have been systematically investigated and are discussed below in light of the results obtained through experimental testing, numerical modeling, and analytical evaluation.

- **Thesis 1:** Mortar mixtures containing higher contents of air lime as a partial substitute for cement binders, despite lower mechanical strength, can still provide adequate structural performance of masonry walls, especially in the façade layers of diaphragm walls, while offering environmental benefits.

This hypothesis has been confirmed, based on extensive experimental campaign, which included multiple tests on masonry elements as well as on mortar material samples. Mechanical testing at the mortar level showed that replacing air lime in the binder significantly decreased mechanical performance. For the two mortar mixes studied, where one had double the air lime content of the other in volume, the compressive strength, splitting tensile strength, and flexural strength dropped by roughly 50%. Shear triplet tests revealed a linear relationship between shear strength and pre-compression. In this context, the characteristic values of the initial shear strength for both mortar mixes met the minimum recommended standard for cohesion. Also, the reduction of the mortar strength itself is less evident in the mechanical performance of masonry made with solid clay bricks and the two mortar mixes. Specifically, the compressive strength decreased by about 16%, with a shift in compressive strain of approximately 40%, indicating greater displacement capacity in the mix with higher air lime content in the binder.

- **Thesis 2:** Changes in the air lime content in the mortar composition significantly, yet positively due to their crack resistance, affect the global behavior of masonry walls, in particular in terms of stiffness, strength, deformability and failure mechanisms.

This hypothesis also has been confirmed by the experimental results, which revealed a clear influence of mortar composition on the overall structural response of masonry walls. Full-scale vertical shearing tests showed that walls constructed with MIX-1 mortar achieved higher vertical peak loads than those built with MIX-2 mortar, regardless of the load scheme applied. However, under the 350 mm load scheme, masonry walls with the higher lime content mortar exhibited greater crack and ultimate displacements compared to their counterpart walls, with increases of 13.27% and 47.45%, respectively. Additionally, masonry

made with higher lime content shows a better redistribution of the stresses and higher local deformation properties. Cyclic lateral tests conducted on two types of walls with different aspect ratios indicated that walls built with MIX-1 mortar generally achieved higher base shear capacities compared to those made with MIX-2. However, walls with MIX-2 demonstrated comparable or even superior ultimate displacement capacities. Notably, despite a reduction of approximately 50% in mortar compressive strength due to the inclusion of air lime in the binder, the corresponding decrease in horizontal lateral load for the tested panels was limited to between 7% and 27%. These findings clearly highlight the potential of air lime-based mortars for structural applications, provided that appropriate design considerations are adopted to account for their specific mechanical behavior. Additionally, the experimental program produced a significant database of mechanical properties that will be invaluable for future material characterization and development of the standard's regulations and requirements.

- **Thesis 3:** Simplified numerical models and existing code and analytical recommendations can describe the mechanical response of masonry elements constructed with air lime mortars, although they may require calibration or adjustment to ensure an adequate level of safety and reliability.

This hypothesis has been partially confirmed. Numerical modeling of the tested walls, performed using macro-modeling strategies based on the Total Strain Crack Model (TSCM), showed promising results after calibration with small-scale experimental data. Under vertical shear loading, the models predicted the critical load at crack initiation with a maximum deviation of 14%, while crack deflections were reproduced with differences ranging from 40% to 8%. For cyclic lateral loading, numerical peak load predictions were within 3% to 26% of the experimental values, and the backbone curves as well as stiffness degradation trends were generally well captured. Nevertheless, the models struggled to accurately replicate local crack patterns, particularly in cases involving rocking mechanisms, revealing the limitations of using homogenized macro-models.

Analytical and semi-analytical models given in current standards, such as Eurocode 6 [13] and Eurocode 8 [159], were also evaluated against the experimental results. These formulations provided reasonably accurate predictions of peak shear strength for squat walls (type B), with deviations limited to 15%. However, for slender walls (type A), significant discrepancies were observed, as previously highlighted in the literature and suggesting the need for refinement of existing equations. Moreover, none of the standards adequately captured the displacement capacity of the walls. Predictions were overly conservative for lateral displacements and underestimated vertical crack deflections, failing to reflect the actual deformability observed in tests. These outcomes highlight the need to adapt current design codes, originally developed for cement-based masonry, to better represent the mechanical behavior of lime-based alternatives. By quantifying these discrepancies, this research offers a foundation for future improvements to masonry design provisions, supporting the adoption of more sustainable construction practices.

In summary, this research demonstrated that air lime-based mortars, despite their lower mechanical strength compared to cement-based alternatives, can still enable the construction of masonry walls with satisfactory load-bearing capacity and enhanced deformation capacity. In particular, although the mortar mix with a higher lime content does not fully meet the minimum compressive strength requirements established by Eurocode 6 [13] for structural applications, and Eurocode 8 [159] for seismic design, it may still be considered for design purposes when taking into account the long-term mechanical gains associated with the carbonation process. This consideration becomes even more relevant given the relatively limited differences observed in the mechanical performance of masonry built with mortars containing lower air lime content. Such findings are particularly significant for the air lime industry, which is increasingly focused on promoting more sustainable construction materials and is moving towards the adoption of eco-friendly binders. Through a combination of extensive experimental testing and validated numerical modeling, this study confirmed that lime-based mortars offer a viable and sustainable alternative both for new masonry construction and for the conservation of historic structures. By bridging the gap between material sustainability and structural performance, this research provides a meaningful contribution to the advancement of sustainable building practices and establishes a foundation for the future development of design codes adapted to environmentally friendly masonry materials. Definitely, this work paves the way for a broader use of sustainable materials in modern structural masonry, combining environmental responsibility with verified mechanical performance.

CHAPTER 7 - DIRECTION FOR FURTHER RESEARCH

While this research provided a solid experimental and numerical foundation for understanding the behavior of air lime-based masonry under vertical and lateral loads, several limitations were identified that open up important directions for future investigation.

One significant limitation concerns the long-term durability of air lime-based mortars. The current study focused on the short-term mechanical behavior after limited curing times, without assessing the influence of environmental factors such as humidity variations, freeze-thaw cycles, or wet-dry exposure on the evolution of mechanical properties. Since carbonation is the main mechanism of strength development in these mortars, understanding how environmental conditions can accelerate or limit this process is crucial. Future research should involve long-term exposure tests and artificial aging to simulate real service conditions.

Another limitation lies in the scale of the experimental tests. The study was based primarily on isolated wall panels, and while providing fundamental insights, it does not fully capture the behavior of complete masonry structures where floor-wall interaction, out-of-plane effects, and structural redundancy play significant roles. Future work should include testing of full structural assemblies or multi-storey prototypes to validate and refine the findings at building scale.

In addition, the numerical modeling approach adopted relied on macro-modelling strategies using homogenized material properties. While effective for capturing global behavior, this approach could not accurately simulate localized cracking patterns or progressive damage mechanisms. Future developments should explore more advanced modeling techniques, such as micro-modelling or discrete element methods, to better represent local failure processes and post-peak behavior.

Moreover, the experimental campaign investigated only a limited range of mortar compositions. While the results obtained are promising, broader experimental programs are needed to evaluate different lime/sand ratios, alternative aggregates, the addition of pozzolanic materials, and recycled components, to optimize mortar formulations for different structural and environmental demands.

Finally, an important limitation concerns the lack of comprehensive environmental impact analysis. Although air lime mortars are recognized as sustainable materials, a detailed lifecycle assessment (LCA), including cradle-to-cradle perspectives, should be performed to quantify their environmental advantages compared to conventional cement-based mortars across the entire service life, including end-of-life scenarios.

Building upon these identified limitations, future research should focus on the following directions to further advance the understanding and application of air lime-based masonry:

- long-term studies are needed to investigate the durability of air lime-based mortars under varying environmental conditions and to assess how these factors influence the carbonation process over time. Accelerated aging tests and monitoring of mechanical evolution over extended periods would provide essential data for durability predictions.

- microstructural analysis coupled with performance-based design of mortars should be pursued. Experimental investigations should focus on the interaction mechanisms between lime binder and aggregates of different granulometries, aiming to optimize mortar formulations for enhanced mechanical performance and improved workability.
- the exploration of innovative reinforcement techniques is a promising path. Incorporating natural fibers, industrial fibers, polymer grids, or other reinforcement strategies within air lime-based mortars could significantly enhance their mechanical properties, particularly for applications in seismic zones or for reinforced plasters. Large-scale tests should validate the effectiveness of these solutions.
- innovative additions through the reuse of construction and demolition waste should be investigated. Using recycled aggregates or filler materials could further reduce the environmental footprint of air lime mortars, promoting a circular economy approach in the construction sector.
- a comprehensive sustainability and environmental impact assessment is crucial. Future studies should carry out detailed LCA comparing air lime mortars with other materials, considering not only the production and use phases but also the possibilities for reuse, recycling, and repurposing at the end of their service life.
- the application of advanced modeling techniques should be expanded. The use of refined finite element methods (FEM), coupled with multi-physics simulations, would allow more accurate prediction of mechanical behavior under complex loading conditions. Integrating these tools into practical engineering workflows and promoting their adoption within the industry could greatly facilitate the wider use of sustainable masonry systems.

By addressing these research directions, it will be possible to unlock the full potential of air lime-based masonry and consolidate its role in future sustainable construction practices, bridging the gap between traditional materials and modern performance requirements. Additionally, integrating experimental advancements with digital design innovations will be key to unlocking the full potential of sustainable masonry in the coming decades.

CHAPTER 8 – APPENDIX

This appendix presents the raw results of the experimental tests, followed by a statistical analysis that includes the possible elimination of outliers. Outlier elimination, typically involving the removal of one or two extreme values, is performed to improve the reliability and representativeness of the dataset. The method relies on calculating a test statistic and comparing it to a critical threshold at a significance level of $\alpha = 0.05$. For instance, assuming x_i is a generic test result and x_s is the value suspected to deviate from the rest of the sample, the ordered dataset is represented as:

$$x_1 \leq x_2 \leq x_3 \ldots \leq x_{n-1} \leq x_n \tag{41}$$

The standard deviation estimator s_0 is given in function of the average $\bar{x}$ by:

$$s_0 = \sqrt{\frac{\sum_1^n (x_i - \bar{x})^2}{n-1}} \tag{42}$$

The corresponding test statistic T_s is calculated as:

$$T_s = \frac{|x_s - \bar{x}|}{s_0} \tag{43}$$

If $T_s > T_\alpha$, where T_α is the critical value (e.g., 1.67, 1.82, 1.94 for number of experimental tests of 5, 6, and 7, respectively), the test statistic falls in the rejection region, and the value x_s is excluded from the dataset. In the subsequent sections, results concerning bricks and mortar main mechanical properties are presented.

8.1 Physical and mechanical properties of clay bricks

The coefficient of water absorption $c_{w,i}$ is determined according EN 772-11 [209], based on the gross area of the face of the specimen immersed in water A_s, the mass of the specimen after drying $m_{dry,s}$ and the mass of the specimen after soaking for 1 min $m_{so,s}$. Table 40 gives all the measured quantities together with the average, standard deviation and coefficient of variation. Table 41 shows the results concerning the elimination of one extreme value

The water absorption W_a is determined according to EN 772-21 [208], based on the difference between the dry mass of the specimen (M_d) and its mass after 24 hours of water soaking, as applied for clay units (M_s). Table 42 gives all the measured quantities together with the average, standard deviation and coefficient of variation. The Table 43 indicates that one extreme value was excluded during the statistical evaluation. Consequently, this value was omitted from further analysis, and both the mean and the coefficient of variation were recalculated without it. The revised results are presented in the main section of the analysis (Section 3.1).

Table 40: Test results for the determination of the initial rate of absorption $c_{w,i}$.

id_bricks	$m_{dry,s}$ [g]	A_s [mm^2]	$m_{so,s}$ [g]	$c_{w,i}$ [kg/(mq min)]
1	2331	13781.6	2378	3.41
2	2288	12536.16	2332	3.51
3	2130	13919.04	2165	2.51
4	2338	14213.5	2382	3.10
5	2317	13811.48	2357	2.90
6	2344	14141.88	2388	3.11
Average				3.09
St. Dev.				0.36
CoV				0.12

Table 41: Elimination of extreme value for the measurement of the initial rate of absorption $c_{w,i}$.

Elimination of one extreme value			
$c_{w,i}$ [kg/(mq min)]	T_α	T_s	$T_s>T_\alpha$
2.51	1.82	1.60	APPROVED
2.90	1.82	0.54	APPROVED
3.10	1.82	0.02	APPROVED
3.11	1.82	0.06	APPROVED
3.41	1.82	0.89	APPROVED
3.51	1.82	1.17	APPROVED

Table 42: Test results for the determination of the water absorption W_a.

id_bricks	M_d [g]	M_s [g]	W_a [%]
1	2192	2436	11.13
2	2291	2538	10.78
3	2134	2351	10.17
4	2132	2586	21.29
5	2307	2570	11.40
6	2391	2579	7.86
Average			12.11
St. Dev.			4.68
CoV			0.39

Table 43: Elimination of extreme value for the measurement of the water absorption W_a.

Elimination of one extreme value			
W_a [%]	T_α	T_s	$T_s>T_\alpha$
7.86	1.82	0.91	APPROVED
10.17	1.82	0.41	APPROVED
10.78	1.82	0.28	APPROVED
11.13	1.82	0.21	APPROVED
11.40	1.82	0.15	APPROVED
21.29	1.82	1.96	REJECTED

For the determination of the flexural properties, the dimensions of the brick are considered (Fig. 159a). The geometric properties are evaluated by dividing the mid cross-section into three rectangular areas (Fig. 159b). For each area, the following parameters are determined: the static moment with respect to the y-axis (S_y), the position of the centroid (y_g),

the moment of inertia about its own centroidal axis (***J₁, J₂*** and ***J₃***), and the contribution to the total moment of inertia relative to the global centroidal axis (***J_g***), using the Huygens-Steiner theorem with corresponding distances x_1, x_2 and x_3. Given the load P recorded at failure, the flexural strength σ_{fl} is determined as (44):

$$\sigma_{fl} = \frac{b_r}{4}\frac{P}{J_g}\left(\frac{a}{2} \pm y_g\right) \qquad (44)$$

where b_r is the distance between the supports and the ± is connected to the determination of the flexural strength in the case of the plain side load application ($\sigma_{f\text{-}Plain}$) and frogged side ($\sigma_{f\text{-}Frog}$). Table 44-45-46 illustrates the geometric, inertial and flexural strength relative to the test with load application on the plain side.

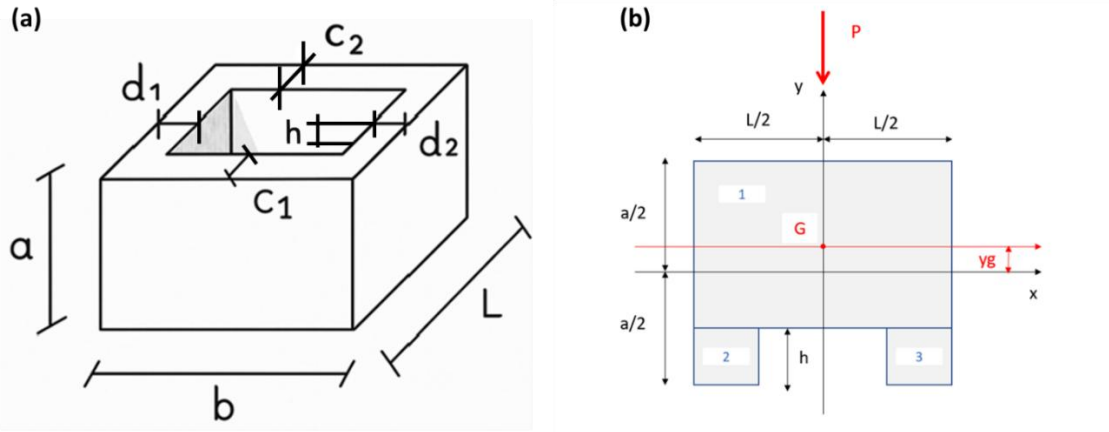

Figure 159: Geometric configuration of the frogged brick unit, with associated dimensions **(a)**. Idealized cross-sectional model divided into three rectangular areas (1, 2, and 3) for the calculation of inertial properties **(b)**.

Table 44: Geometric dimension of tested bricks for flexural strength with load application on the plain side.

id_brick	Mass [Kg]	*a*[mm]	*b*[mm]	c_1[mm]	c_2[mm]	d_1[mm]	d_2[mm]	*h*[mm]	*L*[mm]
1	2.304	61	216	32	30	39	39	11	102
2	2.308	61	217	32	31	38	37	11	101
3	2.311	63	215	30	31	39	37	11	101
4	2.329	63	215	31	31	38	38	12	103
5	2.309	64	212	32	31	38	39	11	102
6	2.35	62	215	32	31	39	38	12	101
7	2.316	61	216	32	31	38	40	11	102

Table 45: Inertial properties of tested bricks for flexural strength with load application on the plain side.

id_brick	S_y [mm³]	y_g [mm]	J_1 [mm⁴]	J_2 [mm⁴]	J_3 [mm⁴]	x_1 [mm⁴]	x_2 [mm⁴]	x_3 [mm⁴]	J_g [mm⁴]
1	11000.0	1.9	1062500.0	3549.3	3327.5	66005.9	254757	238834	1628974.8
2	10450.0	1.8	1052083.3	3549.3	3438.4	68403.7	253190	245278	1625943.7
3	11440.0	1.9	1183450.7	3327.5	3438.4	66881.7	257454	266036	1780589.8
4	12141.1	2.0	1172405.0	3928.9	3928.9	73894.6	274876	274876	1803910.1
5	11368.5	1.9	1265454.5	3549.3	3438.4	71470.2	283189	274340	1901442.2
6	11400.0	2.0	1052083.3	4608.0	4464.0	82281.9	279179	270455	1693071.6
7	10725.0	1.9	1062500.0	3549.3	3438.4	67893.7	253790	245859	1637031.8

Table 46: Flexural strength with load application on the plain side ($\sigma_{f\text{-}Plain}$) and elimination of extreme value.

				Elimination of one extreme value			
id_brick	***P*[KN]**	***b_r* [mm]**	***$\sigma_{f\text{-}Plain}$* [MPa]**		***T_α***	***T_s***	
1	3.98	180	3.6	2.88	1.94	1.19	APPROVED
2	3.22	180	2.9	3.22	1.94	0.94	APPROVED
3	6.81	180	5.8	3.56	1.94	0.67	APPROVED
4	7.58	180	6.3	4.54	1.94	0.08	APPROVED
5	5.67	180	4.5	4.78	1.94	0.26	APPROVED
6	3.67	180	3.2	5.75	1.94	1.00	APPROVED
7	5.38	180	4.8	6.34	1.94	1.45	APPROVED
Average			4.44				
St. Dev.			1.30				
CoV			0.29				

For the evaluation of the flexural properties with the load applied on the frogged side, six additional specimens were considered. The results in terms of geometry, inertial properties, and strength, with the elimination of extreme values, are presented in the following Table 47-48-49.

Table 47: Geometric dimension of tested bricks for flexural strength with load application on the frogged side.

id_brick	**Mass [Kg]**	***a*[mm]**	***b*[mm]**	***c_1*[mm]**	***c_2*[mm]**	***d_1*[mm]**	***d_2*[mm]**	***h*[mm]**	***L*[mm]**
8	2.27	64	215.3	31.1	32	38.6	40.5	10.5	102.4
9	2.294	65.4	215.6	32.2	31.9	39.9	37.1	10.5	102.3
10	2.314	65.1	215.1	32.8	31.3	39.4	37.1	11.5	105.8
11	2.312	65.9	215.7	34	36.9	39.1	40.5	9.7	103.1
12	2.31	65.3	216.7	32.6	33.6	39.6	38.9	10.3	102.2
13	2.277	65.8	217.5	31.3	30.6	38.9	38.5	10.1	101.8

Table 48: Inertial properties of tested bricks for flexural strength with load application on the frogged side.

id_brick	***S_y* [mm^3]**	***y_g* [mm]**	***J_1* [mm^4]**	***J_2* [mm^4]**	***J_3* [mm^4]**	***x_1* [mm^4]**	***x_2* [mm^4]**	***x_3* [mm^4]**	***J_g* [mm^4]**
8	11038.4	1.8	1306712.5	3000.2	3087.0	65301.0	266125.2	273826.6	1918052.5
9	11010.2	1.8	1410624.5	3106.3	3077.4	68775.0	288289.8	285603.9	2059476.8
10	12851.9	2.0	1357684.3	4157.1	3966.9	79508.8	312986.4	298673.0	2056976.5
11	8776.8	1.4	1525058.0	2585.9	2806.5	70815.8	286114.7	310518.5	2197899.4
12	10197.0	1.6	1416960.4	2968.6	3059.6	70128.6	284690.5	293423.4	2071231.1
13	11223.3	1.8	1465993.7	2687.4	2627.3	60529.2	277593.9	271385.7	2080817.2

Table 49: Flexural strength with load application on the plain side ($\sigma_{f\text{-}Frog}$) and elimination of extreme value.

				Elimination of one extreme value			
id_brick	***P*[KN]**	***b_r* [mm]**	***$\sigma_{f\text{-}Frog}$* [MPa]**		***T_α***	***T_s***	
8	4.27	180	3.0	2.10	1.82	1.18	APPROVED
9	3.11	180	2.1	2.58	1.82	0.87	APPROVED
10	8.43	180	5.6	3.03	1.82	0.58	APPROVED
11	7.52	180	4.9	4.86	1.82	0.60	APPROVED
12	3.82	180	2.6	5.39	1.82	0.94	APPROVED
13	8.01	180	5.4	5.63	1.82	1.10	APPROVED
Average			3.93				
St. Dev.			1.54				
CoV			0.39				

For the evaluation of the compressive strength of the bricks, peak load applied *P* at failure is dived for the cross-sectional area (215 x 102 mm) of the bricks obtaining the value of the compressive strength σ_c. Table 50 shows that the dispersion of the results is minimal.

Table 50: Brick compressive strength σ_c evaluated on full units with elimination of one extreme value.

			Elimination of one extreme value			
id_brick	***P* [N]**	**σ_c [MPa]**		***T_α***	***T_s***	
1	566399.9	25.82	23.34	1.94	1.201307508	APPROVED
2	565062.9	25.76	23.41	1.94	1.139917343	APPROVED
3	541696.9	24.70	23.98	1.94	0.60233896	APPROVED
4	554543.3	25.28	24.70	1.94	0.080695703	APPROVED
5	525820.9	23.97	25.29	1.94	0.633388696	APPROVED
6	511899.0	23.34	25.77	1.94	1.085979997	APPROVED
7	513325.9	23.40	25.83	1.94	1.143499413	APPROVED
Average		24.62				
St. Dev.		1.06				
CoV		0.043				

8.2 Mechanical properties of mortar samples

The raw mechanical property values of the tested mortar samples are presented in tabular format for both mortar specimens, including the possibility of excluding one outlier. The flexural strength of mortar prisms is determined according to EN 1015-11 [53] based on the dimensions of the sample Fig. 160a and the static scheme Fig. 160b. The σ_{fl} is evaluated as per equation (39), function of the peak load P applied. Table 51 and Table 52 shows the results in terms of flexural strength of tested specimens with the evaluation of possible outliner for mortar MIX-1. At the same time, Table 53 and Table 54 gives the same overview of experimental values for mortar MIX-2.

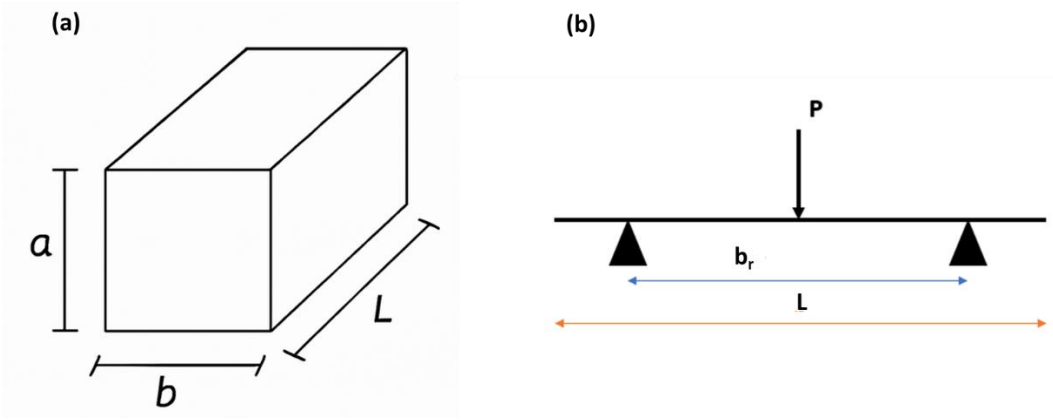

Figure 160: Geometric representation of the standard mortar specimen **(a)**. Schematic of the three-point bending test setup used for flexural strength determination, where P is the applied load, *L* is the total span length, and b_r is the distance between the supports **(b)**.

$$\sigma_{fl} = 1.5\,\frac{P\,b_r}{a\,b^2} \qquad (45)$$

Table 51: Flexural strength σ_{fl} determination for prisms made with mortar MIX-1.

id_mortar	Weight [g]	a [mm]	b [mm]	L [mm]	b_r [mm]	P_{max} [KN]	σ_{fl} [MPa]
1	513	37	39	158	100	0.596	1.59
2	500	36	39	158	100	0.918	2.51
3	532	40	39	158	100	1.006	2.48
4	501	38	40	158	100	0.826	2.04
5	510	39	40	158	100	0.906	2.18
6	496	38	40	158	100	0.996	2.46
Average							2.21
St. Dev.							0.35
CoV							0.16

Table 52: Elimination of extreme value for the measurement of the flexural strength σ_{fl} for prisms made with mortar MIX-1.

Elimination of one extreme value			
σ_{fl} [MPa]	T_α	T_s	$T_s>T_\alpha$
1.59	1.82	1.73	APPROVED
2.04	1.82	0.48	APPROVED
2.18	1.82	0.09	APPROVED
2.46	1.82	0.69	APPROVED
2.48	1.82	0.75	APPROVED
2.51	1.82	0.85	APPROVED

A portion of the resulting prism specimens was subjected to compressive testing, wherein a vertical load was applied over a designated load application area measuring 40 × 40 mm, in accordance with standardized procedures. The comprehensive results obtained from the experimental campaign are presented in Tables 55 and 56. Specifically, these tables detail the performance characteristics and failure behavior observed in specimens incorporating mortar MIX-1. The corresponding results for specimens constructed with mortar MIX-2 are provided and discussed in a separate section to ensure clarity and facilitate direct comparison between the two mortar compositions.

Table 53: Flexural strength σ_{fl} determination for prisms made with mortar MIX-2.

id_mortar	Weight [g]	a [mm]	b [mm]	L [mm]	b_r [mm]	P_{max} [KN]	σ_{fl} [MPa]
1	499	40	39	158	100	0.433	1.07
2	490	40	39	158	100	0.546	1.35
3	508	40	39	158	100	0.477	1.18
4	503	38	39	158	100	0.553	1.44
5	522	40	39	158	100	0.461	1.14
6	496	39	39	158	100	0.479	1.21
Average							1.23
St. Dev.							0.14
CoV							0.11

Table 54: Elimination of extreme value for the measurement of the flexural strength σ_{fl} for prisms made with mortar MIX-2.

Elimination of one extreme value			
σ_{fl} [MPa]	T_α	T_s	$T_s>T_\alpha$
1.07	1.82	1.18	APPROVED
1.14	1.82	0.67	APPROVED
1.18	1.82	0.38	APPROVED
1.21	1.82	0.13	APPROVED
1.35	1.82	0.86	APPROVED
1.44	1.82	1.51	APPROVED

Table 55: Compressive strength σ_c determination for prisms made with mortar MIX-1 with elimination of one extreme value.

			Elimination of one extreme value			
id_mortar	P_{max} [KN]	σ_c [MPa]		T_α	T_s	
1	13.13	8.21	6.43	1.82	1.42	APPROVED
2	13.24	8.28	6.84	1.82	1.03	APPROVED
3	13.97	8.73	8.21	1.82	0.27	APPROVED
4	10.94	6.84	8.28	1.82	0.34	APPROVED
5	10.29	6.43	8.73	1.82	0.78	APPROVED
6	14.41	9.01	9.01	1.82	1.04	APPROVED
Average		7.91				
St. Dev.		1.04				
CoV		0.13				

Finally, the results of the standard splitting tensile strength tests are presented in Tables 57 and 58, corresponding respectively to mortar MIX-1 and MIX-2. For both mixes, all measured values were found to be statistically consistent and thus considered valid for the calculation of both the average tensile strength and the coefficient of variation. These results provide further insight into the mechanical performance differences between the two mortar compositions under tensile stress conditions.

Table 56: Compressive strength σ_c determination for prisms made with mortar MIX-2 with elimination of one extreme value.

			Elimination of one extreme value			
id_mortar	P_{max} [KN]	σ_c [MPa]		T_α	T_s	
1	7.02	4.39	3.70	1.82	1.45	APPROVED
2	6.74	4.21	3.85	1.82	0.98	APPROVED
3	6.16	3.85	4.21	1.82	0.15	APPROVED
4	6.93	4.33	4.33	1.82	0.52	APPROVED
5	7.21	4.51	4.39	1.82	0.69	APPROVED
6	5.92	3.70	4.51	1.82	1.07	APPROVED
Average		4.16				
St. Dev.		0.32				
CoV		0.08				

Table 57: Splitting tensile strength σ_t determination for prisms made with mortar MIX-1 with elimination of one extreme value.

		Elimination of one extreme value			
id_mortar	**σ_t [MPa]**		**T_α**	**T_s**	**$T_s>T_\alpha$**
1	0.45	0.34	1.67	1.38	APPROVED
2	0.42	0.42	1.67	0.37	APPROVED
3	0.51	0.45	1.67	0.07	APPROVED
4	0.57	0.51	1.67	0.55	APPROVED
5	0.34	0.57	1.67	1.27	APPROVED
Average	0.46				
St. Dev.	0.087				
CoV	0.19				

Table 58: Splitting tensile strength σt determination for prisms made with mortar MIX-2 with elimination of one extreme value.

		Elimination of one extreme value			
id_mortar	**σ_t [MPa]**		**T_α**	**T_s**	**$T_s>T_\alpha$**
1	0.26	0.19	1.67	1.57	APPROVED
2	0.24	0.22	1.67	0.22	APPROVED
3	0.24	0.24	1.67	0.33	APPROVED
4	0.22	0.24	1.67	0.35	APPROVED
5	0.19	0.26	1.67	1.11	APPROVED
Average	0.23				
St. Dev.	0.025				
CoV	0.11				

8.3 Mechanical properties of masonry samples

The results from the compressive tests conducted in accordance with EN 1052-1 [97] are presented for masonry constructed with lower air-lime content mortar. These include the compressive strength (Table 59), elastic modulus (Table 60) and ductility (Table 61). Corresponding Tables 62-63-64 report the same set of results for masonry assembled with a higher-lime-content mortar. The overall trend indicates that ductility values are generally accompanied by a certain number of rejected results. Additional test results, such as those from diagonal compression and triplet shear tests, are not included in this evaluation due to the limited number of available specimens for the same mortar type, which prevents reliable statistical analysis. For the same reasons are not included the results from the vertical shear test and the lateral cyclic response of full-scale masonry walls.

Table 59: Compressive strength f_c determination for masonry made with mortar MIX-1 with elimination of one extreme value.

		Elimination of one extreme value			
id_masonry	**f_c [MPa]**		**T_α**	**T_s**	**$T_s>T_\alpha$**
1	8.30711703	6.29	1.82	1.57	APPROVED
2	8.812887082	7.63	1.82	0.57	APPROVED
3	10.16334224	8.31	1.82	0.06	APPROVED
4	6.291730448	8.81	1.82	0.30	APPROVED
5	9.202375989	9.20	1.82	0.59	APPROVED
6	7.626458092	10.16	1.82	1.31	APPROVED
Average	8.40				
St. Dev.	1.33				
CoV	0.159				

Table 60: Elastic modulus E_c determination for masonry made with mortar MIX-1 with elimination of one extreme value.

		Elimination of one extreme value			
id_masonry	**E_c [MPa]**		**T_α**	**T_s**	**$T_s>T_\alpha$**
1	2039.971869	2039.97	1.82	1.59	APPROVED
2	2544.105793	2285.46	1.82	0.74	APPROVED
3	2790.98541	2544.11	1.82	0.15	APPROVED
4	2285.456462	2575.13	1.82	0.25	APPROVED
5	2770.394699	2770.39	1.82	0.92	APPROVED
6	2575.129262	2790.99	1.82	0.99	APPROVED
Average	2501.00				
St. Dev.	290.87				
CoV	0.116				

Table 61: Ductility μ determination for masonry made with mortar MIX-1 with elimination of one extreme value.

		Elimination of one extreme value			
id_masonry	**μ [MPa]**		**T_α**	**T_s**	**$T_s>T_\alpha$**
1	1.23	1.23	1.82	0.85	APPROVED
2	1.32	1.31	1.82	0.51	APPROVED
3	1.89	1.32	1.82	0.46	APPROVED
4	1.32	1.32	1.82	0.45	APPROVED
5	1.55	1.55	1.82	0.45	APPROVED
6	1.31	1.89	1.82	1.83	REJECTED
Average	1.29				
St. Dev.	0.046				
CoV	0.0356				

Table 62: Compressive strength f_c determination for masonry made with mortar MIX-2 with elimination of one extreme value.

		Elimination of one extreme value			
id_masonry	**f_c [MPa]**		**T_α**	**T_s**	**$T_s>T_\alpha$**
1	6.8197	6.72	1.82	0.996	APPROVED
2	6.7972	6.80	1.82	0.691	APPROVED
3	6.9267	6.82	1.82	0.606	APPROVED
4	6.7165	6.93	1.82	0.203	APPROVED
5	7.3090	7.31	1.82	1.238	APPROVED
6	7.3145	7.31	1.82	1.2593	APPROVED
Average	6.98				
St. Dev.	0.265				
CoV	0.0379				

Table 63: Elastic modulus E_c determination for masonry made with mortar MIX-2 with elimination of one extreme value.

		Elimination of one extreme value			
id_masonry	**E_c [MPa]**		**T_α**	**T_s**	**$T_s>T_\alpha$**
1	2049.55469	1606.28	1.82	0.971	APPROVED
2	1606.277708	1706.57	1.82	0.797	APPROVED
3	1970.381999	1970.38	1.82	0.340	APPROVED
4	2522.052284	2049.55	1.82	0.203	APPROVED
5	3146.645345	2522.05	1.82	0.615	APPROVED
6	1706.570634	3146.65	1.82	1.697	APPROVED
Average	2166.91				
St. Dev.	576.99				
CoV	0.266				

Table 64: : Ductility μ determination for masonry made with mortar MIX-2 with elimination of one extreme value.

		Elimination of one extreme value			
id_masonry	**μ_c [MPa]**		**T_α**	**T_s**	**$T_s>T_\alpha$**
1	1.588	1.44	1.82	0.576	APPROVED
2	1.509	1.45	1.82	0.555	APPROVED
3	1.540	1.51	1.82	0.392	APPROVED
4	2.435	1.54	1.82	0.311	APPROVED
5	1.438	1.59	1.82	0.185	APPROVED
6	1.447	2.44	1.82	2.019	REJECTED
Average	1.50				
St. Dev.	0.063				
CoV	0.042				

Bibliography

[1] Watts, J., 2019. Concrete: the most destructive material on Earth. The Guardian, 25, pp.1-9.

[2] Macharia, S.M., 2021. Creep mechanisms in cement and lime mortared masonry (Doctoral dissertation, University of Bath).

[3] Cizer, Ö., Van Balen, K., Van Gemert, D. and Elsen, J., 2009. Competition between carbonation and hydration on the hardening of calcium hydroxide and calcium silicate binders (Vol. 2, No. 33, pp. 353-368). WTA Publications; Karlsruhe, Germany.

[4] Haach, V.G., Vasconcelos, G. and Lourenço, P.B., 2014. Assessment of compressive behavior of concrete masonry prisms partially filled by general mortar. Journal of Materials in Civil Engineering, 26(10), p.04014068.

[5] Smith, A.S. and Givens, R., 2016, November. A review of research and experimental findings on the effects of hydrated (air) lime addition to cement-based masonry mortars on the properties of the mortars and associated masonry. In Brick and Block Masonry: Proceedings of the 16th International Brick and Block Masonry Conference, Padova, Italy, 26-30 June 2016 (pp. 1897-1904). CRC Press.

[6] Hendrickx, R., 2009. The adequate measurement of the workability of masonry mortar.

[7] Mosquera, M.J., Silva, B., Prieto, B. and Ruiz-Herrera, E., 2006. Addition of cement to lime-based mortars: Effect on pore structure and vapor transport. Cement and Concrete Research, 36(9), pp.1635-1642.

[8] Grosso, M., Biganzoli, L., Campo, F.P., Pantini, S. and Tua, C., 2020. Literature review on the assessment of the carbonation potential of lime in different markets and beyond. Report prepared by Assessment on Waste and Resources (AWARE) Research Group at Politecnico di Milano (PoliMI), for the European Lime Association (EuLA), p.333.

[9] Campo, F.P., Tua, C., Biganzoli, L., Pantini, S. and Grosso, M., 2021. Natural and enhanced carbonation of lime in its different applications: a review. Environmental Technology Reviews, 10(1), pp.224-237.

[10] Roca, P., Lourenço, P.B. and Gaetani, A., 2019. Historic construction and conservation: materials, systems and damage. Routledge.

[11] Augenti, N. and Parisi, F., 2019. Teoria e tecnica delle strutture in muratura: Analisi e progettazione. HOEPLI EDITORE.

[12] Kubica, J., 2024. Masonry systems: Past, present and future. In MATEC Web of Conferences (Vol. 403, p. 01003). EDP Sciences.

[13] EN 1996-1-1: Eurocode 6. (2005). Design of masonry structures—Part 1-1: General rules for reinforced and unreinforced masonry structures. European Committee for Standardization (CEN).

[14] Augenti, N., Parisi, F. and Acconcia, E., 2012, September. MADA: online experimental database for mechanical modelling of existing masonry assemblages. In Proceedings of the 15th World Conference on Earthquake Engineering (pp. 24-28).

[15] Mishra, A. K., and Mishra, A. (2021). “Geochemical characterization of bricks used in historical monuments of 14-18th century CE of Haryana region of the Indian subcontinent: Reference to raw materials and production technique,” Construction and Building Materials, 269, 121802.

[16] Ergenç, D., Fort, R., Varas− Muriel, M.J. and Alvarez de Buergo, M., 2021. Mortars and plasters—How to characterize aerial mortars and plasters. Archaeological and Anthropological Sciences, 13(11), p.197.

[17] Vitruvius and Warren, H.L., 1960. The ten books on architecture. Dover Publications.

[18] Burghignoli, A., 1985. Lezioni di meccanica delle terre. ESA.

[19] Ghiassi, B. and Lourenço, P.B. eds., 2018. Long-term performance and durability of Masonry structures: degradation mechanisms, health monitoring and service life design. Woodhead Publishing.
[20] Fernandes, F.M., Lourenço, P.B. and Castro, F., 2010. Ancient clay bricks: manufacture and properties. In Materials, technologies and practice in historic heritage structures (pp. 29-48). Dordrecht: Springer Netherlands.
[21] Lumantarna, R., 2012. Material characterisation of New Zealand's clay brick unreinforced masonry buildings (Doctoral dissertation, ResearchSpace@ Auckland).
[22] Almesfer, N., Dizhur, D.Y., Lumantarna, R. and Ingham, J.M., 2014. Material properties of existing unreinforced clay brick masonry buildings in New Zealand. Bulletin of the New Zealand Society for Earthquake Engineering, 47(2), pp.75-96.
[23] Cultrone, G., Sebastián, E., Elert, K., De la Torre, M.J., Cazalla, O. and Rodriguez–Navarro, C., 2004. Influence of mineralogy and firing temperature on the porosity of bricks. Journal of the European Ceramic society, 24(3), pp.547-564.
[24] Elert, K., Cultrone, G., Navarro, C.R. and Pardo, E.S., 2003. Durability of bricks used in the conservation of historic buildings—influence of composition and microstructure. Journal of Cultural Heritage, 4(2), pp.91-99.
[25] Cultrone, G., Rodriguez-Navarro, C., Sebastian, E., Cazalla, O. and De La Torre, M.J., 2001. Carbonate and silicate phase reactions during ceramic firing. European Journal of Mineralogy, 13(3), pp.621-634.
[26] Dizhur, D., Lumantarna, R., Biggs, D.T. and Ingham, J.M., 2017. In-situ assessment of the physical and mechanical properties of vintage solid clay bricks. Materials and Structures, 50, pp.1-14.
[27] Jafari, S., Rots, J.G. and Esposito, R., 2022. A correlation study to support material characterisation of typical Dutch masonry structures. Journal of Building Engineering, 45, p.103450.
[28] Matysek, P. and Witkowski, M., 2016. A comparative study on the compressive strength of bricks from different historical periods. International Journal of Architectural Heritage, 10(4), pp.396-405.
[29] Lourenço, P.B., Fernandes, F.M. and Castro, F., 2010. Handmade clay bricks: chemical, physical and mechanical properties. International Journal of Architectural Heritage, 4(1), pp.38-58.
[30] EN 772-1. (2011). Methods of test for masonry units–Part 1: Determination of compressive strength. CEN; Brussels.
[31] Cabané, A., Pelà, L. and Roca, P., 2022. Anisotropy and compressive strength evaluation of solid fired clay bricks by testing small specimens. Construction and Building Materials, 344, p.128195.
[32] Cabané, A., Pelà, L. and Roca, P., 2023. Effect of cross section aspect ratio and bearing surfaces treatment on the compressive strength of solid fired clay brick specimens. Construction and Building Materials, 383, p.131397.
[33] Australian Standards, AS/NZS 4456.4 Masonry units and segmental pavers and flags -Methods of test Determining compressive strength of masonry units, (2003).
[34] Standards Council of Canada, CAN/CSA A82:14 (R2018) Fired masonry brick made from clay or shale, (2018).
[35] ASTM, C., 2016. 1552, Standard practice for capping concrete masonry units, related units and masonry prisms for compression testing. Am. Soc. Test. Mater.(2003).
[36] EN 998-2. (2010) Specification for mortar for masonry-part 2: Masonry mortar. CEN; Brussels.
[37] PN-EN 1996-1-1:2008 Projektowanie konstrukcji murowych – Cześć 1-1: Reguły ogólne dla zbrojonych i niezbrojonych konstrukcji murowych (in Polish).
[38] Ministero delle Infrastrutture e dei Trasporti. 2018. NTC 2018 - Norme Tecniche per le Costruzioni di cui al D.M. 17/01/2018. Italy: Gazzetta Ufficiale N. 42 del 20/ 02/2018 (in Italian).
[39] Taylor, H.F., 1997. Cement chemistry (Vol. 2, p. 459). London: Thomas Telford.

[40] EN 197-1. (2011) Cement–Part 1: Composition, specifications and conformity criteria for common cements. CEN; Brussels.
[41] Veiga, R., 2017. Air lime mortars: What else do we need to know to apply them in conservation and rehabilitation interventions? A review. Construction and Building Materials, 157, pp.132-140.
[42] Lawrence, R.M.H., 2006. A study of carbonation in non-hydraulic lime mortars.
[43] Boynton, R.S., 1966. Chemistry and technology of lime and limestone. (No Title).
[44] Oliveira, M.A.N., 2015. A multi-physics approach applied to masonry structures with non-hydraulic lime mortars (Doctoral dissertation, Universidade do Minho (Portugal)).
[45] Van Balen, K., 2005. Carbonation reaction of lime, kinetics at ambient temperature. Cement and concrete research, 35(4), pp.647-657.
[46] Vasovic, D., Terzovic, J., Kontic, A., Okrajnov-Bajic, R. and Sekularac, N., 2021. The Influence of Water/Binder Ratio on the Mechanical Properties of Lime-Based Mortars with White Portland Cement. Crystals, 11(8), p.958.
[47] EN 459-1. (2010) Building lime. Part, 1, pp.19-21. CEN; Brussels.
[48] Lanas, J. and Alvarez-Galindo, J.I., 2003. Masonry repair lime-based mortars: factors affecting the mechanical behavior. Cement and concrete research, 33(11), pp.1867-1876.
[49] Silva, B.A., Pinto, A.F. and Gomes, A., 2014. Influence of natural hydraulic lime content on the properties of aerial lime-based mortars. Construction and Building Materials, 72, pp.208-218.
[50] Silva, B.A., Pinto, A.F. and Gomes, A., 2015. Natural hydraulic lime versus cement for blended lime mortars for restoration works. Construction and Building Materials, 94, pp.346-360.
[51] Lanas, J., Bernal, J.P., Bello, M.A. and Galindo, J.A., 2004. Mechanical properties of natural hydraulic lime-based mortars. Cement and concrete research, 34(12), pp.2191-2201.
[52] Apostolopoulou, M., Bakolas, A. and Kotsainas, M., 2021. Mechanical and physical performance of natural hydraulic lime mortars. Construction and Building Materials, 290, p.123272.
[53] EN 1015-11. (2019) Part 11: Determination of flexural and compressive strength of hardened mortar. CEN; Brussels.
[54] Ergenç, D., Fort, R., Varas− Muriel, M.J. and Alvarez de Buergo, M., 2021. Mortars and plasters—How to characterize aerial mortars and plasters. Archaeological and Anthropological Sciences, 13(11), p.197.
[55] ASTM. (2008). "Standard Test Method for Compressive Strength of Hydraulic Cement Mortars (Using 2-in. or [50-mm] Cube Specimens)." C 109/C 109M - 08, ASTM International, Pennsylvania, United States
[56] Magalhães, A. and Veiga, R., 2009. Physical and mechanical characterisation of historic mortars. Application to the evaluation of the state of conservation. Materiales de Construcción, 59(295), pp.61-77.
[57] Łątka, D. and Matysek, P., 2020. Determination of mortar strength in historical brick masonry using the penetrometer test and double punch test. Materials, 13(12), p.2873.
[58] Łątka, D., Seręga, S. and Matysek, P., 2019. Estimation of mortar compressive strength based on specimens extracted from masonry bed joints. Structural Analysis of Historical Constructions (pp. 577-586). Springer, Cham. 10.1007/978-3-319-99441-3_62.
[59] De Vico, F.S., Zagaroli, A., Rodríguez-Navarro, C., Kubica, J. and Gorski, M., 2023. A Physico-chemical Study of Lime-based Mortars from Different Historical Periods. NanoWorld J, 9(S2), pp.S256-S261.
[60] Zagaroli, A., De Vico, F.S., Ruiz Agudo E., Kubica, J., Rodríguez-Navarro, C. and Gorski, M., 2023. A comparative study of the composition and physico-mechanical properties of bricks from different periods. Proceedings of 14th North America Masonry Conference, USB device.

[61] Ali, A., Chiang, Y.W. and Santos, R.M., 2022. X-ray diffraction techniques for mineral characterization: A review for engineers of the fundamentals, applications, and research directions. Minerals, 12(2), p.205.
[62] Mishra, A.K. and Mishra, A., 2021. Geochemical characterization of bricks used in historical monuments of 14-18th century CE of Haryana region of the Indian subcontinent: Reference to raw materials and production technique. Construction and Building Materials, 269, p.121802.
[63] Han, W., Pei, S. and Liu, F., 2022. Material characterization of the brick in the Ming Dynasty heritage wall of Pianguan County: A case study. Case Studies in Construction Materials, 16, p.e00940.
[64] Arizzi, A. and Cultrone, G., 2021. Mortars and plasters—how to characterise hydraulic mortars. Archaeological and Anthropological Sciences, 13(9), p.144.
[65] Inkson, B.J., 2016. Scanning electron microscopy (SEM) and transmission electron microscopy (TEM) for materials characterization. In Materials characterization using nondestructive evaluation (NDE) methods (pp. 17-43). Woodhead publishing.
[66] Cultrone, G., Sidraba, I. and Sebastián, E., 2005. Mineralogical and physical characterization of the bricks used in the construction of the "Triangul Bastion", Riga (Latvia). Applied clay science, 28(1-4), pp.297-308.
[67] Vásárhelyi, L., Kónya, Z., Kukovecz, Á. and Vajtai, R., 2020. Microcomputed tomography–based characterization of advanced materials: a review. Materials Today Advances, 8, p.100084.
[68] Chung, S.Y., Kim, J.S., Stephan, D. and Han, T.S., 2019. Overview of the use of micro-computed tomography (micro-CT) to investigate the relation between the material characteristics and properties of cement-based materials. Construction and Building Materials, 229, p.116843.
[69] Vicente, M.A., González, D.C. and Mínguez, J., 2019. Recent advances in the use of computed tomography in concrete technology and other engineering fields. Micron, 118, pp.22-34.
[70] Shetty, N., Livitsanos, G., Verstrynge, E., Aggelis, D.G., Hemelrijck, D.V., Balen, K.V. and Wevers, M., 2020. Observation of crack initiation zone in brick masonry couplets under compression using X-ray microfocus computed tomography and digital image correlation. International Journal of Masonry Research and Innovation, 5(4), pp.518-537.
[71] Coletti, C., Cultrone, G., Maritan, L. and Mazzoli, C., 2016. Combined multi-analytical approach for study of pore system in bricks: How much porosity is there?. Materials Characterization, 121, pp.82-92.
[72] DIN 18555-9 (1999) Prüfung von Mörteln mit mineralischen Bindemitteln – Teil 9, Festmörtel: Bestimmung der Fugendruckfestigkeit.
[73] Sassoni, E., Mazzotti, C. and Pagliai, G., 2014. Comparison between experimental methods for evaluating the compressive strength of existing masonry buildings. Construction and Building Materials, 68, pp.206-219.
[74] Šlivinskas, T., Jonaitis, B. and Zavalis, R., 2017. Mortar compressive strength estimation by applying various experimental test methods. Procedia Engineering, 172, pp.1123-1128.
[75] RILEM, T., 1980. Recommended tests to measure the deterioration of stone and to assess the effectiveness of treatment methods. Mater. Struct, 13(75), pp.175-253.
[76] Comité Euro-International du Béton, 1993. CEB-FIP model code 1990: Design code. Thomas Telford Publishing.
[77] Palermo, V., Tsionis, G. and Sousa, M.L., 2018. Building stock inventory to assess seismic vulnerability across Europe. Publications Office of the European Union: Luxembourg.
[78] Kubica, J., 2014. Typical masonry wall enclosures in Poland. In Enclosure Masonry Wall Systems Worldwide (pp. 157-177). CRC Press.
[79] Angelillo, M. ed., 2014. Mechanics of masonry structures (Vol. 551). London, UK: Springer.

[80] Solarino, F., Oliveira, D.V. and Giresini, L., 2019. Wall-to-horizontal diaphragm connections in historical buildings: A state-of-the-art review. Engineering structures, 199, p.109559.
[81] Vlachakis, G., Vlachaki, E. and Lourenço, P.B., 2020. Learning from failure: Damage and failure of masonry structures, after the 2017 Lesvos earthquake (Greece). Engineering Failure Analysis, 117, p.104803.
[82] Giaretton, M., Dizhur, D., da Porto, F. and Ingham, J.M., 2016, May. Construction details and observed earthquake performance of unreinforced clay brick masonry cavity-walls. In Structures (Vol. 6, pp. 159-169). Elsevier.
[83] Baird, A., Palermo, A., Pampanin, S., Riccio, P. and Tasligedik, A.S., 2011. Focusing on reducing the earthquake damage to facade systems. Bulletin of the New Zealand Society for Earthquake Engineering, 44(2), pp.108-120.
[84] Van der Pluijm, R., 1999. Out-of-plane bending of masonry: behaviour and strength.
[85] Barros, J.A., Almeida, J.C. and Lourenço, P.B., 2002. Characterization of brick and brick–mortar interface under uniaxial tension.
[86] McGinley, W.M., 1994. Bond wrench testing—An evaluation of laboratory testing procedures. Proceedings of the 10th IB2MaC, Calgary, AB, Canada, pp.5-7.
[87] Singh, S.B. and Munjal, P., 2017. Bond strength and compressive stress-strain characteristics of brick masonry. Journal of Building Engineering, 9, pp.10-16.
[88] Kubica, J. and Galman, I., 2023. Influence of Mixing Water Content and Curing Time on Bond Strength of Clinker Masonry: The Wrench Test Method. Materials, 16(6), p.2171.
[89] EN 1052-5. (2005) Part 5: Determination of Bond Strength by the Bond Wrench Method. CEN; Brussels.
[90] Gaggero, M.B. and Esposito, R., 2023. Experimental characterisation of flexural bond behaviour in brick masonry. Materials and Structures, 56(3), p.62.
[91] EN 1052-2. (2016) Part 2: Determination of Flexural Strength. CEN; Brussels.
[92] Singhal, V. and Rai, D.C., 2014. Suitability of half-scale burnt clay bricks for shake table tests on masonry walls. Journal of Materials in Civil Engineering, 26(4), pp.644-657.
[93] EN 1052-3. (2002) Part 3: Determination of Initial Shear Strength. CEN; Brussels.
[94] HILSDORF, H.K., 1969. Investigation into the failure mechanism of brick masonry loaded in axial compression. Designing engineering and constructing with masonry products, pp.34-41.
[95] Nalon, G.H., Ribeiro, J.C.L., Pedroti, L.G., da Silva, R.M., de Araújo, E.N.D., Santos, R.F. and de Lima, G.E.S., 2022. Review of recent progress on the compressive behavior of masonry prisms. Construction and Building Materials, 320, p.126181.
[96] AMERICAN SOCIETY FOR TESTING AND MATERIALS, 2012. ASTM C1314-16, Standard Test Method for Compressive Strength of Masonry Prisms.
[97] EN 1052-1. (2001) Part 1: Determination of compressive strength. CEN; Brussels.
[98] Kent, D.C. and Park, R., 1971. Flexural members with confined concrete. Journal of the structural division, 97(7), pp.1969-1990.
[99] Sepe, V., Spacone, E., Raka, E. and Camata, G., 2014, June. Seismic analysis of masonry buildings: equivalent frame approach with fiber beam elements. In Proceedings of the 9th International Conference on Structural Dynamics, Porto, Portugal (pp. 237-244).
[100] DIN EN 1996-1-1:2013-02 Eurocode 6: Bemessung und Konstruktion von Mauerwerksbauten. Teil 1-1: Allgemeine Regeln für bewehrtes und unbewehrtes Mauerwerk; in Ver- bindung mit: DIN EN 1996-1-1/NA:2012-05; Beuth-Verlag, Berlin, (in German).
[101] Kaushik, H.B., Rai, D.C. and Jain, S.K., 2007. Stress-strain characteristics of clay brick masonry under uniaxial compression. Journal of materials in Civil Engineering, 19(9), pp.728-739.

[102] Lumantarna, R., Biggs, D.T. and Ingham, J.M., 2014. Uniaxial compressive strength and stiffness of field-extracted and laboratory-constructed masonry prisms. Journal of Materials in Civil Engineering, 26(4), pp.567-575.
[103] MSJC (Masonry Standards Joint Committee) (TMS 402/ACI 530/ASCE 5 and TMS 602/ACI 530.1/ASCE 6). Building Code Requirements and Specification for Masonry Structures; 2013.
[104] Asteris, P.G., Lourenço, P.B., Hajihassani, M., Adami, C.E.N., Lemonis, M.E., Skentou, A.D., Marques, R., Nguyen, H., Rodrigues, H. and Varum, H., 2021. Soft computing-based models for the prediction of masonry compressive strength. Engineering Structures, 248, p.113276.
[105] Thaickavil, N.N. and Thomas, J., 2018. Behaviour and strength assessment of masonry prisms. Case Studies in Construction Materials, 8, pp.23-38.
[106] Silva, L.M., Vasconcelos, G. and Lourenço, P.B., 2021. Innovative systems for earthquake-resistant masonry infill walls: Characterization of materials and masonry assemblages. Journal of Building Engineering, 39, p.102195.
[107] Borri, A., Castori, G., Corradi, M. and Speranzini, E., 2011. Shear behavior of unreinforced and reinforced masonry panels subjected to in situ diagonal compression tests. Construction and Building Materials, 25(12), pp.4403-4414.
[108] Segura, J., Pelà, L., Saloustros, S. and Roca, P., 2021. Experimental and numerical insights on the diagonal compression test for the shear characterisation of masonry. Construction and Building Materials, 287, p.122964.
[109] Rodríguez-Mariscal, J.D., Ma, Q. and Solís, M., 2020. Experimental analysis of diagonal compression and splitting tests for the characterization of shear and tensile behavior of adobe masonry. Engineering Structures, 215, p.110633.
[110] Joyklad, P., Ali, N., Rashid, M.U., Hussain, Q., Magbool, H.M., Elnemr, A. and Chaiyasarn, K., 2021. Strength enhancement of interlocking hollow brick masonry walls with low-cost mortar and wire mesh. Infrastructures, 6(12), p.166.
[111] ASTM, E. "519-10. Standard test method for diagonal tension (shear) in masonry assemblages." Annual Book of ASTM Standard; American Society for Testing and Materials: West Conshohocken, PA, USA (2010).
[112] RILEM TC 76-LUM. Diagonal tensile strength tests of small wall specimens (1994)
[113] Frocht, Max Mark. "Recent advances in photoelasticity and an investigation of the stress distribution in square blocks subjected to diagonal compression." Trans. ASME 53 (1931): 135-153.
[114] Brignola, A., Frumento, S., Lagomarsino, S. and Podestà, S., 2008. Identification of shear parameters of masonry panels through the in-situ diagonal compression test. International Journal of Architectural Heritage, 3(1), pp.52-73.
[115] Turnšek, V. and Čačovič, F., 1971, April. Some experimental results on the strength of brick masonry walls. In Proceedings of the 2nd international brick masonry conference (pp. 149-156). Stoke-on-Trent, UK: British Ceramic Research Association.
[116] FEMA, P., 2000. commentary for the seismic rehabilitation of building, FEMA-356, Federal Emergency Management Agency. Washington, DC.
[117] Nzsee (new zealand society for earthquake engineering). (2017b). the seismic assessment of existing buildings: Part c8, unreinforced masonry buildings, technical guidelines for engineering assessments. wellington: Nzsee.
[118] Celano, T., Argiento, L.U., Ceroni, F. and Casapulla, C., 2021. In-plane behaviour of masonry walls: numerical analysis and design formulations. Materials, 14(19), p.5780.
[119] DeJong, M.J., 2016, November. Thematic Keynote: Settlement effects on masonry structures. In Structural Analysis of Historical Constructions: Anamnesis, Diagnosis, Therapy, Controls:

Proceedings of the 10th International Conference on Structural Analysis of Historical Constructions (SAHC, Leuven, Belgium, 13-15 September 2016) (pp. 449-456). CRC Press.
[120] Giardina, G., Marini, A., Hendriks, M.A., Rots, J.G., Rizzardini, F. and Giuriani, E., 2012. Experimental analysis of a masonry façade subject to tunnelling-induced settlement. Engineering Structures, 45, pp.421-434.
[121] Giardina, G., Van de Graaf, A.V., Hendriks, M.A., Rots, J.G. and Marini, A., 2013. Numerical analysis of a masonry façade subject to tunnelling-induced settlements. Engineering structures, 54, pp.234-247.
[122] Portioli, F. and Cascini, L., 2016. Assessment of masonry structures subjected to foundation settlements using rigid block limit analysis. Engineering Structures, 113, pp.347-361.
[123] Portioli, F. and Cascini, L., 2017. Large displacement analysis of dry-jointed masonry structures subjected to settlements using rigid block modelling. Engineering Structures, 148, pp.485-496.
[124] Pepe, M., Sangirardi, M., Reccia, E., Pingaro, M., Trovalusci, P. and De Felice, G., 2020. Discrete and continuous approaches for the failure analysis of masonry structures subjected to settlements. Frontiers in Built Environment, 6, p.43.
[125] Piekarczyk, A., 2016. Shear stiffness of solid clay brick wallets sheared perpendicularly to the masonry bed joints. Procedia engineering, 161, pp.1064-1069.
[126] Kubica, J., 2016. Unreinforced clay brick masonry wallettes sheared perpendicular or parallel to bed joints—a comparative study. In Brick and Block Masonry (pp. 1683-1690). CRC Press.
[127] Kubica, J. (2003). Niezbrojone ściany murowe poddane odkształceniom postaciowym wywołanym nierównomiernymi pionowymi przemieszczeniami podłoża [Tesi di abilitazione]. Gliwice: Wydawnictwo Politechniki Śląskiej (https://delibra.bg.polsl.pl).
[128] Piekarczyk, A., 2020. Deformability of the masonry subjected to shearing due to vertical displacements. Budownictwo i Architektura, 19(4), pp.5-16.
[129] Piekarczyk, A., 2019, February. The influence of compressive stress on the load-bearing capacity of masonry subjected to vertical displacements. In IOP Conference Series: Materials Science and Engineering (Vol. 471, No. 5, p. 052017). IOP Publishing.
[130] Mann, W. and Müller, H., 1982. Failure of shear-stressed masonry: an enlarged theory, tests and application to shear walls.
[131] Piekarczyk, A., 2019, February. Cracking and failure mechanism of masonry walls loaded vertically and supported by deflecting structural member. In IOP Conference Series: Materials Science and Engineering (Vol. 471, No. 5, p. 052018). IOP Publishing
[132] Holanda, G., Ramalho, M. and Corrêa, M., 2003, June. Experimental and numerical analysis of masonry load-bearing walls subjected to differential settlements. In Proceedings of the 9th North American Masonry Conference (pp. 134-145).
[133] Holanda, G., Ramalho, M. and Corrêa, M., 2007. Experimental and numerical analysis of masonry walls with openings subjected to differential foundation settlements. In Proceedings of the 10th North American Masonry Conference (pp. 26-27).
[134] Loots, J.J. and Van Zijl, G.P.A.G., 2004, July. Experimental verification of settlement induced damage to masonry walls. In Proceedings of 13th International Brick and Block Masonry Conference (pp. 4-7).
[135] Meyerhof, G.G., 1953. Some recent foundation research and its application to design. The Structural Engineer, 31(6), pp.151-167.
[136] Savalle, N., Funari, M.F., Fernandes, L., Colombo, C., Szabó, S., Hussaini, S., Karimzadeh, S. and Lourenço, P.B., 2022, June. Large static testing equipment: design and testing of a settlement facility. In International Conference on Testing and Experimentation in Civil Engineering (pp. 171-183). Cham: Springer Nature Switzerland.

[137] Kania, T., Derkach, V. and Nowak, R., 2021. Testing crack resistance of non-load-bearing ceramic walls with door openings. Materials, 14(6), p.1379.
[138] Piekarczyk, A. and Jasiński, R., 2016, June. Distortions and the way of damaging masonry walls supported on deflected structural elements. In 16th International Brick and Block Masonry Conference–Trends, Innovations and Challenges (pp. 26-30). Taylor & Francis Group CRC Press.
[139] Piekarczyk, A., 2020. The experimental investigation of the failure of load-bearing masonry walls supported by a deflecting structure. Budownictwo i Architektura, 19(3), pp.123-134.
[140] Vanin, F., Zaganelli, D., Penna, A. and Beyer, K., 2017. Estimates for the stiffness, strength and drift capacity of stone masonry walls based on 123 quasi-static cyclic tests reported in the literature. Bulletin of Earthquake Engineering, 15, pp.5435-5479.
[141] Morandi, P., Albanesi, L., Graziotti, F., Piani, T.L., Penna, A. and Magenes, G., 2018. Development of a dataset on the in-plane experimental response of URM piers with bricks and blocks. Construction and Building Materials, 190, pp.593-611.
[142] Frumento, S., Magenes, G., Morandi, P. and Calvi, G.M., 2009. Interpretation of experimental shear tests on clay brick masonry walls and evaluation of q-factors for seismic design. Pavia: Iuss Press.
[143] Tomaževič, M., 2009. Shear resistance of masonry walls and Eurocode 6: shear versus tensile strength of masonry. Materials and structures, 42, pp.889-907.
[144] Celano, T., Argiento, L.U., Ceroni, F. and Casapulla, C., 2021. Literature review of the in-plane behavior of masonry walls: Theoretical vs. experimental results. Materials, 14(11), p.3063.
[145] Salmanpour, A.H., Mojsilovic, N. and Schwartz, J., 2013. Deformation capacity of unreinforced masonry walls subjected to in-plane loading: a state-of-the-art review. International Journal of Advanced Structural Engineering, 5, pp.1-12.
[146] Anthoine, A., Magonette, G. and Magenes, G., 1995, August. Shear-compression testing and analysis of brick masonry walls. In Proceedings of the 10th European conference on earthquake engineering (Vol. 3, pp. 1657-1662). Duma.
[147] Magenes, G. and Calvi, G.M., 1992. Cyclic behaviour ofbrick masonry walls. In Proceedings of the 10th world conference on earthquake engineering (pp. 3517-3522).
[148] Magenes, G. and Calvi, G.M., 1997. In-plane seismic response of brick masonry walls. Earthquake engineering & structural dynamics, 26(11), pp.1091-1112.
[149] Raijmakers, T.M.J. and Vermeltfoort, A.T., 1992. Deformation controlled tests in masonry shear walls. Delft: Report B-92-1156, TNO-Bouw.
[150] Triller, P., Tomaževič, M. and Gams, M., 2020. Experimental testing of seismic response of brick masonry walls under different boundary conditions. In Brick and Block Masonry-From Historical to Sustainable Masonry (pp. 838-845). CRC Press.
[151] Petry, S. and Beyer, K., 2014. Influence of boundary conditions and size effect on the drift capacity of URM walls. Engineering structures, 65, pp.76-88.
[152] Lourenço, P.J.B.B., 1997. Two aspects related to the analysis of masonry structures: Size effect and parameter sensibility. Technische Universiteit Delft, Faculty of Civil Engineering and Geosciences, Mechanics & Structures, Computational Mechanics.
[153] Aoki, T., Shrestha, K.C., Nonaka, U. and Aoki, H., 2020. In-plane shear strength characteristics of masonry walls with varying mortar types and aspect ratios. In Brick and Block Masonry-From Historical to Sustainable Masonry (pp. 412-418). CRC Press.
[154] Messali, F., Esposito, R., Ravenshorst, G.J.P. and Rots, J.G., 2020. Experimental investigation of the in-plane cyclic behaviour of calcium silicate brick masonry walls. Bulletin of Earthquake Engineering, 18, pp.3963-3994.

[155] Elghazouli, A.Y., Bompa, D.V., Mourad, S.A. and Elyamani, A., 2021. In-plane lateral cyclic behaviour of lime-mortar and clay-brick masonry walls in dry and wet conditions. Bulletin of earthquake engineering, 19, pp.5525-5563.

[156] Tariq, H., Najafgholipour, M.A., Sarhosis, V. and Milani, G., 2023, January. In-plane strength of masonry wall panels: A comparison between design codes and high-fidelity models. In Structures (Vol. 47, pp. 1869-1899). Elsevier.

[157] American Society of Civil Engineers. 2014. ASCE standard ASCE/SEI 41-13: American Society of Civil Engineers: seismic evaluation and retrofit of existing buildings. 10.1061/9780784412855.

[158] NZSEE, New Zealand Society for Earthquake Engineering (2017). The seismic assessment of existing buildings, Part C8: Seismic assessment of unreinforced masonry buildings. Wellington, New Zealand: MBIE, EQC, SESOC, NZSEE and NZGS.

[159] EN 1998-3: Eurocode 8 (2005): Design of structures for earthquake resistance – Part 3: Assessment and retrofitting of buildings. European Committee for Standardization (CEN).

[160] Ministero delle Infrastrutture e dei Trasporti. Istruzioni per l'Applicazione dell'Aggiornamento delle 'Norme Tecniche per le Costruzioni' di cui al Decreto Ministeriale 17 Gennaio 2018, Circolare 21 gennaio 2019, n. 7 C.S.LL.PP; Gazzetta Ufficiale della Repubblica Italiana: Rome, Italy, 2019.

[161] Sansoni, C., da Silva, L.C., Marques, R., Pampanin, S. and Lourenço, P.B., 2023. SLaMA-URM method for the seismic vulnerability assessment of UnReinforced Masonry structures: Formulation and validation for a substructure. Journal of Building Engineering, 63, p.105487.

[162] Beyer, K., Araya, E.A.I. and Saloustros, S., 2022, August. Drift capacity models for the new masonry chapter of Eurocode 8 Part 1-2. In European Conference on Earthquake Engineering and Seismology (pp. 398-416). Cham: Springer International Publishing.

[163] Addessi, D., Marfia, S., Sacco, E. and Toti, J., 2014. Modeling approaches for masonry structures. The Open Civil Engineering Journal, 8(1).

[164] NZSEE (New Zealand Society for Earthquake Engineering). (2017). The Seismic Assessment of Existing Buildings: Part C2, Technical Guidelines for Engineering Assessments. Wellington: NZSEE.

[165] D'Altri, A.M., Sarhosis, V., Milani, G., Rots, J., Cattari, S., Lagomarsino, S., Sacco, E., Tralli, A., Castellazzi, G. and de Miranda, S., 2020. Modeling strategies for the computational analysis of unreinforced masonry structures: review and classification. Archives of computational methods in engineering, 27, pp.1153-1185.

[166] Lourenço, P.B. and Rots, J.G., 1997. Multisurface interface model for analysis of masonry structures. Journal of engineering mechanics, 123(7), pp.660-668.

[167] Haach, V.G., Vasconcelos, G. and Lourenço, P.B., 2011. Parametrical study of masonry walls subjected to in-plane loading through numerical modeling. Engineering Structures, 33(4), pp.1377-1389.

[168] Abdulla, K.F., Cunningham, L.S. and Gillie, M., 2017. Simulating masonry wall behaviour using a simplified micro-model approach. Engineering Structures, 151, pp.349-365.

[169] Guo YT, Bompa DV, Elghazouli AY. Nonlinear numerical assessments for the in-plane response of historic masonry walls. Engineering Structures. 2022 Oct 1;268:114734.

[170] Petracca, M., Camata, G., Spacone, E. and Pelà, L., 2023. Efficient Constitutive model for continuous micro-modeling of masonry structures. International Journal of Architectural Heritage, 17(1), pp.134-146.

[171] Willam K. J., Warnke E. P.; Constitutive Models for the Triaxial Behaviour of Concrete. IABSE Seminar on Concrete Structures Subjected to Triaxial Stresses, Bergamo, IABSE Proc. Vol.19, 1974; p.1-30

[172] SZOJDA, L., 2012. Numerical analysis of strengthened masonry structures due to subsoil deformation. Architecture Civil Engineering Environment, 5(4), pp.69-78.
[173] KRZYWOŃ, R. and WANDZIK, G., 2014. NUMERICAL MODELING OF CONCRETE STRUCTURES–RESEARCH ACHIEVEMENTS OF PROFESSOR STANISŁAW MAJEWSKI. Architecture Civil Engineering Environment, 7(1), pp.19-26.
[174] Kubica, J., 2012. Mechanika muru obciążonego w swej płaszczyźnie. Wydawnictwo Politechniki Śląskiej.
[175] Ungureanu, D., Țăranu, N., Ghiga, D.A., Isopescu, D.N., Mihai, P. and Cozmanciuc, R., 2021. Diagonal tensile test on masonry panels strengthened with textile-reinforced mortar. Materials, 14(22), p.7021.
[176] Jirásek, M., 2011. Damage and smeared crack models. In Numerical modeling of concrete cracking (pp. 1-49). Vienna: Springer Vienna.
[177] Schreppers, G.M.A., Garofano, A., Messali, F. and Rots, J.G., 2016. DIANA validation report for masonry modelling. DIANA FEA report.
[178] Sousamli, M., Messali, F. and Rots, J.G., 2022. A total-strain based orthotropic continuum model for the cyclic nonlinear behavior of unreinforced brick masonry structures. International Journal for Numerical Methods in Engineering, 123(8), pp.1813-1840.
[179] Basili, M., Marcari, G. and Vestroni, F., 2016. Nonlinear analysis of masonry panels strengthened with textile reinforced mortar. Engineering Structures, 113, pp.245-258.
[180] Basili, M., Vestroni, F. and Marcari, G., 2019. Brick masonry panels strengthened with textile reinforced mortar: experimentation and numerical analysis. Construction and Building Materials, 227, p.117061.
[181] Fages, J.M., Tarque, N., Rodríguez-Mariscal, J.D. and Solís, M., 2022. Calibration of a total strain crack model for adobe masonry based on compression and diagonal compression tests. Construction and Building Materials, 352, p.128965.
[182] Lubliner, J., Oliver, J., Oller, S. and Oñate, E., 1989. A plastic-damage model for concrete. International Journal of solids and structures, 25(3), pp.299-326.
[183] Lee, J. and Fenves, G.L., 1998. Plastic-damage model for cyclic loading of concrete structures. Journal of engineering mechanics, 124(8), pp.892-900.
[184] Gatta, C., Addessi, D. and Vestroni, F., 2018. Static and dynamic nonlinear response of masonry walls. International Journal of Solids and Structures, 155, pp.291-303.
[185] Rainone, L.S., Tateo, V., Casolo, S. and Uva, G., 2023. About the use of concrete damage plasticity for modeling masonry post-elastic behavior. Buildings, 13(8), p.1915.
[186] Anthoine, A., 1995. Derivation of the in-plane elastic characteristics of masonry through homogenization theory. International journal of solids and structures, 32(2), pp.137-163.
[187] Pande, G.N., Liang, J.X. and Middleton, J., 1989. Equivalent elastic moduli for brick masonry. Computers and Geotechnics, 8(3), pp.243-265.
[188] Milani, G.A.B.R.I.E.L.E., Lourenço, P.B. and Tralli, A., 2006. Homogenised limit analysis of masonry walls, Part I: Failure surfaces. Computers & structures, 84(3-4), pp.166-180.
[189] Milani, G., Lourenço, P.B. and Tralli, A., 2006. Homogenised limit analysis of masonry walls, Part II: Structural examples. Computers & structures, 84(3-4), pp.181-195.
[190] Addessi, D., Di Re, P., Gatta, C. and Sacco, E., 2021. Multiscale analysis of out-of-plane masonry elements using different structural models at macro and microscale. Computers & Structures, 247, p.106477.
[191] Bertolesi, E., Milani, G. and Casolo, S., 2018. Homogenization towards a mechanistic Rigid Body and Spring Model (HRBSM) for the non-linear dynamic analysis of 3D masonry structures. Meccanica, 53, pp.1819-1855.

[192] Petracca, M., Pelà, L., Rossi, R., Oller, S., Camata, G. and Spacone, E., 2016. Regularization of first order computational homogenization for multiscale analysis of masonry structures. Computational mechanics, 57, pp.257-276.
[193] Lagomarsino, S., Penna, A., Galasco, A. and Cattari, S., 2013. TREMURI program: an equivalent frame model for the nonlinear seismic analysis of masonry buildings. Engineering structures, 56, pp.1787-1799.
[194] Raka, E., Spacone, E., Sepe, V. and Camata, G., 2015. Advanced frame element for seismic analysis of masonry structures: model formulation and validation. Earthquake Engineering & Structural Dynamics, 44(14), pp.2489-2506.
[195] Peruch, M., Spacone, E. and Camata, G., 2019. Nonlinear analysis of masonry structures using fiber-section line elements. Earthquake Engineering & Structural Dynamics, 48(12), pp.1345-1364.
[196] D'Altri, A.M., Cannizzaro, F., Petracca, M. and Talledo, D.A., 2022. Nonlinear modelling of the seismic response of masonry structures: calibration strategies. Bulletin of Earthquake Engineering, 20(4), pp.1999-2043.
[197] Camata, G., Marano, C., Sepe, V., Spacone, E., Siano, R., Petracca, M., Roca, P. and Pelà, L., 2022. Validation of non-linear equivalent-frame models for irregular masonry walls. Engineering Structures, 253, p.113755.
[198] Cattari, S., Camilletti, D., D'Altri, A.M. and Lagomarsino, S., 2021. On the use of continuum Finite Element and Equivalent Frame models for the seismic assessment of masonry walls. Journal of Building Engineering, 43, p.102519.
[199] Quagliarini, E.N.R.I.C.O., Maracchini, G.I.A.N.L.U.C.A. and Clementi, F.A.B.I.O., 2017. Uses and limits of the Equivalent Frame Model on existing unreinforced masonry buildings for assessing their seismic risk: A review. Journal of Building Engineering, 10, pp.166-182.
[200] Cattari, S., Calderoni, B., Caliò, I., Camata, G., de Miranda, S., Magenes, G., Milani, G. and Saetta, A., 2022. Nonlinear modeling of the seismic response of masonry structures: critical review and open issues towards engineering practice. Bulletin of Earthquake Engineering, 20(4), pp.1939-1997.
[201] Vanin, F., Penna, A. and Beyer, K., 2020. A three-dimensional macroelement for modelling the in-plane and out-of-plane response of masonry walls. Earthquake Engineering & Structural Dynamics, 49(14), pp.1365-1387.
[202] Caliò, I., Marletta, M. and Pantò, B., 2012. A new discrete element model for the evaluation of the seismic behaviour of unreinforced masonry buildings. Engineering Structures, 40, pp.327-338.
[203] Pantò, B., Cannizzaro, F., Caliò, I. and Lourenço, P.B., 2017. Numerical and experimental validation of a 3D macro-model for the in-plane and out-of-plane behavior of unreinforced masonry walls. International Journal of Architectural Heritage, 11(7), pp.946-964.
[204] Caliò, I. and Pantò, B., 2014. A macro-element modelling approach of Infilled Frame Structures. Computers & Structures, 143, pp.91-107.
[205] Pantò, B., Caliò, I. and Lourenço, P.B., 2018. A 3D discrete macro-element for modelling the out-of-plane behaviour of infilled frame structures. Engineering Structures, 175, pp.371-385.
[206] Cattari, S. and Magenes, G., 2022. Benchmarking the software packages to model and assess the seismic response of unreinforced masonry existing buildings through nonlinear static analyses. Bulletin of Earthquake Engineering, pp.1-36.
[207] Ottonelli, D., Manzini, C.F., Marano, C., Cordasco, E.A. and Cattari, S., 2022. A comparative study on a complex URM building: part I—sensitivity of the seismic response to different modelling options in the equivalent frame models. Bulletin of Earthquake Engineering, 20(4), pp.2115-2158.

[208] EN 772-21. (2011). Methods of test for masonry units – Part 21: Determination of water absorption of clay and calcium silicate masonry units by cold water absorption. CEN; Brussels.
[209] EN 772-11. (2011). Methods of test for masonry units - Part 11: Determination of water absorption of aggregate concrete, autoclaved aerated concrete, manufactured stone and natural stone masonry units due to capillary action and the initial rate of water absorption of clay masonry units. CEN; Brussels.
[210] EN 459-1. (2010). Building lime: Definitions, specifications and conformity criteria–Part 1. CEN; Brussels.
[211] EN 197-1. (2011). Cement: Composition, specifications and conformity criteria for common cements–Part 1. CEN; Brussels.
[212] Zagaroli, A., Kubica, J., Galman, I. and Falkjar, K., 2024. Study on the Mechanical Properties of Two General-Purpose Cement–Lime Mortars Prepared Based on Air Lime. Materials, 17(5), p.1001.
[213] EN 1015-3. (1999). Methods of test for mortar for masonry-Part 3: Determination of consistence of fresh mortar (by flow table). CEN; Brussels.
[214] EN 12390-13. (2013). Testing hardened concrete- Part-13: Determination of secant modulus of elasticity in compression. CEN; Brussels.
[215] ASTM International Committee C09 on Concrete and Concrete Aggregates, 2017. Standard Test Method for Splitting Tensile Strength of Cylindrical Concrete Specimens1. ASTM international.
[216] Recommendation, R.D., 1985. Determination of the fracture energy of mortar and concrete by means of three-point bend tests on notched beams. Materials and structures, 18(106), pp.285-290.
[217] Standard, J.C.I., 2003. Method of test for fracture energy of concrete by use of notched beam. JCI-S-001e2003, Japan Concrete Institute.
[218] Hillerborg, A.R.N.E., 1983. Concrete fracture energy tests performed by 9 laboratories according to a draft RILEM recommendation. Report to RILEM TC50-FMC, Report TVBM-3015, Lund, Sweden.
[219] British Standards Institution, BS 4551, Methods of testing mortars, screeds and plasters, 1980.
[220] Sahu, S., Teja, P.R.R., Sarkar, P. and Davis, R., 2019. Effect of brick prewetting on masonry bond strength. Journal of Materials in Civil Engineering, 31(10), p.06019009.
[221] Briceño, C., Azenha, M., Vasconcelos, G. and Lourenço, P.B., 2024. Influence of conditioning of clay bricks over shear strength of brick masonry. Journal of Building Engineering, 82, p.108138.
[222] ASTM International, “ASTM C67: Standard Test Methods for Sampling and Testing Brick and Structural Clay Tile,” 2020.
[223] Falkjar, K., Zagaroli, A. and Kubica, J., 2024, July. Experimental Testing Versus Numerical Modelling of Small Masonry Wallettes in Axial Compression. In International Brick and Block Masonry Conference (pp. 412-431). Cham: Springer Nature Switzerland.
[224] Borri, A., Corradi, M., Sisti, R., Buratti, C., Belloni, E. and Moretti, E., 2016. Masonry wall panels retrofitted with thermal-insulating GFRP-reinforced jacketing. Materials and Structures, 49, pp.3957-3968.
[225] Kałuża, M., 2022. Experimental analysis of surface application of fiber-reinforced polymer composite on shear behavior of masonry walls made of autoclaved concrete blocks. Buildings, 12(12), p.2208.
[226] Abdul-Razzaq, Khattab Saleem, Ali Mustafa Jalil, and Sarah Farhan Jebur. "Behaviour of reinforced concrete deep beams in previous studies." IOP Conference Series: Materials Science and Engineering. Vol. 518. No. 2. IOP Publishing, 2019.
[227] Jasiński, Radosław. "Research on the influence of bed joint reinforcement on strength and deformability of masonry shear walls." Materials 12.16 (2019): 2543.

[228] Applied Technology Council, et al. Interim testing protocols for determining the seismic performance characteristics of structural and nonstructural components. Federal Emergency Management Agency, 2007.
[229] Vasconcelos, Graça. "Experimental investigations on the mechanics of stone masonry: Characterization of granites and behavior of ancient masonry shear walls." University of Minho (2005): 266.
[230] Nicolini, Luca. "Equivalent viscous damping and inelastic displacement for strengthened and reinforced masonry walls." (2012): 1-169.
[231] Li, M., Hao, H., Shi, Y. and Hao, Y., 2018. Specimen shape and size effects on the concrete compressive strength under static and dynamic tests. Construction and Building Materials, 161, pp.84-93.
[232] Ramesh, Meera, Miguel Azenha, and Paulo B. Lourenço. "Mechanical characterization of lime-cement mortars: E-modulus and fracture energy." (2019).
[233] Ramesh, Meera, Miguel Azenha, and Paulo B. Lourenço. "Quantification of impact of lime on mechanical behaviour of lime cement blended mortars for bedding joints in masonry systems." Construction and Building Materials 229 (2019): 116884.
[234] Guinea, G.V., Planas, J. and Elices, M., 1992. Measurement of the fracture energy using three-point bend tests: Part 1—Influence of experimental procedures. Materials and Structures, 25, pp.212-218.
[235] Planas, J., Elices, M. and Guinea, G.V., 1992. Measurement of the fracture energy using three-point bend tests: Part 2—Influence of bulk energy dissipation. Materials and Structures, 25, pp.305-312.
[236] Elices, M., Guinea, G.V. and Planas, J., 1992. Measurement of the fracture energy using three-point bend tests: Part 3—influence of cutting the P-δ tail. Materials and Structures, 25, pp.327-334.
[237] Khalilpour, S., BaniAsad, E. and Dehestani, M., 2019. A review on concrete fracture energy and effective parameters. Cement and Concrete research, 120, pp.294-321.
[238] Garijo, Lucía, et al. "Advanced mechanical characterization of NHL mortars and cohesive simulation of their failure behavior." Construction and Building Materials 153 (2017): 569-577.
[239] Elices, M., G. V. Guinea, and J. Planas. "On the measurement of concrete fracture energy using three-point bend tests." Materials and structures 30 (1997): 375-376.
[240] Ramesh, M., Briceno, C., Azenha, M. and Lourenço, P.B., 2020. Impact of type of mortar on shear bond strength of brick masonry. In Brick and Block Masonry-from Historical to Sustainable Masonry (pp. 591-595). CRC Press.
[241] Costigan, Adrian, and Sara Pavía. "Influence of the mechanical properties of lime mortar on the strength of brick masonry." Historic Mortars: Characterisation, Assessment and Repair. Dordrecht: Springer Netherlands, 2012. 359-372.
[242] Ramesh, M., Parente, M., Azenha, M. and Lourenço, P.B., 2023. Influence of lime on strength of structural unreinforced masonry: toward improved sustainability in masonry mortars. Sustainability, 15(21), p.15320.
[243] Segura, Jorge, Luca Pelà, and Pere Roca. "Monotonic and cyclic testing of clay brick and lime mortar masonry in compression." Construction and Building Materials 193 (2018): 453-466.
[244] Drougkas, Anastasios, Pere Roca, and Climent Molins. "Compressive strength and elasticity of pure lime mortar masonry." Materials and structures 49 (2016): 983-999.
[245] Ramesh, Meera, et al. "Evaluating the role of mortar composition on the cyclic behavior of unreinforced masonry shear walls." Materials 17.18 (2024): 4443.
[246] Lourenço, Paulo B., and Angelo Gaetani. Finite element analysis for building assessment: Advanced use and practical recommendations. Routledge, 2022.

[247] Parisse, Francesco, et al. "Finite Element and Equivalent Frame modeling approaches for URM buildings: Implications of different assumptions in the seismic assessment." Journal of Building Engineering 61 (2022): 105230.
[248] Nocera, M., 2021. Micromechanical and macromechanical approaches for the analysis of periodic masonry structures.
[249] Sansoni, C., 2021. Seismic vulnerability assessment of exiting URM structures through a simplified analytical method.
[250] American Concrete Institute. ACI 318-08: Building Code. Requirements for Structural Concrete and Commentary; ACI Committee 318; American Concrete Institute: Farmington Hills, MI, USA, 2008.
[251] Masonry Standards Joint Committee. ACI-530-08/ASCE 5-08/TMS 402-08: Building Code. Requirements for Masonry Structures; Masonry Standards Joint Committee: Farmington Hills, MI, USA, 2004.
[252] UK National Standards Body. BS 5628-2: Code of practice for the use of masonry. In Part 2: Structural Use of Reinforced and Prestressed Masonry; UK National Standards Body: London, UK, 2005.
[253] Deutsches Institut für Normung. DIN 1045-1: Tragwerke aus Beton, Stallbeton und Spannbeton. In Teil 1: Bemessung und Konstruktion; Deutsches Institut für Normung: Berlin, Germany, 2008.
[254] Bureau de Normalisation. NBN B 03-003: Deformations des structures. In Valeurs limites de deformation—Batiments; Bureau de Normalisation: Brussel, Belgium, 2003.
[255] European Committee for Standardization. EN 13747: 2010. Precast Concrete Products—Floor Plates for Floor Systems; European Committee for Standardization: Brussels, Belgium, 2010.
[256] Polish Committee for Standardization. PN-B-03264: 2002: Reinforced and prestressed concrete structures - Static calculations and design; Polish Committee for Standardization: Warsaw, Poland, 2002.
[257] Jarmontowicz, R. and Sieczkowski, J., 2006. Wytrzymałość muru na ściskanie-propozycje do normy PN-B-03002: 2006. Inżynieria i Budownictwo, 62, pp.483-485.
[258] Drougkas, A., Esposito, R., Messali, F. and Sarhosis, V., 2021. Analytical models to determine in-plane damage initiation and force capacity of masonry walls with openings. Journal of Engineering Mechanics, 147(11), p.04021088.
[259] Calvi, G.M., Priestley, M.J.N. and Kowalsky, M.J., 2007, December. Displacement-based seismic design of structures. In New Zealand conference on earthquake engineering (Vol. 2007). IUSS press.
[260] Rezaie, Amir, Michele Godio, and Katrin Beyer. "Experimental investigation of strength, stiffness and drift capacity of rubble stone masonry walls." Construction and Building Materials 251 (2020): 118972.

Abstract

This PhD thesis presents a comprehensive investigation into the performance of air lime-based mortar masonry specifically focusing on the in-plane behavior of masonry at large scale. This study aims to address the knowledge gap in the structural applications of air lime-based mortars, which were frequently used before their substitutions with cement-based mortars due to their improved compressive strength. This study begins with a review of key topics related to masonry and air lime mortar properties at various scales both in terms of experimental testing and numerical modelling. Then it proceeds with an analysis of the properties of the materials used in the research: air lime mortars and clay brick units. Following this, the research delves specifically into the mechanical properties of the masonry constituents, in terms of large-scale testing. This includes lateral cyclic pushover tests and vertical shearing tests on masonry walls on deflecting members to evaluate their structural behavior under complex loading conditions.

Numerical modelling techniques, particularly those relevant to industry and based on finite element methods (FEM), are then employed to simulate the large-scale behavior of the masonry. These models are validated against experimental results and used to predict performance and optimize design parameters. Additionally, current code parameters and recommendations are compared to the performance of air lime-based masonry to assess the safety and reliability of standard predictions for masonry design. Key findings highlight the potential ductility of air lime-based mortars and the masonry constructed with them, demonstrating their ability to sustain significant loads while exhibiting deformation characteristics. This indicates their viability for structural applications, particularly in the context of new masonry buildings where the sustainability of materials is becoming increasingly important. The research acknowledges the importance of considering additional aspects of air lime-based mortars, such as the long-term effects of the carbonation process and the benefits of incorporating recycled materials into their construction. By addressing critical research areas in the context of air lime mortars in full scale masonry applications, this thesis aims to rediscover the potentiality of air lime-based mortar masonry, ensuring its continued use in modern building practices and contributing to more sustainable and resilient construction methods.

List of Figures

Figure 1: Schematic example of masonry cavity wall **(a)** and masonry façade **(b)**. 2

Figure 2: Examples of masonry from different historical periods: Pont du Gard (50) **(a)**, Church of Christ the Worker and Our Lady of Lourdes (1958) **(b)**, Amiens Cathedral (c. 1300) **(c)** and a modern masonry façade **(d)**. 5

Figure 3: Representation of silicate structures: silicon tetrahedral unit **(a)** and octahedral unit **(b)**. Adapted from [18]. 6

Figure 4: Examples of correlation between constituent proportions and minimum of compressive strength from different: polish PN-EN 1996-1 [37] **(a)** and Italian NTC-2018 [38] **(b)**. 9

Figure 5: Closed loop of air lime. 11

Figure 6: Historical brick ready to be tested **(a)** and mortar fragment ready to be tested according double punch compressive procedure **(b)**. 12

Figure 7: XRD patterns of three bricks **(a)** and phase content of the bricks determined from semi-quantitative phase analysis using the RIR method **(b)** [60]. 13

Figure 8: XRD patterns of three mortars **(a)** and phase content of the mortars determined from semi-quantitative phase analysis using the RIR method **(b)** [59]. 13

Figure 9: SEM with elemental maps of brick CB1 **(a)** brick CB2 **(d)**. Micro-CT of bricks CB1**(b)**, CB2 **(e)** and CB3 **(c)** [60]. 15

Figure 10 Micro-CT and petrographic thin section of mortars MR1 **(a-d)**, MR2 **(b-e)** and MR3 **(c-f)** with details of the porosity evidenced in green areas [59]. 15

Figure 11: Hierarchy of failure modes for masonry buildings from Lesvos case study [81]: masonry disgregation **(a)**, out of plane mode **(b)** and in-plane mode **(c)**. 17

Figure 12: Examples of diagonal shear cracking through **(a)** mortar joints and **(b)** through bricks for masonry cavity walls. Adapted by [82]. 18

Figure 13: Typical response of masonry couplet tested in tension **(a)** and result for the actual bonding cross-section (evidenced in red) from tensile prism made of clay units and mortar with volumetric proportions 1:2:9 of cement:lime:sand from Van der Pluijm [84] **(b)**. 19

Figure 14: Typical wrench bond test set-up as for EN1052-5 [89] **(a)**. Failure modes involved in flexural tests as for EN1052-2 [91]: parallel to bed joints **(b)** and perpendicular to bed joints **(c)**. Adapted from Singhal et al. [92]. 19

Figure 15: Results from shear test on couplet subjected to constant vertical load F_n **(a)** Envelope model of the interface brick-mortar for increasing level of pre-compression **(b)**. Adapted from Van Der Pluijm [84]. 20

Figure 16: Compressive stress-strain relationship proposed by Kaushik et al. [99]. 22

Figure 17: Typical test set up scheme for diagonal compressive test on masonry wallettes. From Silva et al. [106]. 24

Figure 18: Representation of the tensional state at the center of the panel according to ASTM [111] and RILEM (Frotch) [113] interpretations, by the Mohr's circles. (σ_x, σ_y represent axial stresses at the center of the panel while τ_{xy} denotes the shear stresses acting in both the horizontal and vertical directions, σ_I and σ_{II} principal stresses, *C* center of the Mohr circle, *R* radius of the Mohr circle, *P* diagonal load applied). 25

Figure 19: Mohr's circles relative to the initial state of the panel (green) defined with coordinates (σ_0; $p\ \tau_0$) of compressive and shear stress, failure associated to Turnšek and Čačovič (black) with maximum shear stress $p\ \tau_t$ corresponding to the σ_t principal tensile stress [115] and failure for pure shear stress (ASTM) (blue) [111]. Adapted from Augenti et al. [14]. (*C* center of the Mohr circle, *R* radius of the Mohr circle, *V* horizontal load applied, *p* factor for the redistribution of the shear stresses at center of the panel). 25

Figure 20: Test set up **(a)** and specimens **(b)** adopted in the experimental investigation by Kubica [127]. 26

Figure 21: Example of failure of wallettes made of clay solid bricks (a) and AAC blocks with common joints (b) tested without pre-compression (top figures) and with pre-compression (bottom figures) - from Kubica [127]). 27

Figure 22: Vertical shear test set up developed at SUT [125]. 27

Figure 23: Typical vertical shear stress-angular deformation response [125] **(a)**. Crack pattern for clay masonry wallettes subjected to vertical shear loads with zero pre-compression p and 1.5 MPa of pre-compression p2. Adapted from Piekarczyk [128] **(b)**. 28

Figure 24: Test stand: 1 – steel frame, 2 – force gauge with range with the range to 500 kN, 3 – hydraulic jack with the range to 500 kN, 4 – steel beam, 5 – reinforced concrete top beam, 6 – tested wall, 7 – members of the system for measuring the vertical displacements, 8 – flexible support (steel beam), 9 – external support of the beam, 10 – elements of the system enforcing vertical displacements, 11,12,13 – hydraulic jack with range to 150 kN, 14 – screws for fixing the deflections. From Piekarczyk [131]. 29

Figure 25 Crack patter of calcium silicate masonry walls 4.55 x 2.45 m tested without vertical loads and increasing vertical displacements **(a)** and with increasing vertical load and deflection **(b)**. Adapted from Piekarczyk [139]. 30

Figure 26: In-plane masonry walls failure modes when subjected to vertical and lateral load: rocking flexural behavior **(a)**, toe crushing **(b)**, diagonal shear sliding **(c)**, diagonal cracking **(d)** and horizontal sliding **(e)**. 31

Figure 27: Failure mechanisms considered in micro-modelling: joint tension cracking **(a)**, joint slip **(b)**, unit tension cracking **(c)**, unit diagonal cracking **(d)** and masonry crushing **(e)**. Adapted from Lourenço and Rots [166]. 36

Figure 28: Composite yield surface proposed by Lourenço and Rots [166]. 36

Figure 29: Yield surface adopted by Majewski in the invariant stress plane (I_1–I_2) with f_{ccc} triaxial compression and f_{ttt} triaxial tension, along with info of its three-dimensional segment envelope, as adapted by Kubica [174]. ... 38

Figure 30: Numerical model for vertical shearing load tests **(a)** and principal stresses in the heterogeneous numerical model **(b)**. Adapted from Kubica et al. [174]. 38

Figure 31: Uniaxial stress-stain relationships of Total Strain Crack Model of DIANA Fea: **(a)** tension and **(b)** compression with secant loading/reloading. Uniaxial stress stain relationships of Concrete Damage Plasticity model of Abaqus: **(c)** tension and **(d)** compression with loading/reloading defined by damage parameters d_t and d_c. 40

Figure 32: Multi-scale Fem model based on homogenization approach adapted from Bertolesi et al. [191]. 41

Figure 33: Equivalent frame method discretization for a masonry façade. Adapted from Raka et al. [194]. 43

Figure 34: Three-dimensional macro-element with axial and shear springs elaborated by Pantò et al. [203] for in/out of plane loads **(a)**. Mesh discretization for infill masonry wall subjected to both in and out of plane loads **(b)** [204-205]. 43

Figure 35: View of the frogged clay solid bricks used in presented investigations. 45

Figure 36: Full size units in submersion for water absorption measurements. 46

Figure 37: Flexural tests on full unit samples with static scheme and dimension in mm on the plain side **(a)**, on the frogged side **(b)** and example of the brick ready to be tested (on plain side) **(c)**. 47

Figure 38: Failed unit with regular surface **(a)** and failed sample with irregular development of cracks from the middle cross-section **(b)**. 47

Figure 39: Compressive tests on full units with static scheme and dimension in mm **(a)** and position of the sample in the testing machine DIC system **(b)**. 48

Figure 40: Expulsion of material in correspondence of the peak load **(a)** and top view of failed brick not able to sustain more vertical loads **(b)**. 49

Figure 41: Adopted sand granulometry from Zagaroli et al. [212]. 49

Figure 42: Static scheme of three-point bending test EN 1015-11 [53] with dimensions in mm **(a)** and example of the prims ready to be tested **(b)**. From Zagaroli et al. [212]. 51

Figure 43: Compression tests conducted on samples of half prism, displaying the static scheme **(a)**, and view of the relative sample positioned within the testing apparatus **(b)**. From Zagaroli et al. [212]. 51

Figure 44: Failed sample from 3-point bending test for MIX-1 **(a)** and for MIX-2 **(c)**. Failed samples from compressive test for MIX-1 **(b)** and MIX-2 **(d)**. From Zagaroli et al. [212]. 51

Figure 45: Axial stress – transversal strain **(a)** and axial strain **(b)** for MIX-1. From Zagaroli et al. [212]. 53

Figure 46: Axial stress – transversal strain **(a)** and axial strain **(b)** for MIX-2. From Zagaroli et al. [212]. 53

Figure 47: Axial stress – Poisson's ratio for MIX-1 **(a)** and MIX-2 **(b)**..... 53
Figure 48: Failure modes evidenced for cylinders in compression: tensile cracks **(a)** and conical expulsion from the lateral surfaces **(b)**. From Zagaroli et al. [212]..... 54
Figure 49: Scheme of the splitting tensile strength test **(a)** and typical sample ready to be tested in the test set up **(b)**. From Zagaroli et al. [212]. 54
Figure 50: Tensile strength – vertical displacement relationships for MIX-1 **(a)** MIX-2 **(b)**. From Zagaroli et al. [212]..... 55
Figure 51: Typical failed sample after splitting load for both mortars. Adapted from Zagaroli et al. [212]. 55
Figure 52: Test set-up for fracture energy evaluation **(a)** and sample specifics with dimensions in mm **(b)**. From Zagaroli et al. [212]. 56
Figure 53: Load-deflection **(a)** and CMOD **(b)** for MIX-1. From Zagaroli et al. [212]. 56
Figure 54: Load-deflection **(a)** and CMOD **(b)** for MIX-2. From Zagaroli et al. [212]. 56
Figure 55: Typical failed sample after splitting load. Adapted from Zagaroli et al. [212]..... 57
Figure 56: Static scheme for the shear triplet test **(a)** and typical triplet ready to be tested **(b)**..... 58
Figure 57: Vertical load F and vertical relative displacement for different level of pre-compression p of triplets made of mortar MIX-1 **(a)** and MIX-2 **(b)**..... 59
Figure 58: Typical failure mode for triplets made of mortar MIX-1 in correspondence of the highest level of p for mortar MIX-1 with failure at the interface mortar-brick (Type A.1) **(a)** and MIX-2 with shear failure along the brick (Type A.4) **(b)**. 60
Figure 59: Dimensions of the chosen wallettes for masonry compressive testing align with the specifications outlined in EN 1052-1 [95] **(a)** and typical sample in the machine ready to be tested **(b)**..... 60
Figure 60: Experimental results in terms of compressive axial stress and strain for masonry made of MIX-1 **(a)** and MIX-2 **(b)**. Different color for each test performed. 61
Figure 61: Crack development for masonry made of mortar MIX-1 **(a)** and MIX-2 **(b)**. Cracks evidenced with red lines. Adapted from [223]. 61
Figure 62: Dimensions of wallettes for diagonal compressive tests **(a)** and typical wallettes in the set-up before the tests **(b)**..... 62
Figure 63: Configuration of the LVDT system: **(a)** Horizontal (H) and vertical (V) LVDTs showing the corresponding elongation (ΔH) and shortening (ΔV); **(b)** Setup of the DIC (Digital Image Correlation) measurement system. .. 63
Figure 64: Minor differences between LVDT measurements on one side of the wall and DIC measurements on the other side for wall MIX-1_DCT_1 **(a)**, while pronounced differences in vertical displacements observed for wall MIX-1_DCT_2 **(b)**. 63
Figure 65: Pronounced differences between vertical LVDT measurements on one side of the wall and DIC measurements on the other side for wall MIX-2_DCT_1 **(a)**, while minor differences in vertical and horizontal displacements observed for wall MIX-2_DCT_2 **(b)**..... 64
Figure 66: Experimental shear stress - shear strain relationships for masonry made of mortar MIX-1 **(a)** and MIX-2 **(b)**..... 65
Figure 67: Failure mode of masonry specimens made of mortar type MIX-1 (116) **(a)** and made of mortar type MIX-2 (129) **(b)**..... 66
Figure 68: Dimensions (mm) of the walls subjected the in plane vertical loads. 67
Figure 69: Static diagram showing the shear force distribution and load application method, where *P* represents the increasing vertical load applied by the actuator, and P_g corresponds to the load due to the self-weight of the wall and testing instrumentation..... 67
Figure 70: Test set-up for in-plane vertical shearing quasi-static test adopted in this study. 68
Figure 71: Measurement system for one side both masonry walls' type with different distance s. 69
Figure 72: Rectangular measurement frames with dimensions of 500 x 900 mm. Frame dimensions and shear deformation angles θ_1, θ_2, θ_3 and θ_4 associated with the generic deformed shape. 69

Figure 73: First crack formation **(a)** and additional crack propagation at the base layer due to increasing deflection **(b)** for VS_116_350. 71
Figure 74: Crack patterns on back and front views of the wall made of mortar VS_116_350. 71
Figure 75: Shear stress-shear strain for all the θ_i angles evaluated for the **(a)** SIDE-A and **(b)** SIDE-B for masonry VS_116_350. 72
Figure 76: Shear stress-shear strain **(a)** and shear modulus-shear stress **(b)** relationships for the wall made with mortar VS_116_350. 72
Figure 77: Total vertical load – deflection for the wall made with mortar VS_116_350. 73
Figure 78: First crack formation **(a)** and crack pattern development at peak load **(b)** for VS_116_600. 73
Figure 79: Crack patterns on back and front views of the wall made of mortar VS_116_600. 74
Figure 80: Shear stress-shear strain for all the θi angles evaluated for the **(a)** SIDE-A and **(b)** SIDE-B for masonry VS_116_600. 74
Figure 81: Shear stress-angular strain **(a)** and transversal stiffness shear stress **(b)** relationships for the wall made with mortar VS_116_600. 75
Figure 82: Total vertical load – deflection for the wall made with mortar VS_116_600. 75
Figure 83: Symmetric response for initial loads **(a)** and development of cracking on both side of the wall for increasing loads **(b)** for VS_129_350. 76
Figure 84: Crack patterns on back and front views of the wall made of mortar VS_129_350. 76
Figure 85: Shear stress-shear strain for all the θi angles evaluated for the **(a)** SIDE-A and **(b)** SIDE-B for masonry VS_129_350. 77
Figure 86: Shear stress-angular strain **(a)** and transversal stiffness shear stress **(b)** relationships for the wall made with mortar VS_129_350. 77
Figure 87: Total vertical load – deflection for the wall made with mortar VS_129_350. 77
Figure 88: Initial crack formation **(a)** and concentration of deformation at both sides of the wall for increasing loads **(b)** for VS_129_600. 78
Figure 89: Crack patterns on back and front views of the wall made of mortar VS_129_600. 79
Figure 90: Shear stress-shear strain for all the θ_i angles evaluated for the **(a)** SIDE-A and **(b)** SIDE-B for masonry VS_129_600. 79
Figure 91: Shear stress-angular strain **(a)** and transversal stiffness shear stress **(b)** relationships for the wall made with mortar VS_129_600. 80
Figure 92: Total vertical load – deflection for the wall made with mortar VS_129_600. 80
Figure 93: Dimensions (mm) of the walls type A subjected the in plane lateral cyclic loads. 81
Figure 94: Dimensions (mm) of the walls type B subjected the in plane lateral cyclic loads. 81
Figure 95: Test set-up for the lateral cyclic response with wall ready to be tested. 82
Figure 96: History of lateral displacements imposed for the cyclic test for walls type A **(a)** and type B **(b)**. 83
Figure 97: Quantities for secant stiffness evaluation. 83
Figure 98: Quantities for hysteretic dissipation evaluation. 84
Figure 99: Bilinearization adopted for negative and positive cyclic direction. 85
Figure 100: Initial crack at the base with consequent rocking movement **(a)**, concentration of cracks at the base **(b)**, and final crack pattern in correspondence of failure for masonry wall HC_116_A_15 **(c)**. 85
Figure 101: Initial crack formation **(a)**, development of cracks at the center of the panel **(b)**, and crack pattern one cycle prior to failure for masonry wall HC_116_A_30 **(c)**. 86
Figure 102 Initial crack at the base with consequent rocking movement **(a)**, minor crack development after rocking movement **(b)**, and **(c)** failure crack pattern for masonry wall HC_129_A_15. 86
Figure 103: Initial crack formation **(a)**, development of cracks at the base due to corner tension **(b)**, and **(c)** crack pattern one cycle prior to failure for masonry wall HC_129_A_30. 87
Figure 104: Experimental cycles (gray), backbone (black) and bilinear curve (red) for **(a)** HC_116_A_15, **(b)** HC_116_A_30, **(c)** HC_129_A_15 and **(d)** HC_116_A_30. 88

Figure 105: Secant stiffness decay vs drift for **(a)** HC_116_A_15, **(b)** HC_116_A_30, **(c)** HC_129_A_15 and **(d)** HC_116_A_30. 88
Figure 106: Equivalent viscous damping vs drift for **(a)** HC_116_A_15, **(b)** HC_116_A_30, **(c)** HC_129_A_15 and **(d)** HC_116_A_30. 89
Figure 107: Initial shear response with limited damage **(a)**, reduction in base shear due to rocking and concentration of cracks at the corner **(b)**, and **(c)** crack pattern in correspondence of the failure for masonry wall HC_116_B_15. 89
Figure 108: Initial crack formation **(a)**, development of diagonal cracking **(b)**, and **(c)** final crack pattern for masonry wall HC_116_B_30. 90
Figure 109: First visible crack formation **(a)**, propagation of previous cracking **(b)**, and **(c)** final diagonal cracking for masonry wall HC_129_B_15. 90
Figure 110: Initial crack formation **(a)**, development of shear/crushing cracks at the center of the panel **(b)**, and **(c)** crack pattern in correspondence of the failure for masonry wall HC_129_B_30. 91
Figure 111: Experimental cycles (gray), backbone (black) and bilinear curve (red) for **(a)** HC_116_B_15, **(b)** HC_116_B_30, **(c)** HC_129_B_15 and **(d)** HC_116_B_30. 91
Figure 112: Secant stiffness decay vs drift for **(a)** HC_116_B_15, **(b)** HC_116_B_30, **(c)** HC_129_B_15 and **(d)** HC_116_B_30. 92
Figure 113: Equivalent viscous damping vs drift for **(a)** HC_116_B_15, **(b)** HC_116_B_30, **(c)** HC_129_B_15 and **(d)** HC_116_B_30. 92
Figure 114: Comparisons strength of mortar mixes. From Zagaroli et al. [212]. 94
Figure 115: Coulomb-Mohr criterion in terms of shear-normal stress for mixes MIX-1 and MIX-2. 96
Figure 116: Average experimental compressive stress-strain comparison for masonry made of mortar MIX-1 and MIX-2. 97
Figure 117: Elastic modulus versus compressive strength from experimental tests for masonry made of mortar MIX-1 **(a)** and MIX-2 **(b)** with relative minimum (E_{min}), maximum (E_{max}) and average (E_{av}) values. 99
Figure 118: Average shear stress - shear strain relations for masonry made of mortar MIX-1 and MIX-2 in diagonal compression test. 99
Figure 119: Total vertical load vs mid-displacement comparisons of MIX-1(116) and MIX-2(129) for the spacing of **(a)** 350 mm and of **(b)** 600 mm. 100
Figure 120: Shear stress vs angular strain comparisons of MIX-1(116) and MIX-2(129) for the spacing of **(a)** 350 mm and of **(b)** 600 mm. 101
Figure 121: Shear stiffness vs shear stress comparisons of MIX-1(116) and MIX-2(129) for the spacing of **(a)** 350 mm and of **(b)** 600 mm. 102
Figure 122: Bilinear curves positive (+) and negative (-) for masonry walls made of MIX-1(116) and MIX-2(129) for **(a)** type A and **(b)** type B walls. 103
Figure 123: Comparison average positive/negative bilinear shear load V for all tested masonry. 104
Figure 124: Comparison average positive/negative bilinear ultimate displacements Δu for all tested masonry. 105
Figure 125: Comparison average positive/negative bilinear ductility μ for all tested masonry. 105
Figure 126: Secant stiffness decay vs drift for masonry walls made of MIX-1(116) and MIX-2(129) for **(a)** type A and **(b)** type B walls. 106
Figure 127: Equivalent viscous damping vs drift for masonry walls made of MIX-1(116) and MIX-2(129) for **(a)** type A and **(b)** type B walls. 106
Figure 128: Macro-mechanical fem model for the compressive test adopted for both masonry types. 109
Figure 129: Comparison of uniaxial compression stress-strain curves for masonry made of MIX-1 **(a)** and MIX-2 **(b)**, showing experimental data (black lines) at minimum and maximum values alongside numerical results (blue line for MIX-1 and orange line for MIX-2). 109
Figure 130: Macro-mechanical fem model for the diagonal compressive test adopted for both masonry types. 110

Figure 131: Comparison of vertical load-relative horizontal and vertical displacements for masonry made of MIX-1 **(a)** and MIX-2 **(b)**, showing experimental data (black lines) at minimum and maximum values alongside numerical results (blue line for MIX-1 and orange line for MIX-2). 111
Figure 132: Macro fem model for the wall subjected to vertical loads. 112
Figure 133: Macro-mechanical fem model for the wall subjected to lateral loads (light blue line representing the tying). 113
Figure 134: Experimental vs numerical vertical load-mid-point deflection for wall **(a)** VS_116_600 and **(b)** VS_129_600. 114
Figure 135: Modelling results of the crack patterns in correspondence of crack formation at point A for **(a)** VS_116_600 and **(b)** VS_129_600. 114
Figure 136: Experimental vs numerical vertical load-mid-point deflection for wall **(a)** VS_116_350 and **(b)** VS_129_350. 114
Figure 137: Modelling results of the crack patterns in correspondence of crack formation at point A for **(a)** VS_116_350 and **(b)** VS_129_350. 115
Figure 138: Experimental vs numerical lateral test results for **(a)** positive and **(b)** negative load direction for masonry HC_116_A_30. 116
Figure 139: Experimental vs numerical lateral test results for **(a)** positive and **(b)** negative load direction for masonry HC_129_A_30. 117
Figure 140: Principal crack strains at peak load for **(a)** HC_116_A_30 and **(b)** HC_129_A_30. 117
Figure 141: Experimental vs numerical lateral test results for **(a)** positive and **(b)** negative load direction for masonry HC_116_A_15. 118
Figure 142: Experimental vs numerical lateral test results for **(a)** positive and **(b)** negative load direction for masonry HC_129_A_15. 118
Figure 143: Principal crack strains at peak load for **(a)** HC_116_A_15 and **(b)** HC_129_A_15. 118
Figure 144: Experimental vs numerical lateral test results for **(a)** positive and **(b)** negative load direction for masonry HC_116_B_30. 119
Figure 145: Experimental vs numerical lateral test results for **(a)** positive and **(b)** negative load direction for masonry HC_129_B_30. 119
Figure 146: Principal crack strains at peak load for **(a)** HC_116_B_30 and **(b)** HC_129_B_30. 120
Figure 147: Experimental vs numerical lateral test results for **(a)** positive and **(b)** negative load direction for masonry HC_116_B_15. 120
Figure 148: Experimental vs numerical lateral test results for **(a)** positive and **(b)** negative load direction for masonry HC_129_B_15. 121
Figure 149: Principal crack strains at peak load for **(a)** HC_116_B_15 and **(b)** HC_129_B_15. 121
Figure 150: Simplified static scheme for the determination of the non-dilatational strain angle Θ_{sd}. Adapted from Kubica [127]. 124
Figure 151: Scheme of deformed wall subjected to irregular settlements for panel-scale elements for local $\Theta_{sd,,L}$ and global non-dilatational strain angle $\Theta_{sd,G}$. Adapted by Kubica [127]. 125
Figure 152: Strength domains for the tested masonry walls of series HC_116_A with dots indicating the experimental values of peak lateral shear load V in relation to the corresponding pre-compression load N. .. 128
Figure 153: Strength domains for the tested masonry walls of series HC_116_B with dots indicating the experimental values of peak lateral shear load V in relation to the corresponding pre-compression load N. .. 129
Figure 154: Strength domains for the tested masonry walls of series HC_129_A with dots indicating the experimental values of peak lateral shear load V in relation to the corresponding pre-compression load N. .. 129
Figure 155: Strength domains for the tested masonry walls of series HC_129_B with dots indicating the experimental values of peak lateral shear load V in relation to the corresponding pre-compression load N. .. 130
Figure 156: Evaluation of b based on experimental data from this study. 131

Figure 157: Shear strength domains modification for tested masonry walls of series HC_116_A with dots indicating the experimental values of peak lateral shear load V in relation to the corresponding pre-compression load N. 131

Figure 158: Shear strength domains modification for tested masonry walls of series HC_126_A with dots indicating the experimental values of peak lateral shear load V in relation to the corresponding pre-compression load N. 132

Figure 159: Geometric configuration of the frogged brick unit, with associated dimensions **(a)**. Idealized cross-sectional model divided into three rectangular areas (1, 2, and 3) for the calculation of inertial properties **(b)**. 141

Figure 160: Geometric representation of the standard mortar specimen **(a)**. Schematic of the three-point bending test setup used for flexural strength determination, where P is the applied load, *L* is the total span length, and b_r is the distance between the supports **(b)**. 143

List of Tables

Table 1: Results of compressive strength of cubic sample from bricks and plates cut from standard samples of the mortar. Elaboration from [59-60]. 16

Table 2: Analytical code expressions for the shear strength of masonry walls subjected to lateral loads for American ASCE 41-13 [157] and New Zealand NZSEE-17 [158]. In table: α: 1 or 0.5 for fixed-fixed or cantilever boundary conditions, P_D: dead load, P_W: weight load, L: wall length, h_{eff}: height to resultant of seismic force, f_a: axial compressive stress, f_m: masonry compressive strength, f_{dt}: masonry diagonal tensile strength, β: 0.67 for h_{eff}/L>1.5 or1 for h_{eff}/L<1.5, μ_f: friction coef., c: cohesion, t: wall thickness, υ_{te}: mean bed-joint strength. 33

Table 3: Analytical code expressions for the shear strength of masonry walls subjected to lateral loads for European EC6 [13] - EC8 [159] and Italian NTC-18 [160]. In the table, identical parameters as those in Tab.2 are included, along with additional parameters: b: $1/\beta$, A_w: area of horizontal wall cross-section, γ_M: partial safety factor, f_{tk}: characteristic masonry diagonal tensile strength, l_c: compressed part of the wall, σ_d: axial stress, f_{vk}: characteristic shear strength equal to $f_{vk0}+0.4\ \sigma_d$ for filled head and bed joints or $0.5f_{vk0}+0.4\ \sigma_d$ for only filled bed joints, f_{vk0}: the characteristic value of f_{vm0} which is how the NTC indicate the cohesion c. 33

Table 4: Drift capacity models for in plane behavior masonry walls according to different codes. In table: h: height to zero bending moment, l: length of the wall. 34

Table 5: Overview of the test types carried out on brick samples. 46

Table 6: Values of the flexural strength with load direction on the plain side ($\sigma_{f\text{-}Plain}$) and frogged side ($\sigma_{f\text{-}Frog}$). 47

Table 7: Compressive elastic mechanical properties of masonry units. 48

Table 8: Mortar mix compositions of mixed cement-lime mortars [212]. 50

Table 9: Testing protocol with dimension specifications. Adapted from Zagaroli et al. [212]. 50

Table 10: Flexural and compressive strength results for EN 1015-11 [53] test. From Zagaroli et al. [212]. 52

Table 11: Cylindrical compressive test results for both mixes. From Zagaroli et al. [210]. 52

Table 12: Average peak tensile splitting strength for both mixes. 54

Table 13: Fracture energy results according two different approaches for both mixes. From Zagaroli et al. [212]. 56

Table 14: Test samples and series for small masonry assemblage. 58

Table 15: Shear stresses – normal pre-compression stress of masonry triplets. 59

Table 16: Mechanical parameters of masonry tested in compression. Adapted from [223]. 61

Table 17: Mechanical parameters of masonry wallettes tested in diagonal compression. 65

Table 18: Programme of tests of masonry walls subjected to vertical shearing tests. 68

Table 19: Summary of critical and peak load values, along with the corresponding critical mid-deflection, ultimate deflection and relative ratios, for both tested masonry walls. 78

Table 20: Summary of critical and peak shear stresses, angular deformation for both masonries tested for both sides. 80

Table 21: Designation of the test specimens for the lateral cyclic pushover tests. 82

Table 22: Peak positive/negative (+/-) lateral loads and corresponding displacements. 93

Table 23: Linearized quantities (Elastic modulus K_e, elastic displacement Δ_e, ultimate displacement Δ_u, lateral load V and ductility μ) for positive and negative direction. 93

Table 24: Mechanical parameters of masonry tested in compression. 94

Table 25: Mohr-Coulomb bond properties evaluated from the tests. 96

Table 26: Prediction of the peak compressive strength (*Characteristic value). 98

Table 27: Comparison between critical shear stresses (τ_{cr}) from VS tests and maximum shear stresses (τ_{max}) from DCT tests for materials 116 (MIX-1) and 129 (MIX-2), including the τ_{cr}/τ_{max} ratio. 102

Table 28: Difference in mortar and lateral base shear strength for masonry walls made with difference mixes. 107

Table 29: Parameters for the TSC model adopted. 108

Table 30: Masonry deflection δ and vertical load Fv prediction in correspondence of crack first cracking and critical value from experimental tests with relative differences. 116
Table 31: Prediction of the masonry peak horizontal load (Fh-num) by numerical models and the corresponding peak experimental strength, along with the relative differences in both positive and negative directions. 122
Table 32: Several codes reviewed by Kania et al. [137] for masonry subjected to vertical deflection. 123
Table 33: Admissible values of non-dilatational strain angle Θ_{adm} [miliradians] given in [257]. 124
Table 34: Comparison vertical displacement limits according to several codes reviewed by Kania et al. [137] for masonry made with MIX-1 (116). 127
Table 35: Comparison vertical displacement limits according to several codes reviewed by Kania et al. [137] for masonry made with MIX-2 (129). 127
Table 36: Comparison non-dilatational strain angles according to PN-B-03002:2006 [257] and experimental ones for both masonry types and sides. 128
Table 37: Prediction of the masonry peak horizontal load (Fh) by existing methods and the corresponding peak experimental strength, along with the relative differences in both positive and negative directions. 130
Table 38: Drift ratios for all masonry specimens in positive (+) and negative (-) load directions at SDLS. 132
Table 39: Drift ratios for all masonry specimens in positive (+) and negative (-) load directions at NCLS. 133
Table 40: Test results for the determination of the initial rate of absorption $c_{w,i}$. 140
Table 41: Elimination of extreme value for the measurement of the initial rate of absorption $c_{w,i}$. 140
Table 42: Test results for the determination of the water absorption W_a. 140
Table 43: Elimination of extreme value for the measurement of the water absorption W_a. 140
Table 44: Geometric dimension of tested bricks for flexural strength with load application on the plain side. 141
Table 45: Inertial properties of tested bricks for flexural strength with load application on the plain side. 141
Table 46: Flexural strength with load application on the plain side ($\sigma_{f\text{-}Plain}$) and elimination of extreme value. 142
Table 47: Geometric dimension of tested bricks for flexural strength with load application on the frogged side. 142
Table 48: Inertial properties of tested bricks for flexural strength with load application on the frogged side.. 142
Table 49: Flexural strength with load application on the plain side ($\sigma_{f\text{-}Frog}$) and elimination of extreme value. 142
Table 50: Brick compressive strength σ_c evaluated on full units with elimination of one extreme value. 143
Table 51: Flexural strength σ_{fl} determination for prisms made with mortar MIX-1. 144
Table 52: Elimination of extreme value for the measurement of the flexural strength σ_{fl} for prisms made with mortar MIX-1. 144
Table 53: Flexural strength σ_{fl} determination for prisms made with mortar MIX-2. 144
Table 54: Elimination of extreme value for the measurement of the flexural strength σ_{fl} for prisms made with mortar MIX-2. 145
Table 55: Compressive strength σ_c determination for prisms made with mortar MIX-1 with elimination of one extreme value. 145
Table 56: Compressive strength σ_c determination for prisms made with mortar MIX-2 with elimination of one extreme value. 145
Table 57: Splitting tensile strength σ_t determination for prisms made with mortar MIX-1 with elimination of one extreme value. 146
Table 58: Splitting tensile strength σt determination for prisms made with mortar MIX-2 with elimination of one extreme value. 146
Table 59: Compressive strength f_c determination for masonry made with mortar MIX-1 with elimination of one extreme value. 147
Table 60: Elastic modulus E_c determination for masonry made with mortar MIX-1 with elimination of one extreme value. 147
Table 61: Ductility μ determination for masonry made with mortar MIX-1 with elimination of one extreme value. 147

Table 62: Compressive strength f_c determination for masonry made with mortar MIX-2 with elimination of one extreme value. 148
Table 63: Elastic modulus E_c determination for masonry made with mortar MIX-2 with elimination of one extreme value. 148
Table 64: : Ductility μ determination for masonry made with mortar MIX-2 with elimination of one extreme value. 148